Development of non-invasive, optical methods for central cardiovascular and blood chemistry monitoring

Jake Donald Campbell

A thesis presented for the degree of
Doctor of Philosophy
in
Mechanical Engineering
at the
University of Canterbury,
Christchurch, New Zealand.

24 May 2022

ACKNOWLEDGEMENTS

I would like to thank many people for their support over the duration of my thesis:

Firstly, I would like to thank my primary supervisor, Prof Chris Pretty, for encouraging me to pursue my PhD, and having confidence in my work. I always appreciate your visits to the Bio-engineering office, whether to provide advice, or for your uplifting conversations.

I am also grateful to my co-supervisors. Firstly, Dist Prof Geoffery Chase, who is ever enthusiastic, and encouraging for me pursuing commercialisation. Secondly, Prof Phil Bones for his willingness to take me on as a student and his signal processing guidance.

Also Jennifer Knopp, Chris Mckinlay, Jane Alsweiler, Lisa Mravicich, Sabine Huth, Rachel Smith, and Francis Pooke for helping acquire, and run the NICU trial so smoothly. I am honoured to have had your time, enthusiasm, and expert medical advice in the project.

To the technicians, Julian Murphy, Rodney Elliot, and Scott Lloyd, for helping build my sensors, especially the NICU sensors. The trial has been much more of a success with your inputs.

The bio-engineering office, from the 4pm disc golf rounds, to the willingness to collaborate on projects not their own, as well as undergraduates Connor Benton and Josie Dixon for aiding in sensor testing. Especially a big thanks to Lui Holder-Pearson, Lachlan McKenzie, Sarah Howe, for their hardware design skills around board design and circuit layout. The REWA program would not have been a success without such strong team.

To the UC Māori department and the MAI team (Grace, Rory and Mariah) for encouraging me to attend conferences and providing valuable perspectives aiding the direction of my research.

Finally, thanks to my family, Rae, Bruce, and Amy for being ever supportive, and my partner Lalitha, for your encouragement and enthusiasm.

ABSTRACT

Cardiovascular disease and sepsis are leading causes of mortality, morbidity and high cost in hospitals around the world. Failure of the circulatory system during cardiogenic shock and sepsis both can significantly impair the perfusion of oxygen through organs, resulting in poor patient outcome if not detected and corrected early.

Another common disorder which goes hand-in-hand with cardiovascular disease is Diabetes Mellitus. Diabetes is a metabolic disorder resulting from the inability of the body to regulate the level of glucose in the blood. The prevalence of diabetes worldwide is increasing faster than society's ability to manage cost effectively, with an estimated 9% of the world population diagnosed with metabolic disease.

The current gold standard measurements for venous oxygen saturation, arterial pulse wave velocity (PWV), and diabetes management through blood glucose concentration monitoring are all invasive. Invasive measurements increase risk of infection and complications, are often high cost and disposable, and have a low patient compliance to regular measurements.

The aim of this thesis is to develop non-invasive methods of monitoring these important dynamic physiological variables, including, venous oxygen saturation, pulse wave velocity, and blood glucose concentration. A novel photoplethysmography-based NIR discrete wavelength spectrometer was developed using LEDs to both emit light, and detect the light reflected back through the tissue. Using LEDs to detect light simplifies sensing circuit design, lowering hardware costs, allowing adaptable sensing specific to the needs of the user.

A reflectance pulse oximeter was developed to measure the oxygen saturation at both the external jugular vein, and carotid artery. Measuring the jugular venous pulse (JVP) allows estimation of the venous oxygen saturation through either the JVP, or through breathing induced variation of the JVP. In addition to oxygenation, the device developed is capable of adapting the sensing layout to measure the arterial pulse waveform at multiple sites along a peripheral artery, such as the carotid or radial. The PWV local to the carotid artery, and radial artery can then be measured, providing key information of cardiovascular risk. A novel algorithm for PWV measurement over multiple pulse waveforms was also developed. Expanding the sensor to use multiple different wavelength LEDs allow discrete spectroscopy in pulsatile blood. An absorption model of components in blood at specific wavelengths was created to isolate the spectral fingerprint of glucose.

The sensor successfully measured the oxygen saturation at the carotid artery, and external jugular vein across 15 subjects, giving mean oxygen saturations of 92% and 85% respectively, within the expected physiological ranges. Venous oxygen saturation calculated using breathing induced changes to JVP was 3.3% less than when calculated on the JVP alone, with a standard deviation of 5.3%, compared to 6.9%. Thus, future work on the sensor will focus on extraction of the breathing induced venous pulse, rather than measuring from the JVP itself.

The PWV on the carotid and radial artery was successfully measured within the expected physiological ranges, with the novel phase difference algorithm proving more robust to noise than the gold standard foot-foot method. The phase difference method returned a mean PWV at the radial artery of 4.7 $\pm 0.6\,\mathrm{m\,s^{-1}}$, and a mean CoV of 20%, compared to 4.0 $\pm 1.4\,\mathrm{m\,s^{-1}}$, and a moan CoV of 58% for the foot-foot method. The proof of concept PWV sensor gives promising results, but needs to be calibrated against invasive gold standards, such as aorta and femoral pressure catheters.

A glucose trial involving adult and neonatal subjects provided validation of the NIR non-invasive pulse glucometer. The sensor has an R^2 of 0.47, and a mean absolute relative difference (MARD) of 19% compared to gold standard reference measurements.

Clarke error grid analysis returns 85% of measurements in Zone A, 11% in Zone B, and 4% in Zone C. While the sensor is not as accurate as the gold standard invasive measurements, the ability to constantly measure without any pain or discomfort will help increase measurement compliance, improving user quality of life, plus further development may improve this.

Overall, this thesis provided novel contributions in non-invasive venous oxygen saturation, PWV, and glucose concentration monitoring. The adaptability of the sensor shows promise in helping reduce the pain and inconvenience of the current invasive measurements, especially in diabetes management, where the sensor has the most potential for impact.

CONTENTS

Abbreviations

BGC blood glucose concentration

CBF cerebral blood flow

CEG Clarke error grid

CGM continuous glucose monitor

$CMRO_2$ cerebral oxygen consumption

CoV coefficient of variation

DWT discrete wavelet transform

EJV external jugular vein

FIR finite impulse response

GMD geometric mean derivation

GPIO general purpose input/output

Hb haemoglobin

HbA_{1c} glycated haemoglobin

HbO_2 oxyhaemoglobin

ICU intensive care unit

IIR infinite impulse response

JVP jugular venous pulse

MARD mean absolute relative difference

NICU neonatal intensive care unit

NIR near infrared

OGTT oral glucose tolerance test

PEEP positive end expiratory pressure

PPG photoplethysmograph

PSD power spectral density

PWV pulse wave velocity

RMS root mean square

SaO_2 arterial oxygen saturation

$SjvO_2$ jugular venous oxygen saturation

$SpcO_2$ carotid artery oxygen saturation

$SpjvO_2$ pulse oximeter estimated jugular venous oxygen saturation

SpO_2 peripheral oxygen saturation

$SpvO_2$ peripheral venous oxygen saturation

SvO_2 venous oxygen saturation

TLS total least squares

+P positive predictive value

LIST OF FIGURES

Chapter 1

INTRODUCTION

This chapter outlines the primary motivation, goals and novel aspects of this thesis. Also presented here is a brief overview of the background physiology relevant to the research in this thesis. In particular, the cardiovascular system and the transfer of oxygen and glucose to cells in the metabolic system.

1.1 MOTIVATION

"*With a new principle and a simpler and less costly instrument within reach, sphygmography will rise into a definite and useful science.*" Holden and Newmark [1871].

Cardiovascular disease and sepsis are leading causes of mortality, morbidity and high cost in hospitals worldwide [Atlas Writing Group 2021]. Failure of the circulatory system during cardiogenic shock and sepsis can significantly impair the perfusion of oxygen through organs, resulting in poor patient outcomes if not detected and corrected early [Nunnally et al. 2021]. A pulse oximeter is a vital tool for measuring tissue perfusion in a clinical setting.

Pulse oximeters estimate SpO_2 and provide information on the amount of oxygen getting to the tissues through the arteries. However, the blood returning to the heart in the veins has no analogous sensor [Thiele et al. 2011]. Thus, a non-invasive method is needed to determine both SpO_2 and $SpvO_2$. Measuring SpO_2 and $SpvO_2$ can indicate oxygen consumption, for example, the cerebral oxygen consumption in the brain. Low-cost assessment of tissue perfusion by calculating the difference between SpO_2 and

$SpvO_2$ could potentially advance the diagnosis, care and management of cardiovascular disease and sepsis. Cerebral venous oxygen saturations can be obtained using pulsatile information from the carotid artery and external jugular vein representing a significant advance in clinical monitoring.

In addition to oxygen saturation into and out of the brain, the pulse oximeter can calculate arterial PWV [Colquhoun et al. 2012]. The velocity of the arterial pulse wave is a crucial indicator of cardiovascular risk [Vlachopoulos et al. 2010], Pulse wave velocity (PWV) is used as a surrogate to indicate arterial stiffness, with risk of health complications increasing with higher stiffness levels seen in higher PWV [Darwich et al. 2015]. However, the current gold standard technique for measuring PWV consists of invasive aortic and femoral catheters, putting the patient at increased risk of complications. Alternatively, a synchronised measurement of the pulse oximeter waveform at two locations could provide a reliable, non-invasive way to measure PWV.

Another common disorder that goes hand-in-hand with cardiovascular disease and could benefit from non-invasive sensing is Type One Diabetes Mellitus. Diabetes is a metabolic disorder resulting from the inability of the body to regulate the level of glucose in the blood. The worldwide prevalence of diabetes, both type one and two, is increasing faster than society's ability to manage cost-effectively. Management of diabetes accounts for 1 in 4 healthcare dollars spent in the United States of America [Riddle and Herman 2018]. An estimated 9% of the world population has a diagnosis of metabolic syndrome [Ampofo and Boateng 2020].

People living with diabetes currently need to use invasive methods, such as finger-stick testing, to monitor their blood glucose concentration. The discomfort and possible complications caused by these methods lead to significantly reduced frequency of monitoring by patients [Chowdhury et al. 2013]. A non-invasive glucose sensing method would facilitate improved adherence to monitoring, thus reducing complications and improving quality of life.

There is scope to develop non-invasive optical devices to monitor these critical components of the cardiovascular and metabolic systems. This sensing method should be

able to monitor the venous oxygen saturation (SvO_2), the arterial pulse wave velocity (PWV), and blood glucose concentration. Non-invasive and low-cost solutions to the issues mentioned above have the potential to dramatically improve outcomes for patients as well as minimise the burden on their social and economic position

1.2 OBJECTIVES

This thesis focuses on the development of LED-LED based reflectance PPG sensors for non-invasive measurement of physiological variables important to cardiovascular and metabolic health; specifically, SvO_2, PWV, and blood glucose concentration. An initial proof of concept sensor was developed, which used LEDs to both emit and detect light. This sensor was then adapted to measure each of the three components focused on in this thesis.

- Design a non-invasive reflectance photoplethysmograph (PPG) sensor capable of using multiple different wavelength LEDs, which both emit and detect light.
- Develop and validate a sensor to measure the jugular venous pulse (JVP) and conduct a pilot trial to measure jugular venous oxygen saturation (SvO_2) utilising this pulse.
- Develop and validate a sensor to measure arterial pulse wave velocity (PWV) local to a single artery.
- Develop and validate a sensor capable of estimating blood glucose concentration (BGC).

1.3 NOVELTY

This thesis presents the design of a novel photoplethysmograph sensor that uses LEDs to both emit and detect light. This sensor utilises discrete wavelength spectroscopy to non-invasively measure jugular venous oxygen saturation, pulse wave velocity, and blood

glucose level. A phase difference method has been developed for use on aorta-femoral arterial pulse waveforms to calculate PWV at higher noise levels than the current gold standard method. A model was developed to analyse the voltage decay of a reverse biased LED, reducing the required sampling time. This method has not been repeated in literature before. The sensors developed are low cost and open-source, enabling free use of data to maximise patient benefit and outcomes. In addition, it enables potential commercial opportunities in the value of data and software as a service.

1.4 CARDIOVASCULAR SYSTEM

Blood is a complex mixture of cells, proteins, lipids, and ions, which is kept in constant motion throughout the body by the cardiovascular system. This system distributes nutrient materials and oxygen to each cell and takes away the by-products of their metabolism. Figure 1.1 shows the circulation of blood through the cardiovascular system. The blood flows out the left side of the heart via the aorta, then through the arteries, arterioles, capillaries, venules, veins, and the vena cava back to the heart. Blood is then sent through the pulmonary artery to the lungs to retrieve oxygen, remove carbon dioxide, and then back to the heart to be pumped out through the aorta [Fozzard et al. 1986, Guyton and Hall 2006].

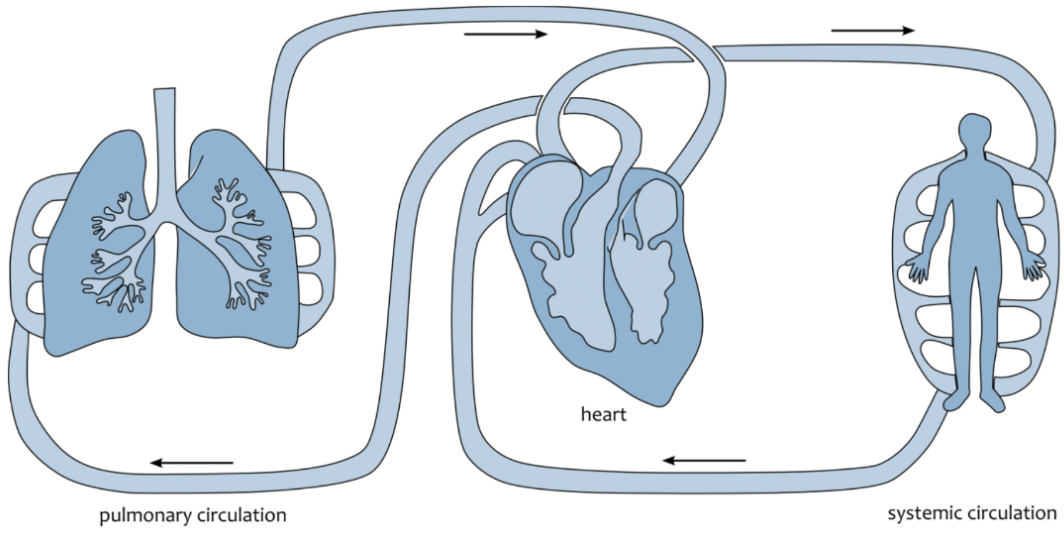

Figure 1.1 The 3 separate systems of the cardiovascular system: the heart, the systemic circulation and the pulmonary circulation. Arrows indicate the direction of flow [Paeme 2013].

The heart is the organ responsible for sustaining the other organs in the body by pumping blood. Without a properly functioning heart, other organs will not have a supply of the oxygen and nutrients needed for cellular life. The heart distributes blood using a network of veins and arteries. The haemoglobin molecules in the red blood cells are the primary transporter of oxygen through the body to individual cells. Only 2% of the oxygen carried by the blood is dissolved in the plasma, with the remaining 98% bound to haemoglobin molecules [Nitzan et al. 2014].

1.4.1 Arterial system

The arteries carrying the nutrients and oxygenated blood away from the heart are high-pressure vessels, which adapt to varying flow and pressure conditions by enlarging or contracting to meet haemodynamic demands [Ku 1997]. From the arteries, blood flows into the arterioles. Arterioles are the blood vessels on the arterial side of the vascular tree [Martinez-Lemus 2012]. Arterioles are essential for the role of blood pressure regulation and tissue perfusion as they provide 80% of the resistance to blood flow in the body [Intengan and Schiffrin 2000], and are a vital component in the ability to stress blood volume and perfuse tissue [Desaive et al. 2019, Murphy et al. 2020a, Pironet et al. 2015]. From the arterioles, blood flows into the capillaries. The primary point of interaction between cells and blood is in the capillary bed which serves both transport and exchange functions.

1.4.2 Venous system

Veins are the vessels responsible for returning blood to the heart. Venules begin with a small diameter at the capillaries, increasing in size to form veins as they return to the heart. Veins are characterised as low-pressure vessels containing approximately 64% of the blood in the body [Guyton and Hall 2006]. The EJV is a vein located on both the left and right side of the neck along the border of the platysma muscle [Shah and Rosenberg 2009]. The JVP represents pressure changes in the EJV, and consists of three positive waves (A, C and V) and two negative troughs (X and Y), shown in

Figure 1.2. A benefit of measuring PPG signals at the EJV is the ability to measure respiratory pulsation and the JVP [Naveen and Nitish 2000].

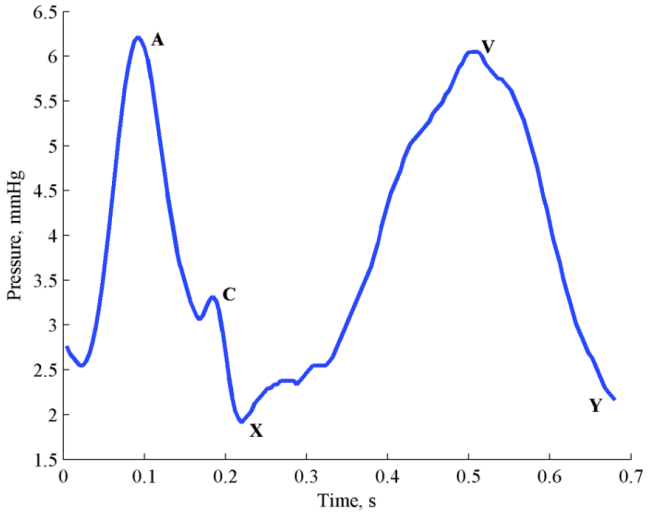

Figure 1.2 A typical JVP pressure waveform, where the A and C peaks are the result of the downstream action of the right heart, while the V peak is the result of the upstream flow of blood from the left heart [Davidson 2017].

Four studies investigated the use of NIR PPG on venous waveforms for estimating SvO_2, showing that PPG could provide useful clinical information [Colquhoun et al. 2012, Khan 2016, Thiele et al. 2011, Walton et al. 2010]. However, there were no conclusive research results in this area at the time of the publication of this thesis.

1.5 PULSE WAVE VELOCITY

One metric used as an indicator of cardiovascular health is the arterial pulse wave velocity (PWV). Defined as the velocity of propagation for the pulse wave in the artery [O'Rourke et al. 2002], PWV is a promising technique for continuous, non-invasive measurements of cardiovascular health [Peter et al. 2015]. PWV measurement enables the non-invasive estimation of blood pressure, stroke volume, arterial stiffness, and detection of early-onset sepsis [Gurovich and Braith 2011, Jianwen Luo et al. 2012, Kadoglou et al. 2012, Li et al. 2019, Ma et al. 2018].

The physiological range for PWV increases with age from $<6\,\mathrm{m\,s^{-1}}$ below 30 years old to $11\,\mathrm{m\,s^{-1}}$ over 70 years old [Boutouyrie and Vermeersch 2010]. A typical PWV in

the radial artery in a healthy individual is 4.73 $\pm 1.2\,\mathrm{m\,s^{-1}}$ [Obeid et al. 2021]. Higher PWV with values greater than $10\,\mathrm{m\,s^{-1}}$ is associated with increased arterial stiffness and increased risk of poor cardiovascular outcomes [Mancia et al. 2018]. Increased arterial stiffness and high central arterial pressure can lead to higher arterial pulsatility, leading to damage to the microcirculation of several organs, especially the kidneys and the brain [Jani et al. 2014], as well as reduced tissue perfusion and stressed blood volume [Desaive et al. 2019, Murphy et al. 2020a, 2019, 2020b].

During the ventricular contraction (systole), a pressure wave propagates along the arterial tree. As it travels from large arteries to the peripheries, the speed of the wave changes due to the increase in arterial stiffness further from the heart [Kim et al. 2007]. Figure 1.3 shows the arterial pulse wave travelling through the carotid artery. The difference in arrival time of the pulse wave along a known distance can be used to calculate the PWV.

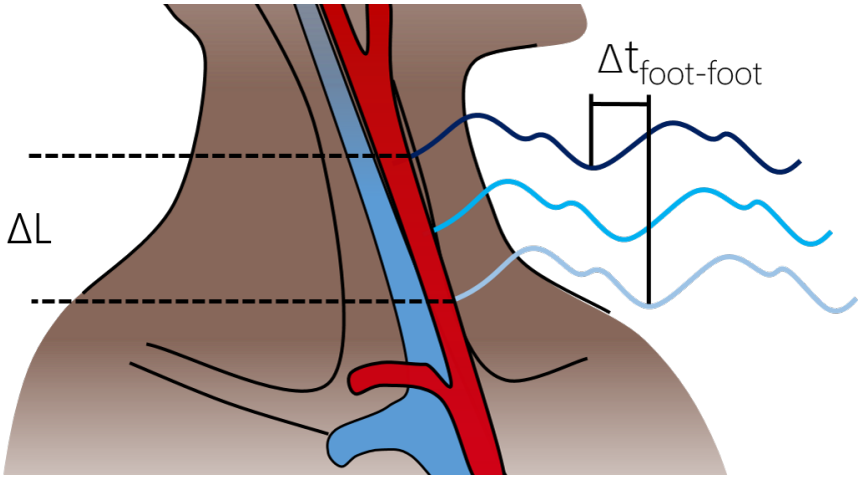

Figure 1.3 The arterial pulse wave travelling through the carotid artery. PWV can be calculated using the distance between two pulses along the carotid artery (ΔL) and the pulse transit time (Δt) between the "foot" of two pulse waveforms.

A stiffened arterial wall is linked to an increased aortic pulse pressure and left ventricular afterload. This increased afterload can restrict left ventricular filling and potentially lead to heart failure [Auseon et al. 2007]. The majority of the reservoir capacity of the arterial system is in the proximal part of the aorta [Westenberg et al. 2012]. Stiffness assessment in this region provides essential information on the overall health of the aorta and its function [Smith et al. 2020]. As the aorta changes structure with age,

non-invasive assessment of PWV may provide insight into the underlying physiology and progression of the heart and circulatory functions, which would be very useful in monitoring of chronic cardiovascular disease.

1.6 DIABETES

Diabetes Mellitus is a complex and multidimensional medical condition. Fundamentally, the body cannot regulate its blood glucose concentration due to either reduced production or increased resistance to insulin. Insulin is a hormone the body uses to enable glucose to enter cells from the blood and eventually fuel energy production for the cell. Incorrect insulin levels in the body can lead to hyperglycemia (high blood glucose levels) or hypoglycemia (low blood glucose levels). The bodys normal physiological glucose range is $4\,\mathrm{mmol\,l^{-1}}$ to $8\,\mathrm{mmol\,l^{-1}}$ [Vashist 2013], with glucose values outside this range potentially leading to poor health outcomes [Lind et al. 2021].

The global economic burden is expected to increase from $1.5 billion USD in 2015, to over $2.1 billion USD by 2030 [Bommer et al. 2018]. The social cost is shouldered by lower-middle social demographic index [Liu et al. 2020]. Management of glucose levels is vital to improving health outcomes, quality of life and reducing management costs for both the patient and healthcare provider. There are three main types of Diabetes Mellitus: type-one, type-two and gestational diabetes [McIntyre et al. 2019]. Type-one diabetes, also known as juvenile diabetes, is often diagnosed early in life (children - young adults) [Forlenza et al. 2016]. This form of diabetes manifests as the inability to produce sufficient insulin. Since a person with type-one diabetes is unable to produce endogenous insulin, they are fully reliant on exogenous insulin delivery and require life-long insulin replacement therapy [Gingras et al. 2018]. Individuals living with type-one diabetes must regularly measure their blood glucose and use the information to calculate the quantity and type of insulin required [Huckvale et al. 2015].

Type-two diabetes occurs when there a resistance to the effect of insulin. Muscle, fat cells and the liver do not adequately respond to the insulin produced by the pancreas,

potentially leading to insulin dependency [Roden and Shulman 2019]. Individuals living with type-two diabetes have a more varied requirement for blood glucose monitoring than type-one [Critchley et al. 2018]. Individuals on intense insulin therapy, similar to type-one, also require the same frequency of blood glucose measurements.

The type-two diabetics who are not at risk of hypoglycaemia are often only assessed every few months via HbA_{1c} testing [BPAC 2021]. HbA_{1c} is a common metric used to assess glycaemic control over extended periods of time [Danne et al. 2017, Sherwani et al. 2016]. Gestational diabetes is a transient form of diabetes occurring during pregnancy [Plows et al. 2018]. No definite cure for any of these types of diabetes is currently available.

Inadequate control of blood glucose levels has complications including; diabetic retinopathy, kidney damage, heart disease, stroke, neuropathy and birth defects [Aronson 2008]. There is strong evidence that tight glycaemic control delays and even prevents the onset of long-term complications in all forms of diabetes mellitus.[Critchley et al. 2018, (DCCT)/(EDIC) Study Research Group 2016, Hayward et al. 2015, Tottman et al. 2018].

Self-monitoring of diabetes improves glycaemic control and quality of life in both insulin dependent and non-insulin dependent diabetics [Kato et al. 2013]. For individuals on insulin replacement therapy, testing blood glucose concentration should be done prior to each administration of insulin, after meals, when exercising, and before and after sleeping. Additional measurements are also recommended if they feel any symptoms of hyper/hypoglycaemia [King et al. 2016, Moser et al. 2019]. Thus, a thorough testing regime of up to eight times daily would improve glycaemic control [Minder et al. 2013, Wong et al. 2009]. However, this is invasive and challenging to adhere to for patients so is an unrealistic goal. Often, during the early stages of type-two diabetes, minimal blood sugar monitoring is recommended, as blood glucose levels are generally well controlled. However, research has shown regular blood glucose measurements to improve control [Polonsky et al. 2010, 2009]. Individuals with diabetes who regularly monitor their blood glucose have improved quality of life [Jing et al. 2018].

The current gold standard of diabetes management involves artificially recreating the role of the pancreas, known as the "artificial pancreas" [Boughton et al. 2021]. A model-based virtual patient control approach has become more common recently, especially in intensive care unit blood sugar control [Chase et al. 2018, 2019, Dickson et al. 2018]. The artificial pancreas consists of a continuous glucose monitor (CGM) connected to an insulin pump, where the CGM controls the rate of insulin delivery by the pump [Zaharieva et al. 2019]. CGM devices with their 1-5 minute intervals have the potential to remove the need for patient input, further increasing diabetes control [Girardin et al. 2009].

1.6.1 ICU and NICU control

Critically ill patients in the ICU often experience stress-induced hyperglycaemia [McAllister et al. 2014, Umpierrez et al. 2012]. Hyperglycaemia in this setting is defined by having multiple consecutive blood glucose measurements yielding a result of >8-10 $\mathrm{mmol\,l^{-1}}$ or higher [Umpierrez et al. 2012]. There is evidence that hyperglycaemia increases the risk of adverse clinical outcomes, including sepsis and septic shock [Branco et al. 2005], infections [Bistrian 2001], and organ failure [Ellahham 2010].

Similarly to the adult ICU, the NICU also faces problems with management of glucose. Neonatal hypoglycaemia is defined as low glucose levels in a new born baby. A infant with a blood glucose concentration at or below 2.6 $\mathrm{mmol\,l^{-1}}$ is defined as experiencing hypoglycaemia [McKinlay et al. 2015]. Generally, infants born prematurely, or small for gestational age, or having a diabetic mother, are at higher risk of developing hypoglycaemia [Harris et al. 2010]. Hypoglycaemia in this vulnerable demographic can lead to seizures and permanent brain injury [Harris et al. 2016, McKinlay et al. 2015, Signal et al. 2012b, Thomas et al. 2014]. Currently, blood must be drawn via heel-prick testing to measure blood glucose in a neonate and repeated sampling is often required. The repeated breaking of the skin barrier makes the infant more susceptible to infection[Lemyre et al. 2015]. In addition, the perceived pain and blood loss [Hellström et al. 2020] can be upsetting for parents/caregivers and can delay timely measurement

and identification of hypoglycaemia.

1.7 CHAPTER OVERVIEW

This thesis is presented in four parts: *Part I* presents a review of the current literature in this field, *Part II* develops hardware and software required to validate non-invasive venous oxygen saturation, *Part III* designs pulse wave velocity sensors for use on the carotid and radial artery and *Part IV* develops a NIR reflectance sensor for non-invasive glucose monitoring.

- **Chapter 1** introduces the motivation and goals of the thesis, as well as a description of the physiology related to this work.

- **Chapter 2** outlines the background and literature behind current invasive measurement methods and their non-invasive alternatives. In particular, jugular venous oxygen saturation, pulse wave velocity measurement and blood glucose estimation.

- **Chapter 3** covers the background and use of LEDs as discrete wavelength light detectors.

  Part II: Estimation of Venous Blood Oxygen Saturation

- **Chapter 4** presents the design of a reflectance pulse oximeter using LEDs of different wavelengths to emit and detect light for pulse oximetry and NIR spectroscopy. Material in Chapter 4 has been submitted to HardwareX: *J. D. Campbell, L. R. Mckenzie, C. G. Pretty, P. Bones, and J. G. Chase, Digital Sensing LED Emission and Detection Array for Pulse Oximetry HardwareX (submitted)*

- **Chapter 5** develops an algorithm to detect the peaks and troughs of the photoplethysmograph waveform in real time for use with the sensor developed in Chapter 4. Material in Chapter 5 has been published in:

J. Campbell, C. Pretty, G. Chase, and P. J. Bones, A Robust Method of a Peak Detection in Noisy PPG Signals Using a Structure of IIR Filters, in 2018 14th IEEEASME International Conference on Mechatronic and Embedded Systems and Applications (MESA), Oulu, Finland, Jul. 2018, vol. 14

J. Campbell, C. Pretty, J. G. Chase, and P. J. Bones, Near-Real-Time Detection of Pulse Oximeter PPG Peaks Using Wavelet Decomposition, in 10th IFAC Symposium on Biological and Medical Systems, Sao Paulo, Brazil, Sep. 2018, pp. 181186.

- **Chapter 6** Validates the sensor designed in Chapter 4 to measure the jugular venous pulse and estimate the oxygen saturation of the external jugular vein and the carotid artery at different levels of supine.

Part III: Estimation of Arterial Pulse Wave Velocity

- **Chapter 7** describes the design and testing of a non-invasive pulse wave velocity sensor using an array of LEDs to detect the arterial pulse at three different places along the carotid artery. Material in Chapter 7 has been published in: *J. D. Campbell, L. Holder-Pearson, C. G. Pretty, P. Bones, and J. G. Chase, Pulse Wave Velocity Measurement in the Carotid Artery Using an LED-LED Array Pulse Oximeter, in 21st IFAC World Congress, 2020, vol. 53*

- **Chapter 8** presents a phase difference algorithm used to calculate pulse wave velocity across a collection of beats in aorta-femoral measurements. The algorithm is tested on porcine data and is measured against the gold standard 'foot-foot' pulse wave velocity measurement.

- **Chapter 9** covers the validation of a photoplethysmograph pulse wave velocity sensor tested on the radial artery, adapted from sensor designs presented in Chapters 4 and 7. Material in Chapter 9 has been submitted to: *J. D. Campbell, C. G. Pretty, R. Smith, P. Bones, and J. G. Chase Peripheral Pulse Wave Velocity*

Measurement with the Phase Difference Method, Submitted to Biomedical Signal Processing and Control (submitted)

Part IV: Non-invasive Estimation of Blood Glucose Concentration

- **Chapter 10** presents the design of a discrete spectrometric non-invasive blood glucose sensor. Testing of the sensor is conducted on porcine blood in-vitro. Material in Chapter 10 has been published in: *J. D. Campbell, L. Holder-Pearson, C. G. Pretty, P. Bones, and J. G. Chase, Pulse Wave Velocity Measurement in the Carotid Artery Using an LED-LED Array Pulse Oximeter, in 21st IFAC World Congress, 2020, vol. 53*

- **Chapter 11** develops a model for predicting the voltage decay of a reverse biased LED for the use of measuring photocurrent. Material in Chapter 11 has been published in: *J. Campbell, C. G. Pretty, J. Knopp, P. Bones, and J. G. Chase, A model for the digital method of measuring LED incident photocurrent, in ASME 2021 International Design Engineering Technical Conferences & Computers and Information in Engineering Conference, Online, Virtual, 2021, p. 9.*

- **Chapter 12** describes the validation of the non-invasive glucose monitor through trials on healthy subjects and a clinical trial on patients in the neonatal ICU.

- **Chapter 13** Conclusions

- **Chapter 14** Future work and directions.

Part I

Background and Literature Review

Chapter 2

BACKGROUND OF CARDIOVASCULAR AND BLOOD GLUCOSE SENSING

This chapter builds on the physiology and thesis statement in Chapter 1, providing background on current sensing methods measuring cardiovascular and metabolic markers, as well as their non-invasive alternatives. In particular, using NIR spectroscopy to measure arterial pulse waveforms to extract information on oxygen level, pulse wave velocity, and blood glucose concentration.

2.1 PULSE OXIMETERS

Pulse oximeters are medical devices used in hospitals and home life. These sensors allow continuous, non-invasive monitoring of heart rate and arterial blood oxygen saturation [Ortega et al. 2011]. Through ease of use, accurate results, and very low development costs, the sensors are a standard of care for oxygen monitoring in hospital wards, operating rooms, and intensive care units around the world.

Pulse oximeters use two LEDs and a photo-detector usually placed on either side of a finger to produce photoplethysmograph (PPG) signals. These signals indicate changes in blood volume as well as the oxygen saturation level in the blood. The PPG waveforms are generated by the pulsatile nature of blood in the arteries [Allen 2007, Daly and Leahy 2013]. The sensor is able to determine the oxygen levels in the blood by measuring the absorption ratio of red to infrared light absorbed by oxyhaemoglobin and deoxyhaemoglobin. Due to HbO_2 and Hb having different light absorption character-

istics, the peripheral oxygen concentration can be calculated, where oxygen saturation estimated by a pulse oximeter is denoted SpO_2.

2.1.1 History of Pulse Oximeters

The concept behind the pulse oximeter was first investigated by J. R Squire in 1940. Squire recognised red light and infrared light are absorbed differently by pneumatically compressed tissue. This difference permitted Squire to compute the oxygen saturation in the tissue. The term "oximeter" was first coined by Glen Allen Millikan during the second world war [Millikan 1942]. He designed a light weight, optical, ear based device to continuously monitor the blood oxygen level.

Using the work by Millikan, Earl Wood made a sensor measuring the absolute saturation level using ratios of the absorbed light [Allwood and Burry 1954]. The oximeter worked by fully occluding blood from a section of the ear; then measured the transmitted light through the tissue. When the pressure was released, the light through the tissue was measured again. The resulting difference in measurement gives the oxygen concentration.

This sensor was the standard for years until an engineer at Nihon Kohden, Takuo Aoyagi, introduced the idea of the ratio of ratios in 1972 [Severinghaus 2007]. Aoyagi was experimenting with combining conventional pulse oximeters with dyes. He discovered when he held his breath, pulsatile waves were introduced into the signal, showing a change in oxygen concentration [Miyasaka et al. 2021]. Reduced amounts of oxyhaemoglobin in the blood changed the ratio of densities at the red and infrared wavelengths. The pulsatile and non-pulsatile blood have the same information of blood colour, which leads to these principles:

1. Using two appropriate wavelengths of light, the optical density and ratios of the pulsating to non-pulsatile parts of blood could be found. The resulting ratio should be the same as Wood's ratio [Westhorpe and Ball 2008].

2. The non-pulsatile venous blood does not affect the measurement. As only the arterial blood is measured, the position of the sensor is no longer restricted to the ear.

3. Using this method, the reference is set with each pulse, rather than a preset preference.

The sensor designed by Aoyagi based on these principles was taken to market by Minolta in 1978, remaining the standard until the early 1980s when other firms started improving their sensors. This competition in designs led to rapid development of oximeters, which, in turn resulted in a 90% reduction in anaesthesia related deaths [Severinghaus 2007]. By the early 1990's pulse oximetry was the standard of care for monitoring of perfusion during anaesthesia [Allen 2007].

In the years since, studies have examined the accuracy of pulse oximetry [Abdallah et al. 2007, Jubran 1999]. The combination of accuracy, non-invasive measurement, and relatively low cost, led to the pulse oximeter being adopted in hospitals around the world. Pulse oximeters have also been adopted outside of clinical settings with home users, athletes, and veterinaries using the sensor [Tamura et al. 2014].

2.2 PRINCIPLES OF PULSE OXIMETRY

Pulse oximetry uses plethysmograph signals to record changes in blood volume due to heartbeat [Elgendi 2012]. The term plethysmograph is of Greek origin with "plethysmos" meaning "to increase" and "grapho" meaning "write". The version of plethysmography used in pulse oximetry is photoplethysmography (PPG).

The technique of photoplethysmography is used to monitor the peripheral blood volume. Designed by Alrick Hertzman, PPG replaced previous mechanical plethysmography methods [Hertzman 1938], and is widely used to study and monitor the cardiovascular pulse wave produced by arteries.

2.2.1 Photoplethysmograph Signals

The raw data measured by the pulse oximeter consists of multiple components. Pulsations in the data result from arterial blood flow, thermo-regulation, respiration, and vasomotion activity [Achakri et al. 1994]. The arterial pulse needs to be extracted from these signals. Thus, the PPG signal is broken into "AC" and "DC" components. The AC component is only composed of frequencies greater than 0.5 Hz and is associated with heart-rate. Importantly, this signal is usually comprises less than 1% of the total PPG waveform.

The DC component consists of the remaining 99% of the signal and contains the low frequency signals (< 0.5 Hz) and scattering effects of the surrounding tissue [Mendelson 1992]. This DC component also contains person-person variable absorption, due to differing melanin concentrations. This difference must be accounted for in calibration as darker skin has a 3x greater risk of missed diagnosis of hypoxaemia [Sjoding et al. 2020].

2.2.2 Shape of Arterial PPG Waveform

Figure 2.1 shows a typical PPG waveform. During systole and diastole in the cardiac cycle of the heart, blood is pushed through the arterial vascular bed. During the systolic phase, the volume of blood in the arteries increases, increasing light absorption and therefore reducing the amount of reflected light. The blood volume then drops through the diastolic phase, decreasing light absorption. This relationship is shown in Figure 2.1. The baseline of the PPG signal is directly related to the volume of blood in the tissue, with the amplitude proportional to the increase in blood volume during the systolic phase. By measuring the time between the diastolic or systolic peaks, the heart-rate can be found.

During the decay of the waveform after systole, a notch is usually present. This dicrotic notch is due to an increase in blood volume created by pressure wave reflection at bifurcations of the arterial tree [Sherebrin and Sherebrin 1990]. An aortic pressure

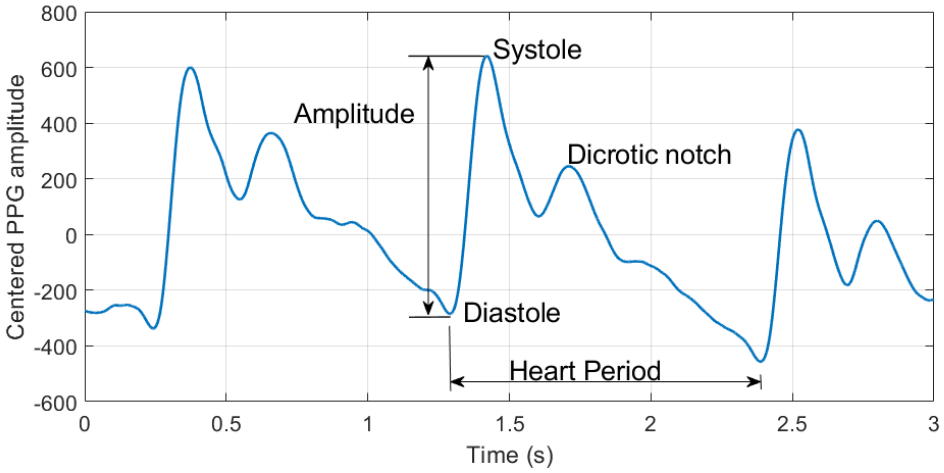

Figure 2.1 Example PPG waveform recorded from the radial artery by a reflectance pulse oximeter.

waveform also displays the diastolic notch due to the closure of the heart's aortic valve, which causes a similar change in blood flow. The notch can be seen in Figure 2.1 in the change from the systole phase to the diastole phase.

2.2.3 Relationship Between Haemoglobin and Light Absorption

The two wavelengths of light conventionally used for pulse oximetry are red (660 nm) and infrared (940 nm) [Tremper and Barker 1989]. The ratio of the AC component to the DC creates a normalised absorption ratio at each wavelength. Following this calculation, the ratio of each wavelength ratio can then be used to compare light absorption. Aoyagi uses the term SpO_2 to define the ratio of ratios, with the "p" subscript denoting measurement by a pulse oximeter. The ratio of ratios equation is given:

$$R = \frac{(AC_{Red}/DC_{Red})}{(AC_{IR}/DC_{IR})} \tag{2.1}$$

Where,

R: Ratio of ratios from each wavelength.

AC_{red}: Pulsatile component of the detected signal produced by red light.

DC_{red}: Non-pulsatile component of the detected signal produced by red light.

AC_{IR}: Pulsatile component of the detected signal produced by infrared light.

DC_{IR}: Non-pulsatile component of the detected signal produced by infrared light.

The R value is then used to calculate SpO_2 [Mendelson and Ochs 1988]:

$$SpO_2 = 110 - 25 \times R \tag{2.2}$$

The oxygen contained in blood is predominantly contained by the haemoglobin carrying red blood cells, as little oxygen is freely dissolved in the blood. As the red blood cells travel through the body, oxygen is released from the haemoglobin. Thus, SaO_2, where a denotes arterial oxygen, is deemed to be the ratio of oxygenated haemoglobin to the total amount of haemoglobin in the blood, defined:

$$SaO_2 = \frac{\text{Oxygenated Haemoglobin}}{\text{Total Haemoglobin}} = \frac{HbO_2}{HbO_2 + Hb} \tag{2.3}$$

Haemoglobin can be in states other than oxygenated and deoxygenated, affecting the accuracy of the measurement. These states include methaemoglobin and carboxyhaemoglobin. Methaemoglobin can be formed spontaneously in the blood when the iron in the heme group is in the ferric (Fe^{3+}) state, rather than the normal ferrous (Fe^{2+}) state. Methaemoglobin is unable to carry oxygen around the body and is a blue-brown colour. Carboxyhaemoglobin forms upon exposure to carbon monoxide [Barker et al. 1989, Ralston et al. 1991]. Carbon monoxide (CO) has a higher affinity to haemoglobin than oxygen, so the CO attaches to the haemoglobin and does not get released. This binding reduces the total amount of oxygen carried in blood [Hampson et al. 2006].

Figure 2.2 shows the extinction coefficients for the four states of haemoglobin and shows that HbO_2 absorbs infrared light better than Hb. In contrast, Hb absorbs red light better than HbO_2. Using this relationship, wavelengths for the red and infrared light

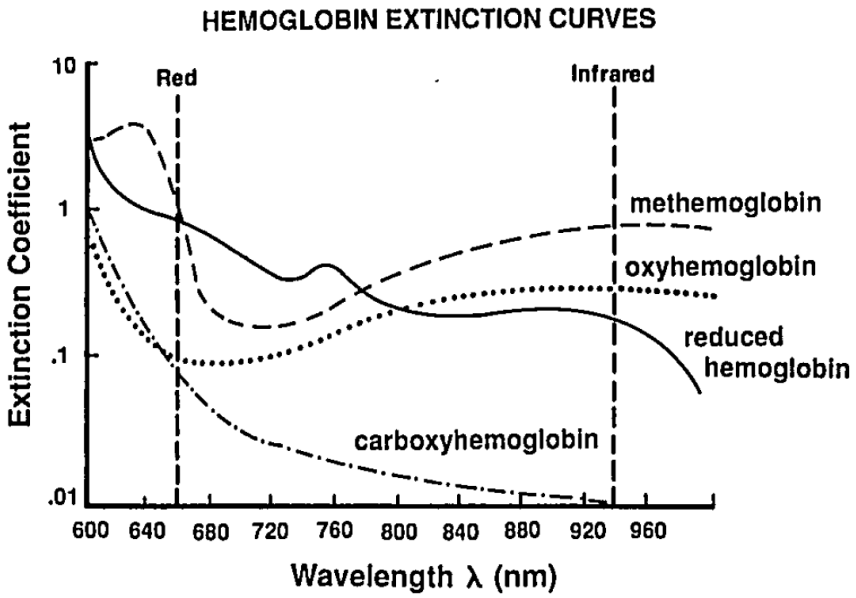

Figure 2.2 Extinction coefficients ($1\,\mathrm{mmol}^{-1}\,\mathrm{cm}^{-1}$) of the four haemoglobin types over a red and infrared spectra Tremper and Barker [1989].

are chosen for the varying absorption characteristics.

The measured Hb concentration in the blood is proportional to the amount of absorbed light from the LEDs. The higher the level of oxygenated haemoglobin, the more red light is absorbed and the less infrared light is absorbed. The relationship between amount of Hb and light absorption is described by "Beers Law" [Baker et al. 2014].

2.2.4 Beer-Lambert Model

The theory behind pulse oximetry can be derived through the Beer-Lambert model for light absorption. This model describes the exponential decay in light intensity as it passes through a non-scattering, light absorbing medium [Mannheimer 2007]. The decay of intensity through the tissue is defined:

$$I_{out} = I_{in}e^{-\varepsilon(\lambda)cd} \tag{2.4}$$

Where,

$\mathbf{I_{in}}$: Incident light intensity.

$\mathbf{I_{out}}$: Transmitted light intensity.

$\boldsymbol{\varepsilon}$: Extinction coefficient of absorbing substance at given wavelength $\boldsymbol{\lambda}$.

c: Constant concentration of absorbing substance.

d: Optical path length through substance.

The ratio (R) of transmitted light to incident light at the red and infrared wavelengths is given by:

$$R = \frac{\log(I_{out_R}/I_{in_R})\lambda}{\log(I_{out_{IR}}/I_{in_{IR}})\lambda} \tag{2.5}$$

Using the R value and knowledge of extinction coefficients for haemoglobin, SaO_2 can be estimated. The relationship between the ratio of ratios and the extinction coefficients of haemoglobin defines SaO_2:

$$SaO_2 = \frac{\varepsilon_{Hb}(\lambda_1) - R\varepsilon_{Hb}(\lambda_2)}{R[\varepsilon_{HbO_2}(\lambda_2) - \varepsilon_{Hb}(\lambda_2)] + [\varepsilon_{Hb}(\lambda_1) - \varepsilon_{HbO_2}(\lambda_1)]} \times 100\% \tag{2.6}$$

Where,

$\boldsymbol{\varepsilon_{Hb}}$: Extinction coefficient of haemoglobin.

$\boldsymbol{\varepsilon_{HbO_2}}$: Extinction coefficient of oxygenated haemoglobin.

Figure 2.3 shows the decay in R with increasing SpO_2. At high SpO_2, the pulse wave peak to peak amplitude is less for red light than infrared. At low SpO_2 values, the infrared waveform amplitude is smaller than red. This relationship between wavelengths is also shown in Figure 2.2 where low SpO_2 indicates higher levels of deoxyhaemoglobin. As deoxyhaemoglobin absorbs red light better than oxyhaemoglobin, there will be a larger peak to peak amplitude of red light absorption throughout the pulse cycle. Therefore, a lower SpO_2 will have a larger red pulse waveform.

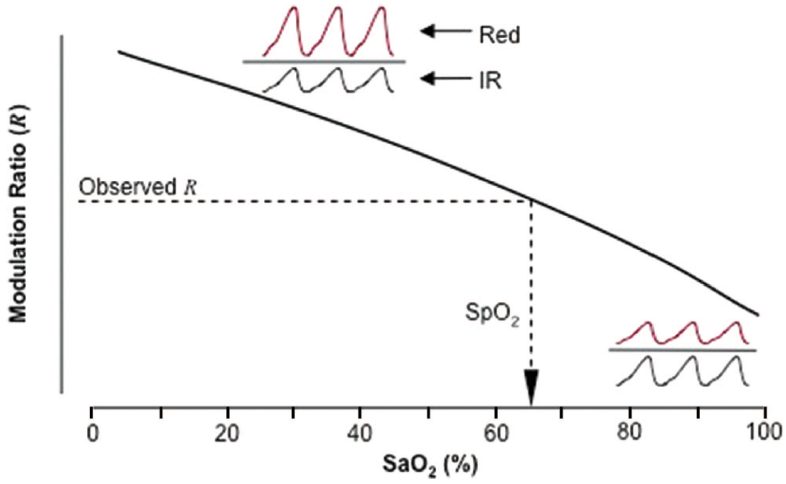

Figure 2.3 Decay curve of red / IR modulation ratio (R) against SpO_2 [Mannheimer 2007].

Unfortunately, the human body is an effective light scattering medium [Mannheimer et al. 1997], rather than the uniform substance assumed in the Beer-Lambert model. This issue leads to unexpected scattering of light resulting in a complicated function of path length. Thus, development of a sensor cannot rely solely on the Beer-Lambert model to determine SpO_2.

2.2.5 Oxygen Saturation through Empirical Calibration

As the Beer-Lambert law does not fully model the scattering of light through the human body, a calibration function is needed. The pulse oximeter is calibrated against arterial gas oxygen levels in healthy, normothermic people, giving a baseline for expected results. By using the arterial blood gas oxygen levels, the pulse oximeter is calibrated against the gold standard in blood oxygen measurements [Kamat and others 2002]. The calibration is usually conducted on subjects by inducing hypoxaemia and measuring the drop in SaO_2. This test and calibration successfully corrects the errors in the Beer-Lambert model R curve. However, each type of pulse oximeter requires a calibration unique to the electronics used.

Figure 2.4 compares the Beer-Lambert model and empirical calibration [Flewelling 2000]. Rather than a linear decrease in oxygen saturation, the empirical calibration

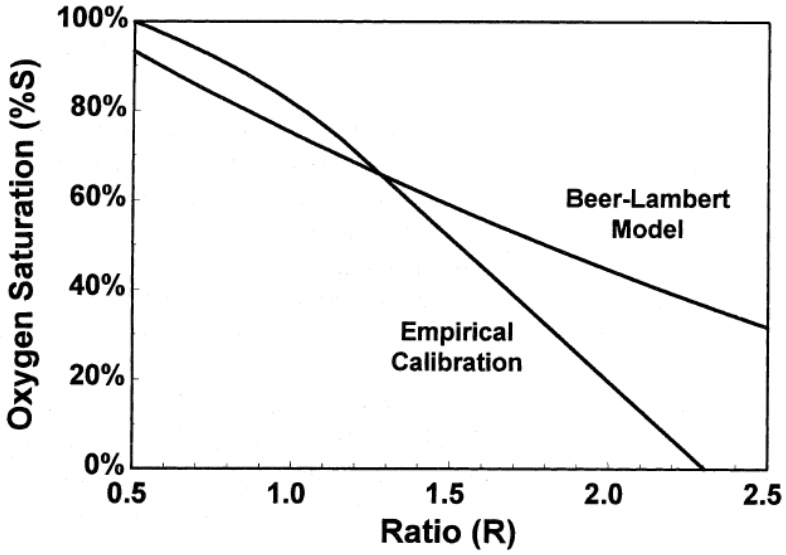

Figure 2.4 Comparison of R curves between the Beer-Lambert model and empirical pulse oximeter calibration [Flewelling 2000].

non-linearly decays down to 70% oxygen saturation. After an R value of 1.25, the data has been linearly interpolated to give a linear decay. Empirical calibration ensures that an oxygen saturation level up to 100% can be represented, whereas, the Beer-Lambert model only shows between 95% and 30%.

The estimated R values are mapped to SaO_2 using an equation from Mendelson and Kent [1989].

$$SaO_2 = SpO_2 = \frac{k_1 - k_2(Red/IR)}{k_3 - k_4(Red/IR)} \tag{2.7}$$

Where, k_2 is multiplied by the ratio of red light to infrared light deflected by the tissue.

The k values are empirically derived coefficients related to the extinction coefficients of Hb and HbO_2. These extinction coefficients do not exactly match those in Equation 2.6. In theory, the principle relationship between R and SpO_2 are the same. However, there remains a difference between theoretical modelling of the sensor and actual calibrations shown by the differences in coefficients.

Equation 2.1 can be normalised by dividing the AC component of the red and infrared

light by the corresponding DC component [Goldman et al. 2000]. Normalisation also removes the dependence on path length through the tissue. This normalisation simplifies into:

$$SpO_2 = k_1 + k_2 R \tag{2.8}$$

The constants k_1 and k_2 are derived from the calibration curve shown in Figure 2.4, with typical values being $k_1 = 110$ and $k_2 = -25$, where R is defined by Equation 2.1

2.2.5.1 Using RMS to estimate R values

The RMS value of the AC signal combined with the mean DC signal can also be used to calculated the R value for pulse oximetry [Oak and Aroul 2015], as given:

$$SpO_2 = \frac{(AC_{RMS}/DC)_{red}}{(AC_{RMS}/DC)_{ir}} \tag{2.9}$$

To calculate the AC component, the signal is filtered using a bandpass filter with a pass-band from 0.67 Hz to 10 Hz. A rolling RMS of the signal is then calculated to form an array of RMS similar to beat-to-beat peak and trough detection. The benefit of this method is the removal of the need to find the peaks and troughs in a noisy signal. However, as the peaks and troughs are not used, there is a risk that a signal may have no pulsatility, but the filter will continue to return an AC component.

2.2.6 Transmission and Reflectance PPG Method Comparison

There are two common methods for measuring the PPG signals, transmission and reflectance. These methods are defined by the relative position of the LEDs and photodetector on the body. Figure 2.5 shows the different positions of the sensor on the finger. Transmission pulse oximetry places the emitting LEDs and photodetector either side of an arterial bed [Mendelson 1992]. As the transmittance sensor must be placed

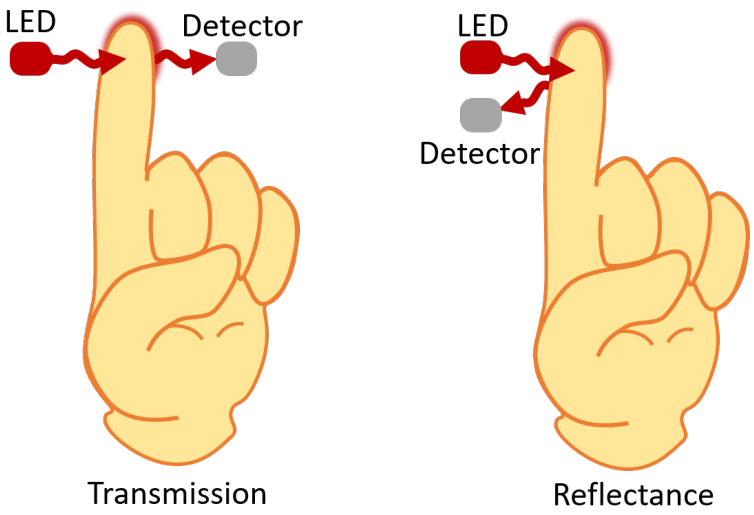

Figure 2.5 Comparison between transmission and reflectance sensor types

either side of tissue, the location of the sensor is generally restricted to relatively thin areas of the body, such as the finger or ear.

Reflectance sensors have the LEDs and photodetector placed next to each other. The photodetector receives the light scattered from the LED source at a distance of about 12 mm [Reuss 2005]. Reflectance pulse oximeters are able to be placed on parts of the body the transmission sensor cannot, most commonly on the arm, chest, or forehead. As a small fraction of scattered light reaches the emitter, the reflectance method produces a lower SNR and pulse amplitude than the transmission method. Another application of the reflectance sensor is to provide reliable intrapartum fetal monitoring [Dassel et al. 1997]. Traditionally, transmission sensors are used as larger AC signals can be measured.

2.3 CALCULATING VENOUS OXYGEN SATURATION FROM VENOUS PULSE WAVEFORMS

2.3.1 Forced Venous Pulsation

The AC signals of the PPG signal are conventionally used to calculate SpO_2. The frequencies of the arterial pulse are due to the heart rate (∼1 Hz). For venous oxygen

saturation to be measured, there needs to be a pulse in the veins. Studies have investigated the periodic oscillations in the thoracic cavity induced by normal or mechanical ventilation to generate pulses in the veins [Phillips et al. 2012, Shafqat et al. 2015, Walton et al. 2010]. These invasive or forced respiratory ventilation methods were able to estimate SvO_2 in the central regions. As the sensors are central, peripheral SvO_2 is unable to be measured.

2.3.2 External Venous Pulsation

By compressing veins and arteries, artificial pulses can be generated. [Schoevers et al. 2009] investigated a system that occluded blood flow on the finger. The apparatus consisted of three pressure cuffs. Each cuff would be periodically inflated to occlude the blood flow creating the artificial pulse. Using the arterial to venous compliance ratio developed in [Alian and Shelley 2014], SaO_2 and SvO_2 could be estimated. A subsequent study [Cloete et al. 2013] determined that Schoevers et al's results were neither comprehensive nor conclusive.

Figure 2.6 shows the experimental setup for the pressure cuff occlusion. The pressure cuffs were operating at very high pressures of 660 mmHg. As normal systolic pressure is less then 120 mmHg, the cuffs interrupted both venous and arterial flow through the finger. It was concluded fully occluding blood flow in both the arteries and veins would not give accurate results. The extended use of induced venous pulsations also carried risks, including: venous stasis; venous thrombosis; and interference, with intravenous access [Shafqat et al. 2015].

An alternative method of external venous pulsation was investigated in [Chan 2002]. Rather than fully occlude both the veins and arteries, a lower pressure was used so that only the veins were occluded. Arteries are thick walled to withstand the pressure of the blood flow. In contrast, veins are larger and thin walled and require less pressure to occlude. Using a pressure of 40 mmHg, below diastolic pressure, blood flow in the veins are interrupted while the arteries remain unaffected [Chan 2002]. Chan et al filed a patent for this concept, calling it the Venox concept [Chan et al. 2007]. The pressure

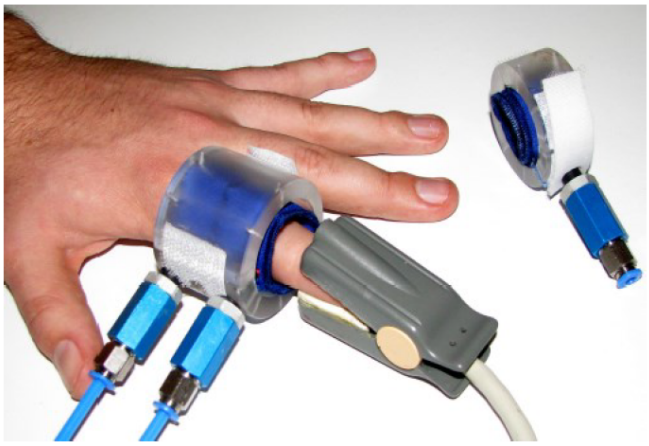

Figure 2.6 Artificial pulse generation using a finger cuff [Cloete et al. 2013].

cuffs operated at a frequency of 7.5Hz, much higher than the natural heart rate, and the resulting PPG signal could then be decomposed to extract the cardiac and artificial frequencies.

The Venox concept was investigated by Echiadis et al. [2007]. Patients undergoing heart bypass surgery had the SpO_2 and SvO_2 monitored with the Venox method. Thiele et al. [2011] did another study on this method and concluded the previous research did not provide suitable data for clinical use. The SvO_2 detected at the finger was compared to the central SvO_2 recorded during the heart bypass surgery by a cardiopulmonary bypass machine (CPB). Echiadis et al. [2007] was comparing the central to peripheral SvO_2 with is not applicable as discussed above. Further research is needed on healthy people rather than solely patients undergoing surgery.

Another method of external venous pulsations was investigated by Khan [Khan et al. 2015b, 2017] in the MOOSE study. Khan proposed the artificial pulsations should be at a frequency below the heart rate rather than higher, as investigated by Chan et al. [2007] because of the relaxation dynamics of veins. Using a pressure cuff inflation frequency of 0.2 Hz at a pressure between 40 and 50 mmHg, an R^2 value of 0.95 was generated between measured SvO_2 and venous blood samples. The study concluded that the proposed $SpvO_2$ estimation model could be used as an indicator for low O_2E, oxygen consumption and tissue hypoxaemia. SvO_2 measurement can be done in real time, giving live readings of peripheral oxygen levels. Khan also showed the importance

of temperature monitoring to the PPG signal quality [Khan et al. 2016]. Future work on the venous O_2 sensor was recommended to improve the accuracy of SvO_2 measurement.

2.3.3 Natural Venous Pulsation

The jugular vein feeds blood from the head directly to the right atrium. Due to the vein being close to the core of the body, there is a small respiration induced venous pulse. This pulse is present in the superficial internal and external jugular veins. The frequency of respiration is approximately 0.1 Hz, compared to the heart rate of 1 Hz so the frequency components from SaO_2 and SvO_2 can be extracted with a Fourier transform. Watson et al [Walton et al. 2010] generated an algorithm to estimate SvO_2 from the PPG signal.

A thesis by Aniagyei-Mensah showed measurement of the venous pulse wave with a pulse oximeter is possible [Aniagyei-Mensah 2014]. A laser diode was introduced to increase the light intensity reaching the photodiodes. The sensor was held against the neck with a rubber band to minimise the pressure on the skin.

Coloquhoun et al investigated the use of NIRS over the internal jugular vein to estimate cerebral venous oxygen saturation [Colquhoun et al. 2012]. The paper recommends a method to align the sensor with the jugular vein and additional sensors to remove interference from intervening tissue. The additional sensors would also allow the user to target specific depths of tissue as well as removing the influence of tissue beds. The final conclusion by Coloquhoun on the use of NIRS was placement of an oximeter directly over the internal jugular vein would be most likely to estimate change in the cerebral oxygen supply. Thiele et al recommends a change in LED wavelength to optimise oxygen saturation sensitivity to the 60% to 85% range [Thiele et al. 2011].

2.3.4 Venous Oxygen Saturation Summary

This section discussed the principles behind pulse oximetry and their limitations. One limitation is the inability to monitor the oxygen saturation of venous blood due to the

need for a pulsatile signal. Various methods of non-invasively monitoring venous oxygen saturation have been explored using external pulsations, or the natural pulsation in the EJV, but none have reached clinical use. Chapters 4-6 in this thesis focus on developing a novel pulse oximeter capable of monitoring venous oxygen saturation in the EJV.

2.4 PULSE WAVE VELOCITY MEASUREMENT

Invasive dual lumen catheters can be commonly used to measure the pulse transit time (PTT) of the arterial pulse wave used to calculate the PWV, but are not likely to be inserted to solely measure PTT, so a measurement of PTT is usually only a secondary outcome [Kamoi et al. 2017]. Moderately invasive measurements methods have been investigated with reduced reliability during haemodynamic instability, so have not become standard [Bein et al. 2007]. Measuring PTT gives an indicator of cardiovascular health. These PTT values can be used to calculate PWV, giving insight into arterial elastance, blood pressure, and early onset sepsis [Li et al. 2019, Ma et al. 2018].

2.4.1 Regional vs Local pulse wave velocity

PWV measured across different vessels, such as aorta-femoral and aorta-radial, are considered regional measurements, where the calculated PWV is the average over different arteries with varying compliance [Boutouyrie et al. 2009]. Consequently, regional PWV may mask changes in compliance in small segments [Pannier et al. 2002]. The regional PWV is defined by the distance between measurement points and the pulse transit time (PTT) delay between the two points [Pereira et al. 2015].

While PWV measurement is usually performed regionally, measurement local to an individual artery has also been investigated [Darwich et al. 2015]. Figure 2.7 shows the use of the foot-foot method at using the PTT measured on the carotid artery to calculate PWV. A major advantage of this approach to measuring PWV is the distance between measurement sites can be accurately known. Local PWV measurement in-vitro

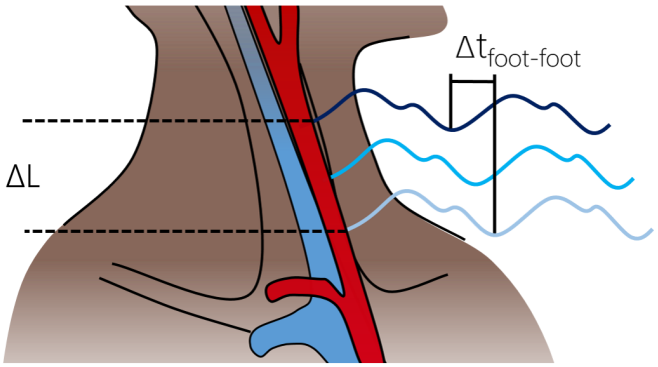

Figure 2.7 The local foot-foot PWV method calculated using the distance between two pulses along the carotid artery (ΔL) and the pulse transit time (Δt) between the "foot" of two pulse waveforms.

has shown good results, but in-vivo errors up to 30% have been recorded [Hermeling 2009, Pereira et al. 2011, Xu 2002].

The main difficulty in PTT calculation, especially local PTT, is the high velocity of the pulse wave ($1\,\mathrm{m\,s^{-1}}$ to $10\,\mathrm{m\,s^{-1}}$). This high pulse velocity means there is only a very short time (1 ms to 20 ms) between pulse arrival times at both locations, meaning a high sampling rate is necessary. For example, a pulse wave travelling at $5\,\mathrm{m\,s^{-1}}$ takes 10 ms to travel 50 mm. A sample rate of 1 kHz gives a PWV resolution of $\pm 0.5\,\mathrm{m\,s^{-1}}$ at this 50 mm spacing [Sorensen et al. 2008]. To mitigate the requirements of fast sampling, the time difference between pulses can be calculated at longer distances along the artery, such as the regional method of aorta-femoral waveforms. However, unless the distance is accurately measured, or a dual lumen catheter with known length is used, the estimated distance can be inaccurate [Laurent et al. 2006].

2.4.2 Non-invasive measurement of PWV

To facilitate primary measurement of PTT in a clinical setting, non-invasive devices must be developed to measure PTT without the need for insertion of catheters. The main non-invasive methods used include: magnetic resonance imaging (MRI) [Wentland et al. 2014], ultrasound [Calabia et al. 2011, Sorensen et al. 2008, Williams et al.

2007], tonometry [Butlin and Qasem 2016, Lowenthal et al. 2014, ORourke 2015] and photoplethysmography [Campbell et al. 2020, Kazune et al. 2014, Yung-Kang Chen et al. 2004].

The commercial PulsePen (DiaTechne, Milan, Italy) and SphygmoCorVx (CardieX, Sydney, Australia) non-invasive PTT sensors use arterial tonometry combined with the ECG R-wave to calculate PTT [Meigas et al. 2001, Salvi et al. 2008, Yung-Kang Chen et al. 2004]. High fidelity tonometers are placed on the carotid and femoral arteries, measuring the carotid-femoral propagation time using the intersecting tangent algorithm to identify the foot of the waveform.

The Complior (Complior) system uses two mechanotransducers to obtain carotid and femoral waveforms, comparing the point of maximum upstroke in each signal to get PTT [Butlin and Qasem 2016]. These three commercial devices use the common foot-foot method to calculate PTT, making assumptions at the distance the pulse wave travelled.

Hsu et al developed a local PWV sensor capable of being placed on either the radial or the carotid artery [Hsu and Young 2014]. Their approach used two packaged silicone-coated microelectromechanical sensors (MEMS) pressure sensors. Results from this sensor gave an average PWV of $5.1\,\mathrm{m\,s^{-1}}$ on the neck, inline with the expected carotid PWV in healthy patients [Jani et al. 2014]. Another study by [Fabian et al. 2019] compared the brachial occlusion-cuff technique to a SphygmoCorVX, obtaining a correlation of $r = 0.88$ ($p < 0.001$).

Previous attempts at removing the need for one of the two catheters replaced the pressure wave signal with the start of the Q wave of the ECG signals to indicate the start of the pulse wave at the carotid artery. Work by Kamoi and Balmer investigated the measurement of the arterial pulse wave velocity (PWV) with only one required catheter [Kamoi et al. 2017]. While this method was not fully non-invasive, the work determined the ECG does not provide reliable timing values for the start of the pulse because the start of the R wave occurs before blood is ejected, causing varying timing delays within and between subjects [Balmer et al. 2017, 2018b]. Thus, it was recommended

to investigate PPG signals.

2.4.3 Pulse Wave Velocity Summary

The sensing methods, and their non-invasive alternatives for $SpvO_2$ and PWV monitoring have been presented in this cardiovascular section. This thesis will develop a reflectance pulse oximeter capable of non-invasively measuring $SpvO_2$, placed on the external jugular vein (Chapters 4-6). A specially designed PPG sensor placed on the carotid or radial artery also has the potential to non-invasively measure the PWV that would otherwise be measured by a pressure catheter. The sensor concept is developed in Chapter 7, with design refinement and validation in Chapter 9.

2.5 GLUCOSE MEASUREMENT

After oxygen, glucose is the primary source of energy in the body, and correct management of its levels is crucial to living a healthy, long life. Normally the body regulates the concentration of glucose using insulin. However, metabolic disease impacts the ability to manage BGC. Thus, a means to monitor the BGC is critical to health management. Current glucose sensors either invasively measure venous or arterial blood using finger stick measurements, or the ISF in continuous glucose monitors (CGMs). This section introduces the current methods of blood glucose concentration monitoring as well as the use of NIR spectroscopy for non-invasive glucose measurement.

2.5.1 Glucose Sensor Evaluation

Various metrics have been introduced to evaluate the effectiveness of glucose sensors. A common method of assessing results is the CEG. The CEG was first introduced in the 1970s to compare the accuracy of personal glucose sensors in a clinical decision making context compared to a reference value [Clarke 2005], with an updated error grid presented in 2000 [Parkes et al. 2000]. The grid is separated into five risk levels: A, B, C, D and E, shown in Figure 2.8. Each risk level indicates the effect of the sensors

reading on the ability of the clinician to take clinical action. Values in zone A are classed as having zero effect on clinical action, zone B has little to no effect on clinical action, zone C alters clinical action likely effecting outcomes, zone D alters clinical action with significant clinical risk and zone E measurements could have dangerous consequences. Readings falling in zones C, D or E are defined as over reactions, such as misidentifying hypoglycemia as hyperglycemia and giving insulin as treatment. Figure 2.8 shows the testing results of two glucose monitors, the Libre Freestyle Libre against an earlier version of the Dexcom G4 [Boscari et al. 2018].

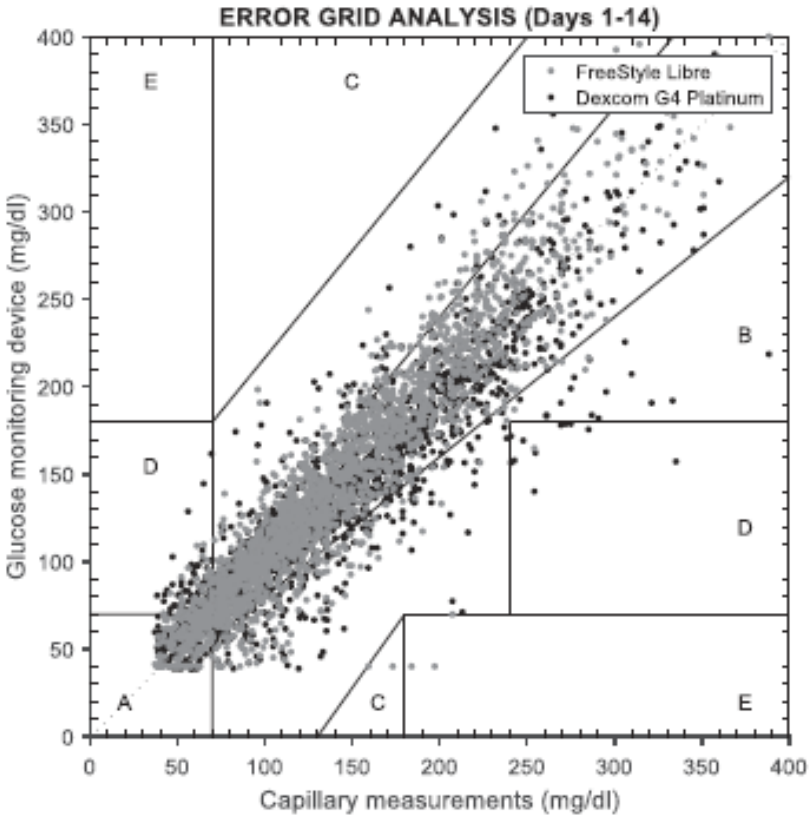

Figure 2.8 Clarke Error Grid of the Freestyle Libre and Dexcom G4 during 14 days of measurement, adapted from [Boscari et al. 2018].

An additional metric for assessing the performance of a glucose sensor is the MARD. The MARD is calculated using matched glucose readings between a reference glucometer, such as a blood gas analyser, and the sensor being tested [Heinemann et al. 2020]. Reported as a percentage difference between the two glucose measurements, the lower the MARD value, the better the agreement between sensors.

2.5.2 Finger stick glucometer

The ability to self monitor glucose levels using a finger stick glucometer has been one of the most important advancements in management of diabetes [Kato et al. 2013, Kaufman et al. 2001, Olansky and Kennedy 2010]. The finger stick glucometer uses a lancet to prick the skin, drawing a drop of blood to the surface. A test strip is placed on the drop of blood, drawing the blood up the strip using capillary action. The test strips contain an enzyme, glucose oxidase, which reacts with the glucose present in the drop of blood. This reaction generates a very small electrical current at the sensor electrode proportional to the blood glucose concentration [Mamkin et al. 2008].

There are several downsides to this method of blood glucose measurement. The need to draw blood causes apprehension for the pain of the lancet, inconvenient disruptions to daily life, and unwanted attention from measuring in public, all of which reduce the adherence to proper diabetes care [Diabetes Control and Complications Trial Research Group 1994]. Thus, the average individual living with diabetes measures their blood glucose levels less than twice daily, compared to the recommended seven times [He and Zhu 2010].

2.6 CONTINUOUS GLUCOSE MONITORS

The next step in personal glucose monitoring was the introduction of *continuous glucose monitors* (CGMs). CGMs were first introduced by DexCom and Medtronic in 2006 [Mamkin et al. 2008]. Real-time CGMs uses electrodes at the end of small filaments (<13 mm in length) placed in the subcutaneous layer of the skin, usually the upper arm or stomach. The sensor's electrode measures the glucose present in the interstitial fluid through a glucose oxidase reaction, similar to a finger-stick measurement. These sensors stay attached to the body between 3-10 days, and produce readings at about 5 minute intervals.

By continuously taking measurements, these sensors give much greater information than finger stick measurements. Trends in glucose direction can be estimated, reducing

the risk of hyper- and hypo-glycaemia. An additional benefit is the ability to monitor while sleeping, detecting the onset of nocturnal hypoglycemia. Over 65% of children living with diabetes experience asymptomatic hypoglycemia, regardless of the form of insulin therapy, be it multiple daily injections (MDI), or insulin pump therapy [Boland et al. 2001].

Modern CGMs have improved measurement errors over previous generations, and their use in hospital ICUs has become more prevalent [Klonoff et al. 2017, McKinlay et al. 2017b, Nguyen et al. 2020, Umpierrez and Klonoff 2018].

Figure 2.9 shows two of the commonly used CGMs in New Zealand. These sensors have a lifespan of almost 2 weeks, providing glucose readings without the need for calibration finger stick testing, but suffering some significant drift [Zhou et al. 2018].

(a) Dexcom G6 CGM [NZMS Diabetes 2021]

(b) Abbott Freestyle Libre CGM [Mediray 2021]

Figure 2.9 The Dexcom G6 and Freestyle Libre. Two CGMs available for use in New Zealand.

2.6.1 Abbot Freestyle Libre

The Freestyle Libre, produced by Abbott is a CGM with features different to currently available CGMs. The sensor is factory calibrated and claims to not need finger stick calibration during the 14 days of wear. The sensor does not continuously talk to a device. such as a smartphone. Instead, it provides glucose information with a scan. This scan gives information on the previous 8 hours of glucose values, as well as the current glucose trend. The Freestyle Libre shows 85.5% of readings falling in section A of the Clarke error grid when placed on the arm. This value drops to 68% when the sensor is placed on the stomach [Fokkert et al. 2017].

Owing to its two week life-span, costs can be lowered compared to conventional 3-7 day sensors. However, early sensor loss is common with %18 of sensors being lost before the 14 day life-span expectation, resulting in a lower reduction of the high cost of CGM systems [Marsters 2020].

The New Zealand government does not subsidise the Freestyle Libre sensor, so providers are required to import from other countries. In New Zealand, the cost of a Freestyle Libre reader is NZ $85 + GST and a single sensor also costs NZ $98 [Mediray 2021]. The reader has an indefinite life-span, so after initial setup cost, the Freestyle Libre costs NZ $196 per month.

2.6.2 Dexcom

The Dexcom G6 is another CGM available in New Zealand that claims to not need finger stick calibration and has an expected life-span of 10 days [Vettoretti et al. 2019]. The G6 takes a reading every 5 minutes, sending the result directly to your smartphone. Features such as "Urgent low soon" and customisable alerts gives users the ability for greater glucose control with improved long term outcomes compared to finger stick glucose management [Roze et al. 2021].

The Dexcom G6 costs NZ $532 + GST per month for 3 sensors and one transmitter [NZMS Diabetes 2021]. The transmitter has a three month lifespan, which was factored into the costs. Both the Freestyle Libre and Dexcom G6 costs assume no early loss of a sensor. If a sensor is lost early, for any reason or fault, a replacement must be used. Thus, if a sensor is lost early in it's life span, another NZ $126 Dexcom or NZ $98 Freestyle Libre sensor is required. With 1 in 5 sensors not lasting their full life-span, the actual cost of CGM use in New Zealand is much higher than advertised [Marsters 2020].

2.6.3 Limitations of CGMs

CGMs detect the glucose present in the interstitial fluid (IF) as opposed to capillary blood glucose. Early CGMs had a lag time of 20 minutes between changes in blood glucose and IF irrespective of rising or falling levels[Tamada et al. 1999]. This log is the subject of debate and can var with activity, calibration, and other factors [Beck et al. 2020, Heinemann 2018, Signal et al. 2012b, Thomas et al. 2016, Zaharieva et al. 2019]. Sensors have also required calibration using a finger stick glucometer to ensure correct readings, although that is starting to change with the newer models of CGMs.

As the sensors are attached to the body using glue, adverse reactions have been reported (11% of patients experienced discomfort [Chico et al. 2003]). The longer the sensor is attached to the skin, the greater the discomfort and risk of skin irritation/pruritis. Technologies for CGMs provide gains in diabetes management, but require patient education for proper use and correct interpretation of the data to guide care and realise benefit.

2.6.4 Non-invasive Glucose Measurements

Continuous non-invasive glucose sensing has been a topic of research for over 20 years [Liu et al. 2005], but as of the beginning of 2021, there have been no commercialised products providing a solution with glucose prediction errors between $1.5\,\mathrm{mmol\,l^{-1}}$ to $2\,\mathrm{mmol\,l^{-1}}$ [Lindner et al. 2021, Tang et al. 2020]. Products using NIR measurements have reported good correlation with blood glucose, but too many of the estimations were not clinically acceptable [Nybacka 2016, Smith 2017]. Figure 2.10 shows the commonly investigated non-invasive glucose measuring techniques:

There have been many attempts at creating and commercialising a non-invasive glucose sensor. Listed below are previous attempts at commercial products [Lin 2017, N. A. B. Abd Salam et al. 2016, Slade et al. 2016, Vashist 2013].

Orsense: The OrSense NBN-200G device used an optical platform, combined

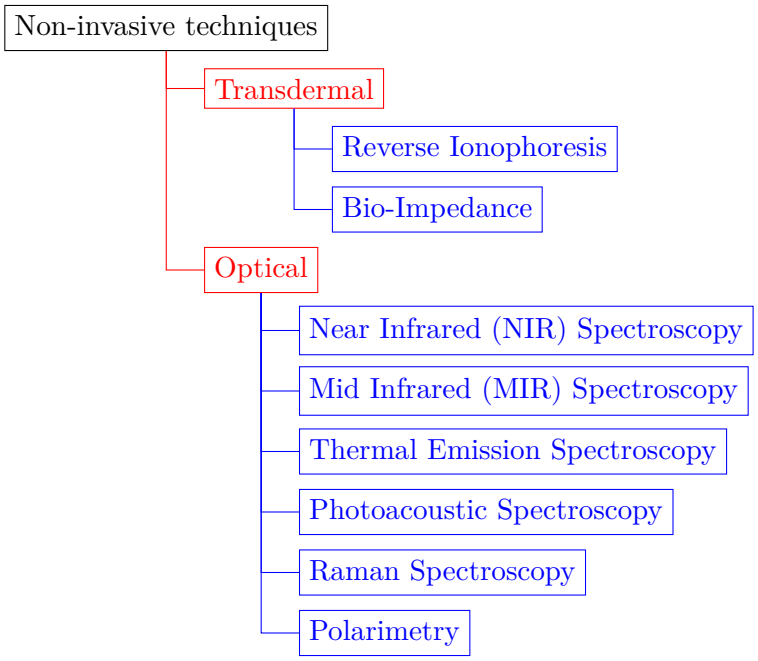

Figure 2.10 Non-invasive glucose measuring techniques

with a finger attached ring-shaped probe containing red and infrared emitters and detectors. A pneumatic cuff occluded blood flow, generating a change in the optical signal for glucose monitoring. A trial of 23 patients was conducted with CEG A and B zones containing 95% of the readings and a MARD of 17.2% [Amir et al. 2007]. However, even with CE-approval, no commercial device has been released.

GlucoTrack This sensor combines ultrasonic, electromagnetic and thermal methods to determine glucose levels. Placed on the earlobe, the sensor measures glucose related shifts in ion concentration. A clinical trial on 17 patients returned 98% of readings in CEG zones A and B, with 54% in zone A and a MARD of 22.8% [Horman et al. 2016]. The device is CE mark approved and has been released in several countries.

GlucoWatch This device was the first commercial device to be registered (CE approved in 1999) as a non-invasive glucose monitor and is the only 'non-invasive' device to be approved by the FDA (2001). However, the device was based on extraction of interstitial fluid through the skin, which was considered minimally invasive [Tierney et al. 2000]. However, the device was withdrawn from the

market due to skin irritation and poor accuracy during exercise, sweating or rapid temperature changes.

Gluco Wise The Gluco Wise sensor extracts glucose levels using low-power radio waves. A section of the body such as the area between the thumb and index finger or the earlobe is used. Pre-orders were expected in late 2018, but no commercial device has been released to date, 3 years later.

2.6.5 NIR Spectroscopy

Conventional NIR spectroscopy for identification of glucose has generally consisted of two wavelength regions in the range 500 nm to 2000 nm. These regions are 1400 nm to 2000 nm (first overtone) and 750 nm to 1400 nm (second overtone) [Yadav et al. 2015]. A major difficulty with in-vivo blood glucose measurement is the small concentration of glucose compared to water, haemoglobin, proteins and lipids [Tang et al. 2016]. Glucose accounts for less than 0.1% of absorption in the NIR spectrum [Jeon et al. 2006]

Optical path-length through tissue also reduces with increasing wavelength, reducing to under 1 mm at wavelengths >1000 nm, so a small emitter to detector distance is required [Yamakoshi et al. 2017]. At this small path-length, the light predominantly travels through the epidermis, dermis and subcutaneous tissue. The epidermis and subcutaneous tissue contain little blood flow, so the dermis is the source of the photoplethysmograph (PPG) signal. Light with a wavelength of 1600 nm only penetrates 0.54 mm into the skin and has a path-length of 1.5 mm [Maruo et al. 2003]. Dermis thickness in the finger ranges from 2.5 mm in men and 2.1 mm in females [Oltulu et al. 2018]. The thickness of the tissue must be correct for a quality signal. In particular, the tissue must be thick enough to contain sufficient concentrations of analyte within the optical path, while not being too thick so too much light is scattered and the signal is lost [Chowdhury et al. 2013].

Transmission mode sensing works well for wavelengths below 1000 nm, but the optical path is too long for higher NIR wavelengths [Yamakoshi et al. 2017]. Jeon et al in-

vestigated the results from transmission and reflectance sensing, concluding that transmission gives a higher signal [Jeon et al. 2006]. However, their transmission samples were recommended to be smaller than 2 mm, which is not feasible to recreate in-vivo. Thus, the sensor developed is used in reflectance mode to account for the reduced path lengths at higher wavelengths (>1000 nm).

2.6.5.1 Wavelength choice

Many sensors have been developed to use a variety of sensing wavelengths, providing a near continuous spectrographic absorption spectra of glucose. Yamakoshi et al developed a sensor ranging from 900 nm to 1700 nm in increments of 100 nm [Yamakoshi and Yamakoshi 2006]. However, due to the bulk required to generate a wide range of wavelengths, specific wavelengths have been chosen to generate discrete spectrometry [Kasahara et al. 2018]. Figure 2.11 shows the absorption spectrum of glucose compared to other components in blood that have similar absorption spectra (water, haemoglobin, protein, lipids). The chosen wavelengths must be producible by a 1206 footprint, or smaller, LED to ensure small sensing distance.

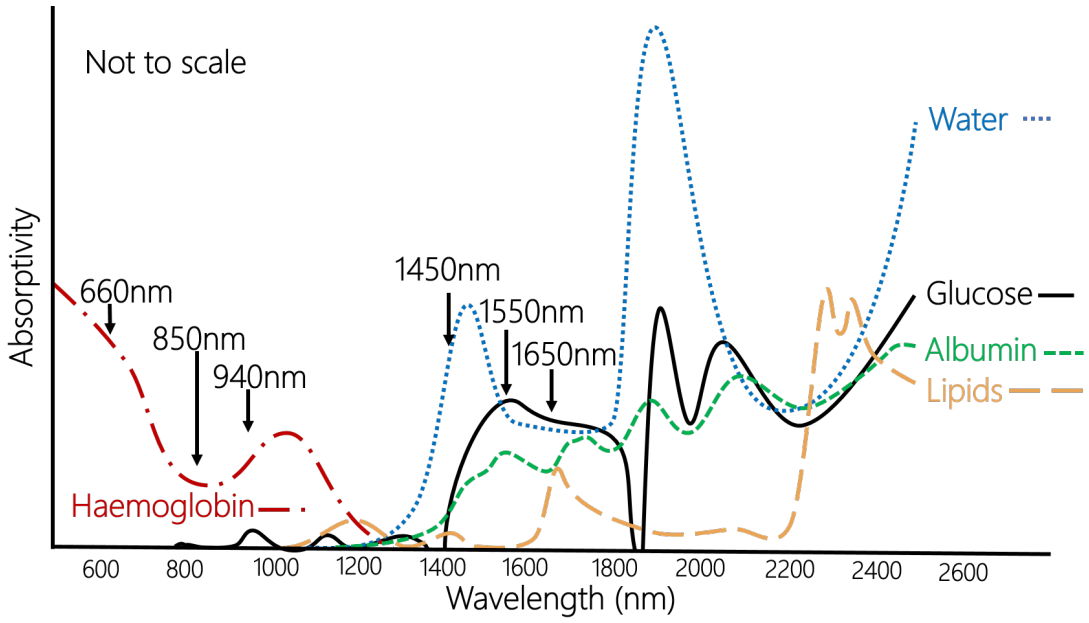

Figure 2.11 Absorption spectrum of the major light absorbers in blood in the NIR range. Adapted from [Amerov et al. 2004, Yadav et al. 2014].

In the first overtone (1400-2000 nm) glucose has the strongest light absorption. However, in this band, water is the dominant absorber due to the O-H bonds. At 1450 nm, water is the most dominant absorber [Abd Rahim et al. 2016, Guo et al. 2015]. At 1550 nm and 1650 nm, absorption rises with glucose due to the C-H stretch vibrations [Gayathri et al. 2017, Kohl et al. 1995, Uwadaira et al. 2016, Yoon et al. 1998]. Using a sensing wavelength at 1450 nm provides a reference measurement to water. Comparing the reading at 1450 nm to readings at 1550 nm and 1650 nm demonstrates a change in glucose absorption proportional to the water level, enabling discrimination.

While the absorption spectrum for glucose in the second overtone is much smaller, the absorption of water is not present [Kraitl et al. 2005]. In this region haemoglobin is the dominant absorber, so changes in blood oxygen will skew the results [Bashkatov et al. 2005]. Glucose has an absorption peak at 950 nm, which is a common wavelength used in pulse oximetry [Haxha and Jhoja 2016]. To measure oxygen saturation, a wavelength LED of 660 nm is also used. The isosbestic point of haemoglobin and deoxyhaemoglobin is at 808 nm [Kraitl et al. 2005]. Using an LED of 850 nm provides a reference for the haemoglobin measurement with regards to the glucose absorption peak at 940 nm [Guo et al. 2015]. Devices using the second overtone have been investigated, but none have yielded conclusive results at this time [Uwadaira et al. 2010].

2.6.6 Comparison of NIR glucose sensors in literature

There have been many attempts at using NIR spectroscopy to non-invasively detect glucose in the blood. One of those studies by Yamakoshi and Yamakoshi introduced the term "pulse glucometry" [Yamakoshi and Yamakoshi 2006]. This term means the pulsatile nature of arterial blood waveforms are analysed for blood glucose. Similar to pulse oximetry, pulse glucometry works to isolate the pulsatile nature of blood from absorption of surrounding tissue [Yamakoshi et al. 2009]. Partial least squares (PLS) is then used to calibrate a model of glucose absorption. The most recent work in this field introduced side-scattered finger photoplethysmography to ensure measurement of a pulse in the 1160 nm to 1750 nm wavelength region [Yamakoshi et al. 2017].

Artificial neural networks (ANN) have also been used to estimate non-invasive blood glucose [Guo et al. 2015, Han et al. 2021]. Ramasahayam et al also developed a PPG blood glucose sensor using an ANN to analyse adaptively filtered PPG combined with ECG [Ramasahayam et al. 2017]. The ANN was trained on 100 subjects with 95% of results in region A of the Clarke error grid. Marou et al developed a method of glucose prediction without requiring multivariate analysis using an imaginary spectra to adjust for scattering changes in the skin [Maruo and Yamada 2015]. This study found that the main difficulty in predicting blood glucose concentration is the change in baseline absorption parameters of skin tissue.

2.7 GLUCOSE SUMMARY

The current methods used to monitor BGC are all invasive. Invasive measurement increases pain, risk of infection, and reduces compliance to making measurements. As a result, there has been much research into using NIR spectroscopy to detect glucose concentrations in the blood. However, as of 2021, none are widely available commercially. Non-invasive glucose sensors have shown promise in-vitro. However, few have been able to transition to in-vivo.

This thesis will further investigate using NIR spectroscopy using LEDs rather than photodiodes to detect light, acting as discrete wavelength spectrometers. The sensor will first be validated in-vitro in porcine blood in Chapter 10, then in adult and neonatal trials in Chapter 12.

2.8 SUMMARY

This chapter covered the background and theory of pulse oximetry, venous oxygen saturation, pulse wave velocity, and blood glucose monitoring, as well as the limitations of each. Methods of measuring venous oxygen saturation was discussed. Gaps in research were identified, with the ability to non-invasively measure venous oxygen saturation not yet viable. Various pulse wave velocity sensors have been developed, but none

measure locally to a single artery. Non-invasive NIR glucose sensors have been a field of research for over 20 years, but none have been accurate, or reliable enough to replace the invasive devices.

This thesis will further investigate $SjvO_2$ measurement through recording natural pulsations in the external jugular vein on the neck. Pulse wave velocity will be investigated, measuring local to the carotid and radial artery. Finally, a non-invasive NIR glucose spectrometer will be developed using pulse oximetry principles.

Overall, each example represents a significant change in the state of the art for light-based biomedical sensing, and each has potential significant associated clinical impact.

Chapter 3

USING WAVELENGTH-SPECIFIC LEDS AS LIGHT DETECTORS

3.1 INTRODUCTION

Conventional pulse oximeters consist of an LED emitting light through the skin and a photodiode to detect the resulting photoplethysmograph (PPG) waveform. The PPG waveforms are generated by the pulsatile nature of blood in the arteries and capillaries [Allen 2007, Daly and Leahy 2013]. When a pulse of blood moves past the sensor, the additional volume of blood absorbs more light. This variation in the light absorbed allows the estimation of the blood oxygen saturation. The absorption ratio of red to infrared light absorbed by oxyhaemoglobin and deoxyhaemoglobin.

Photodiodes are designed to be sensitive to varying light intensities, producing a photocurrent proportional to the incident light intensity [De Santis et al. 2006]. These photodiodes are typically PIN type [Rhee et al. 2001]. In addition to the photodiode, operational amplifiers and mid to high resolution analogue to digital converters (ADCs) are required. The requirement for additional components not only increases circuit complexity, but also power consumption, both important factors in creating miniature, battery powered sensors [Stojanovic and Karadaglic 2007a]. Photodiodes are also not ideal for specific wavelength sensing for applications such as pulse oximetry, due to their wide spectrum detection range in the ultraviolet to near infrared (NIR).

While LEDs are generally used to emit light, they can also be used to detect light [Miyazaki et al. 1998]. Photodiodes are much more sensitive than LEDs to varying

light intensities when measuring the generated photocurrent. However, despite this relatively low sensitivity of LEDs to incident light, this phenomenon can be exploited to produce similar results to photodiodes using the decay waveform of a reverse biased LED [Mims 1992].

An additional benefit of using LEDs to detect light is their narrow spectral absorption band [Kowalczyk and Siuzdak 2017]. This narrow band operates as a wavelength specific bandpass filter. The voltage decay, $V(t)$, of the reverse biased LED is a function of time (t)), diode junction capacitance, and the shunt resistance:

$$V(t) = V_0 e^{-t/RC} - I_p(\phi) \tag{3.1}$$

Where,

V_0: Reverse bias voltage at $t = 0$

t: time

R: Shunt resistance of the LED

C: Junction capacitance of the LED

$I_p(\phi)$: Photocurrent as a function of incident light (ϕ)

Figure 3.1 shows the equivalent circuit for an LED reverse biased by a microcontroller pin to V_{cc}. The cathode of the LED is connected to the microcontroller pin and the anode is typically connected to ground. The photocurrent, I_p, typically in the region of 0.5 µA, flows to ground [Miyazaki et al. 1998].

Figure 3.2 shows the emission and corresponding absorption spectrum from an example 660 nm LED [De Santis et al. 2006]. The peak absorption spectrum is shifted to a lower wavelength than the emission spectrum. If another LED of the same wavelength is used as an emitter, the detecting LED would detect light only in the spectrum overlap.

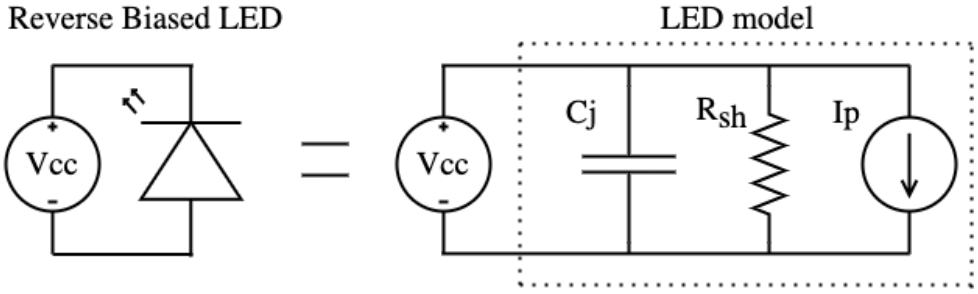

Figure 3.1 Equivalent circuit for a reverse biased LED. Typically a microcontroller pin drives the cathode to V_{cc}, and the anode is connected to GND.

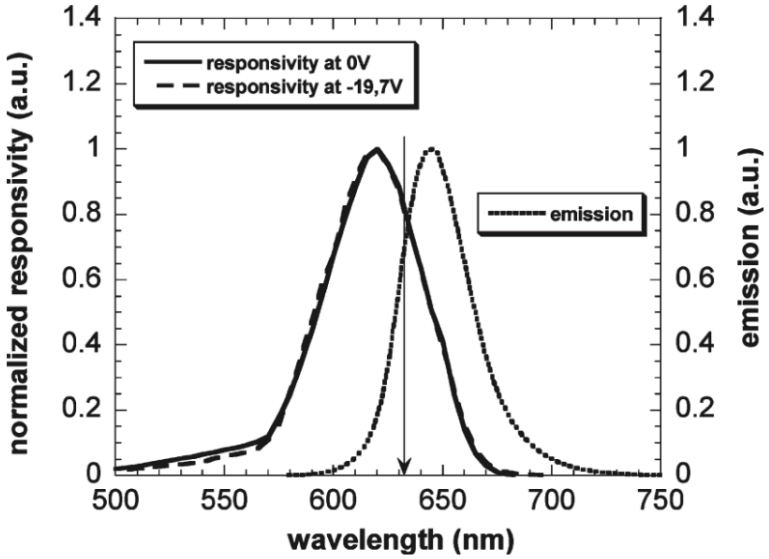

Figure 3.2 Emission spectrum and absorption spectrum of a reverse biased 660 nm LED [De Santis et al. 2006]

.

The use of an LED to detect light for various applications has been investigated, including: colour based pH measurements, monitoring UV emissions from the sun, liquid chromatography, half-duplex bidirectional communications and photoplethysmography. [Otoole et al. 2005, OToole and Diamond 2008, Schmid et al. 2013, Shin and Eom 2013, Shin et al. 2016, Stojanovic and Karadaglic 2007b]. Further development by Stojanovic and Karadaglic developed a digital pulse oximeter removing the need for a photodiode, operational amplifiers and ADCs [Stojanovic and Karadaglic 2007a]. This sensor used LEDs to produce and detect the wavelengths of light required for pulse oximetry. Rather than measure the current produced by the LED, a clock timer is used to time the drop in voltage across a reverse biased LED transitioning between logic high and low.

Timing the voltage decay across the LED integrates the current produced by the LED over the time of the decay [Lau et al. 2006], removing the need for accurate current amplifiers. The detecting LED has the anode connected to ground and the cathode connected to a tristate buffered I/O pin on a microcontroller. Using a tristate buffered I/O pin allows the pin to change state from driving the cathode high to detecting the voltage across it in the high impedance state.

These described applications use dedicated LEDs for emitting, and additional LEDs for detection. While it is possible to connect both the anode and cathode of the LED to pins of the microcontroller to enable both emitting and sensing from the same LED, variable current driven LEDs are only possible with a dedicated LED driver. Figure 3.3 shows the voltage decay waveforms of a 660 nm LED from 3.3 V through logic low (dashed line at 1.6 V). Under zero incident light, the decay waveform is solely represented by the *RC* time constant of the diode junction. When the radiant intensity of the emitting LED increases, the sensing LED photocurrent reduces the final resting voltage.

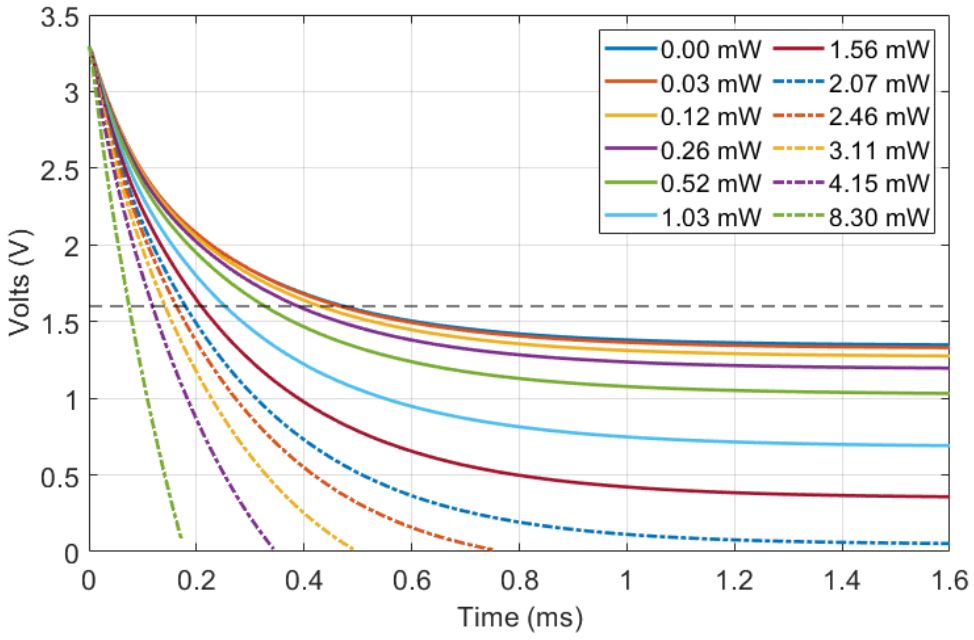

Figure 3.3 Discharge curve for a 660 nm LED decaying from 3.3 V under the influence of another 660 nm LED emitting at varying radiant light intensities.

This thesis presents work on using LEDs as non-invasive light emitters and detectors with the purpose of making an array of detectors to provide improved cardiovascular

and glucose sensing, compared to conventional, often invasive, sensing methods. Using multiple specific wavelengths of light allows the sensor to extract more information out of the PPG signal, such as the other states of haemoglobin (carboxyhaemoglobin, methaemoglobin), or other analytes in blood, including glucose.

3.2 LED SENSING METHODS

There are two methods of capturing the voltage decay of the reverse biased LED waveform. The simplest method involves using a microcontroller to time the voltage decay between digital logic HIGH and LOW. The second method involves measuring the voltage decay waveform with an ADC, and using a model to calculate the photocurrent.

3.2.1 Digital Timing Method

The timing method is a purely digital method of measurement, based on timing the decay of a reverse-biased LED. This method is digital as no analogue front end is used, only a microcontroller GPIO pin and and an LED are required to detect light. The time taken for the LED voltage to transition from digital logic HIGH to logic LOW is linearly proportional to the incident light intensity and can be measured with the microcontroller's inbuilt clock timer.

The digital sensing method involves multiple steps to complete. Rather than taking an individual analogue voltage reading at the sample frequency like traditional photodiodes, measuring the light intensity with the LED-LED sensor requires monitoring the input state of a microcontroller's GPIO pin. The steps required with an LED set up as shown in Figure 3.1 are:

1. Reverse bias the LED to V_{cc} (3.3 V or 5 V depending on microcontroller architecture) by driving the GPIO pin of a microcontroller to output HIGH.

2. Wait 50-100 µs for the voltage across the LED to reach V_{cc}.

3. Switch the GPIO pin state from output HIGH to high impedance INPUT and start a microcontroller clock timer.

4. Stop timer when the voltage decay across the GPIO pin crosses the threshold for logic LOW (usually 1.6 V).

5. Repeat measurement by setting GPIO pin back to output HIGH.

Accurate timing of the voltage decay allows the relative light intensity to be found. The more accurate the timer, the higher the resolution of measurement. The micro-processor used by Stojanovic and Karadaglic ran at clock frequencies of 8 MHz and 16 MHz, giving time resolutions of 0.125 µs and 0.0625 µs respectively [Stojanovic and Karadaglic 2007b]. A further paper by Stojanovic and Karadaglic used an FPGA rather than a micro-processor in order to run each LED in parallel with a clock rate of 48 MHz [Stojanovic and Karadaglic 2013]. The microcontroller clock rates used in this thesis range from 8 MHz to 600 MHz.

A downside of this sensing method is the need to wait for the LED voltage to decay past the threshold for logic low. This means that to detect low light levels, the microcontroller must wait in the range of milliseconds for the decay. Thus, maintaining a constant sample rate means the microcontroller must always wait that long during each sample, even if the voltage had already decayed past logic LOW. This problem is further compounded when sensing with multiple LEDs sequentially, as the next sensing LED must first wait for the other to finish before starting the sensing cycle.

3.2.2 ADC method

The alternative method of light detection presented in this thesis is the use of an ADC to measure the voltage decay waveform directly. By measuring the LED voltage decay with the ADC at multiple points in time, the microcontroller can then predict the incident light intensity. The model developed in Chapter 11 presents the ADC method as a way to measure the LED decay voltage over a short time, such as 500 µs, and

predict the remaining decay waveform. By measuring the voltage for a short time, then projecting the remaining decay, the sensor can increase the sample rate of the sensor, compared to the timing method.

The in-built microcontroller ADC of the Teensy 4.0 used in Chapter 10, has a 12-bit resolution. An external ADC may also be used to track the microcontroller pin voltage, allowing the use of higher resolutions, such as the 24-bit ADC used in Chapter 12.

A downside of this method is the increased complexity in circuitry. While the inbuilt Teensy 4.0 ADC can work for high light levels, an external ADC with higher resolution is required for low light detection.

3.2.3 Sequential LED sampling algorithm

To improve the sample rate and accuracy of the digital sensing method, an algorithm has been developed to adapt the LED sensing order. The sensors developed in this thesis use different wavelength LEDs, each needing to be sampled sequentially to avoid the sensing LED detecting light at the wrong wavelength. Every wavelength of LED has a unique voltage decay waveform, taking from 100 µs to 10 ms to decay, meaning that a one size fits all approach to voltage decay timing does not work. For example, to sample six LEDs sequentially at 200 Hz, the sum of the LED discharge times must be <5 ms, which could be done by allocating the 833 µs equally to each sensing LED. However, as some LEDs take <500 µs to decay, the remaining 300 µs allocated to each would be wasted.

Thus, an adaptive sensing order has been created to minimise wasted sensing time. At the start of a sensing cycle, each LED is given an initial reading timeout of 833 µs, with the assumption that all LEDs require the same amount of time to decay. The order that each wavelength LED is sensed is set by the previous decay times, where the LED voltage decay times are ranked from fastest to slowest, setting the new read order. After the first LED decay is has finished reading (crossing 1.6 V, or timeout reached), the decay time is subtracted from the total sensing time of 5 ms. This remaining time

is then divided by the number of LEDs left to read, and is evenly allocated to each.

While the emitting LEDs could be driven at maximum brightness to ensure the fastest possible LED voltage decay time, the ADC sample time is limited. For example the external ADC used in Chapter 12 has a sample rate of 33 kHz, meaning that the algorithm must compromise between sampling speed and the required number of ADC measurements to reliably fit the decay model. Having a goal LED decay time of 400 µs provides a compromise between sampling speed and sufficient samples (13 samples). A PI controller was created to adjust the output LED light intensity, keeping the sensing LED discharge time at 400 µs. LEDs often don't reach this goal discharge time when next to tissue, as a result, the controller sets these emitting LEDs to the maximum light intensity possible.

By reading the fastest LEDs first, the remaining time can be reallocated to the slower LEDs. For example, if the first three of the six LEDs take a combined 1.2 ms (400 µs each), the remaining three LEDs that have longer inherent decay times are each allocated 1.26 ms timeouts. Should any of these LEDs take less time than 1.26 ms to decay, the timeout value for the remaining LEDs is adjusted accordingly. Using an adaptive LED sensing order, and a goal LED discharge time of 400 ns, all six wavelength LEDs are able to be sequentially read within the allowed 5 ms window, while giving the LEDs the longest time that they require to capture the LED voltage decay.

3.3 LED EMISSION INTENSITY AND SAFETY

The LEDs used in this thesis range in emission wavelength from 660 nm to 1650 nm, spanning the visible (red) to near infrared spectrum (NIR). Potential causes of injury from the LEDs include emitted light and heat. As the human eye does not see infrared light, precautions must be taken to avoid eye damage from the LEDs [ICNIRP 2013]. However, NIR light is non-ionising, unlike UV light, so the exposure risk is reduced [Ham et al. 1976].

Lau et al investigated the safety of high-intensity LEDs in biomedical applications, such

as pulse oximetry [Lau 2013]. Their research showed that although LEDs are currently classed as safe [ICNIRP 2020], advances in LED optical power and brightness makes this assumption invalid, as LEDs are now sold exceeding the power levels to qualify for exemption from IEC 62471 rating. The standard IEC 62471 gives guidance for evaluating the photobiological safety of lamps and lamp systems at a standardised distance of 200 mm between emitter and observer. Lau et al noted that this distance is not valid for use in pulse oximeters, as the LEDs are placed in contact with the skin. They instead applied the IEC 60285-1, the standard for safety of laser products as it addresses close in irradiation [Schulmeister 2013]. The IEC 62471 hazard limit for irradiance is $100\,\mathrm{W\,m^{-2}}$.

The brightest LED used in this thesis is the 660 nm LED with a radiant flux of 8.3 mW, corresponding to an irradiance of $0.2\,\mathrm{W\,m^{-2}}$. This brightness reaches the eye hazard threshold at a distance of 10 mm. The IEC 80825-1 safe skin contact is $6\,\mathrm{kW\,m^{-2}}$. Using the lens diameter of 1.6 mm for the XZM2MRTNI55W-8 LED [SunLED 2017], the maximum contact irradiance is $3.2\,\mathrm{kW\,m^{-2}}$, sitting within the safe limits. Thus, the LEDs used in this thesis are safe for skin contact, but should not be viewed at a distance closer than 10 mm.

3.3.1 Skin detection

To further reduce the risk of eye injury, every sensor designed in this thesis for clinical trial use used a skin detection feature. An infrared LED pulses 10 times per second with low intensity light, searching for skin contact. Once contact is sensed, the sensor would begin sensing with all LEDs.

The infrared LED, typically 940 nm, or 1450 nm, measures at two different light intensities, ambient, and with the emitter running at 50% light intensity. To further reduce the amount of light emitted, the sensor checks for skin contact 10 times a second, emitting for 10 ms each time, resulting in the LED emitting at a duty cycle of 10%.

Under ambient light conditions, a decrease in LED voltage decay time indicates the

room is either dark, or the sensor is covered. Using the emitting LED clarifies whether the sensor is covered, as the LED voltage decay under emitted light increases when the ambient decay time decreases, the sensor knows that it is covered. Whereas, if the decay time with the emitting LED on does not change, then the sensor knows it is just a change in ambient lighting. Thus, the difference between the ambient voltage decay time and the decay time with the emitter on indicates sensor coverage.

Further use of skin absorption characteristics are utilised. When covered by an object such as cloth, or metal, the LED voltage decay time decreases linearly with distance, reaching the fastest decay time when in contact with the LED. However, due to the absorption of light by tissue, when the LED is in contact with tissue, the LED voltage decay time increases. By tracking the voltage decay time, the sensor is able to discern tissue contact from other objects.

The skin detection feature also proves useful when recording data. The sensor does not start recording until it detects skin, so the recording may be started with the sensor away from the measurement site, and moved to the site to begin recording. Recording may also be paused by lifting the sensor off the tissue.

3.3.2 Temperature effect on LED emissions

LED temperature can affect the emitted light intensity [Baumgartner et al. 2018]. A rise in temperature linearly increases the emitted light intensity [Reynolds et al. 1991]. While this rise would be a problem with a traditional LED-photodiode sensor, an LED-LED sensor is minimally affected. Stojanovic et el found an increase of only 0.4% per °C with LED-LED sensors [Stojanovic and Karadaglic 2007a]. As the sensor increases in temperature, the LED emits at a higher light intensity. However, the increase in temperature also decreases the light absorption from the detecting LED. The increased intensity, but decreased absorption counteract each other resulting in minimal change due to temperature.

In addition to emitted light, heat is also a potential source of safety concern. Bozurt

et al investigated the safety of common LEDs used in pulse oximetry, finding that the approximate (10 °C) temperature increase at the contact point with human skin is due to the semiconductor junction of the LED (9 °C), rather than the radiated heat from the LED (1 °C) [Bozkurt and Onaral 2004]. The temperature threshold for pulse oximeter burn injury at 8 hours of use is 43 °C [Greenhalgh et al. 2004].

3.4 SENSORS DESCRIBED IN THIS THESIS

This section describes the different versions and applications of the LED sensing array, developed in this thesis. The sensors were designed to be modular and have the capability to measure different parameters as seen in the $SpjvO_2$ sensor (Figure 3.4). While using LEDs to detect light is consistent between sensors, the choice of wavelengths and arrangement of emitting and detecting LEDs vary between applications. Further details of the hardware for each application are contained in the Hardware chapters (Chapter 4 for $SpjvO_2$, Chapter 7 for PWV and Chapter 10 for the glucose sensor).

Initial testing of algorithms for pulse oximetry in this thesis used a traditional pulse oximeter probe containing a photodiode. The data generated from the photodiode sensor is analysed in Chapters 5. All other chapters use the digital sensing method for generating PPG waveforms.

3.4.1 Jugular venous oxygen sensor

The measurement of $SpjvO_2$ requires two different wavelength LEDs (660 nm and 940 nm). These two wavelengths are commonly used in pulse oximeters to calculate SpO_2. Placement along the EJV requires a reflectance pulse oximeter that can be held with light pressure against the skin to not occlude the EJV. Figure 3.4 shows the sensor used to measure $SpjvO_2$.

While the sensor contains multiple different wavelength LEDs, only the 660 nm and 940 nm LEDs are used to estimate $SpjvO_2$, streaming at 200 Hz. The remaining LEDs on the board allow additional use for analysing blood glucose concentrations. The

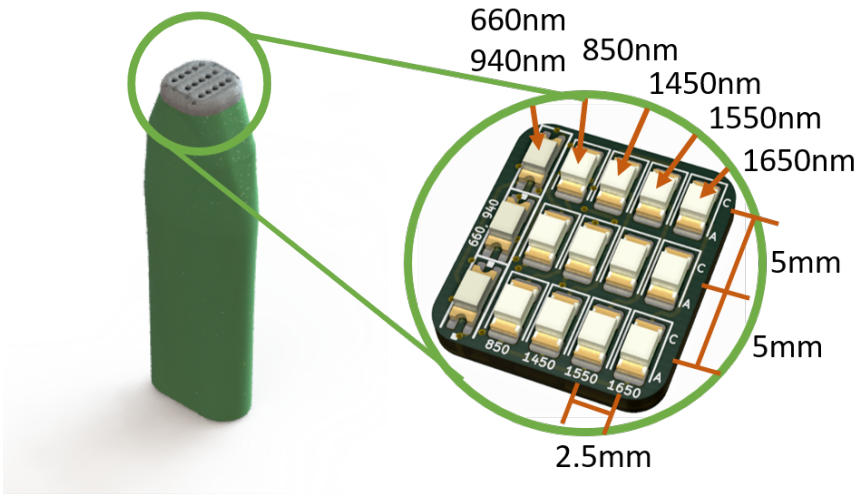

Figure 3.4 Sensor used to estimate $SjvO_2$ in the external jugular vein. A 660 nm and 940 nm LED are used for calculating oxygen saturation. The remaining LEDs on the board allow additional use for analysing blood glucose. The central row of LEDs are used to detect the light emitted by the two outer rows of LEDs.

hardware description for this board is further developed in Chapter 4 and validation of the sensor is described in Chapter 6.

3.4.2 Pulse Wave Velocity sensors

The initial design of the PWV sensor included a matrix of LEDs to ensure measurement of the carotid arterial pulse in the neck. Figure 3.5 shows the layout of the PWV sensor. There are three rows spread apart to measure the carotid pulse at three different positions along the artery. Each row included 20 LEDs of two wavelengths (10 at 660 nm and 10 at 940 nm) capable of both emitting and detecting light. To save footprint space, a single LED package contained both wavelengths for sensing. Each LED package along the array was separated by 5 mm. This spacing ensured that the arterial pulse was contained within the total area of 45 mm by 50 mm.

While measuring both wavelengths provides the ability to measure oxygen saturation, only the 660 nm wavelength LED was used to measure the pulse wave velocity, sampling at 570 Hz. This sample rate was the fastest possible while sequentially sampling each LED. The use of this sensor is described in Chapter 7. By using an array of LED sensors, the sensor can be placed approximately in the correct place along the neck and

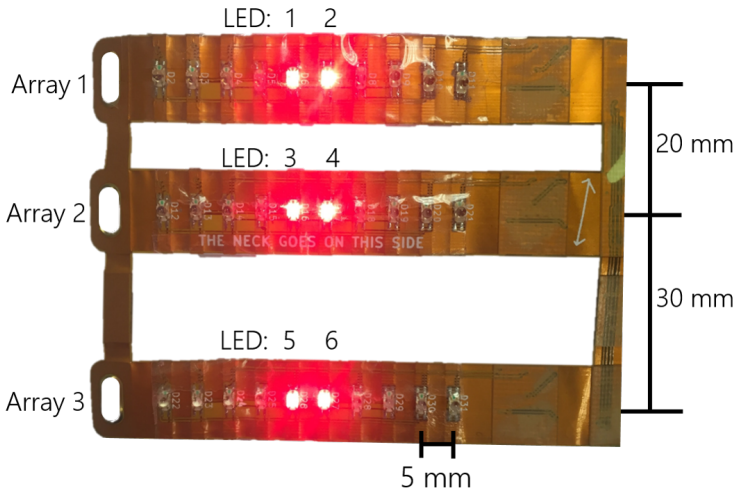

Figure 3.5 Sensor used to measure pulse wave velocity in the carotid artery. The sensor consists of three lateral rows of 10 660 nm and 940 nm LEDs to ensure that the carotid pulse is located within the sensor area (45x50 mm). Two emitting LEDs in each row are illuminated.

the best signals from each array are used for further analysis.

A subsequent PWV was developed to address the issues identified in the matrix PWV sensor. The new sensor is an adaption of the hardware in the SpjvO_2 sensor, with three sets of emitting and detecting LEDs spaced by 20 mm, as shown in Figure 3.6. As PWV only requires a single wavelength to measure the pulse, the 660 nm wavelength LED was used. The sample rate of the sensor was 3 kHz. Validation of this sensor for measuring PWV is described in Chapter 9.

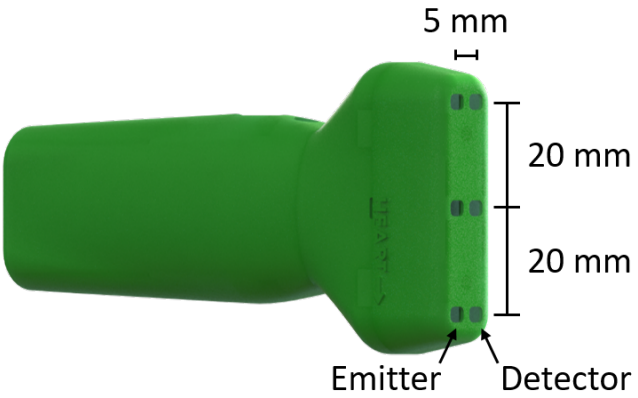

Figure 3.6 Sensor used to measure pulse wave velocity in the carotid artery and radial artery. Emitting and detecting pairs of 660 nm and 940 nm LEDs are spaced by 5 mm, with 20 mm between each sensing LEDs.

3.4.3 Glucose sensors

The first glucose sensor developed is described in Chapter 10. This sensor contains 6 different wavelength LEDs (660 nm, 850 nm, 940 nm, 1450 nm,1550 nm, 1650 nm) to identify the spectral fingerprint of glucose in blood. The board contains an emitting and detecting LED for each wavelength arranged in a circle with 10 mm spacing. Figure 3.7 shows the layout of the glucose sensor. This sensor was developed to measure non-pulsatile blood glucose in-vitro using the LED decay digital timing method.

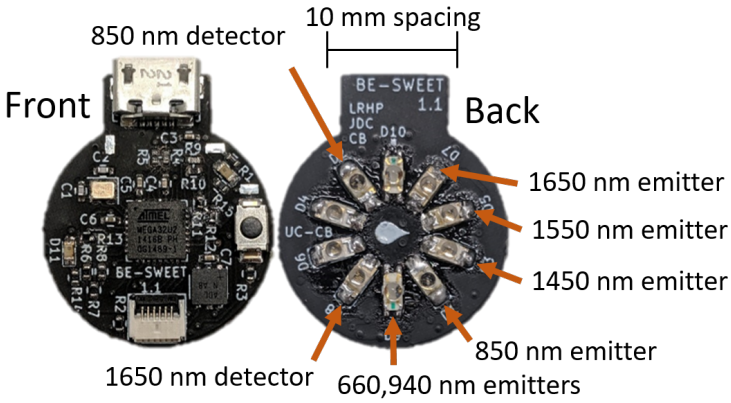

Figure 3.7 Sensor used to track changes in blood glucose concentration in-vitro in porcine blood. Emitting and detecting pairs are separated by 10 mm in a rosette shape, with the emitting and detecting LEDs located across from each other. The corresponding detecting LEDs for 850 nm and 1650 nm is shown.

In-vivo testing of blood glucose on adults and neonates required a different arrangement of the 6 wavelength LEDs, as well as a new sensing method using an external ADC to monitor the voltage across the sensing LEDs. The emitting and detecting LEDs are arranged in a matrix described in Figure 3.8. One requirement of the sensor was to be used on neonates in the neonatal intensive care unit (NICU), so the sensing end of the LEDs had additional design requirements, as described in Chapter 12. This sensor uses the ADC voltage decay method of measuring light intensity.

3.5 SUMMARY

This chapter outlined the digital sensing method using LEDs to detect light. Under reverse bias conditions, LEDs can have greater sensitivity than photodiodes, while

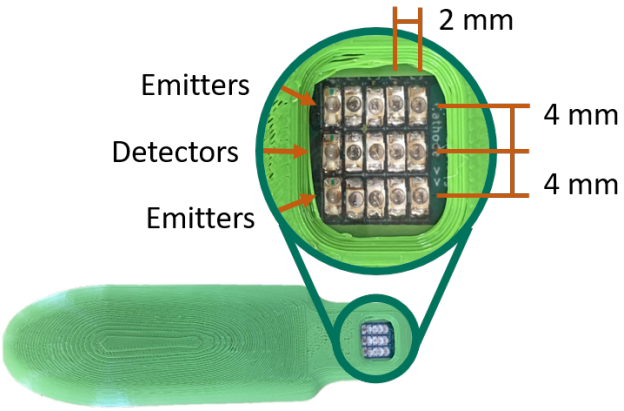

Figure 3.8 Sensor designed for use in the neonatal ICU. Each of the 6 wavelength LEDs are separated by 2.5 mm, with 4 mm between emitting and detecting rows. The LED wavelength order from left to right is 660 nm, 850 nm,940 nm, 1450 nm,1550 nm, 1650 nm.

also providing the benefit of not requiring additional analogue circuitry to detect light. Only an LED and a microcontroller GPIO pin is required to detect the arterial pulsatile waveform for pulse oximetery. This simplicity in circuit design allows greater design flexibility from using an array of LEDs of the same wavelength to determine pulse wave velocity, to using multiple different wavelength LEDs for NIR spectroscopy of components in blood, such as glucose. A brief outline of each sensor developed in this thesis was also presented to provide a reference for further reading of the thesis.

Part II

Estimation of Venous Blood Oxygen Saturation

Chapter 4

REFLECTANCE PULSE OXIMETER HARDWARE DESIGN

Measuring the venous pulse in the external jugular vein requires a custom reflectance pulse oximeter. This chapter details the design of a reflectance pulse oximeter using LED-LED light detection. The sensor is also designed to use other wavelength LEDs in addition to the conventional 660 nm and 940 nm used in pulse oximeters. A right leg driver circuit is also implemented to reduce the effect of mains power noise on the signal.

4.1 INTRODUCTION

Most commercial pulse oximeters are not open source hardware and can be costly to purchase. Further, many manufacturers do not divulge their sensing method and signal processing, so clinicians must trust the results they are given. This lack of access means a person cannot record their own raw data from these sensors to process it independently. The key to unlocking the potential of the pulse oximeter is unrestricted access to the raw signal, as well as standardised methods [Shelley 2007].

This chapter presents the development of a sensor using discrete wavelength LEDs as light emitters and detectors in a multi-wavelength array to provide greater information than a conventional pulse oximeter. A right leg driver circuit is included to reduce the effect of capacitively coupled mains noise on the signal. Using multiple wavelengths of light allows the sensor to extract more information from the PPG signal, such as the

other states of haemoglobin (carboxyhaemoglobin, methaemoglobin), or other analytes in blood.

While traditional, analogue pulse oximeters require analogue circuits to amplify photodiode signals, the digital pulse oximeter only requires a microcontroller and LEDs. This change reduces the overall complexity and cost of the sensor in both money and power consumption. Almost any microcontroller can be used for this project. However a microcontroller with a higher clock rate will give more accurate readings.

Typically, a pulse oximeter is placed on the peripheral tissue, commonly a finger or ear, using transmission mode where the emitter and detector are either side of the tissue. Reflectance mode sensing has the emitter and detector adjacent to each other on the same side of the tissue, allowing measurement on additional sites to transmission mode sensing. The sensor developed in this work is a reflectance pulse oximeter designed to measure the pulse on the finger, neck, radial artery, or other peripheral surface with pulsatile blood flow. Measuring the pulse at central places on the body such as the neck also helps reduce the main detrimental effects on pulse signal such as low external temperature [Khan et al. 2015a, Reynolds et al. 1991] and motion artefacts [Ralston et al. 1991].

The goal of this chapter is to develop a simple, low cost pulse oximeter, which can change detection wavelengths by changing LEDs. Hospital grade pulse oximeters cost upwards of USD $500-$1000, and while low cost pulse oximeters are more readily becoming available, their accuracy, filtering, and reliability are not up to research standards [Lipnick et al. 2016]. None of these options provide easy, inter-operable access to the raw data. These issues are important for COVID-19 home monitoring, where incorrect oxygen saturations have negative health outcomes [Greenhalgh et al. 2021].

4.2 METHODS

The design presented allows full access to raw PPG data, is low cost with a BOM <$250, and open source. Depending on the required level of accuracy, the cost can

be <$50 to build. The faster the clock on a microcontroller, the more accurate the sensor, but also the more expensive. Using an Arduino Pro Micro running at 16 MHz is recommended for low cost design, and a Teensy 4.0 at 600 MHz is recommended for $20 USD if higher accuracy is preferred. For LEDs, the desired wavelength is the main driver in cost. Visible light and low NIR LEDs used for pule oximetry cost <$1 USD, increasing to $20 USD for the LEDs >1000 nm used for spectroscopy.

The total cost of the system is less than $218 USD for components, 3D printing and boards from PCBWay (China). If the end user uses different LEDs, the cost for the whole system can be reduced to below $37 USD.

4.2.1 RLD driver design

As the LED's are placed against the skin, common mode noise is capacitively coupled to the subject from mains power supply can be coupled to the sensor. While digital filters can remove this 50-60 Hz noise at high sample rates, this sensor may be required to measure at 50 Hz or near mains frequency. This lower sample rate removes the ability to digitally filter this noise.

Conventionally, a right leg driver (RLD) is used in ECG and EMG systems to reduce noise generated by common-mode interference [Fortune et al. 2017]. To the best of the author's knowledge, there are no pulse oximeters incorporating a RLD in their sensor.

This noise is predominantly 50-60 Hz noise coupled from electrical mains. The RLD reduces this noise by measuring the common mode voltage [Winter and Webster 1983], then driving the inverted signal back into the body. As this µA current is 180° out of phase to the original noise signal, the waves destructively interfere.

Electrodes used in a RLD circuit are typically single-use, adhesive silver-silver chloride electrodes. However, as the adhesive surface requires a large area with a minimum spacing of 20 mm, it is not feasible to use these electrodes on this sensor as the total area of the LED matrix is 20x20 mm. To solve both the size and re-usability issues, 1 mm diameter 99.99% pure silver wire is used as the electrodes. Three electrodes are

threaded through the sensor housing to ensure skin contact. Two electrodes, E1 and E2, are used to measure the common mode noise, and the third electrode as the RLD. The electrodes are 20 mm in length with a spacing of 5 mm.

This board uses a wide range of LED wavelengths to act as a discrete spectrometer. Shin et al showed this sensing method is best used at wavelengths greater than 440 nm [Shin and Eom 2013]. Depending on the analyte to be detected, LEDs with different specific wavelengths can be chosen. For example, 660 nm and 940 nm are commonly used in pulse oximetry.

4.3 HARDWARE

The hardware consists of two boards: 1) the LED driver board; and 2) the LED sensor board. The LED driver board houses the Teensy 4.0, RLD and LED driver. A 24 pin FPC cable is used to connect between boards. The LED sensor board contains only the LEDs and the temperature sensor. This separation allows full customisation of the sensing board.

While six sensing LEDs are used on this board, the driver board is capable of running up to 9 sensing LEDs and the emitting LEDs of the same wavelength. The assembled boards are shown in Figure 4.1.

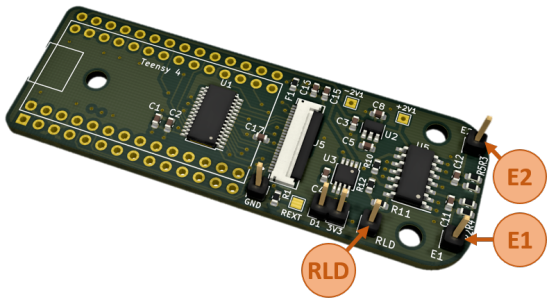

(a) LED driver board populated with the Teensy 4.0 socket shown. The electrode headers are at E1 and E2, and the RLD is given.

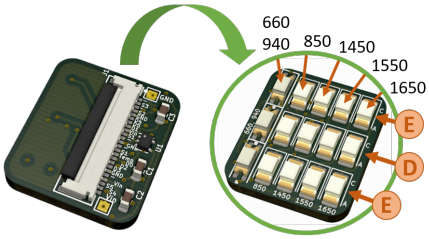

(b) Both sides of the LED sense board with each LED wavelength and the emitting (E) and detecting (D) rows shown .

Figure 4.1 Assemblies of both the LED drive and sense boards.

4.3.1 LEDs

Two wavelengths of light are predominantly used to estimate blood oxygen saturation, red (centred around 660 nm) and infrared (centred around 940 nm). While any LEDs in these ranges can be chosen, it is advisable to use LEDs advertised for use in pulse oximeters. The LEDs used in this chapter for pulse oximetry are from the SunLED (USA) pulse oximeter series (XZM2MRTNI55W-8). The red and infrared LEDs are contained in a single package to reduce the footprint size and provide the same emission and detection points. The LED emission spectrum also influences the amount of light detected as the narrow spatial emission produced by the chosen LEDs increases the distance the light travels into the skin before it returns to the detecting LED.

The maximum recommended driving current of the 660 nm and 940 nm LEDs is 20 mA. However, the LED driver chosen is capable of driving the LEDs at 57 mA. The 57 mA range is equivalent to 0-3880 mcd light intensity for the 660 nm LED. This maximum drive current can be used when the reflected signal is otherwise too small, but is not recommended for normal use as the lifetime of the LED is reduced [SunLED 2017]. However, for applications requiring fast sampling using the LED-LED digital sensing method, the two LEDs are capable of emitting at maximum brightness.

In the NIR infrared range above 1000 nm (1450 nm, 1550 nm, 1650 nm (Marktech, USA)), the recommended drive current is 50 mA [Marktech 2017a]. To maximise signal intensity, these LEDs can be safely driven at the full 57 mA. The design layout for the LEDs is shown in Figure 4.1b with the LEDs in ascending wavelength order (from 660 nm to 1650 nm). While the optimum distance between emitter and detector is 4 mm [Chung and Sun 2016], the 1206 surface mount footprint of the LEDs mandated a distance of 5 mm. In this orientation it is possible to rotate the sensing and emitting LEDs to reduce the emitter-detector spacing, but the difference wavelength LEDs would have different emitter-detector separations. This increase in distance reduces the amount of light returning through the skin as the optical path-length is longer.

4.3.2 Microcontroller choice

The Teensy 4.0 was chosen as the microcontroller as the CPU (Cortex M7 processor) runs at a clock speed of 600 MHz, giving an LED-LED decay timing resolution of 1.6 ns. With 25 GPIO pins available, there is space for many sensing LEDs, although this space is reduced as SPI communications to the LED driver requires the MOSI, MISO, CS, CLK, and two debug pins. Programming the Teensy 4.0 is straightforward via USB using the Teensyduino package for Arduino (available on the PJRC website [Stroffregen 2021]. While this sensor only uses 6 distinct sensing LEDs, the FPC cable and microcontroller combination enables up to 9 sensing LEDs and the corresponding emitting LEDs of the same wavelength.

4.3.3 Right Leg Driver

The right leg driver (RLD) employed is adapted from [Fortune et al. 2019]. The RLD creates a feedback loop between the sensor and subject, reducing the interference of EMI. By driving the inverted common-mode voltage into the subject, the EMI is attenuated [Winter and Webster 1983]. The minor adaptations made here include:

- The REG710NA was used to regulate the 5 V from USB to 2.5 V.
- The LTC1550LCMS8 was used to regulate the 5 V from USB to -2.5 V.
- The quad opamp TLC2274 was used to measure the common mode voltage using two electrodes (E1, E2), then generate an inverse signal to drive back into the body using the RLD header.
- The RLD driver voltage and current is limited to ±2.5 V and 25 µA respectively.

4.3.4 LED driver

The PCA9745BTWJ LED driver was chosen to drive the emitting LEDs [NXP Semiconductors 2020b]. This 16 channel constant current LED driver is capable of driving

at 57 mA with both PWM (31.25 kHz) and an 8-bit DAC capable of driving between 225 µA and 57 mA. However, as the sensing LED decay is proportional to light, having a PWM controlled signal introduces steps into the decay, changing the continuous exponential decay waveform to a staircase. Thus, the 8-bit DAC is used at 100% duty cycle PWM to provide constant light emission and a continuous sensing LED decay waveform. The LED driver connects to the Teensy 4.0 via SPI as a slave.

The LED driver pulls the 3.3 V to GND through the series connected emitting LEDs as shown in Figure 4.2. Each wavelength of LEDs are on individual channels. As the forward voltage drop of all LEDs except for the 660 nm LED is <1.6 V, two emitting LEDs can be connected in series. The 660 nm LED has a forward voltage drop of 2.1 V, so only one LED can be driven from 3.3 V.

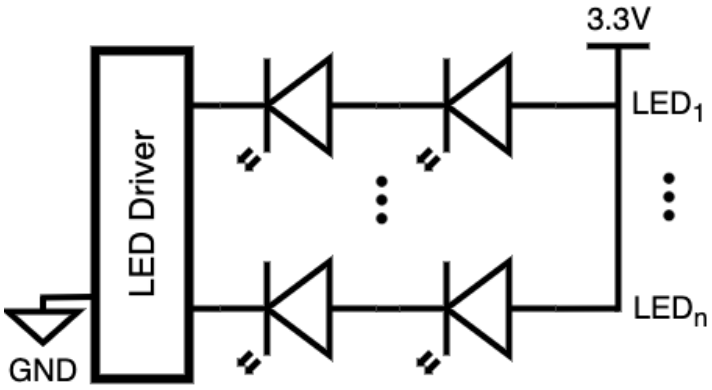

Figure 4.2 Schematic for the operation method of the PCA9745BTWJ LED driver board.

4.3.5 Temperature Sensor

The TMP20AIDRL low power, analog temperature sensor is used to monitor the temperature at the LEDs. With a ±2.5 °C error running on the 3.3 V supply, the temperature sensor ensures that the LED sensing board is monitored for abnormal temperatures. If the temperature sensor detects temperatures above 40 °C, the LED driver is turned off and the user is notified over serial to the PC.

4.4 DESIGN FILES

Although commercial software was used in the development of this pulse oximeter (MATLAB 2020), all files required to manufacture and understand the operation of the sensor are provided in an open access format (KiCad, Arduino). Figure 4.3 shows an image of the sensor with the array for the LEDs and the spacing for the electrodes showing. The sensing area at the end of the sensor is 20x20 mm in area, with a row of sensing LEDs and two rows of emitting LEDs at 5 mm spacing. Each wavelength detected has one detecting and two emitting LEDs. The circuit schematics can be found in Appendix A.1. The schematics and design files can also be found online at *https://doi.org/10.17605/OSF.IO/VA3JW*.

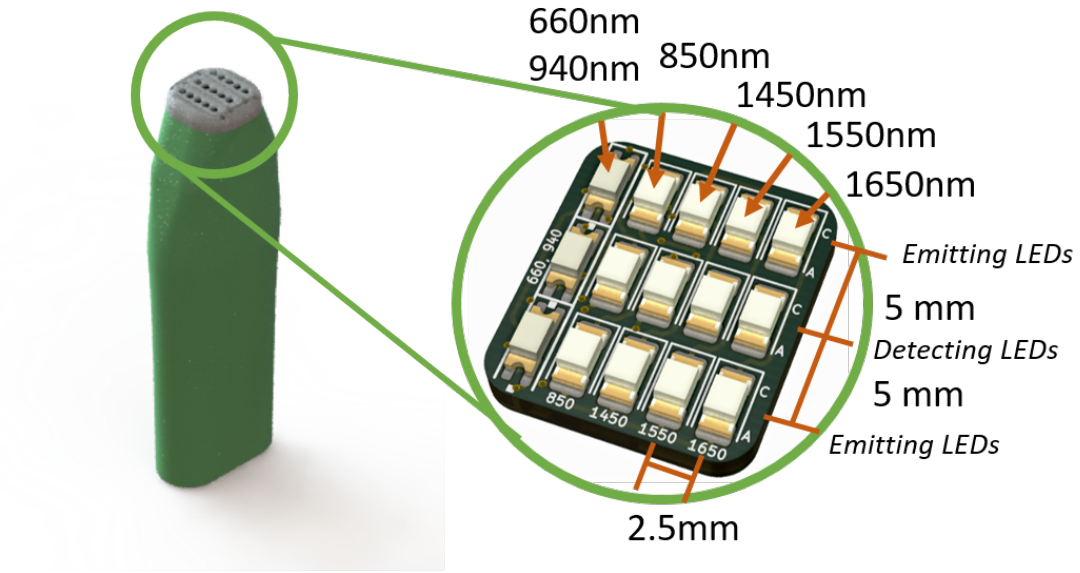

Figure 4.3 Image of the reflectance pulse oximeter sensor used to measure $SpjvO_2$. The array of sensing LEDs is separated by two emitting LEDs of the same wavelength at 5 mm spacing.

4.4.1 Bill of materials

A complete bill of materials (BOM) is included in Appendix A.1, containing both the LED driver board and the LED sensor board components. The total cost of components is $240 USD with the NIR LEDs and $65 USD if other LEDs are used.

4.5 VALIDATION AND CHARACTERISATION

The sensor is designed to be used as a reflectance pulse oximeter. For a pulse oximeter to calculate the oxygen saturation, pulsatile data at different wavelengths must be measured. The amplitudes of each wavelength LED's pulse is then used to calculate arterial oxygen saturation (SpO_2). Thus, the sensor must accurately measure the pulsatile data at each wavelength.

Each pulse waveform is measured using the LED-LED digital light sensing method, where the discharge time of the reverse biased LED is proportional to the incident light intensity. The time taken to decay is in the region of 100-600 µs, depending on parameters such as, ambient light conditions, skin temperature, and sensor application pressure.

4.5.1 RLD noise removal

Figure 4.4 demonstrates the effect of mains noise on the signal. Sampling at 1 kHz shows the 50 Hz mains noise in the plot without the RLD present. Adding the RLD to the circuit greatly reduces the effect of common mode noise from the signal. The plotted PSD spectrum shows the 50 Hz noise (and 100 Hz harmonic) obvious in the signal without the RLD.

4.5.2 Pulsatile Data

Placing the sensor onto a fingertip provides pulsatile data. This data is representative of the blood flow through the capillaries in the finger and can be used to determine peripheral blood oxygen saturations. Figure 4.5 shows raw pulsatile data at the finger tip from two different microcontrollers. Other than the microcontroller, the setup between the two sensors remains the same.

In Figure 4.5a the Arduino Pro Micro clock timer runs at 16 MHz, giving a discharge time resolution of 62.5 ns. This resolution limit is evident in the 660 nm pulsatile data

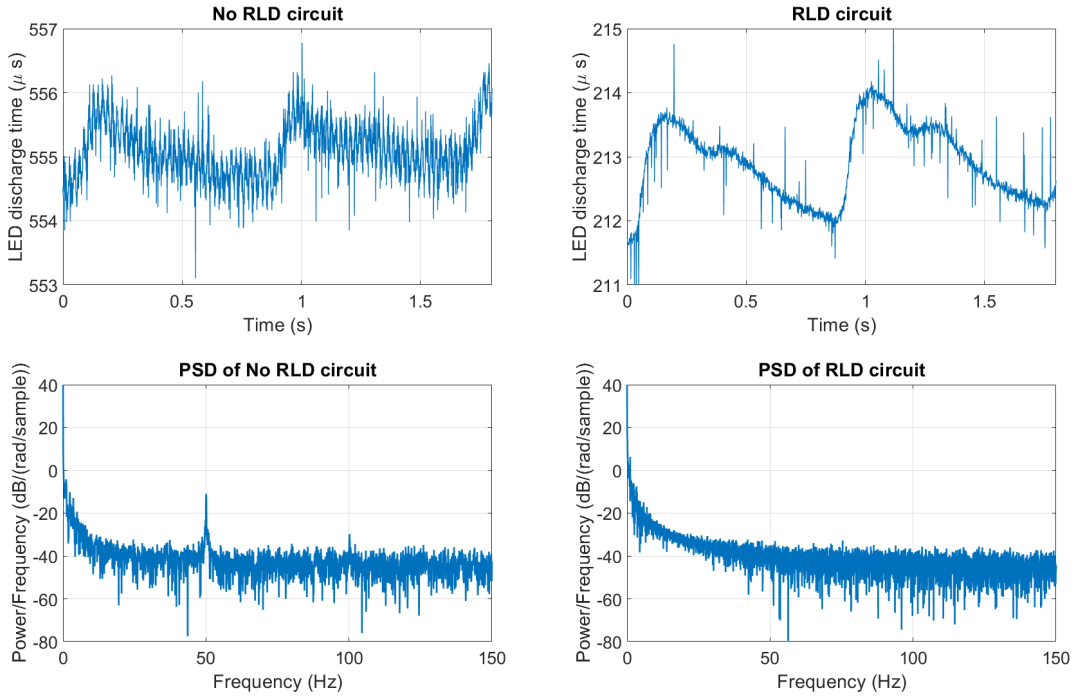

Figure 4.4 Arterial pulse data without the RLD (left) and with the RLD (right) and the resulting and Power Spectral Density (PSD).

of the Arduino Pro Micro. Using a faster microcontroller clock such as the 600 MHz clock on the Teensy 4.0 provides a resolution of 1.6 ns. This increased resolution is present in the raw pulsatile data for the 660 nm LED in Figure 4.5b.

To avoid the emitted light from one wavelength LED interfering with the sensing of another, each wavelength LED must be sampled sequentially. The effect of sequential LED sampling on the sample rate is shown in Figure 4.5b. The combined discharge time is 13 ms, resulting in a sampling frequency of 75 Hz, across the 6 LEDs. Without the RLD, it would be impossible to remove mains noise (50 Hz) from the signal with this sampling frequency. The difference in pulse amplitude (discharge time) for each test is due to the environmental conditions the test is under, such as the applied pressure of the sensor, the temperature of the finger, or the ambient light levels.

The pulsatile data is clearly visible in the both the 16 MHz and 600 MHz clock timer rates, with the 600 MHz signal having a greater pulse amplitude resolution as seen in the 660 nm and 850 nm plots. The pulsatile frequency of interest is centred around the

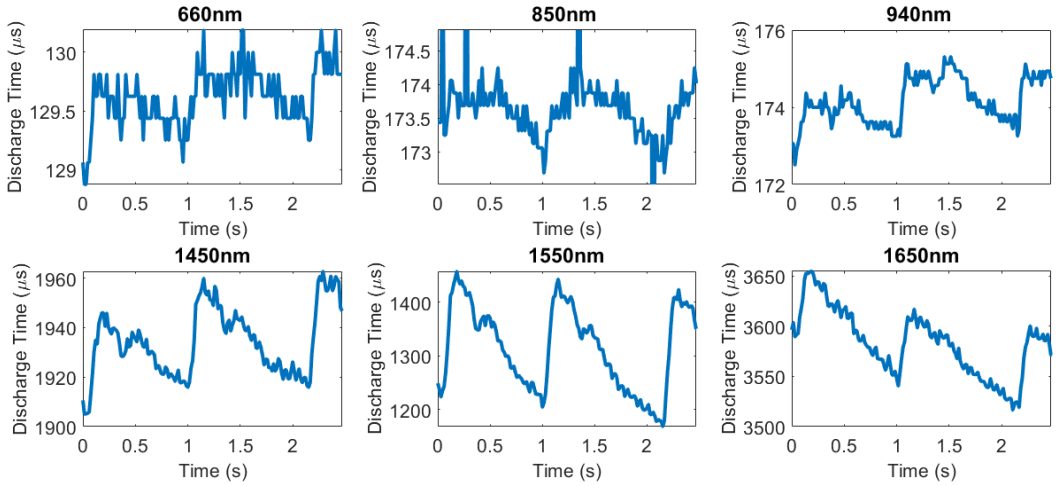

(a) Pulsatile data with Arduino Pro Micro timer running at 16 MHz.

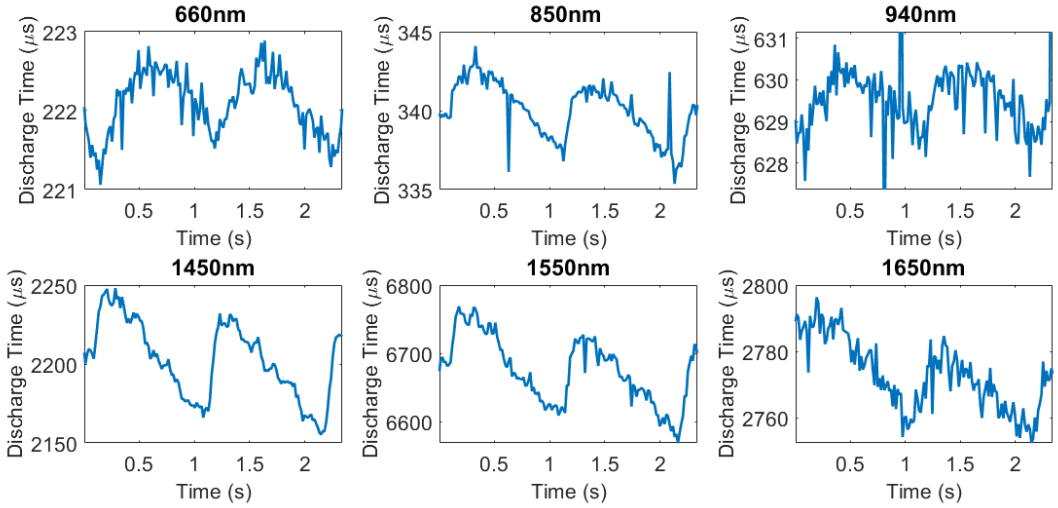

(b) Pulsatile data of the Teensy 4.0 timer running at 600 MHz.

Figure 4.5 Comparison between two different clock rates (16 MHz on Arduino Pro Micro and 600 MHz on Teensy 4.0) as well as the range in discharge time of each wavelength LED.

heart rate of 1 Hz (60 bpm). Thus, the operation of the sensor is validated.

4.6 LIMITATIONS

While the introduction of the right leg driver circuit to the board greatly reduced the effect of 50 Hz power lines noise, the limiting factor of the slow sampling time remains. If multiple LEDs are to be sampled sequentially, then a different method than the timing method must be used to ensure the typical sample rate of a pulse oximeter (200 Hz).

As the board is powered by the USB (5 V), the rails of the RLD are limited to ± 2.5 V. These rail voltages would need to increase to further remove noise from the system. However, increasing the rail voltage would require an external power supply to the USB and the driver board would need to be redesigned.

The flat flexible cable (FPC) used to connect the driver board to the sense board introduces majority of the noise to the sensor. As power and ground are required to be routed to the sense board, ground loops are introduced into the circuit. These loops act to increase the power line noise present in the signal. Further board design would benefit from incorporating the drive and sense boards into one PCB, either as a solid board, or a flexible board to retain the same form factor as the design presented in this chapter.

The FPC connector also has a very limited life cycle. Each insertion and removal of the cable increases the wear, requiring multiple replacement cables throughout the testing program. This issue can be readily overcome in any redesign.

4.7 SUMMARY

The operation of the sensor was validated, showing a clear arterial pulse waveform for six different wavelength LEDs. As this sensor is a reflectance pulse oximeter, it can be used on any site on the body with a detectable pulse, including the carotid artery and the external jugular vein. Analysis of the pulsatile signal will enable the oxygen saturation of each site to be estimated.

The aim of this study was to develop a sensor to be used as both a pulse oximeter using 660 nm and 940 nm LEDs, as well as provide the potential to measure other constituents in blood. Up to 6 different wavelength LEDs can be implemented with an emitting LED drive current of 57 mA capable of powering LEDs in the range of 660 nm to 1650 nm. While the sensor can sample wavelength LEDs less than 1000 nm at a sufficient sample rate (<1 ms), further development is needed to improve the sample rate of LEDs with wavelengths greater than 1000 nm.

Designs of analogue pulse oximeters are often detailed in literature, but as most pulse oximeter hardware is proprietary, design files and details are not readily available. This chapter detailed the design, validation and limitations of a sensor used to record reflectance arterial pulse waveforms. The sensor uses LED-LED sensing to reduce the sensing circuit complexity and a right leg driver to reduce the effects of mains power supply noise. The build process of the sensor only requires open-source software and has a total component cost of USD $261, or a cost of USD $86 if the specialist LED wavelengths are not used.

Chapter 5

PPG PEAK AND TROUGH DETECTION ALGORITHM

The ability of a pulse oximeter to measure the oxygen saturation depends on accurate detection of the pulse waveform. Any noise in the signal has the potential to cause errors in the calculated SpO_2 values. Thus, a signal processing method, robust to various noise levels, is required to ensure accurate SpO_2 calculations. This chapter presents an IIR filtering approach to arterial pulse waveform peak and trough detection. The hardware used in this chapter is an earlier version of the sensor presented in Chapter 4 and still uses a photodiode to detect light.

5.1 INTRODUCTION

Continuous monitoring of intensive care unit patients is required to detect changes in cardiovascular condition. One continuous real-time monitoring device is the pulse oximeter [Abdallah and Bolz 2011]. Pulse oximeters monitor heart rate and blood oxygen saturations SpO_2 [Ortega et al. 2011]. The algorithm used to estimate SpO_2 requires filtering to remove noise from the pulse oximeter signal for accurate detection of peaks and troughs. The goal of this chapter is to accurately, and consistently track the peaks and troughs of the PPG signal using adaptable IIR filters to maximise that accuracy.

Unfortunately, most pulse oximeters on the market do not allow access to the raw signal produced by the sensors, providing only scaled PPG data as the typical filtering

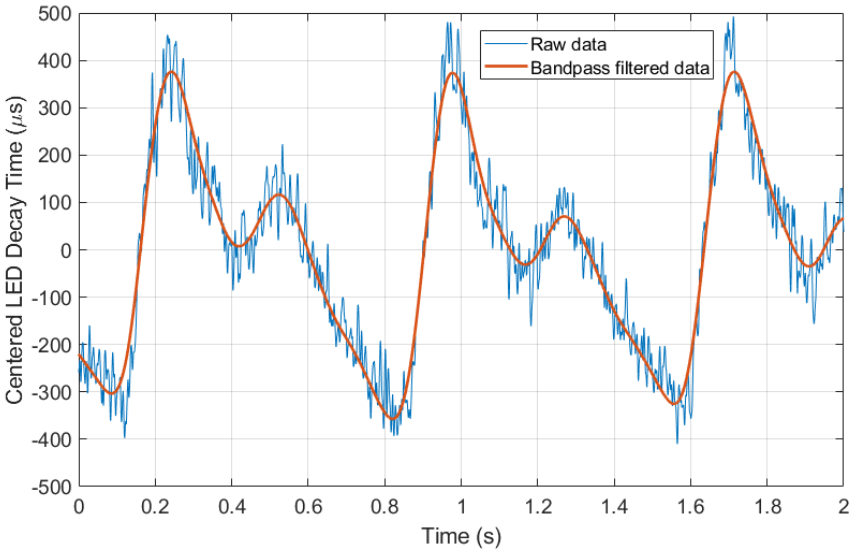

Figure 5.1 Photoplethysmograph waveform measured by the SpjvO$_2$ sensor. The orange data (raw) is filtered with an 0.67 Hz to 4.5 Hz bandpass filter (blue).

method removes the DC component of the signal required to calculate SpO$_2$ [Li and Warren 2012]. Thus, an in-house pulse oximeter was developed for this research to provide access to the raw signals.

The raw waveform measured by the in-house sensor is subject to various sources of interference, such as motion artefacts, light scattering and absorption, light shunting, and power supply noise [Lee et al. 2011]. Filtering is necessary to obtain accurate results, as illustrated in Figure 5.1. The pulsatile component of the PPG waveform typically represents less than 1% of the signal [Mendelson 1992], requiring these signal features to be extracted using digital signal processing.

Figure 5.1 shows a typical PPG waveform formed from red light absorption used to calculate SpO$_2$. The amplitude difference between the peak and trough of each pulse waveform is used to calculate SpO$_2$, and each peak and trough must be accurately located to ensure the accuracy of the pulse oximeter.

Infinite impulse response (IIR) and FIR filters are frequently used to process PPG waveforms. These filters are computationally simple and effectively remove power line noise from the signal. The data in Figure 5.1 was filtered by a 10 Hz bandpass equiripple IIR filter and represents the first of three filtering methods investigated in this chapter.

The 50 Hz noise has been removed, keeping the signal features intact.

Depending on the response of the filter, different features can be extracted from the raw waveform. For example, a low pass filter with a cut-off frequency at the heart rate frequency can remove the dicrotic notch from the signal, leaving just the pulse at the heart rate frequency. This pulse represents a sine wave, with all features except the peaks and troughs removed. The second filtering method investigated in this chapter uses this feature removal method to isolate peaks and troughs.

The third filtering method investigates wavelet decomposition, and subsequent reconstruction, to filter the raw data to accurately track the peaks and troughs of the PPG signal. Joseph et al. [2014] used wavelet decomposition to de-noise synthetic PPG data and Li et al. [2017] developed a hybrid wavelet decomposition method for PPG peak detection. Further wavelet processing analysis gave good results [Fingar and Podraj 2018, Nguyen 2016]. Each of these papers applied the wavelets through post processing. Kasambe et al investigated real time mains noise removal using wavelets [Kasambe and Rathod 2015]. However, none have yet implemented DWTs in real time for peak and trough detection, a core task in using PPG signals.

Wavelet transforms use a fixed function called a mother wavelet to represent the decomposed signal. The choice of mother wavelet allows different features of the signal to be extracted [Mallat 1989]. Wavelets represent the signal as a combination of scaling and wavelet functions. The scaling functions provide an overview of the signal, while the wavelets represent the finer details at various scales [Lee and Yamamoto 1994]. The combination of the coarse signal with the details provide a multi-resolution representation of the signal.

Wavelet transforms have been successfully applied in many applications, including, image analysis, structural health monitoring, communication systems and biomedical signal analysis [Abdulkareem 2018, Baig et al. 2018, Rabiepour et al. 2022, Tuncer et al. 2020, Zhou et al. 2017]. In the wavelet transform, lowpass and highpass filter information at different signal levels can provide good levels of energy compression [Ashraf et al. 2018]. In this chapter, the *Coiflets 3*, *Reverse Biorthogonal 1.5*, *Symlets*

2, and *Daubechies 3* mother wavelets are investigated for their ability to track the features arterial pulse waveform.

A common method for peak and trough detection is to use the least squares gradient of the signal to find the inflection points of the pulse waveform [Karlen et al. 2012]. Elgendi investigated finding the second derivative [Elgendi 2012], concluding the least squares gradient was sufficeint to locate the peaks and troughs. Aboy implemented a method of analysis by using multiple bandpass filters to extract the signal to then find the turning points [Aboy et al. 2005]. The algorithm developed by Aboy was used to classify both arterial blood pressure and SpO_2. This study achieved a high specificity of 0.99, but was tested on a low-noise signal and was also deemed too computationally expensive to run in real-time.

5.2 METHODS

This chapter covers three different filtering methods, used to remove noise from the raw signal for peak and trough detection. These consist of the conventional bandpass commonly used for PPG analysis; a new method using two adaptable IIR filters; and the DWT. A peak and trough detection algorithm then uses the outputs of each of these three methods to detect the peaks and troughs.

5.2.1 Subjects

Ten minutes of continuous raw PPG data was recorded from the finger of a 23 year old male sitting at rest. This same raw data was used for each of the three filtering methods.

5.2.2 Equipment

A transmission mode finger sensor (model: 302701001, Biometric Cables, Guindy, Chennai, India) was used in this chapter to obtain the PPG data. The red and infrared LEDs

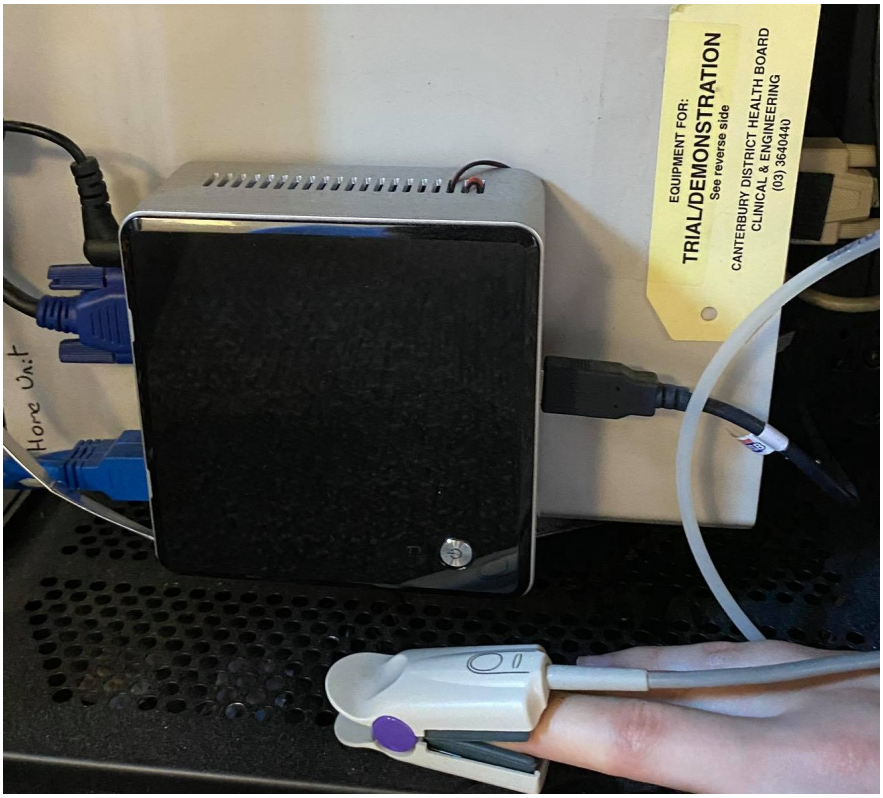

Figure 5.2 Setup used to record the photoplethysmograph waveform. A transmission mode pulse oximeter connects to the Intel NUC for serial communications and processing.

have wavelengths of 660 nm and 940 nm respectively. The sensor is an in-house developed pulse oximeter, giving the algorithm access to the raw photodiode voltage. Serial communication with the sensor at 50 Hz is provided by an Intel NUC running Ubuntu 16.04 LTS on an Intel Celeron processor with 4 GB of RAM. A graphical user interface (GUI) displays the raw and filtered waveforms in real time.

Initial testing of the algorithm used a traditional photodiode method of detecting light. This early prototype is different to the hardware described in Chapter 4 as it is a transmission mode pulse oximeter and is shown in Figure 5.2. However, the wavelengths used and signal recorded is equivalent to that described in Chapter 4.

5.2.3 Sensor output processing

The analysis layout of the chapter is shown in Figure 5.3. The raw data is filtered with each of the three filtering methods. The filtered data is then analysed using the peaks

and trough algorithm.

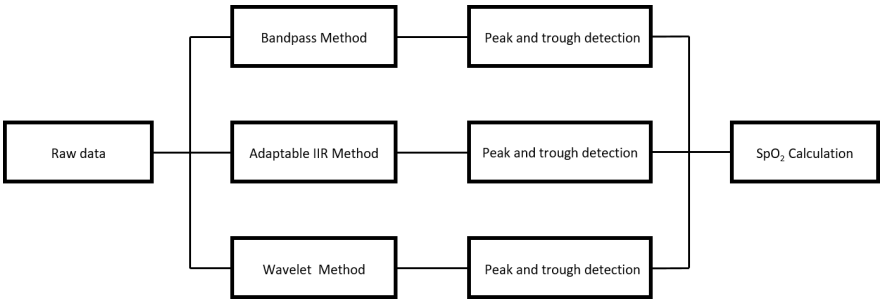

Figure 5.3 Analysis method for the three filtering methods and their effect on peak and trough detection.

5.2.3.1 Bandpass filtering method

A bandpass filter is commonly used in pulse oximetry to remove noise, such as 50 Hz mains noise coupled into both the sensor and the subject [Fortune et al. 2021]. The bandpass filter used in this chapter is a Chebyshev Type II, a length of four coefficients, and a passband between 0.67 Hz to 4.5 Hz. This frequency range removes the effect of low frequency noise such as breathing rates, as well as higher frequency noise that could introduce additional peaks and troughs into the signal. An example of the bandpass filtered data is shown in Figure 5.1.

5.2.3.2 Adaptable IIR method

This filtering method uses two IIR filters, and one FIR filter to locate the peaks and troughs in the pulse waveform. One IIR filter has a cut-off frequency at the subjects heart-rate. This filter removes all signal features, leaving only the fundamental frequency of the signal. Thus, the peaks and troughs of the signal are the only turning points in the filtered signal. However, the amplitudes of each peak and trough does not represent the true peak and trough amplitude seen in the raw data. Thus, an additional IIR filter with a higher cut-off frequency is used to closely track to the raw data. This higher frequency cut-off filter (5 Hz above the cut-off frequency of the first IIR filter) retains the same pulse amplitudes as the raw data, while removing 50 Hz

mains coupled noise. An example waveform from the GUI used to record the data is shown in Figure 5.4.

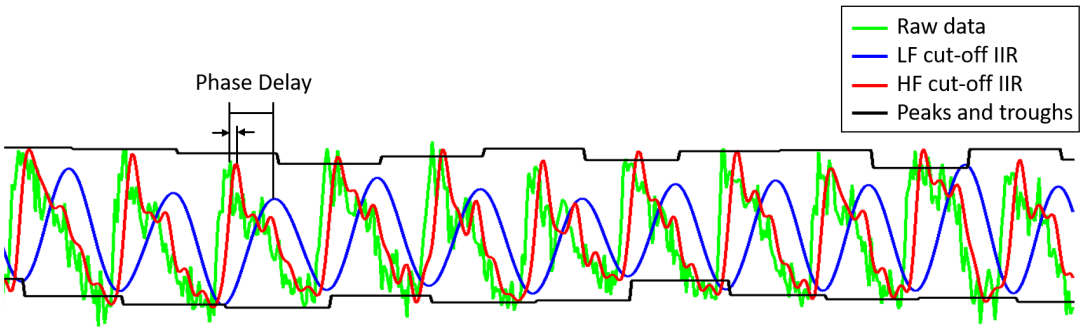

Figure 5.4 Example output from the monitoring GUI plotting the multi-IIR filtering method. The raw data (green) is filtered by two IIR filters. A low frequency cut-off IIR filter (blue) identifies the peaks and troughs, while the higher frequency cut-off IIR filter (red) closely tracks the raw data. Each peak and trough is identified at the black lines, and is updated at each blue peak or trough. The phase delay between these two filters is used to locate the peaks and troughs.

This method adapts the cut-off frequency of the two IIR filters to an integer value of the heart rate to ensure that the low frequency cut-off IIR filter only returns the fundamental frequency. As the cut-off frequency is an integer value, the range of cut-off frequencies available to either IIR filter is 1 Hz to 10 Hz. For example, a heart rate of 75 BPM gives cut-off frequencies of 1 Hz and 6 Hz for the low and high cut-off frequency IIR filters.

IIR filters introduce phase delay to the filtered signal, with the lower the frequency cut-off, the greater the delay. This phase delay is shown in Figure 5.4. As the lower cut-off frequency IIR filter is used to locate peaks and troughs, the higher frequency cut-off IIR filter locates its own peaks and troughs a known point in time earlier than the lower frequency cut-off filter. The maximum and minimum values of the higher frequency cut-off IIR filter within a set period of time is taken as the peaks and troughs respectively.

A complementary filter uses the heart rate calculated by the FIR and LF IIR filters to simultaneously adjust which IIR filter is used, as shown in Figure 5.5. By combining the FIR and IIR heart rate, the complementary filter prevents the IIR filter heart rate

from self adjusting frequency and thus becoming unstable, and is given:

$$\texttt{HR} = \alpha \times \text{IIR\_HR} + (1 - \alpha) \times \text{FIR\_HR} \tag{5.1}$$

Where,

α: The weighting coefficient of the filter

IIR_HR: Heart rate calculated using the IIR filter

FIR_HR: Heart rate calculated using the FIR filter

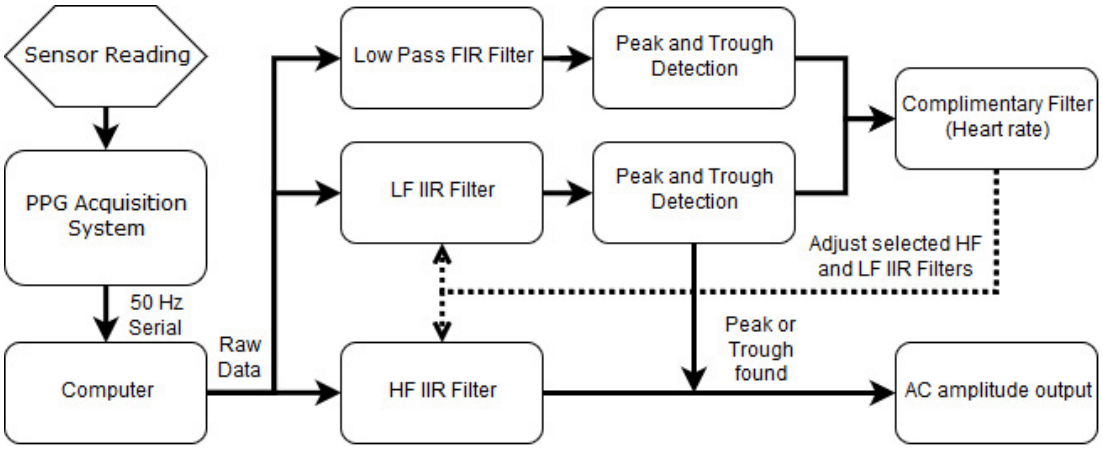

Figure 5.5 Flow chart showing the logic flow through the algorithm. LF IIR and HF IIR represent the lower and higher frequency cut-off IIR filters.

5.2.3.3 Wavelet decomposition

This method of filtering uses the same principles as the IIR phase delay method. However, the higher frequency cut-off IIR filter used to closely track the raw waveform is replaced with the output of discrete wavelet transform (DWT).

The DWT is used to obtain near-real-time analysis of the signal by analysing the signal in segments [Goelz et al. 2000]. To run in near-real-time, the time series data is segmented into sections for analysis. The length of this time series sectioning is the

response rate of the DWT, as the data must first be collected before returning the results.

To minimise the time delay caused by the block method of wavelet analysis, a buffer size of 128 was used. With a sample rate of 50 Hz, the time delay is 2.56 s. This time delay was deemed sufficiently responsive in a clinical context for use in near real time as change of patient condition is negligible over such a short time frame. Once the wavelet has filtered the 128 samples, the buffer is passed into the peak and trough detection algorithm for analysis.

The DWT runs through multiple levels of decomposition, at each stage the length of the signal vector is halved, leaving the high and low frequency components of the signal. Table 5.1 shows the decomposition levels of the wavelets used in this paper. Because the sample rate of the system is 50 Hz, the highest possible frequency component of the signal is 25 Hz. The second level of decomposition was chosen for signal reconstruction, giving a compromise between removing noise, and retaining signal features.

Table 5.1 Frequency decomposition using the DWT

Level	Filter	Frequency Range(Hz)	Data Length
3	Low	0 - 3.125	16
	High	3.125 - 6.25	16
2	Low	0 - 6.25	32
	High	6.25 - 12.5	32
1	Low	0 - 12.5	64
	High	12.5 - 25	64

Once each filter has decomposed the signal into the three levels, each wavelet deconstruction is reconstructed into the time domain using the 1^{st} and 2_{nd} levels. The 3_{rd} level of decomposition contains the high frequency noise, so is removed from the signal when reconstructing. This reconstructed waveform has the same role as the higher frequency cut-off IIR filter presented in the adaptable IIR method, retaining the signal features for peak and trough detection.

5.2.3.4 Peak and Trough Detection

The amplitude of the PPG is contained in the AC component (>0.67 Hz), while the DC component (<0.67 Hz) is the mean of the signal. Hence, peaks and troughs must be found to obtain the amplitude for analysis. The method used in this work finds the turning points through the method described in Algorithm 5.1.

Algorithm 5.1 Peak and Trough Detection Algorithm

```
current_grad ← 1                                   ▷ Initialise to a positive gradient
prev_trough ← [0, 0]
prev_peak ← [0, 0]
T_amp ← [0.01,1]                                   ▷ Initial amplitude tolerances (V)
i ← 0
x ← new data                                       ▷ New data point measured by the sensor
data_buffer ← [0, 0, 0, 0, 0]
while 1 do
    data_buffer[i] = x
    grad = gradient(data_buffer)                   ▷ Get the gradient
    if grad < 0 && current_grad > 0 then           ▷ Peak found
        amp = x - prev_trough
    else if grad > 0 && current_grad < 0 then      ▷ Trough found
        amp = prev_peak - x
    end if
    if withintol(amp,T_tol) then                   ▷ Acceptable amplitude
        T_amp = [(0.95T_amp[0] + 0.6amp)/2, (1.2T_amp[1] + 1.2amp)/2]
        turning_point_found = TRUE
        current_grad = grad
    else                                           ▷ Expand the tolerance
        T_amp = [0.5T_amp[0], 1.5T_amp[1]]
    end if
    i ± 1
    if i > length(data_buffer) then i = 0
    end if
end while
```

To obtain the gradient of the signal, the linear least squares method is employed. Rather than taking the derivative of the new data point and the previous value, a line fitted to the five previous data points to estimate the gradient are incorporated. This approach reduces the influence of outliers, as the five points must have an overall gradient direction change to indicate a turning point. However, this approach adds an additional 5 sample delay to the process.

A sign change in least squares gradient implies a turning point has occurred within the 5 most recent samples. If a turning point is detected, but the subsequent amplitude calculation does not fit within the tolerance for an acceptable amplitude, the turning point is discarded as a potential peak or trough. This feature allows the algorithm to avoid detecting the dicrotic notch as a false series of heart beat peaks and troughs.

To ensure fast conversion to accurate peak and trough detection, the tolerance expansion is proportional to the difference between the tolerance and the calculated amplitude. On start up, the tolerances rapidly expand to the size of the largest amplitudes present in the signal. On every successful amplitude detection, the tolerance is reduced and on detection of false peaks, the tolerance expanded. Tolerance factors are used to keep an envelope between the maximum and minimum tolerances, where, on incorrect amplitude detection the minimum tolerance value is reduced by 50% and the maximum tolerance value is increased by 150%. Rather than having a single amplitude value as the tolerance, a minimum and maximum value for the amplitude means the pulse wave must be of similar DC offset to the previous pulses.

5.2.4 Analysis

The three filtering methods were analysed with beat-to-beat analysis by a trained expert human identifying the peaks and troughs. Ten seconds of data at the start of the recording was excluded from analysis to allow the algorithm to converge. A total of 651 beats were identified for analysis.

The results from the experiment are shown in a confusion matrix. A true positive detection (TP) is classified as correct detection of a peak, false positive (FP) is detection of a peak or trough when there should not be. More specifically, a peak might have been identified, but in cases such as the dicrotic notch, the amplitude is falsely measured. False negative (FN) classifies no detection of a peak when there is a peak. The true negative (TN) is not possible to identify in these results, as correctly identifying no peaks when there are none is not viable with continuous heart beats. Thus, the sensitivity and +P are analysed in a resulting confusion matrix. Equations for sensitivity

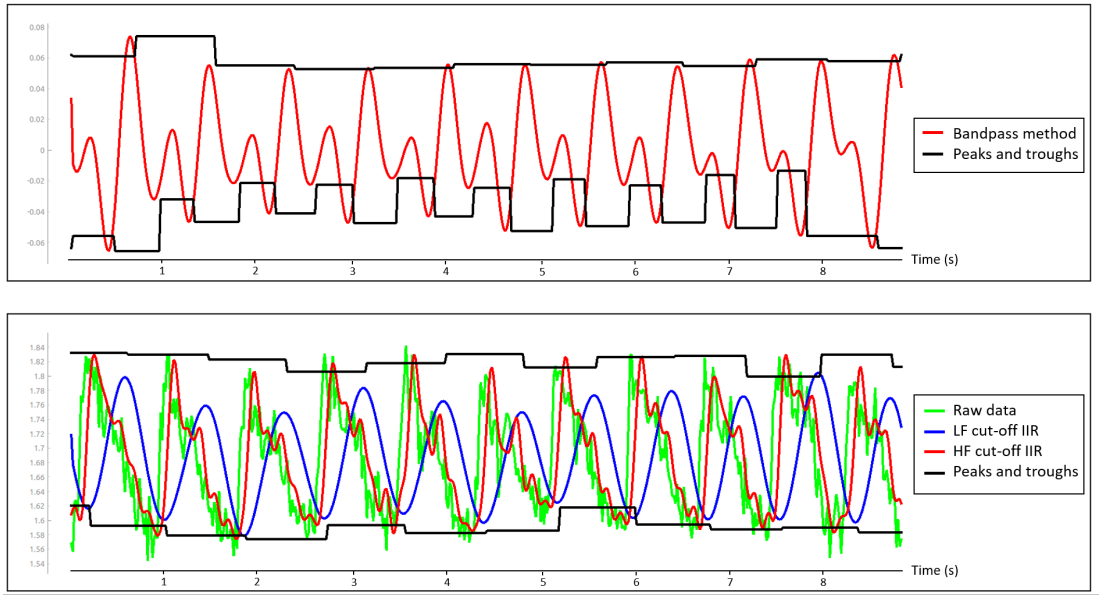

Figure 5.6 User interface showing the response of the bandpass filter (top) and IIR method (bottom) to the same raw data. The output from the bandpass method lags behind the adaptable IIR method by 0.5 seconds.

and +P are given:

$$Sensitivity = \frac{TP}{TP + FN} \tag{5.2}$$

$$+P = \frac{TP}{TP + FP} \tag{5.3}$$

5.3 RESULTS

Each of the three methods filtered the same 10 minutes of recorded data. An example output from the user interface used to record bandpass and adaptable IIR method are shown in Figure 5.6. The bandpass method accurately locates the positions of the peaks, while falsely identifying each of the dicrotic notches as troughs. The adaptable IIR method tracks to every peak and trough located in the window.

Each of the four mother wavelets were compared to determine their ability to filter the

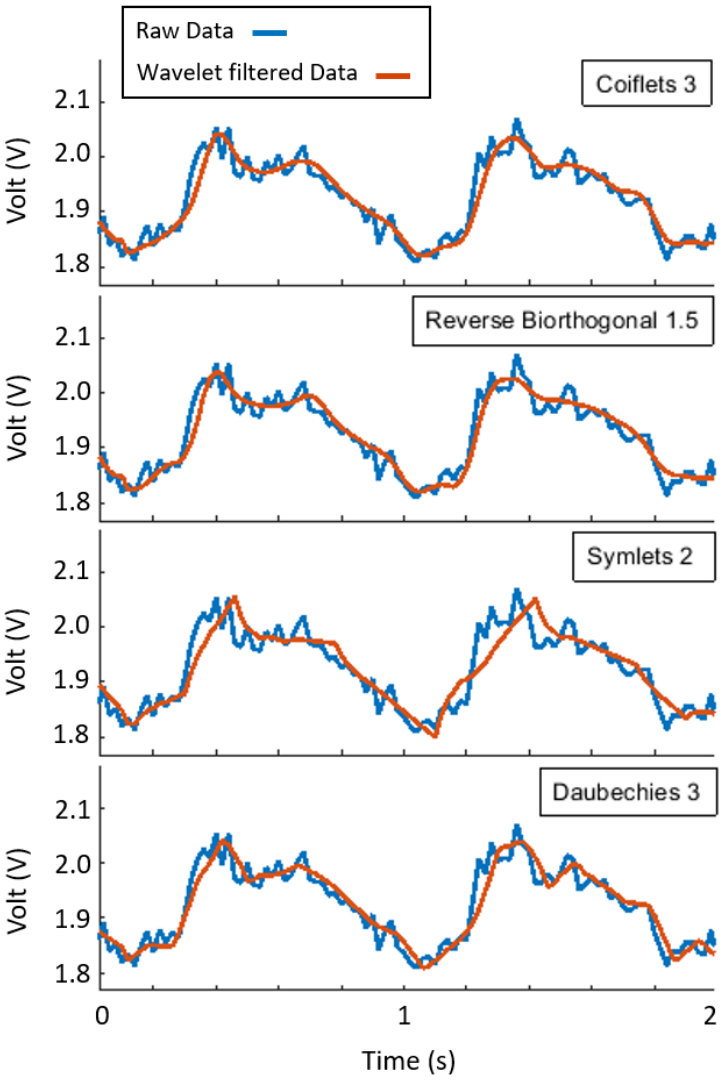

Figure 5.7 Comparison between each reconstructed signal (red) to the raw data (blue). Each mark on the x-axis represents 0.2 seconds.

signal, acting as the high cut-off frequency IIR in the adaptable IIR method. Figure 5.7 displays the response of each wavelet to the same raw data. Each mother wavelet was tested at the decomposition level with the fewest false peaks generated upon reconstruction. The *Reverse Biothorgonal 1.5*, *Coiflets 3*, and *Daubechies 3* mother wavelets were reconstructed with the 2^{nd} and 3^{rd} level, whereas *Symlets 2* was reconstructed with just the 2^{nd} level as only two levels of decomposition could be achieved at a buffer size of 256 samples.

5.3.1 Confusion Matrix

A confusion matrix is shown in Table 5.2, where the sensitivity and +P were calculated. The bandpass filter performed poorly with 232 false positives, giving a +P of 0.65. Often, the peak would be correctly detected, but the dicrotic notch would be identified as the trough. The sensitivity is high (0.98) as the algorithm failed to detect few beats. However, this high sensitivity is countered by the high rate of false positives.

As SpO_2 requires the amplitude of the AC component, any dicrotic notches identified as troughs result in incorrect SpO_2 estimation. In comparison to the bandpass method, the adaptable IIR filter method only falsely identified 18 pulses, giving a +P of 0.97. Each wavelet performed similarly, with good sensitivity and positive predictive values (+P). *Coiflets 3* had the most false positives, resulting in a lower +P.

Table 5.2 Results of the confusion matrix

Method	TP	FP	FN	Sensitivity	+P
Bandpass	429	232	11	0.98	0.65
IIR	610	18	26	0.96	0.97
Coif3	609	26	23	0.96	0.96
Db3	613	19	24	0.96	0.97
Sym2	611	19	24	0.96	0.97
Rbio1.5	610	22	21	0.97	0.97

5.4 DISCUSSION

The adaptable IIR filtering method shows a clear improvement over the bandpass filtering method at identifying the AC amplitude in noisy signals. The bandpass filter accentuates the dicrotic notch present in the signal, falsely identifying the dicrotic notch as a trough, as shown in Figure 5.6. The DWT produced equivalent results to the higher frequency IIR method when reconstructing with the higher frequency features. However, the method is much more computationally intensive, and introduces a measurement time delay of 2.56 seconds. Thus, the adaptable IIR method was chosen as the filtering method for peak and trough detection to use in this thesis.

Accurate peak and trough detection is vital to the accuracy of pulse oximetry. The

measured amplitude is used as the AC component in the pulse oximeter R value calculation. Each peak and trough must be identified in the presence of noise and other similar features, such as the dicrotic notch. Further chapters in this thesis will use the algorithm presented in this chapter to identify peak and troughs for pulse oximetry in both the arteries and veins.

The proposed method using IIR filters at incremental cut off frequencies allows the baseline frequency of the pulse to be measured, while preserving the higher frequency features. This means that only the fundamental frequency needs to be present in the signal to identify peaks and troughs. As the higher frequency cut-off IIR filter has a peak a known time period earlier than the lower cut-off frequency IIR, the correct peak can be located in noisy data.

As the cut-off frequency of the IIR filters are adaptable to changing heart rate frequencies, the method ensures the arterial pulse waveform resembles a sine wave. A large increase in heart rate results in the lower frequency cut-off filter removing too much signal, reducing the amplitude of its output to a near DC signal. Thus, the filter with the correct cut off frequency is chosen to produce the closest representation of the signal, while still removing the dicrotic notch. The higher frequency cut-off filters are also incremented and decremented as a frequency of 6 Hz is the high frequency cut off at very low heart rates, but represents the lowpass cut off for very high heart rates. A fixed higher frequency cut-off IIR filter at 10 Hz would follow the raw signal too closely at low heart rates, increasing the effect of noise on the signal.

Four different mother wavelets were tested for suitability of PPG signal analysis. A low sample rate of 50 Hz and the requirement for a minimal time delay resulted in a buffer length of 128 samples used for each wavelet decomposition and subsequent reconstruction. Such a small wavelet length reduces the levels of decomposition available. However, it was deemed an acceptable depth as the desired signal frequencies occur below 3.125 Hz.

If the tolerance of the peak and trough detection algorithm were to be reduced to avoid identifying the dicrotic notch as a peak or trough, the risk of missing actual peaks and

troughs increases. So there is a trade-off between having tight amplitude tolerances and risk of missing the peaks and troughs. The amplitude of the bandpass PPG signal can vary from peak to peak as shown in Figure 5.6. However, as shown by the raw data, the amplitude is not necessarily varying in size. Having the IIR filter closely track the raw signal ensures the PPG amplitude is closely followed.

5.5 SUMMARY

This chapter outlined the design and testing of a filtering method for use on noisy PPG signals as well as a peak and trough detection method. Using a method which adapts the IIR filters in use were used to isolate the baseline pulse rate, while also closely mapping the raw signal. The current bandpass filtering method removes important features from the signal, as well as detecting beats where there are none, resulting in highly variable AC amplitudes. As the bandpass filter was unable to closely track the signal amongst high noise (SNR of 13 dB), the filter misidentified turning points and therefore inaccurate SpO_2.

The adaptable IIR filtering method had a 140% increase in correctly identified pulse amplitudes, showing a large improvement in peak detection, giving a sensitivity of 0.96 and a +P of 0.97 This good result is due to the method's ability to track the pulse through highly noisy signals by the use of HF and LF cutoff IIR filters. This peak detection algorithm can be used on real-time or post processed data to calculate the AC component of the raw pulsatile signal.

The discrete wavelet transform yields an accurate AC amplitude measurement, but minimal improvement over the lowpass IIR method presented in Chapter 5. An increase in sample rate is needed to take full advantage of the discrete wavelet decomposition. This required increase in sample rate, combined with minimal improvements over the lowpass IIR filter makes the real time wavelet filtering method not worth the extra computation. Future work with peak detection will use the original low pass IIR filter algorithm.

Chapter 6

VENOUS OXYGEN SATURATION SENSOR VALIDATION

This chapter combines the sensor developed in Chapter 4, with the peak detection algorithm presented in Chapter 5 to measure the $SpjvO_2$, $SpcO_2$, and the peripheral capillary pulse waveform in the thumb (SpO_2). The pulse waveform shape, and subsequent calculated oxygen saturation at each of these three sites are also compared.

6.1 INTRODUCTION

Oxygenation of cerebral venous blood outflow has been studied for the last 90 years [Lennox 1935], and is used as an indirect assessment of cerebral oxygen consumption to guide clinical decisions in treating brain injury and similar cases [Bhardwaj et al. 2015]. Currently, the only method to measure $SjvO_2$ is invasively through a jugular venous bulb catheter [Jeon et al. 2006]. $SjvO_2$ accurately reflects the global $CBF/CMRO_2$ ratio in a clinical setting. However, $SjvO_2$ measured through a catheter is difficult to use, and may overlook regional changes in peripheral cerebral oxygen consumption [Jeong et al. 2012].

Non-invasive measurement of $SpjvO_2$ has been investigated by Colquhoun et al, concluding reflectance NIR devices placed directly over the jugular vein are most likely to reflect changes in cerebral oxygen supply [Colquhoun et al. 2012], but further work was needed to improve accuracy. They also found changes in cerebral oxygen status is clinically more important than measurement accuracy as the normal range for $SjvO_2$

is between 60%-90%, so all measurements are likely to be within that range [Schneider et al. 1995]. Additional literature repeated measurements of the jugular venous pulse (JVP) with photoplethysmography, but did not estimate the $SpjvO_2$ [Abdallah and Bolz 2011, Amelard et al. 2021, Aniagyei-Mensah 2014, Zhong et al. 2021], leaving a clear gap in knowledge.

To calculate the percentage of oxygenated haemoglobin (SpO_2 and $SpjvO_2$ in this chapter), two wavelengths of light (660 nm and 940 nm) are used, following the principles of pulse oximetry. The amplitude of each wavelength pulse (AC component) is normalised by the mean DC signal offset. The ratio between the two normalised wavelength pulses then indicates the percentage of haemoglobin carrying oxygen [Ortega et al. 2011], as defined:

$$R = \frac{\frac{AC_{red}}{DC_{red}}}{\frac{AC_{ir}}{DC_{ir}}} \tag{6.1}$$

The ratio calculated in Equation 6.1 is then used to estimate SpO_2 [Mendelson 1992]:

$$S_{pa}O_2 = 110 - 25 \times R \tag{6.2}$$

However, this equation has been shown to overestimate the actual SaO_2 [Singh 2017]. Pulse oximeters also have reduced accuracy in hypoxia ($< 90\%$ oxygen saturation) [Webb et al. 1991], with almost 25% to 66% of hypoxia cases potentially missed [Singh 2017]. Thus, for the expected range of 60-90% oxygen saturation of SvO_2, this equation is not adequate. Recent work by Khan introduced a new equation for SvO_2 estimation [Khan et al. 2015b, 2017]:

$$S_{pv}O_2 = 111 - 40.5 \times R \tag{6.3}$$

Equation 6.3 was developed using artificial pulses introduced into the venous blood in the finger using a pneumatic finger cuff [Khan 2016], and was calibrated to blood gas

measurements below 50% saturation. These generated pulses mimicked the expected breathing rate of 0.2 Hz [Chan et al. 2007, Khan et al. 2015b]. Measuring the pulse at the external jugular vein (EJV) allows pulsatile venous blood to be measured without external pulsations. In particular, because the EJV is in close proximity to the chest, pressure changes from breathing are present in the signal, creating the same effect as the external pulsations used by Khan. Figure 6.1 shows an example pulse waveform recorded at the EJV with both the JVP, and breathing induced pulse present.

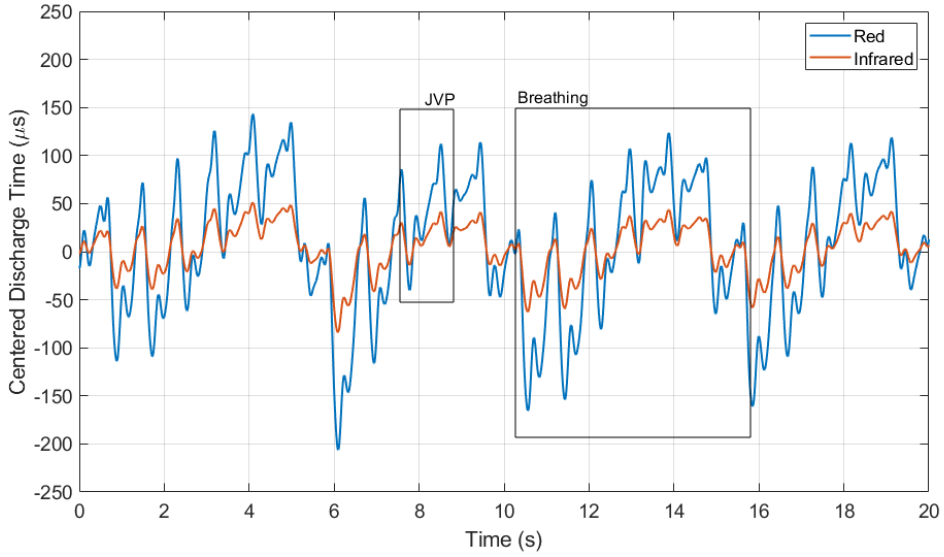

Figure 6.1 Pulse waveforms recorded at the EJV of a test subject showing the overlay of the breathing rate on the JVP. The blue plot is the red (660 nm) LED pulse and the orange plot is the IR (940 nm) LED pulse. Data is filtered using a 0.01 Hz to 10 Hz Chebyshev bandpass filter, length 4.

This chapter presents results from a pilot study into the viability of measuring carotid artery and jugular vein oxygen saturation, $SpcO_2$ and $SjvO_2$, using reflectance pulse oximetry on the carotid artery and external jugular vein. Specifically, whether the $SpcO_2$ measured on the carotid artery reflects the SpO_2 measured on the thumb and the EJV pulse waveform gives values for $SpjvO_2$ in the expected physiological range of 60-90%. The $SpjvO_2$ calculated from the JVP waveform is also compared to the $SpjvO_2$ calculated from the breathing rate at the EJV.

6.2 METHODS

A trial was conducted on healthy volunteers to validate the design of the $SpvO_2$ sensor described in Chapter 4. The trial investigates the PPG pulse waveform from 15 subjects recorded at the thumb, carotid artery, and EJV. These pulse waveforms are then used to calculate the respective oxygen saturation at each site. Ideally the trial would involve invasive validation with a jugular bulb catheter. However, the methods presented here use conventional signal processing methods for analysing arterial pulse waveforms and will be compared to the typical 60-90% SvO_2 range [Schneider et al. 1995].

The trial required the subject to lie supine on a recliner as described in [Chiaco et al. 2013]. With shoulders touching the mattress, the head is turned towards the left shoulder with the jaw slightly elevated. Ideal head elevation angle is between 30° to 60° [Short 1957]. Features discerning the venous pulse from the arterial includes pulsations, which:

- Are soft and not palpable.
- Have two crests and two troughs per cardiac cycle.
- Have crests which are not simultaneous with the cardiac cycle seen in the arterial pulse.
- Have a waveform obliterated by light pressure at base of the neck.

Subjects had their carotid arterial and external jugular venous pulse measured while supine. Once 50 seconds at each site was recorded, the subject was instructed to sit upright. The carotid artery was then re-measured with the participant sitting with their back at 90°. A measurement at the thumb was taken as the final measured site.

6.2.1 Subjects

This study uses data obtained from an in-house study of 15 patients, recruited from the University of Canterbury. All subjects were healthy, with no known cardiovascular

health problems. The patient demographics are included in Table 6.1. This study was approved by the Human Ethics Committee, University of Canterbury (HEC2019/153) and informed consent was obtained from each participant prior to the experiment.

Table 6.1 $SjvO_2$ trial subject demographics. Data is shown as median [IQR] where appropriate.

Subjects	15
Age (years)	25 [22-28]
Sex (M/F)	9/6
Ethnicity (Maori/ NZ European/ other)	3/12/0

6.2.2 Equipment

Data was streamed from the SvO_2 sensor via USB serial to a dual core I5 2013 MacBook Air for data collection, and recorded for 50 seconds at each site for each participant. The sensor sampled at 200 Hz using the XZM2MRTNI55W-8 (SunLED [2017], USA) package of 660 nm and 940 nm LEDs to estimate the oxygen saturation.

6.2.3 Sensor output processing

The pulsatile data is recorded using the digital LED-LED light detection method, where a change in LED voltage discharge time is proportional to changes in light intensity. Thus, all recorded waveforms in this chapter are presented as a function of LED voltage discharge time. The ratio of the "AC" and "DC" components are taken, making the calculation unitless.

Each data-set was analysed using the adaptable IIR peak detection algorithm presented in Chapter 5. The peaks and troughs were then used to calculate the AC/DC ratios required for pulse oximetry. Equation 6.2 and 6.3 were used to estimate the arterial and venous oxygen saturations respectively. For visual analysis, a 0.67 Hz to 8 Hz Chebyshev bandpass filter is used to identify the shape of each waveform.

A lowpass filter with a cut-off frequency of 0.67 Hz was used to isolate the breathing induced pulsatile signal in the jugular venous pulse waveform. The peaks and troughs

of this lowpass filtered data were then used to calculate the AC/DC ratio, and subsequently, the EJV $SpjvO_2$.

6.2.4 Analysis

The mean and standard deviation of the SpO_2, $SpcO_2$, and $SpjvO_2$ were calculated for their respective sites. The recorded JVP pulse waveform represents the volume change of blood, rather than the pressure in the EJV. However, as the EJV is highly elastic, the change in volume is expected to reflect the pressure waveform. Figure 6.2 shows the expected volume pulse waveform in the EJV. In the venous waveform, the A wave and X wave of the JVP are taken as the peaks and troughs for $SpjvO_2$ calculation.

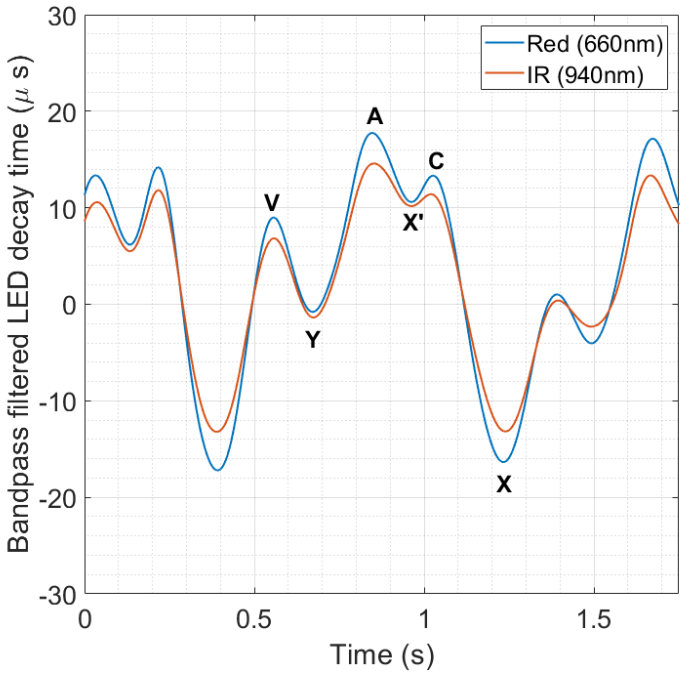

Figure 6.2 Example waveform at the EJV representing a change in blood volume. Data is filtered using a 0.67 Hz to 6 Hz Chebyshev bandpass filter.

Oxygen saturation estimation will be analysed using a box plot to represent the variance in data. The narrower the variance in calculated values, the more certain the estimation. The distribution for each subject will also be analysed, comparing the oxygen saturation at each site. The thumb is expected to have the highest SpO_2. The carotid artery $SpcO_2$

measured sitting up is also compared to the supine measurement. The $SpjvO_2$ for each subject is expected to sit below the corresponding $SpcO_2$ values.

6.3 RESULTS

Figure 6.3 plots the recorded PPG wavform from the thumb. Subjects 1 and 3 have a poorly defined systole in either the red or IR pulse waveforms. Figures 6.4 and 6.5 plot arterial pulse waveforms recorded at the carotid artery. Subject 2 of Figure 6.5 appears to contain the V wave from the venous waveform superimposed on the arterial pulse.

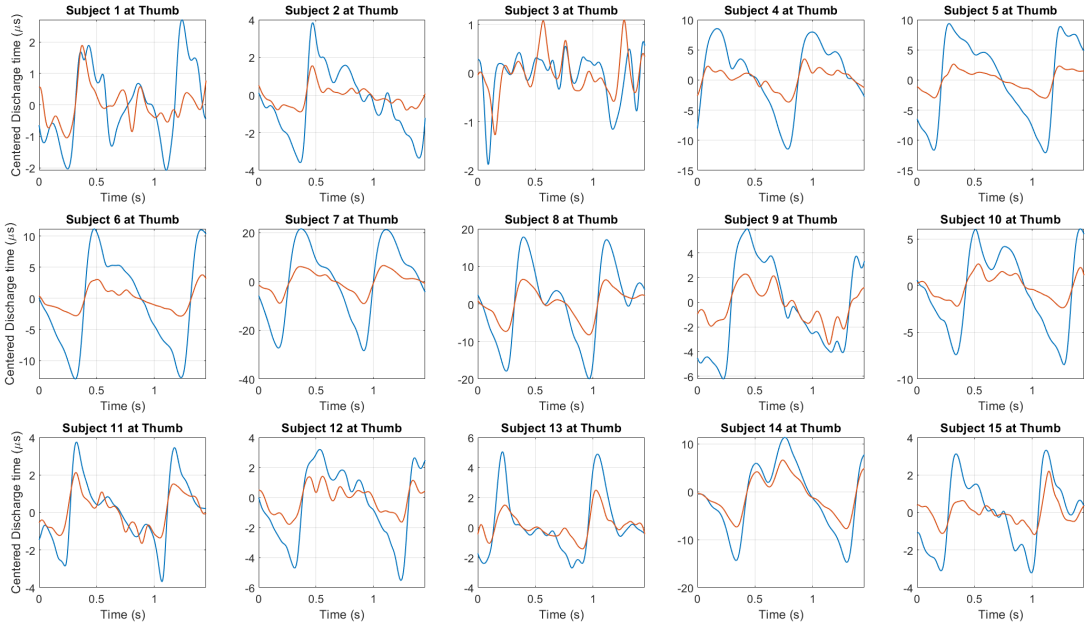

Figure 6.3 Pulse waveforms recorded at the thumb for each test subject. The blue plot is the red (660 nm) LED pulse and the orange plot is the IR (940 nm) LED pulse. Data is filtered using a 0.67 Hz to 8 Hz Chebyshev bandpass filter.

Figure 6.6 plots the jugular venous pulse of each subject, with Subject 3 having a poorly defined pulse waveform. Each subject had different amplitudes for the V wave and subjects such as Subjects 4, 13 and 14 have a higher C wave than A wave.

The results from the data recorded at each position are plotted in Figure 6.7. The box plots show the beat to beat SpO_2 for each subject at each site. The calculated SpO_2 in the thumb for each subject is >90%. Subjects 1 and 3, who had poorly defined

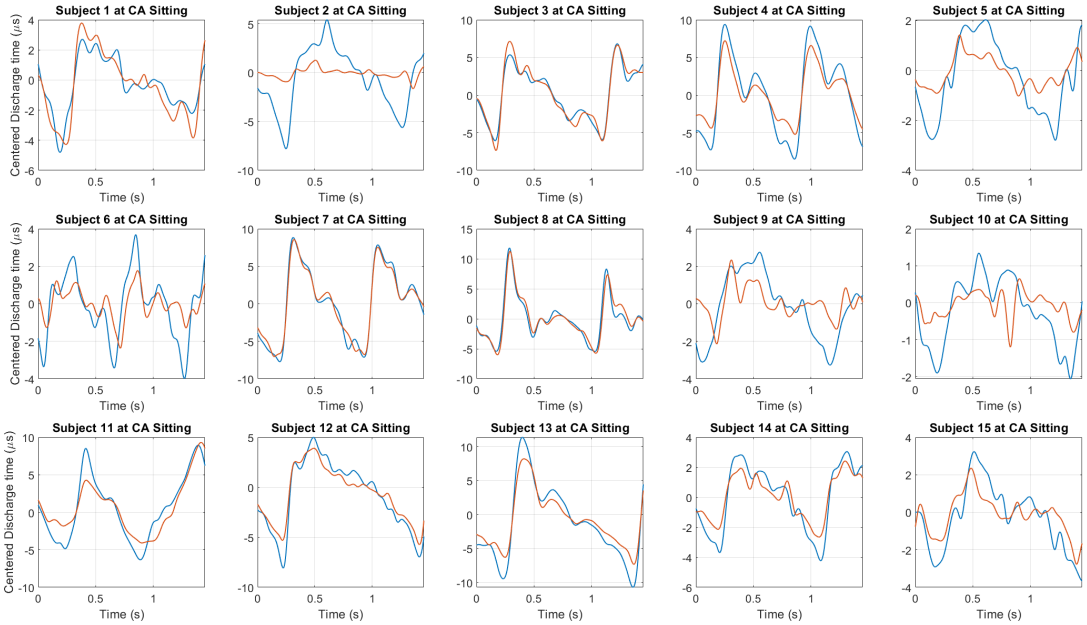

Figure 6.4 Pulse waveforms recorded at the carotid artery for each test subject sitting upright. The blue plot is the red (660 nm) LED pulse and the orange plot is the IR (940 nm) LED pulse. Data is filtered using a 0.67 Hz to 8 Hz Chebyshev bandpass filter.

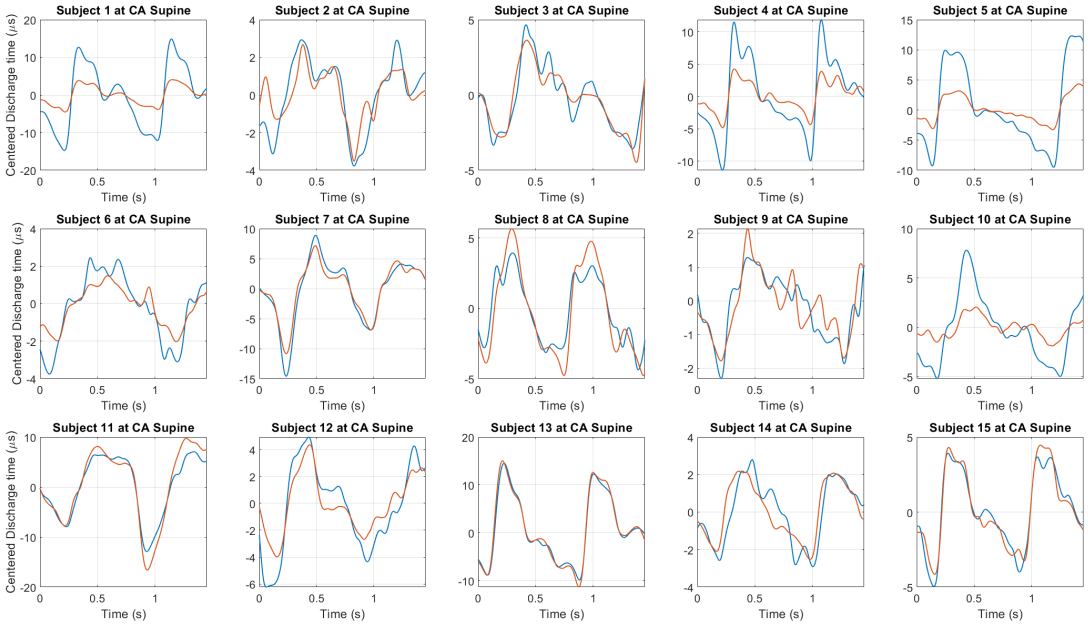

Figure 6.5 Pulse waveforms recorded at the carotid artery for each test subject lying supine. The blue plot is the red (660 nm) LED pulse and the orange plot is the IR (940 nm) LED pulse. Data is filtered using a 0.67 Hz to 8 Hz Chebyshev bandpass filter.

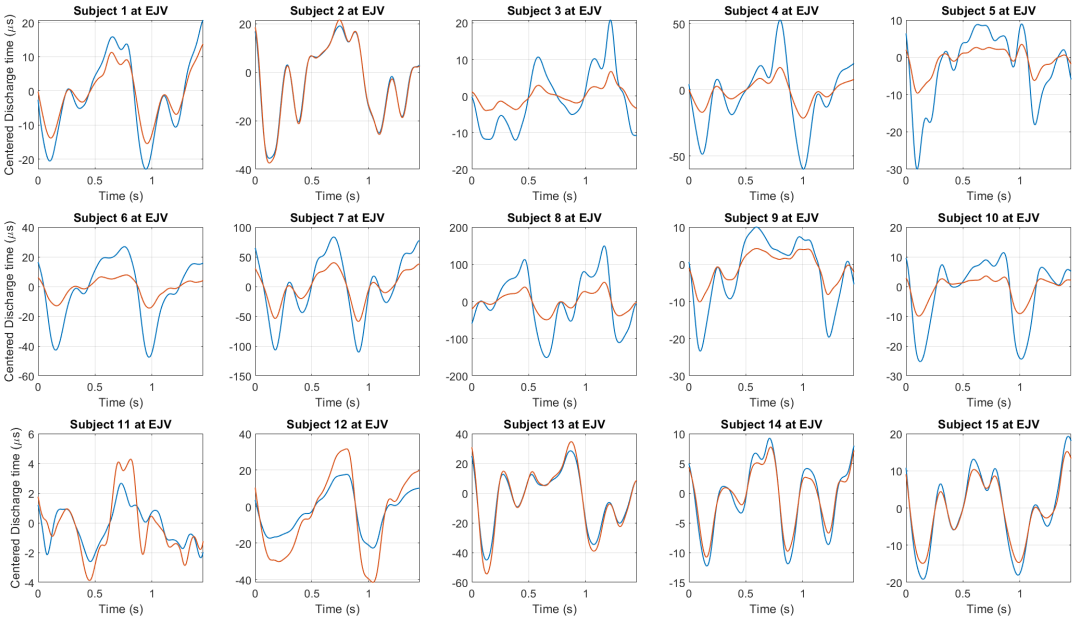

Figure 6.6 Pulse waveforms recorded at the external jugular vein for each test subject. The blue plot is the red (660 nm) LED pulse and the orange plot is the IR (940 nm) LED pulse. Data is filtered using a 0.67 Hz to 8 Hz Chebyshev bandpass filter.

pulse waveforms, have the largest variance in calculated SpO_2. All subjects except for Subjects 1 and 5 had a mean $SpcO_2$ higher in the sitting rather than the supine position. Measurements on the EJV gave a wide range of results with mean $SjvO_2$ for each subject ranging from 76% to 96%. Figure 6.8 shows the box plots from the $SjvO_2$ calculated using the breathing induced pulse waveform rather than the JVP.

The combined results for testing at the thumb, carotid artery, and external jugular vein are presented in Table 6.2. The thumb had the highest mean oxygen saturation, followed by the carotid artery in sitting and supine, with the EJV presenting the lowest oxygen concentration. $SjvO_2$ measurements at the EJV had the largest standard deviation (SD) of 6.9%, while measurements of the carotid sitting upright had the lowest SD of 1.8%. The $SjvO_2$ calculated using the breathing rate at the EJV gave lower estimates for all subjects except 6 and 11, where there was no change. As seen in Figure 6.8, Subject 12 is the only subject with a calculated $SjvO_2$ above 90%.

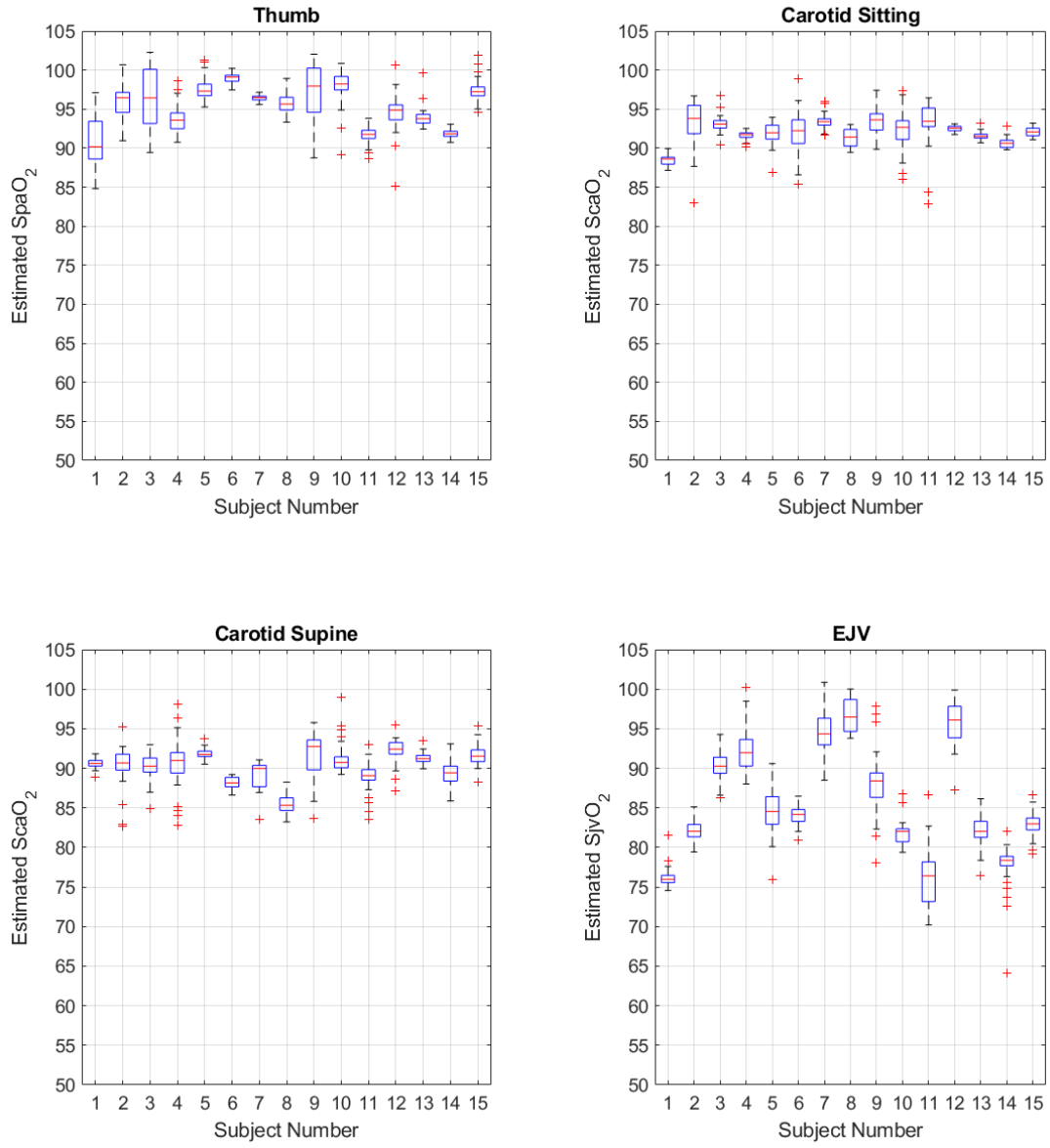

Figure 6.7 Box plots showing the calculated oxygen saturation at each of the sites measured.

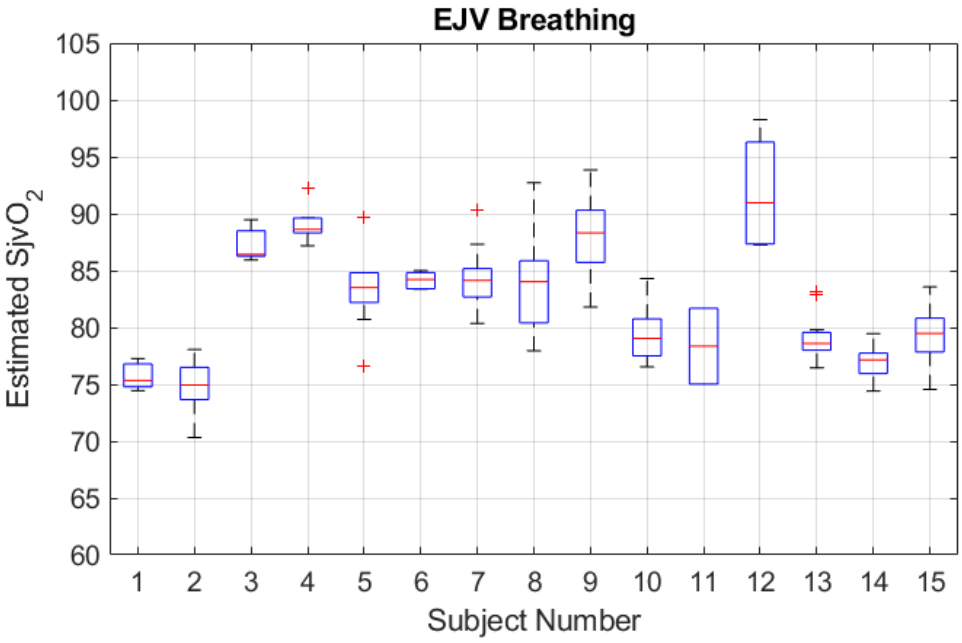

Figure 6.8 Box plots showing the calculated oxygen saturation at the EJV using the breathing induced pulse waveform.

Table 6.2 Oxygen saturation (SpO_2) at each measured site.

	Thumb	Carotid sitting	Carotid supine	EJV pulse	EJV breathing
Mean SpO_2 (%)	95.4	92.1	90.1	85.7	82.4
SD (%)	2.5	1.3	1.8	6.9	5.2

6.4 DISCUSSION

The sensor showed clear differences in oxygen saturation estimations between each site. Sensor readings at each site returned oxygen saturations consistent with literature [Bhardwaj et al. 2015, Colquhoun et al. 2012]. The mean $SpjvO_2$ calculated using the JVP was 85.7%, and had the highest standard deviation (6.9%), while the $SpjvO_2$ calculated using the breathing induced pulse returned a lower mean $SpjvO_2$ (82.4%) and had a lower standard deviation (5.2%). Thus, the estimated $SpjvO_2$ using the breathing rate is recommended for future analysis. The thumb had the highest estimated SpO_2 for each subject, followed by the carotid sitting, carotid supine, and finally the EJV.

The plots presented in Figure 6.6 follow the expected shape of the jugular venous pulse waveform shown in Figure 6.2. The V, A and C waves are evident in the waveforms,

which do not appear in either of the carotid artery tests. Subjects with less defined pulse shapes, such as Subject 3 at the thumb, had a larger variance in calculated SpO_2, showing the accurate calculation of SpO_2 requires accurate extraction of the peaks and troughs of the pulse waveform.

There was a greater range in EJV pulse waveform shapes compared to the arterial waveforms measured at the thumb and carotid artery. This greater range is likely due to user influence on the pules shape. As the JVP is very low pressure, typically <30 mmHg, any difference in pressure from the sensor on the skin can change the shape of the pressure waveform. Compared to the venous pulse, arterial pulse waveforms are at much higher pressure (>50 mmHg), and are thus less likely to be influenced by the applied sensor pressure.

The mean $SpjvO_2$ was in the higher region of the expected physiological range (60-90%), while, the calculated carotid artery saturation was lower than the expected >95% $SpcO_2$. These results are likely due to the influence of the carotid and venous waveforms on each reading. The EJV is located next to the carotid artery, so the measured JVP likely contains some influence from pulsatile arterial blood, in the reflected light, increasing the calculated $SjvO_2$. This influence is evident in the results from the carotid artery while supine and sitting. A lower calculated $SpcO_2$ while supine indicates the JVP extended along the neck to influence the measured pulse. However, while sitting, the JVP collapses and minimal venous pulse influence is seen on the arterial pulse waveform. This positioning and position issue is also evident in the JVP vs breathing $SjvO_2$, as the arterial waveform can only affect the JVP as no breathing induced changes in the arterial pulse waveform were recorded.

The typical range of $SjvO_2$ is 60-90% [Schneider et al. 1995]. As each of the subjects were healthy, measured at rest, and lying supine, the oxygen extraction at the brain is expected to be low, leading to $SjvO_2$ readings high in the expected range. Each subject except for Subject 12 had a breathing $SjvO_2$ lower than their $SpcO_2$, indicating that those outside the expected 60-90% $SjvO_2$ range still had a higher $SpcO_2$, implying reduced oxygen uptake in these patients.

6.4.1 Limitations

A limitation of the trial is the inability to measure the actual venous and arterial oxygen saturations using invasive blood sampling as a reference. However, the design of the trial was to show the influence of the carotid and venous waveforms on each other, rather than the exact SpO_2 and values. The results are further confirmed by their meeting clinical expectations, where direct validation measurement would have been risky and invasive, although, invasively measuring SvO_2 would validate Equations 6.2 and 6.3.

The sensor recorded 50 s at each site for 15 subjects. Future testing would require longer recordings of each subject, as well as more subjects, to get a better understanding of the variance of measured $SjvO_2$ values. Different angles of supine positioning would also show the effect of the JVP as the amplitude of the pulse extends further along the neck.

6.5 SUMMARY

This chapter validated the use of an in-house developed pulse oximeter to measure the oxygen saturation at various sites on the body. A total of 15 subjects were tested at the thumb, carotid artery and external jugular vein. SpO_2 measured at the thumb gave expected saturation values. However, carotid and venous oxygen percentages were influenced by each other due to their close proximity, leading to slightly lower than expected $SpcO_2$ and slightly higher than expected $SjvO_2$. Thus, the influence of the carotid and venous waveforms must be accounted for to calculate the actual oxygen consumption by the brain. This issue is offset by clinical studies showing changes in volume, versus the absolute value itself, are clinically more relevant.

Better sensor locating and improved sensing precision may also be possible, given the proof-of-concept sensor presented here. Using the breathing induced pulse waveform on the EJV gave more promising $SjvO_2$ results than using the JVP itself due to the ability to isolate the venous pulse from the arterial at this frequency.

Part III

Estimation of Arterial Pulse Wave Velocity

Chapter 7

PULSE WAVE VELOCITY HARDWARE

Measurements of PWV in a clinical setting are not commonly done as the clinical benefit of PWV does not warrant the required, additionally invasive measurements from using two pressure catheters. This chapter describes the design and testing of a non-invasive pulse wave velocity sensor to enable regular use of PWV in clinical settings. The main goal of this chapter is to develop hardware capable of locating a pulse waveform at several points along the carotid artery to determine the speed of the pulse wave. The speed of the pulse wave is calculated using two different algorithms: the gold standard foot-foot method; and a phase difference algorithm.

7.1 INTRODUCTION

Cardiovascular disease is a leading cause of death, responsible for an estimated 30% of deaths worldwide [Mendis 2015]. Many methods for early risk detection have been investigated, with arterial pulse wave velocity being an indicator of changing blood pressure, as well as early detection of the onset of sepsis [Kadoglou et al. 2012, Kazune et al. 2014]. Pulse wave velocity (PWV) is used as a surrogate to indicate arterial stiffness, with risk of health complications increasing with higher stiffness levels seen in higher PWV [Darwich et al. 2015].

Traditional PWV sensing uses invasive catheters placed at two sites along the arterial tree, usually the aorta and femoral artery. This regional PWV provides information across multiple vessels, each with different vascular stiffness [Jani et al. 2014]. Com-

pared to regional PWV measured between different arteries, PWV measurement of a single artery provides PWV estimation across the same vascular stiffness. Local measurement of PWV at an artery has been investigated using non-invasive photoplethysmography using two light sensors a known distance apart to measure the pulse transit time [Kazune et al. 2014, Peter et al. 2015].

When a wave of increased pressure and therefore volume propagates along a blood vessel, a pulse of blood moves past the sensor, and the additional volume of blood absorbs more of the emitted light. The recorded pulse is proportional to the pressure waveform in the measured artery. The time this pressure pulse takes to travel between two detectors placed along the artery is called the pulse transit time.

Peter et al developed a dual channel photoplethysmograph sensor with sensors placed 60 mm apart and a sample rate of 1 kHz [Peter et al. 2015]. Sorenson et al measured PWV in the range of $3\,\mathrm{m\,s^{-1}}$ to $4\,\mathrm{m\,s^{-1}}$ at a measurement separation of 10 mm [Sorensen et al. 2008], which was similar to the $4.5\pm1.2\,\mathrm{m\,s^{-1}}$ found by Obeid et al. [2021]. These sensors had promising results, but no local PWV sensor has yet to be further developed into a commercial sensor.

Shen et al developed a 4x4 array of photodiodes to generate a 2D PPG plot for pulse oximetry [Shen et al. 2010]. However, each photodiode required an analogue bandpass filter, an ADC, and a PPG controller. As a result, the system could no fit onto a single board within the sensing area of the photodiodes, so additional boards were required to keep the sensing board a usable size. Additional 2D array PPG sensors using an array of organic LEDs and organic photodiodes (PD) have been developed [Khan et al. 2018, Simone et al. 2020]. However, these boards require custom fabrication laboratories and none measure PWV.

This chapter develops a new 2D PPG sensor using the LED-LED detection method to detect light, allowing construction on a single circuit board, increasing simplicity, and reducing cost of design, and allowing detection of the arterial pulse wave with an array of detectors at several distances.

7.2 METHODS

A sensor with 60 LEDs was built (30 at 660 nm and 30 at 940 nm LEDs). Three arrays of 20 LEDs (10 at 660 nm and 10 at 940 nm) were used to measure the pulse at different points along the carotid artery. To reduce footprint size, both the 660 nm and 940 nm LEDs are contained in a single package. Each package of two LEDs is separated along the array by 5 mm. Figure 7.1 shows the LED layout on the board.

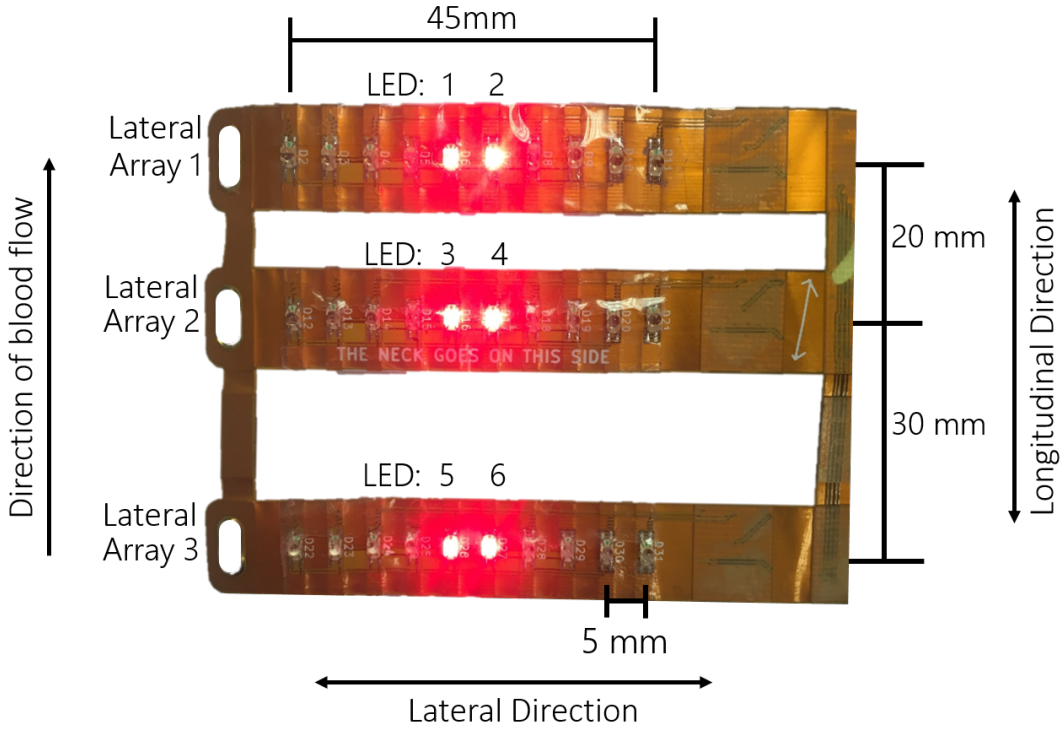

Figure 7.1 LED layout of the flexible PWV board. Each array is controlled by individual microcontrollers with 10 660 nm and 940 nm LEDs in each array. To save space, both wavelengths are placed in a single LED package. Each package is separated by 5 mm.

The sensor has been designed for the simplest placement over the carotid artery. Using a 2D array of sensing LEDs spanning 50 mm in the longitudinal direction and 45 mm laterally, ensures that whatever the placement on the neck, the arterial pulse falls within the area of the sensor. To measure the pulse wave velocity, three lateral arrays of sensing LEDs are used, spaced at different points along the carotid artery.

Within the three lateral arrays of 20 LEDs, each LED package of the two wavelengths is separated by 5 mm, giving a total measurement range of 45 mm across the neck. The

largest arterial pulse amplitude of the 20 measured (10 at 660 nm and 10 at 940 nm) in each array is taken to be used in PWV calculation. The hypotenuse between detecting LEDs is taken as the pulse travel distance.

The carotid arterial pulse waveform is measured at three different points along the carotid artery with a spacing between detection points of: 0 mm, 20 mm, and 50 mm. The sensor board was setup as shown in Figure 7.2, where three arrays of emitting and sensing LEDs span across to the carotid artery, separated by 0 mm, 20 mm, and 50 mm.

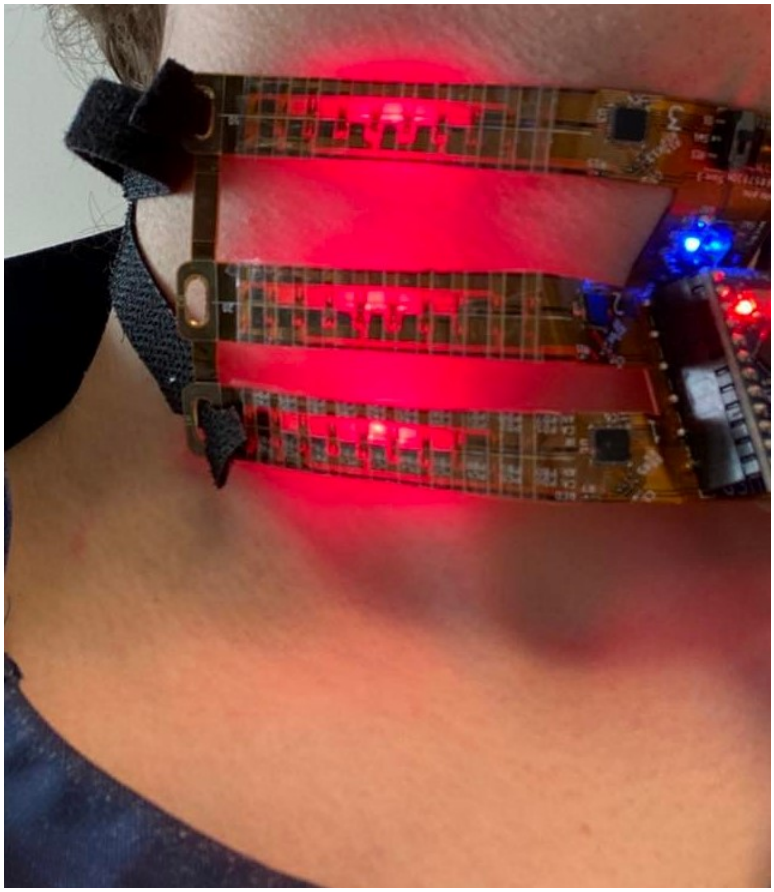

Figure 7.2 Placement of the PWV sensor over the carotid artery. The three arrays of sensing LEDs spaced by 0 mm, 20 mm and 50 mm. The timing difference between the pulse waveform recorded by each array is used to calculate the PWV.

The 1D lateral array ensures that the sensor can capture the arterial pulse waveform at each measuring site. Thus, the sensor does not need to be perfectly located over the carotid artery to ensure each array is capable of capturing the arterial pulse waveform, as the 'best' signal can be selected from the detectors across each 1D array. The time the arterial pulse wave takes to pass each of the three measuring sites on the carotid

artery is used to calculate PWV.

7.2.1 Subjects

Data was recorded from a healthy 24 year old male sitting at rest. The sensor was applied to the neck with minimal pressure using Velcro straps to maintain skin contact. Five blocks of data, each composed of 30 s of sensor data were recorded over eight hours.

7.2.2 Equipment

Data was recorded on a PC with an Intel Core I7, 32 GB RAM running Windows 10. The sensor connected to the PC via USB, and data was recorded using a custom built user interface. The sampling rate of the sensor was limited to a maximum of 570 Hz by the limitations of sequential sampling using the LED sensing method.

Figure 7.3 shows the top view of the sensor with the placement of the Arduino Micro and the ATtiny88 microcontrollers. The two switches are used for switching between programming the board (connect to reset on ATtiny88) or SPI (slave select on attiny88). The push button is used to reset the Arduino and the dip switches are to dynamically adjust settings during operation.

On the edges of the board are mounting holes for straps. These straps are used to hold the sensor against the skin with minimal pressure. The board produced uses Velcro (attachment points on the left of Figure 7.3). However, other forms such as elastic would work sufficiently.

As previous methods of PWV detection use between 20 mm and 60 mm reading distances [Peter et al. 2015, Sorensen et al. 2008], the sensor was constructed with reading distances of 20 mm, 30 mm and 50 mm to cover this range from literature. These three 1D lateral array spacings are shown in Figure 7.1. At these distances, for an expected PWV of $5\,\mathrm{m\,s^{-1}}$, the delay times between pulse arrival times at each array are expected

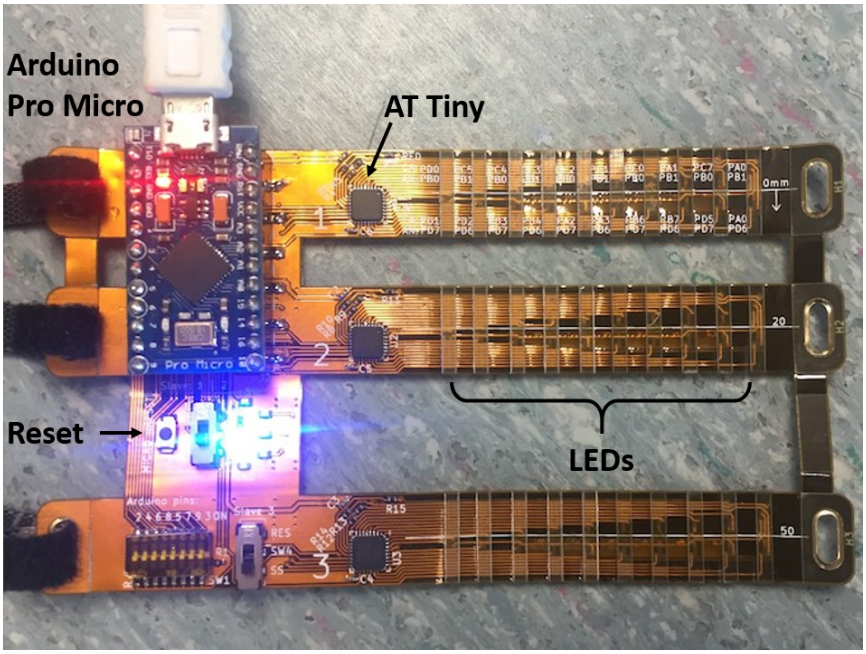

Figure 7.3 Top view of LED-LED sensor. Visible are the three ATtiny microcontrollers powering each array of sensing LEDs (underneath the board) and the Arduino Pro micro used to connect to a PC via USB serial.

to range from 4 ms at 20 mm and 10 ms at 50 mm.

The circuit layout used in the sensing array is shown in Figure 7.4. The cathode of every LED is connected to an individual microcontroller GPIO pin, while the anode of every alternating LED is connected to dedicated GPIO pins, with a 70 Ω current limiting resistor. To emit light, one anode GPIO pin (A_1) drives output high. Pins C_1, C_3, C_5, etc can then be individually pulled to logic low to turn each LED on. To detect light, an anode GPIO pin (A_2) pulls to logic low so that pins C_2, C_4, C_6, etc can be driven output high to reverse bias each cathode to 5 V and subsequently measure the LED voltage decay time.

Once the sensor located the largest arterial pulse amplitudes in each array, each of the 3 1D lateral arrays switches to only reading from their two LEDs (6 total readings). An example set up of sensing LEDs is shown in Figure 7.1, where LEDs 1 and 2, 3 and 4, and 5 and 6 return a pulsatile signal from each respective 1D lateral array. The maximum allocated time for each LED to decay was set to 300 µs to provide a compromise between sampling rate and low light sensitivity. As each LED is sampled

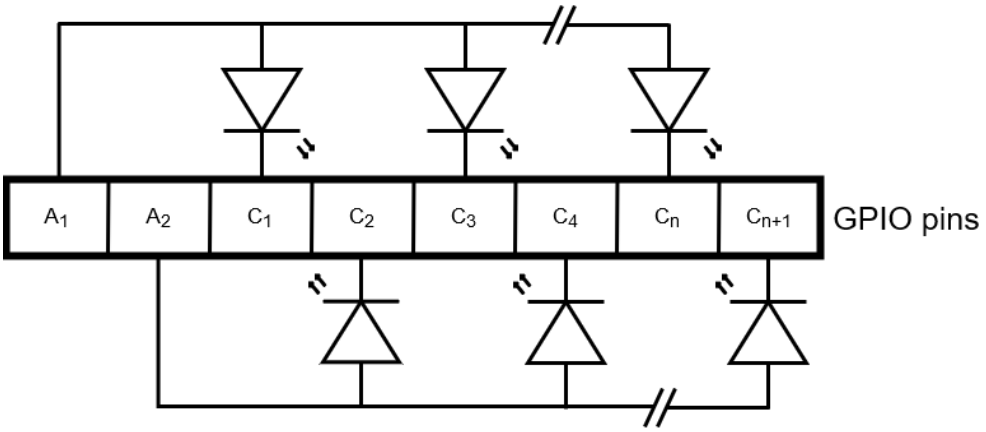

Figure 7.4 Circuit diagram for a single wavelength LED-LED detection method used in a 1D lateral array of sensing LEDs. Each array of detecting LEDs has the anode (A_1, A_2) of every second LED connected to a GPIO pin. When detecting light, one LED emits light (C_1) and the adjacent LED (C_2) detects the returning light.

sequentially, reading all six LEDs takes a combined 1.8 ms, giving an overall sample rate of 570 Hz.

7.2.3 Sensor output processing

The voltage discharge time of the reverse biased LED is proportional to the incident light intensity. A pulse oximeter normalises the light intensity by dividing by the emitted light intensity, making the recording unit-less. Further, only the pulsatile component of the signal is analysed, removing the influence of any constant conditions affecting light absorption. Thus, the arterial pulse waveforms recorded in this chapter are represented as α/I_D, a relative light reflection intensity of the detected light.

Two different signal processing techniques are implemented to calculate the PWV from the PPG signals. The first method uses an expert human who manually identifies the position of the PPG inflection point at the start of systole (foot of the waveform) of two arterial pulse waveforms recorded a known distance apart. The pulse transit time (PTT) between the feet recorded at each array is then used to calculate PWV, as given:

$$PWV = \frac{(d_{LEDx-LEDy})}{PTT_{LEDx-LEDy}} \tag{7.1}$$

where:

d: Distance between sensing LEDs.

LEDx: Sensing LED that the pulse wave first travels through.

LEDy: Sensing LED that the pulse wave travels through second.

PTT: Pulse transit time between LEDx and LEDy.

The phase difference method analyses the two arterial pulse waveforms in the frequency domain, analysing both the FFT magnitude and phase. The phase from LEDy is subtracted from LEDx to get the phase difference. The phase difference is then reconstructed into the time domain using the combined magnitude spectrum from each signal. The reconstruction in the time domain gives the PTT as the time the peak of the waveform occurs at. Further detail of this method will be presented in Chapter 8.

7.2.4 Analysis

Analysis of the sensor uses the data recorded from the PWV sensor at three sites along the carotid artery. A 30 second data-set consisting of 65 beats is used to determine the accuracy of the PWV sensor. Time series plots of both the 660 nm and 940 nm wavelength LEDs shows the validity of using an array of LEDs spaced approximately perpendicular to the carotid artery. Combining the readings at each LED into a 3D plot would demonstrate the sensors capability to find the pulse, even with inaccurate placement over the carotid artery.

The foot-foot method and phase difference method are used to calculate PWV from the PPG waveforms. A trained expert was used to manually identify the location of the foot at each waveform for analysis. The mean PWV and standard deviation will be calculated for each method.

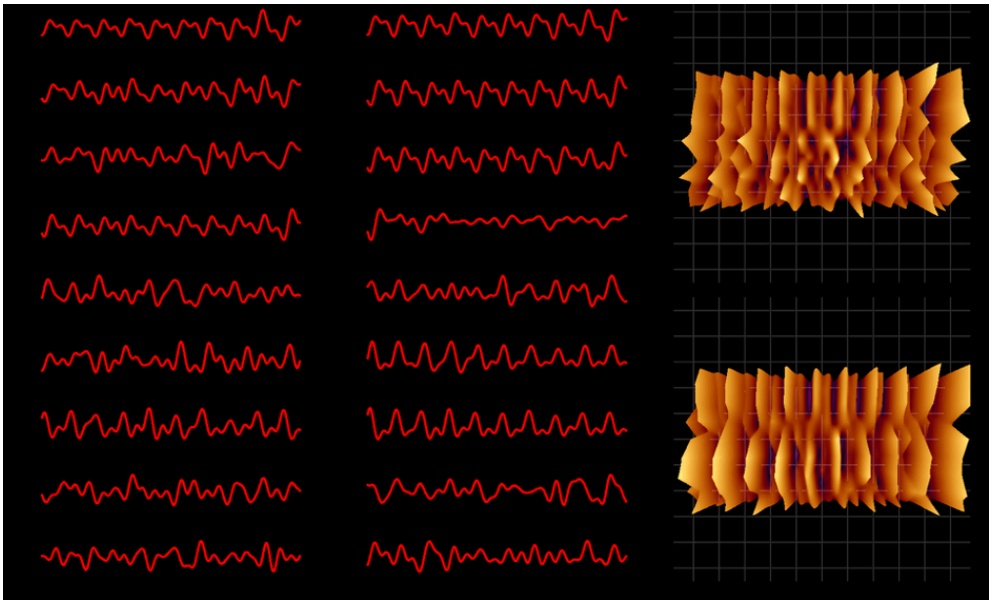

Figure 7.5 Example plot from one of the three sensing arrays. The first column of arterial pulse waveforms are the recordings of the nine 660 nm sensing LEDs. The second column is recorded waveforms of the 940 nm LEDs. The top (660 nm) and bottom (940 nm) 3D plot shows the time series pulse waveform across the neck.

7.3 RESULTS

The readings from each LED in a single array are shown in Figure 7.5. The first column of arterial pulse waveforms are the recordings of the 9 660 nm sensing LEDs. The second column is the recorded arterial pulse waveforms of the 940 nm LEDs. These waveforms can be combined to form a time-series plot of the pulse waveform across the neck, where the top 3D plot shows the 660 nm waveforms and the bottom 3D plot shows the 940 nm waveforms.

During testing of the sensor was placed on the neck, as shown in Figure 7.2. The 5^{th} and 6^{th} LEDs in each 1D lateral array gave the strongest pulse amplitudes. These are the LEDs labelled 1-6 in Figure 7.1. The data from these LEDs are shown in Figure 7.6. Time series data was filtered with a 15 Hz cut off low-pass Butterworth IIR filter.

Figure 7.6 shows the recorded arterial pulse waveforms at the carotid artery. A five beat section of data recorded by LEDs 1-6 (from Figure 7.1) are plotted for analysis. The amplitude of each LED pulse in Figure 7.6 ranges from 12 clock counts (1.5 µs, LED 5) to 70 clock counts (8.75 µs, LED 3) with a resolution of 2 clock counts (250 ns).

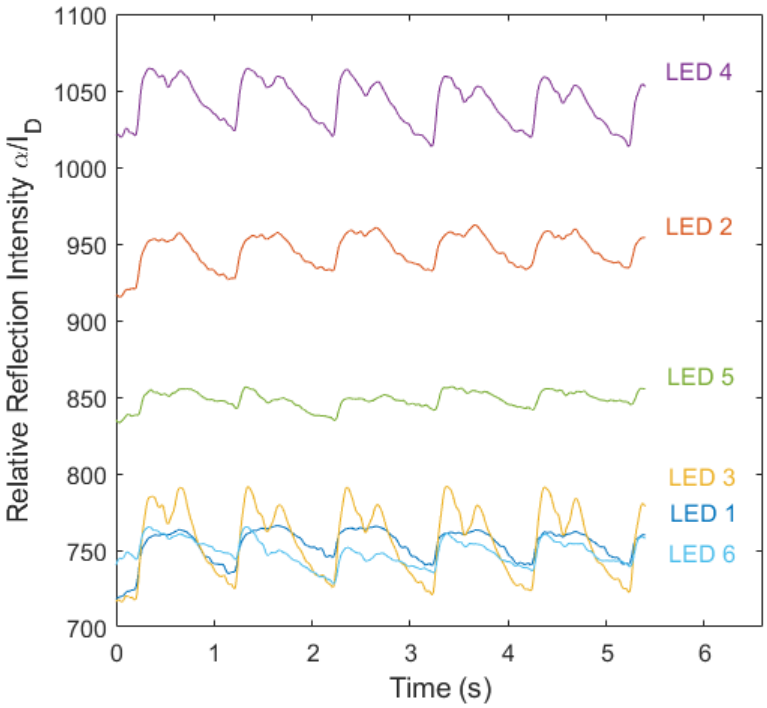

Figure 7.6 Pulse amplitudes in the carotid artery at 0 mm (LED 1 and 2), 20 mm (LED 3 and 4) and 50 mm (LED 5 and 6).

As the LEDs integrate the reflected light intensity, greater light absorption, i.e. less returning light, is represented by a longer LED discharge time.

Table 7.1 compares the foot to foot and the phase difference method within the expected range for a select few LEDs. Both the foot-foot and phase difference methods struggled with the data from LEDs 2 and 5, providing PTT results that were unrealistic. Possibly due to some feature of the waveform shape.

For both methods, all results from testing between LEDs 1-3, 1-4, 3-6, 4-6, 1-6 were acceptable. This result shows that using many LED across the array provides a robust method to identify and exclude erroneous data.

7.4 DISCUSSION

The PWV sensor developed in this work gave results within the expected physiological range. However, only at the maximum 50 mm sensor separation did the mean of the foot-foot and phase difference method return similar results. The foot-foot method gave

Table 7.1 Comparison between foot-foot PWV and the phase detection PWV method for different LED reading distances.

Sensor Spacing	LEDs	Foot-Foot $\mathrm{m\,s^{-1}}$	Phase Difference $\mathrm{m\,s^{-1}}$
20 mm	1-3	6.8	7.4
	2-3	2.0	10.5
	1-4	4.6	4.4
	2-4	1.7	-12.6
mean (±std)	All LEDs	3.8 (±2.4)	2.4 (±10.3)
	LEDs 1-3,1-4	5.5 (±1.3)	5.9(±2.1)
30 mm	3-6	3.8	4.3
	4-6	4.7	4.2
	3-5	4.7	1.9
	4-5	6.0	1.4
mean (±std)	All LEDs	4.8 (±0.9)	2.9 (±1.4)
50 mm	1-6	4.6	4.5
	2-6	2.8	6.3
	1-5	5.3	2.2
	2-5	3.0	2.7
mean (±std)	All LEDs	3.9 (±1.2)	3.9 (±1.8)
	LEDs 1-6,1-5	4.9(±0.5)	3.4(±1.6)

more reliable results than the phase difference method, with a lower standard deviation across all measurement distances, although, the position of each foot is difficult to locate, and had to be done manually. The time resolution of each measurement is 1.75 ms, meaning the associated variation in PWV may vary by as much as $1.5\,\mathrm{m\,s^{-1}}$, a large (30%) variation when the expected range is $6\,\mathrm{m\,s^{-1}}$ to $11\,\mathrm{m\,s^{-1}}$. Thus, a faster sample rate is needed to improve accuracy. With a faster sample rate, the phase method is expected to perform better than the foot-foot method.

The phase difference method has the same time resolution as the foot-foot method. However, the phase is taken across the whole signal, essentially averaging the errors in each foot position of each waveform. It was expected each LED plot would be the same shape, meaning the phase difference results solely from the PWV and not other effects. This assumption did not hold, as sensor pressure was different for each LED, giving different pulse shapes and amplitudes. An increase in pressure reduces the volume of blood under the sensor, reducing the pulse amplitude, and changing the local arterial elastance and thus potentially PWV.

Signal amplitudes varied between each LED reading, with the systole of LED 5 much

less pronounced than the others. LED 5 had a pulse amplitude of 12 clock counts, with a resolution of 2 clock counts. These values only gave a range of 6 different values between the peak and trough of the waveform. While filtering did smooth the signal, the pulse amplitude is required to be larger to reliably give the waveform foot.

The benefit of the regional carotid-femoral PWV method is the large distance between sensors. Local measurement must occur at a faster sample rate to get the same PWV calculation reliability. At 570 Hz, the sensor was shown to estimate PWV within physiological regions. However, a sample rate of at least 1 kHz would improve both methods of detection. At 20 mm, 30 mm and 50 mm, a PWV of $5\,\mathrm{m\,s^{-1}}$ would result in a PTT of 4 ms, 6 ms and 10 ms respectively. A benefit of this sensor is the ability to isolate the largest amplitude signal across each array. The sensor can be placed on the neck, with the carotid artery highly likely to be within the 50 mm each array spans. Thus, signals such as LED 2 and LED 5 can be discarded for better signals.

7.4.1 Limitations

Data from only one subject was collected for analysis and no gold standard data was available to compare the results to. A trial with more subjects would produce a greater variety of PWV measurements.

The sensor was capable of locating the pulse at each array, but accuracy was limited by the sensing resolution and sample rate. The microcontroller is only able to sample at only 570 Hz, with a clock rate of 8 MHz.

7.4.2 Recommendations

The next design of the sensor should have dedicated emitting and detecting LEDs. This choice removes the driving current restriction of 20 mA and allows a constant current LED driver to power the LEDs at higher current. A higher emitter drive current results in more light detected by the detecting LED and thus, a faster LED voltage

decay time. To measure this faster decay time, a microcontroller with a clock rate greater than 16 MHz is recommended.

7.5 SUMMARY

This chapter described the design and testing of a pulse wave velocity (PWV) sensor placed on the carotid artery. The sensor measured arterial pulse waveforms at each 1D lateral array, and calculated the pulse transit time between them. The foot-foot method gave more reliable PWV calculations (SD $<2.4\,\mathrm{m\,s^{-1}}$).

The sample rate of 570 Hz was fast enough to give PWV values in the region of $4\,\mathrm{m\,s^{-1}}$. However, it is recommended to use a faster sample rate as PWV may vary by $1.5\,\mathrm{m\,s^{-1}}$ using the foot-foot method. Further work on the sensor will increase the power of the LEDs, have a microcontroller clock rate >16 MHz and will sample at 1 kHz or faster.

The accuracy of the sensor must be improved before further testing to validate against known PWV values. Additional testing of the phase detection method is recommended on regional aorta-femoral pulse wave velocity to validate the method.

Chapter 8

PULSE WAVE VELOCITY PHASE DIFFERENCE ALGORITHM

This chapter develops a phase difference method to calculate pulse transit time. The sensor developed in Chapter 7 did not sample at a high enough frequency to accurately determine PTT over the short measurement distances with either the foot-foot or phase difference method. Thus, this chapter analyses the use of these methods using aorta-femoral arterial pressure waveforms recorded in porcine trials.

8.1 INTRODUCTION

The "foot-foot" method measured between the aorta and femoral artery is the current gold standard for measuring PWV, where the time difference between a feature common to the two recordings of PTT, which can be converted to PWV with known separation in space. The foot of the waveform is the most commonly used feature, defined as the inflection point of the pulse waveforms at the start of systole [Boutouyrie et al. 2009]. The difference in timing between the foot of each waveform gives the pulse transit time (PTT). If the distance between two points of measurement is known (carotid-femoral or aorta-femoral), the PTT can be used to calculate PWV.

The PTT between the aorta and femoral arteries are commonly measured using an invasive dual lumen catheter inserted through the aorta. The distance the arterial pulse waveform travels along the arterial tree is either calculated using the length of the dual lumen catheter, or by estimating the distance using calipers [Jianwen Luo et al.

2012]. Measuring between different arteries along the arterial tree is called "regional" pulse wave velocity [Hermeling et al. 2007]. During systolic cardiac contraction, the pressure wave propagates down the arterial tree, travelling from the large arteries to the peripheries, with a corresponding increasing arterial stiffness, and therefore propagation speed [Jani et al. 2014].

For regional PTT (aorta-femoral) calculation, using the phase difference method was estimated to be negatively impacted by the wave reflectance due to the different pulse features evident in the aortic and femoral pulse waveforms at different parts along the artery in Figure 8.1 [Bertram et al. 1997, Segers et al. 2009]. However, the phase difference across the low frequency harmonics (1 Hz to 30 Hz) has not yet been investigated for regional PWV. Only PWV local to a single artery (carotid, radial or femoral) has been investigated [Pereira et al. 2011, Xu 2002], with good results in-vitro, but poor in-vivo results due to low sample rates and high noise levels.

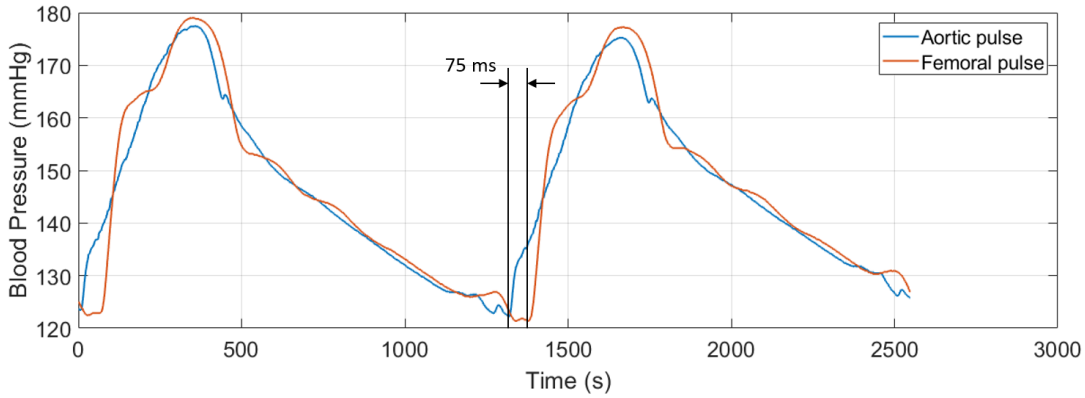

Figure 8.1 Section of filtered pulse waveforms from the aorta and femoral artery used to calculate pulse transit time. The time difference between the identified feet of the aortic and femoral waveforms is the PTT.

The goal of this chapter is to compare the foot-foot common feature PTT detection method to the phase difference method in regional PTT estimation (aorta-femoral PTT), where the shape and features of the two waveforms are different.

8.2 METHODS

This chapter uses aortic and femoral pulse waveforms acquired from 5 pigs undergoing induced cardiovascular changes. These experiments were part of a larger study into cardiovascular monitoring. A subset of the data acquired can be used to investigate the effect of differently shaped pulse waveforms on the accuracy of the phase difference method at calculating PTT [Ghuysen et al. 2008, Morimont et al. 2012]. Catheters placed in the aorta and femoral artery of each pig continuously measured the arterial pressure signal. Previous research with this data by Balmer et el investigated using a shear transform method to identify the foot of each waveform [Balmer et al. 2018a]. Each identified foot was then used to calculate the beat-beat PTT. This study compares the phase difference method of measuring PTT to the shear transform method developed by Balmer et el.

8.2.1 Subjects

Pig experiments were conducted at the Centre Hospitalier Universitaire de Liège, Belgium and approved by the Ethics Committee of the University of Liège Medical Faculty, permit number 1452 [Ghuysen et al. 2008, Morimont et al. 2012].

Five pure Piétrain pigs were used, weighing 18.5 kg to 29.0 kg. Diazepam ($1\,\mathrm{mg\,kg^{-1}}$) and Zoletil ($0.1\,\mathrm{mL\,kg^{-1}}$) were used for initial sedation and anaesthesia. To maintain sedation and anesthesia, sufentanil ($0.1\,\mathrm{mL\,kg^{-1}\,h^{-1}}$ at $0.005\,\mathrm{mg\,mL^{-1}}$), Thiobarbital ($0.1\,\mathrm{mL\,kg^{-1}\,h^{-1}}$) and Nimbex ($1\,\mathrm{mL\,kg^{-1}\,h^{-1}}$ at $2\,\mathrm{mg\,mL^{-1}}$) were delivered via superior vena cava catheter [Balmer et al. 2020]. A PEEP of 5 $\mathrm{cmH_2O}$ and tidal volume of $10\,\mathrm{mL\,kg^{-1}}$ were maintained with mechanical ventilation via tracheostomy delivered by a GE Engstrom CareStation mechanical ventilator (GE 92 Healthcare, Waukesha, WI, USA). Blood pressure was measured in the proximal aorta (P_{ao}) and femoral artery (P_{fem}) using high fidelity pressure catheters (Transonic, Ithaca, NY, USA). The placement of the pressure catheter is shown in Figure 8.2.

Each pig has two recordings of 5 minutes (445 pulse waveforms for each recording)

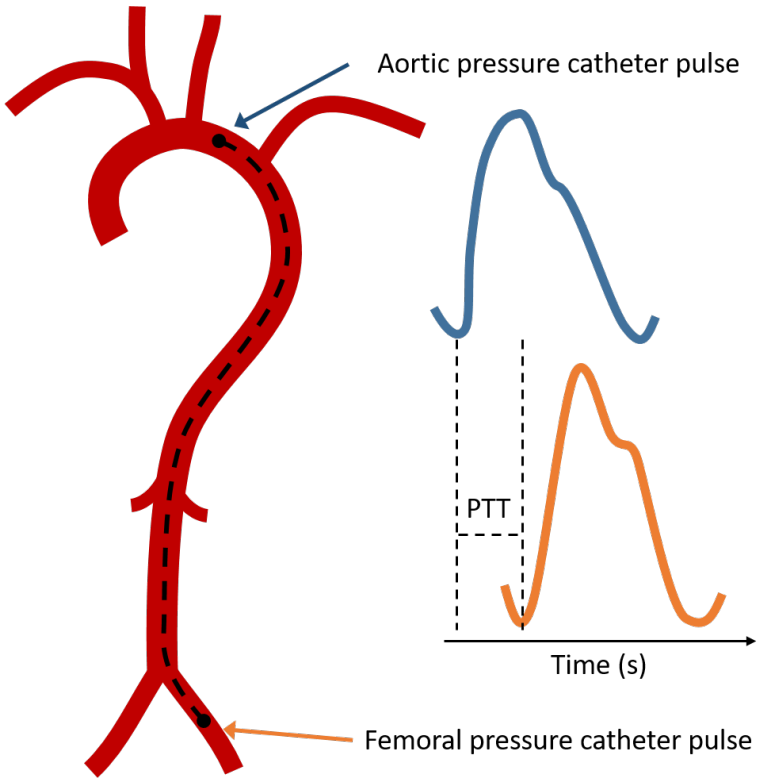

Figure 8.2 Placement of the high fidelity pressure catheter in the porcine trial. The pressure waveforms are measured in the proximal aorta and the femoral artery.

at different haemodynamic states, totalling 4450 beats. While only 5 pigs have been investigated, different cardiovascular states were recorded for each pig, so a range of waveform shapes occurred in each recorded dataset. All data was sampled at 1 kHz and then filtered with a 5^{th} order Butterworth lowpass filter, with a cut-off frequency of 20 Hz for the foot-foot method. The phase difference method used the unfiltered data as inputs to the algorithm.

8.2.2 Sensor output processing

The main difference between the foot-foot and phase difference algorithm is the foot-foot method returns beat-to-beat PTT, while, the phase detection method measures across a section of beats, returning the average PTT. Calculation of PTT using the foot-foot method is done in the time domain by locating a shared feature on each waveform, usually the foot, and the time between the foot of each waveform is the PTT.

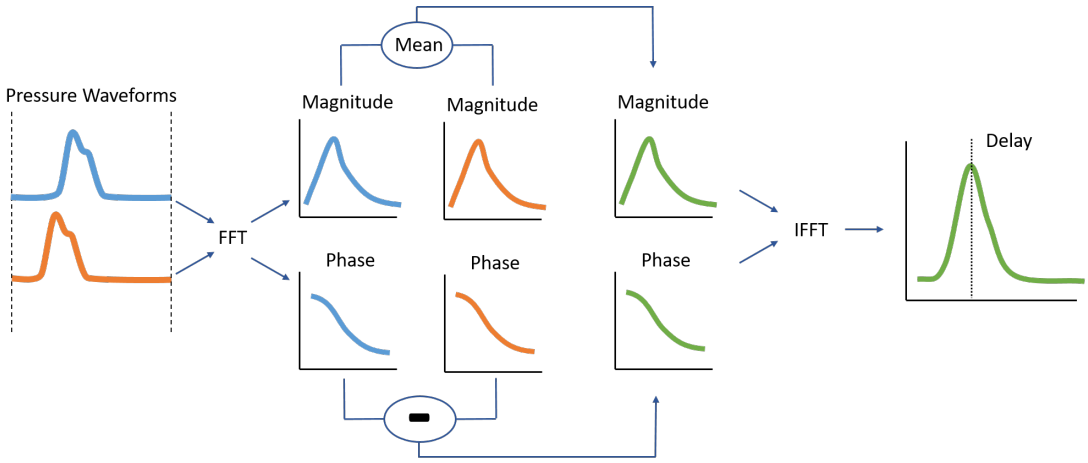

Figure 8.3 Path of pulsatile data through the phase difference algorithm to calculate PTT.

In the phase difference method, each waveform of a common time base must first be converted to the frequency domain, returning the frequency magnitude and phase information. The phase from one FFT phase is then subtracted from the phase of the other FFT to get the phase difference. As the shape of each waveform is expected to be similar, the difference between the two phase waveforms is assumed to be the time taken for the pulse waveform to travel between the two sites of measurement. The flow of data through the algorithm is shown in Figure 8.3.

Reconstructing the phase difference back into the time domain using the geometric mean spectral magnitude of the two waveforms creates a waveform with a peak amplitude occurring at the maximum phase difference, i.e. the pulse transit time. Thus, the phase difference can be used to determine the time delay. Figure 8.4 shows the reconstructed phase difference between the arterial pulse waveform measured at two sites along the arterial tree (aorta-femoral).

By using geometric mean of the two spectral magnitudes, the reconstructed waveform favours the FFT with the larger magnitude at the reconstructed frequencies, such as the harmonic [Pintelon et al. 1988]. Thus, the two arterial pulse waveforms can be different amplitudes, and the reconstruction will bias towards the larger amplitude signal. The steps used in the phase difference method are defined in Algorithm 8.1:

The phase delay is assumed to be consistent across a section of beats recorded at two

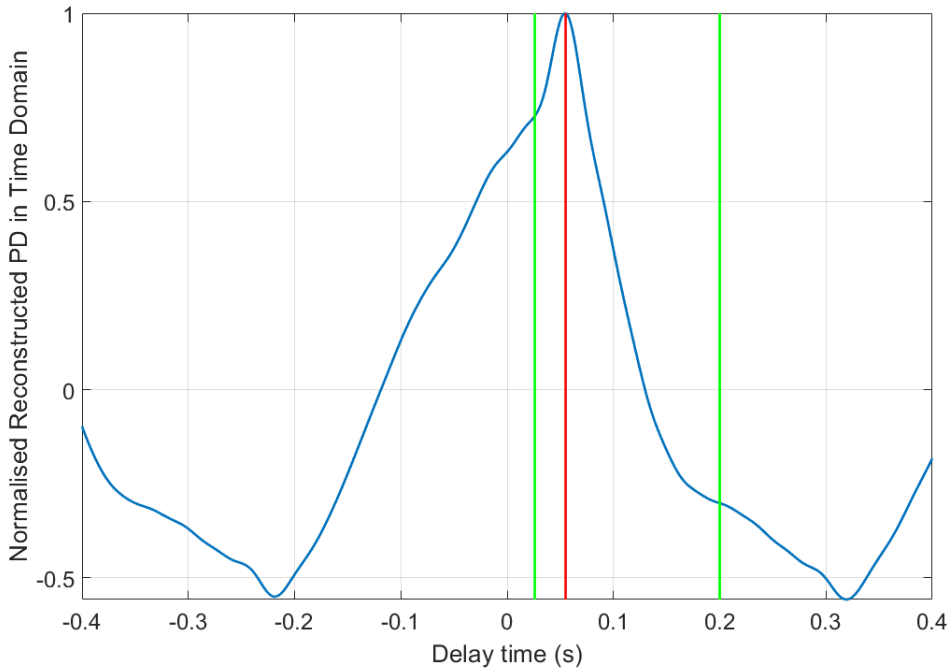

Figure 8.4 Normalised phase difference (PD) waveform reconstructed in the time domain. The time delay with the highest reconstructed phase difference is the pulse transit time (PTT). The green lines represent the physiological boundaries of the expected PTT, and the red line shows the estimated PTT.

Algorithm 8.1 Phase Difference Algorithm

1: $x_1 \leftarrow$ aortic waveform
2: $x_2 \leftarrow$ femoral waveform
3: $X_1 = FFT(x_1)$ ▷ Generate FFT of data.
4: $X_2 = FFT(x_2)$
5: $PD = \text{phase}(X_1) - \text{phase}(X_2)$ ▷ Calculate phase difference (PD)
6: $magn = \text{sqrt}(\text{abs}(X_1) \times \text{abs}(X_2))$ ▷ Compute the geometric mean spectral magnitude
7: $recon = \text{real}(\text{ifft}(magn \times \exp(i * PD)))$ ▷ Reconstruct weighted PD in time domain.
8: $[PeakTime, PeakAmp] = \max(recon)$ ▷ Locate the maximum peak in time domain
9: **return** $PTT \leftarrow PeakTime$

sites. Therefore, the aortic and femoral waveforms are compared in the frequency domain to obtain the phase difference. The resolution of the phase difference method is limited to the sample rate of the sensor, for example a 1 kHz sample rate has a timing resolution of 1 ms. Using the phase of the whole waveform is shown to improve timing [Zhang et al. 2018]. The method takes in two waveforms of equal length and sample rate. Various parameters of the model can be changed to fit different requirements:

- To improve algorithm response time to changing PTT, the algorithm can be run on just a few beats, increasing time response, but reducing robustness to noise.
- Lowering the cutoff frequency for the low pass filter allows slower sampling rates, but flattens the peak in Figure 8.4, increasing the risk of incorrect phase difference time domain reconstruction.
- Sample rates also affect the accuracy of the algorithm as high frequency features such as the feet of the waveforms, which may be lost at low sample rates.

8.2.3 Analysis

To investigate the effect of different sample lengths and sample rates over a range of 4450 porcine beats, a sensitivity analysis was generated, comparing the low-pass filter cutoff frequency, the time series sample length and the sampling frequency. The original sample rate recorded at 1 kHz was decimated to lower sample rates, ranging from 1 (1 kHz) to 10 (100 Hz). A time series sample length of 1 s to 15 s was tested. Four different cutoff frequencies were also tested (16, 20, 24, 28 Hz). This analysis will show the RMSE between the foot-foot and phase difference PTT values at each of these settings. Using the sensitivity analysis, we can determine the minimum of each setting required to maximise accuracy.

The results of the foot-foot method and the phase difference method were compared using correlation analysis and Bland-Altman plots. Correlation plots show the regression analysis as well as the coefficient of determination (R^2). The coefficient of determina-

tion represents the fraction of total observed variation between the two PTT calculation methods captured by the model.

The closer R^2 is to 1, the smaller the variation between methods. However, correlation does not imply agreement in the absolute sense [Bland and Altman 1986]. Therefore, Bland Altman analysis was used to assess the degree of agreement between the foot-foot method and phase difference method and identify any model bias in the phase difference method.

To compare the sensitivity to noise, pink noise was introduced in the frequency band of 1 Hz to 500 Hz to the data to compare the sensitivity to noise of both the foot-foot method and phase difference method. The signal to noise ratio (SNR) values of the noisy data ranged from 4 dB to 36 dB. The phase method used a cut-off frequency of 35 Hz with a sample length of 5 beats.

8.3 RESULTS

The data from 5 pigs was sampled at 1 kHz for 890 (2x 445 beat sections) beats per pig. To reduce spectral leakage in the computation of the signal spectrum, an interval corresponding to 5 complete beats was processed in each instance. Figure 8.5 shows the varied pulse shapes measured in the pigs. Example 1 has the aortic and femoral pulses overlapping other than the feet of each waveform. Examples 2 and 5 show a femoral pulse with accentuated dicrotic notches, while examples 3 and 4 have defined femoral systolic peaks, but differently shaped dicrotic notches. Example 6 displays a completely different pulse shape with no femoral dicrotic notch and an aortic pulse with a delayed dicrotic notch.

A sensitivity analysis was performed to assess the effects of the sample rate, low-pass cut-off frequency and buffer length and is shown in Figure 8.6. The RMSE between the foot-foot method and the phase method ranged from 2 ms to 8 ms.

For all cutoff-frequencies, the minimum acceptable buffer length was found to be two seconds (two heart beats). Increasing the cut-off frequency of the Kaiser window reduces

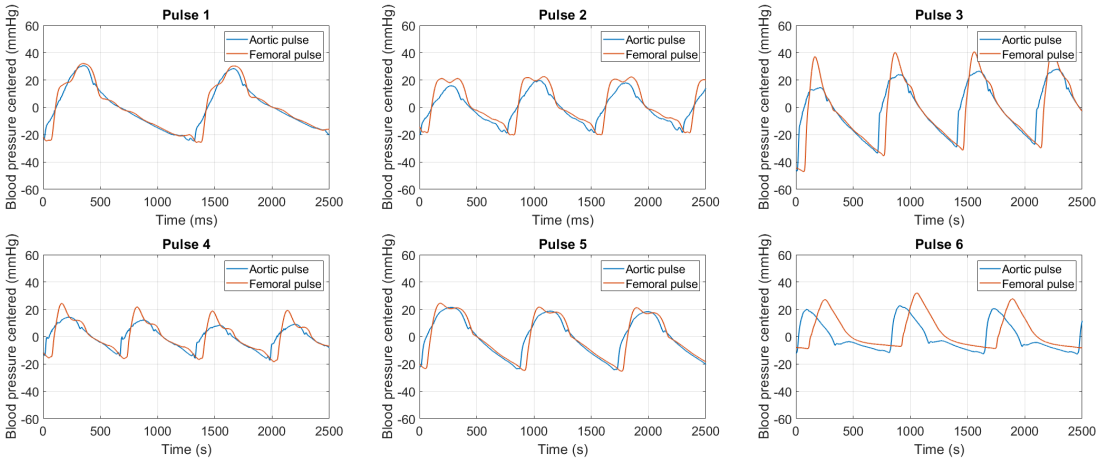

Figure 8.5 Example mean-centred waveforms showing the variation in beat shape across the data-set.

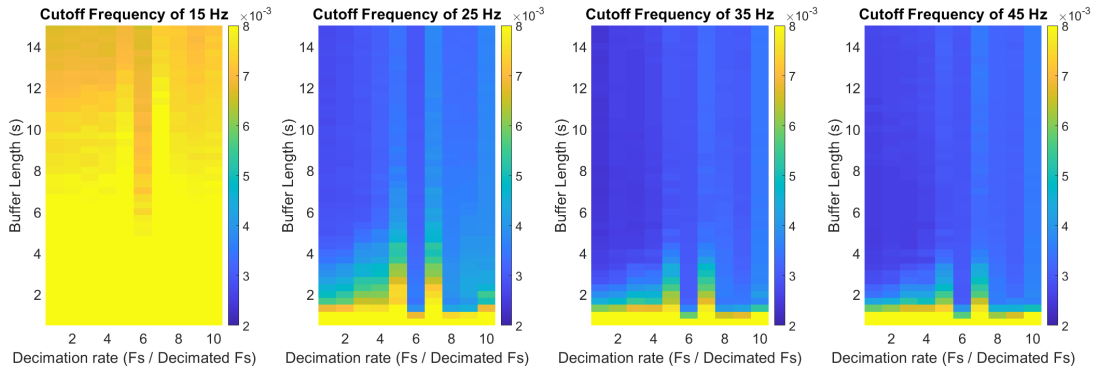

Figure 8.6 Sensitivity analysis of the RMSE between the foot-foot and phase difference method. Each plot shows the effect of changing the decimation rate, low-pass cut-off frequency and the buffer length.

RMSE as the reconstructed time domain peaks are more pronounced. The decimation rate of the data ranged from 1-10 (1 kHz-100 Hz).

Figure 8.7 compares the results from the foot-foot method and the phase difference method. The phase difference method used a cut-off frequency of 35 Hz, a buffer length of 4 seconds, and a sample rate of 1 kHz. Depending on the pig, the phase difference PTT sits just above or below the foot-foot PWV. Only Pig 1 has the phase difference PTT change between over- and under-estimating the PTT, compared to the foot-foot method.

The correlation (left) and Bland-Altman (right) plots in Figure 8.8 show the overall regression analysis for the 5 pigs, with a total of 4450 beats. A cut-off frequency of 35 Hz with 5 beats sampled at 1 kHz was used for the phase difference method. The R^2 value is 0.99, with PTT values ranging from 44 ms to 108 ms. However, these results can be misleading due to the clustering of each individual pig data Bewick et al. [2003].

The correlation plot shows a modest underestimation of PTT at lower PTT values and an overestimation at higher PTT values. The mean PTT offset is -1 ms (phase method leads foot-foot by one sample) with a standard deviation of 3 ms.

The Bland-Altman plot in Figure 8.8 shows that Pig 1 has the highest variation in PTT estimations by the phase difference algorithm. Pigs 3 and 5 show close fit between methods with few outliers in the reading, while Pigs 2 and 4 show a consistent under estimation in the phase difference method. Pig 4 shows a high variation in the foot-foot method, jumping between PWV values.

8.3.1 Noise Sensitivity

Table 8.1 shows the results of introducing pink noise (0 Hz to 500 Hz) to the raw aortic and femoral pulse data, increasing the SNR by 4 dB each step. The RMSE error in Table 8.1 is the difference between the foot-foot method results on the original signal and the response of the phase difference and foot-foot method at each SNR level. The phase difference method retains lower RMSE values at lower SNR values (higher noise).

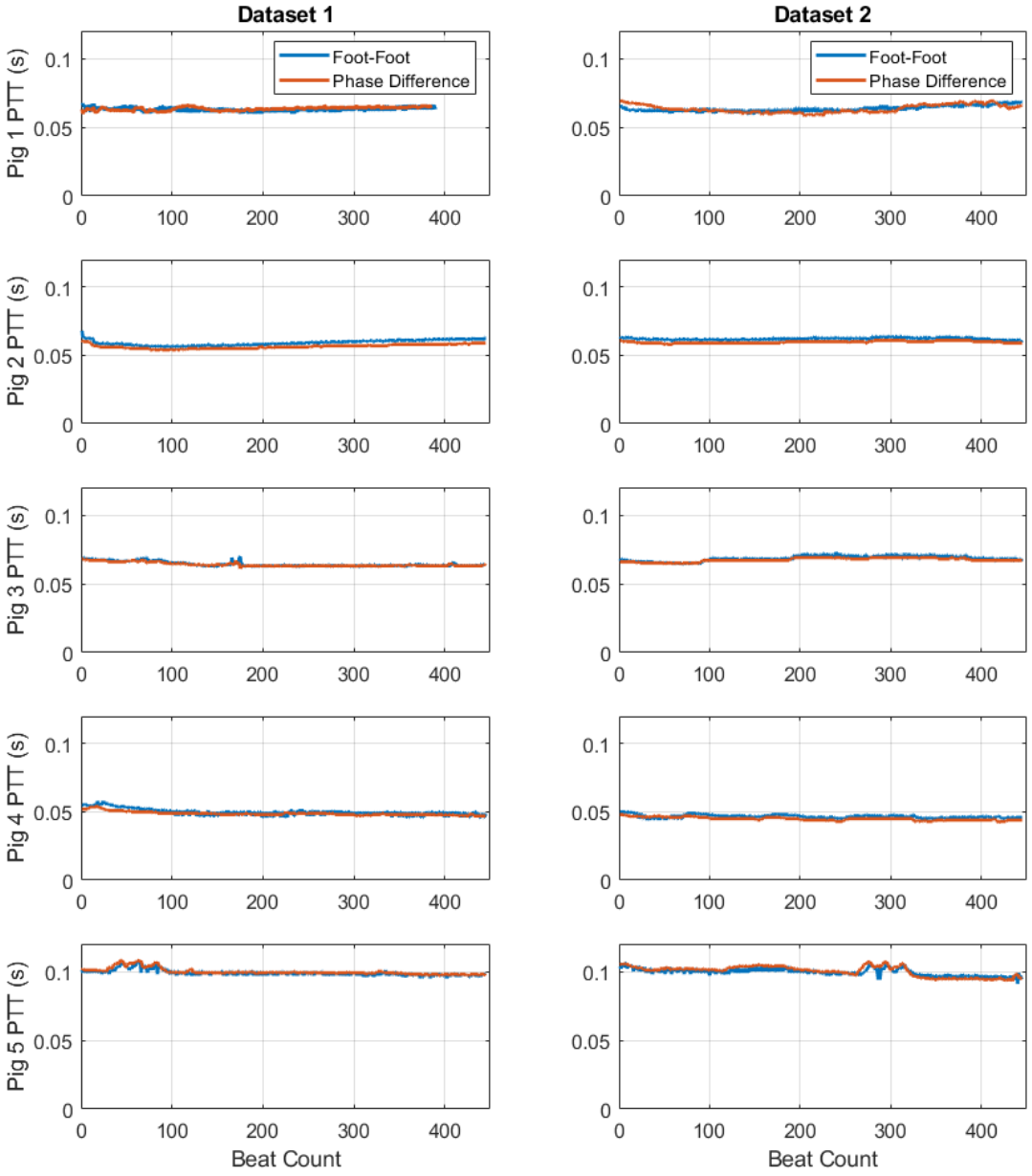

Figure 8.7 Calculated PTT values for the foot-foot method (blue), and the phase different method (orange). Results from the two data-sets from each of the five pigs is shown.

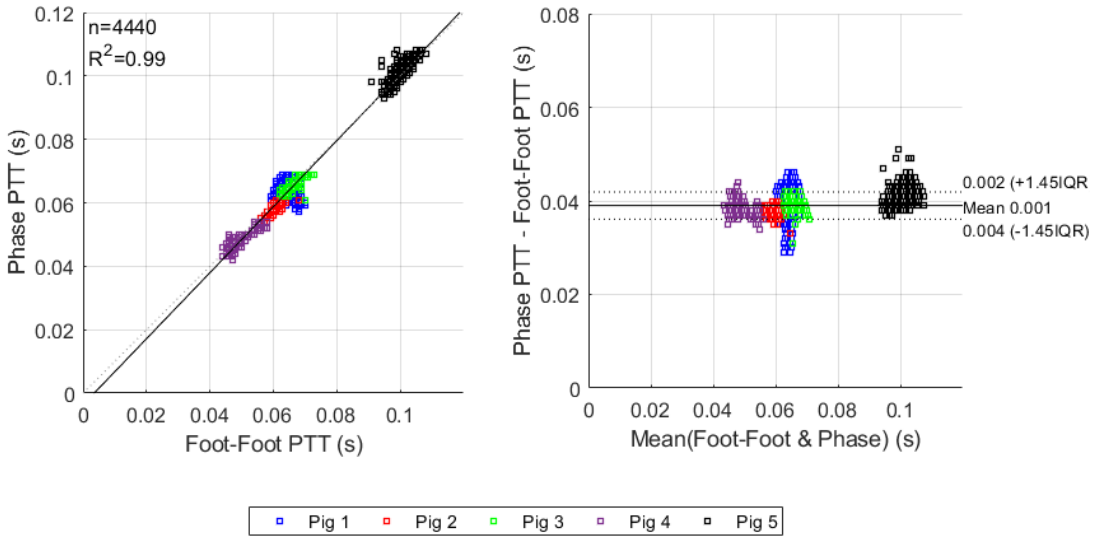

Figure 8.8 Correlation and Bland-Altman analysis: The correlation plot (left) shows the relationship between relative change in the phase difference method relative to the foot-foot method. The Bland-Altman plot (right) shows the agreements between the foot-foot and phase difference method for all pigs.

Table 8.1 The response of the foot-foot method and phase difference method to signals with increasing SNR. The RMSE error is the difference between the foot-foot method results on the original low noise signal, and the response of the phase difference and foot-foot method at each SNR level.

	Waveform SNR (dB)								
	4	8	12	16	20	24	28	32	36
Phase difference RMSE (ms)	23.7	20.7	14.0	7.8	3.5	2.8	2.5	2.4	2.4
Foot-Foot RMSE (ms)	54.2	34.4	17.4	9.0	4.7	3.4	2.4	2.3	2.2

8.4 DISCUSSION

The results from the phase difference method gave consistent results with the gold standard foot-foot method at a range of arterial pulse waveform shapes, and in the presence of increasing noise levels. Thus, the phase difference method is viable for use in calculating PTT.

The pig trials introduced various changes to the haemodynamic state [Ghuysen et al. 2008, Morimont et al. 2012], generating a wide range of aortic and femoral beat shapes as shown in Figure 8.5. Pulse 1 (Pig 1) has the aortic and femoral pulse sharing the same fundamental frequency and phase with only the feet of each waveform being different. As the phase method reconstructs the phase difference with the geometric mean of the two FFT magnitudes, the phase change at the foot is most prominent, allowing the method to track PTT closely. However, as shown in Figure 8.8, this pulse has the highest variation compared to the foot-foot method. Pulses 2 and 5 have poorly defined femoral feet waveforms, causing the foot-foot method to often track to the start or end of the flat section.

The phase method consistently tracked to the start of the poorly defined foot, causing a constant offset in estimated PTT. The aortic and femoral waveforms in pulses 3 and 4 have the highest shape variance, but the lowest error in PTT calculation, implying that the shape of the waveforms is not a large factor in PTT accuracy. Pulse 5 also shows a waveform shape with low PTT measurement error, confirming while there are only 5 pigs in this study, there is a wide variety of pulse waveform shapes to compare the foot-foot method to the phase difference method.

Figure 8.6 shows the results of the sensitivity analysis. A cut-off frequency of 15 Hz led to a high RMSE as the reconstructed phase difference waveform lacked high frequency components needed for accurate reconstruction and a cut-off frequency above 35 Hz was deemed unnecessary for retaining necessary frequency components. Thus, a cut-off frequency above 25 Hz gives satisfactory results (RMSE < 3 ms) at higher sample rates.

As expected, the RMSE increased with decimation rate, with sample rates decimated

to 250 Hz having minimal increases in error. This result shows the method will work with sensors operating at 250 Hz, or, sampling at 1 kHz with a 4x reduction in distance between measurement sites.

The buffer length for the phase difference method ranged from 0.5 s to 15 s in increments of 0.5 s. An increase in accuracy coincided with an increase in buffer length. However, a buffer length above 4 s gives minimal improvement and decreases sensitivity to beat to beat changes in PTT, as shown in the minimal changes in RMSE after 4 s in Figure 8.6 .

All analyses used a sample rate of 1 kHz, a cut-off frequency of 35 Hz and a buffer length of 5 beats. Integer beats were used to reduce spectral leakage in the FFTs, although Figure 8.6 shows that this has minimal effect. The correlation and Bland-Altman plot in Figure 8.8 show the high accuracy of the phase detection method (R^2) of 0.99. However, there is an offset of -1 ms (one sample at 1 kHz) shown in the Bland-Altman plot. This offset is likely due to the lower frequency harmonics of the waveforms having higher amplitudes than the higher frequencies responsible for the sharp edge forming the feet of the waveforms.

Table 8.1 shows the phase difference method is less sensitive to noise than the foot-foot method, as the phase difference method measures across multiple beats, using the whole waveform to estimate PTT. In contrast, the foot-foot method only takes a single point of the waveform, which is more susceptible to noise introduced errors. For the phase method, an SNR of 20 dB has an acceptable RMSE of 3.5 ms, while the foot-foot method requires an SNR of 24 dB to achieve the same RMSE.

As the phase difference method is capable of calculating PPT with different aortic and femoral pulse shapes, this method should also be applicable to PTTs measured locally to one artery. In this circumstance, the two waveforms are likely to have very similar shape with all FFT harmonics experiencing the same time delay.

8.5 SUMMARY

This chapter investigated the phase difference method for measurement of peripheral pulse transit time (PTT) between the aorta and femoral artery, identifying the PTT in differently shaped pulse waveforms. The phase difference method gave the same PTT results as the gold standard foot-foot method across a wide range of aortic and femoral pulse shapes obtained from haemodynamic interventions during a porcine trial, but had better immunity to noise.

The correlation between the two methods had an R^2 of 0.99 and a mean PTT difference of 1 ms (one sample at 1 kHz). Noise at varying SNR values of 4 dB to 36 dB was introduced to the system, with the phase difference method producing an RMSE of 3.5 ms at 20 dB, while the foot-foot method required an SNR of 24 dB to achieve the same result. Final parameters for the phase difference method uses a buffer size of 5 beats sampled at 1 kHz and a low-pass cut-off frequency of 35 Hz. Therefore, the phase difference method is a viable option to measure PTT for peripheral PWV calculation.

The minimum sample rate identified by the sensitivity analysis was 250 Hz at an estimated distance of 0.4 m between sites. Thus, for measuring the local PWV of an artery, such as the radial artery, at a distance of 40 mm, the minimum sample period would be 2.5 kHz. The sensor presented in Chapter 7 should be redesigned to run at 3 kHz with a spatial distance of 40 mm to ensure sufficient timing resolution.

Chapter 9

PULSE WAVE VELOCITY SENSOR VALIDATION

The phase difference method developed in Chapter 8 was shown to be accurate at calculating regional pulse wave velocity between the aorta and femoral artery in porcine data. However, for the method to work on PWV local to an artery, an improved sensor needed to be developed. This sensor combines the pulse wave velocity concept developed in Chapter 7 with the hardware developed in Chapter 4. As the previous PWV sensor array was not accurate enough, the SvO_2 sensor was adapted to measure PWV. Both the foot-foot and phase detection methods are used to analyse human data measured by the sensor.

9.1 INTRODUCTION

Pulse wave velocity measured locally in a single artery has the potential to provide novel, clinically useful cardiovascular health information currently requiring invasive methods [O'Rourke et al. 2002]. A non-invasive light-based sensor using reflectance PPG allows measurement on arteries such as the carotid and radial arteries, providing similar cardiovascular information to the aortic pulse waveform recorded invasively [Millasseau et al. 2003]. The sensor presented in Chapter 7 demonstrated the ability to measure the arterial pulse wave in the carotid artery. However, this sensor had several limitations, including the low sample rate, low emitter light intensity, and intermittent contact with the neck.

To obtain the high sample rate required to measure PTT along the radial artery, high-

fidelity 'pencil type' micro-manometers are traditionally used [Gurovich and Braith 2011]. Commercial devices using oscillographic techniques have been released to market, but are not yet accurate enough to be considered gold standards [Mahmud et al. 2009, Nemcsik et al. 2009].

Obeid et al developed a piezo-electric sensor to measure the pulse wave at the radial artery and finger tip, giving the radial-digit PWV [Obeid et al. 2021]. Results from this sensor were consistent with the commercial device, Compilor (Alam Medical, France), measuring at the same sites, giving an average radial PWV of $4.5 \pm 1.2\,\mathrm{m\,s^{-1}}$. However, the authors did not disclose the design of the sensor, or the sample rate.

This chapter builds on the initial proof of concept sensor from Chapter 7, replacing the 2D array of LEDs with three individual sensing LEDs at 20 mm intervals. This design approach has the potential downside of requiring accurate sensor placement. However, arterial pulse waveforms were able to be consistently detected across each of the 20 LEDs in each 1D lateral array of the previous design, so this change was expected to have minimal impact on outcomes. This chapter also compares the foot-foot method and phase difference methods for calculating PTT, using this sensor, as well as the impact and quality of sampling at 3 kHz.

9.2 METHODS

A trial was run to validate the performance of the improved PWV sensor. This trial measured the radial artery pulse at three site separated by 20 mm for analysis. Both the foot-foot and phase difference method are used to analyse the raw signals. The sensor used in this chapter combines an array of LEDs as presented in Chapter 7, but uses the Teensy 4.0 microprocessor used in Chapter 4 to achieve the 3 kHz sampling rate required to measure the PWV at the radial artery.

Figure 9.1 shows the position of the sensor along the radial artery. The sensor is placed over the radial artery with LED 1 proximal to the heart, as shown by the indicator pointing to the heart in Figure 9.2. This specific placement ensures that the pulse wave

first travels past LED 1, then LED 2, and finally LED 3. Analysis of this sensor will focus on the 40 mm spacing between LEDs 1 and 3 as this separation is expected to give the most accurate PWV measurement.

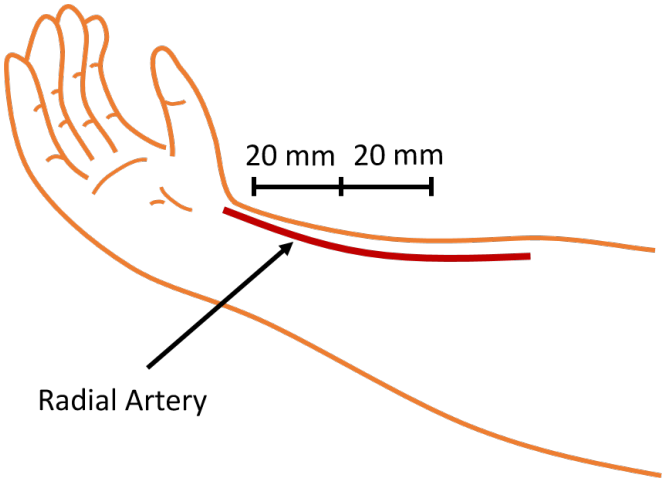

Figure 9.1 Approximate position of the pulse wave velocity sensor along the radial artery.

9.2.1 Subjects

The validate the local PWV sensor, a trial including four subjects was run. This trial uses radial pulse data recorded from 4 subjects. All subjects recruited were healthy individuals with no known cardiovascular health problems. The patient demographics are included in Table 9.1. This study was approved by the Human Ethics Committee, University of Canterbury (HEC2019/153) and informed consent was obtained from each participant prior to the experiment.

Table 9.1 Local PWV trial subject demographics. Data is shown in median [IQR] where appropriate.

Subjects	4
Age (years)	26[24-28]
Sex (M/F)	3/1
Ethnicity (Maori/ NZ European/ other)	3/1/0

Each subject was requested to be rested and seated at the time of measurement. The radial artery in the right arm was held level with the heart for measuring PWV, and the patient themselves applied the sensor for each test.

9.2.2 Equipment

The sensor designed to measure $SpvO_2$ in Chapter 4 was adapted to measure pulse wave velocity on the radial artery, with a sample rate of 3 kHz. Figure 9.2 shows the adapted sensor. The drive board of the $SpvO_2$ sensor is retained, with only the sense board changed to contain 3 sensing locations using the XZM2MRTNI55W-8 (SunLED [2017], USA) package of 660 nm and 940 nm LEDs.

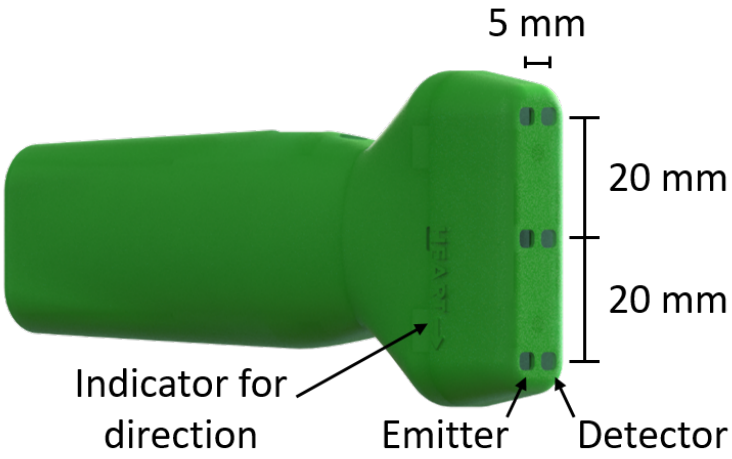

Figure 9.2 Pulse wave velocity sensor design for local PWV measurement on the radial artery. The arterial pulse is measured at 20 mm intervals along the radial artery.

Data was transmitted from the sensor via serial for recording on a PC with an Intel Core I7, 32 GB RAM running Windows 10. A graphical user interface was developed to plot the photoplethysmograph waveform measured along the radial artery, shown in Figure 9.3. Each of three coloured plots in the window represents one of the three 660 nm LED. A 20 Hz FIR lowpass filter was implemented to aid data visualisation. The subject number, notes, and site measured are entered into the window for data-logging. Once the data has been entered, the "Press To Save Info" button saves the subject details. The "Start" button is then pressed and the GUI displays and records 30 s of pulse waveforms.

If the subject moves, or the signal quality drops, the recording can be restarted with the "Restart Recording" button. Once the GUI has finished recording for 30 s, "Save and stop recording" saves the data to file.

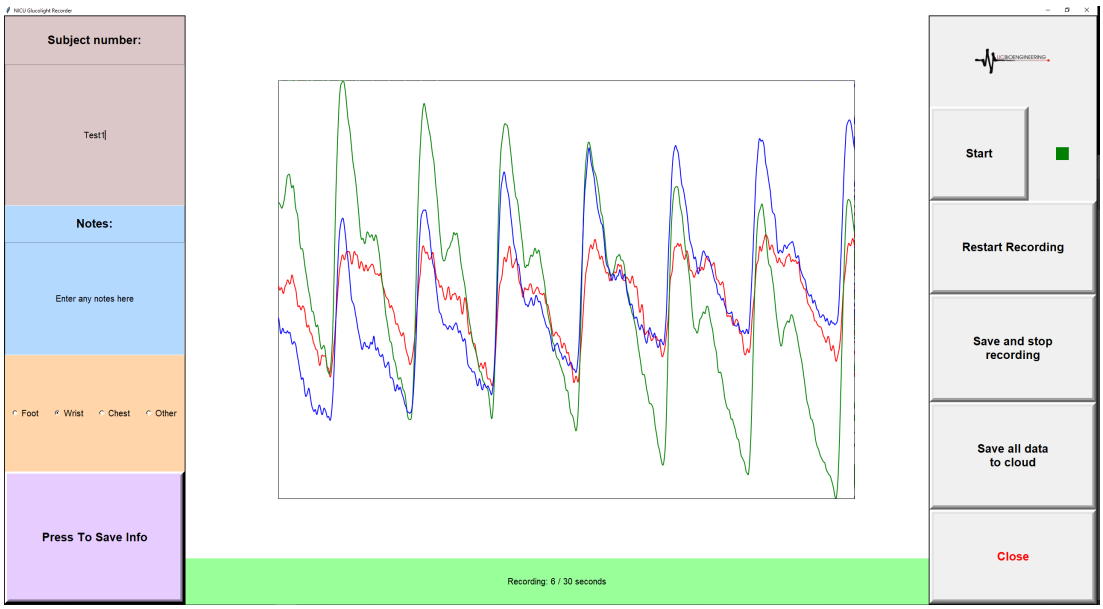

Figure 9.3 User interface developed to plot the three measured pulse waveforms along the radial artery.

Each sensing location is separated by 20 mm to measure the arterial pulse at 0, 20 and 40 mm. The distance between emitting and detecting LEDs is 5 mm. As in the PWV sensing array sensor presented in Chapter 7, only the 660 nm LEDs are used to measure the PWV. Each of the three sensing LEDs sample at the same time. This simultaneous sampling removes the delay included by sequentially sampling each LED present in the previous version of the sensor. The light emitted by each emitting LED is assumed to not interfere with the other sensing LEDs due to the 20 mm spacing.

As the required sensing LED discharge voltage discharge time is $<333\,\mu s$ (sample rate of 3 kHz), the emitting LEDs are run at the maximum 57 mA to provide maximum illumination. To reduce risk of eye light exposure from the bright emitters, the system use the skin detection feature described in Chapter 3 to avoid unnecessary light exposure.

9.2.3 Sensor output processing

Once pulsatile data was recorded at the radial artery for each of the four subjects, the foot-foot and phase difference methods were used to analyse the data. The foot-foot method used the shear transform detection method developed by Balmer et al. [2018a].

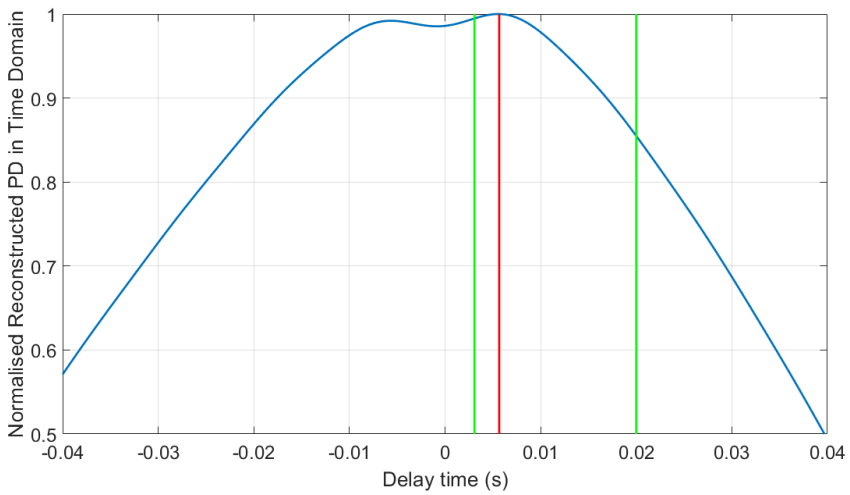

Figure 9.4 Normalised phase difference (PD) waveform reconstructed in the time domain with a filter cut-off frequency of 35 Hz and time series buffer length of 4 seconds. The time delay with the highest amplitude within the expected range is the pulse transit time (PTT). The green lines represent the physiological boundaries of the expected PTT, and the red line shows the estimated PTT.

The settings for the phase difference algorithm were first tested with the same settings used in Chapter 8. Specifically, a filter cut-off frequency of 35 Hz and a time series buffer size of four seconds. Once the signals have been converted to the frequency domain, and the phase difference calculated, the phase difference is then combined with the FFT magnitude spectrum of each signal to reconstruct a time domain waveform. The time the peak of this reconstructed waveform occurs is the PTT.

The cut-off frequency of 35 Hz was found to be too low, not producing a definite peak in the time domain reconstruction. This flat peak is shown in Figure 9.4, with the calculated time delay varying greatly within the physiological range, shown in green. Thus, the cut-off frequency and time series buffer length were increased to 75 Hz and 5 s respectively. While the new cut-off frequency was heuristically chosen, the settings were consistent across all measured data. The time domain reconstruction with these settings is shown in Figure 9.7.

9.2.4 Analysis

Pulse wave velocity was assessed in four subjects at the radial artery. The range of acceptable PWV values was limited to expected physiological range of $1.5\,\mathrm{m\,s^{-1}}$ to $15\,\mathrm{m\,s^{-1}}$. The performance of the foot-foot and phase difference method was analysed for their mean, CoV, and percentage of data outside of physiological range.

The required adjustment to the parameters of the phase difference method presented in Chapter 8 is also assessed, as the increase in sample rate and decrease in distance between measurement sites required new filter parameters.

9.3 RESULTS

Figure 9.5 plots an example set of three waveforms used to calculate PWV. A 0.67 Hz to 15 Hz IIR bandpass filter is applied to the data for visualisation. The arterial pulse waveforms for Subjects 1,3, and 4 are clearly visible for each of three sites measured. However, each of the three pulse waveforms for Subject 2 have poorly defined pulse features.

The foot of a single pulse in Subject 1's data-set is shown in Figure 9.6. This plot shows the raw data recorded by the sensor with the mean-centred lowpass filtered data overlayed. The foot of the filtered waveform is visible just before 0.05 s. However, the foot is unable to be located in the raw waveform due to the high noise floor.

The time domain reconstructed phase difference (PD) waveform for the first 5 seconds of Subject 4's arterial pulse waveform is shown in Figure 9.7. The reconstruction contains a peak at a delay of zero seconds in all reconstructions due to mains noise occurring in all pulse waveforms with zero phase difference. The second peak within the physiological PWV range of $1.5\,\mathrm{m\,s^{-1}}$ to $15\,\mathrm{m\,s^{-1}}$ is taken as the PTT for calculating PWV.

Figure 9.8 shows the calculated PWV by both the phase difference method and the foot-foot method at 40 mm separation. The bounds for acceptable PWV values were

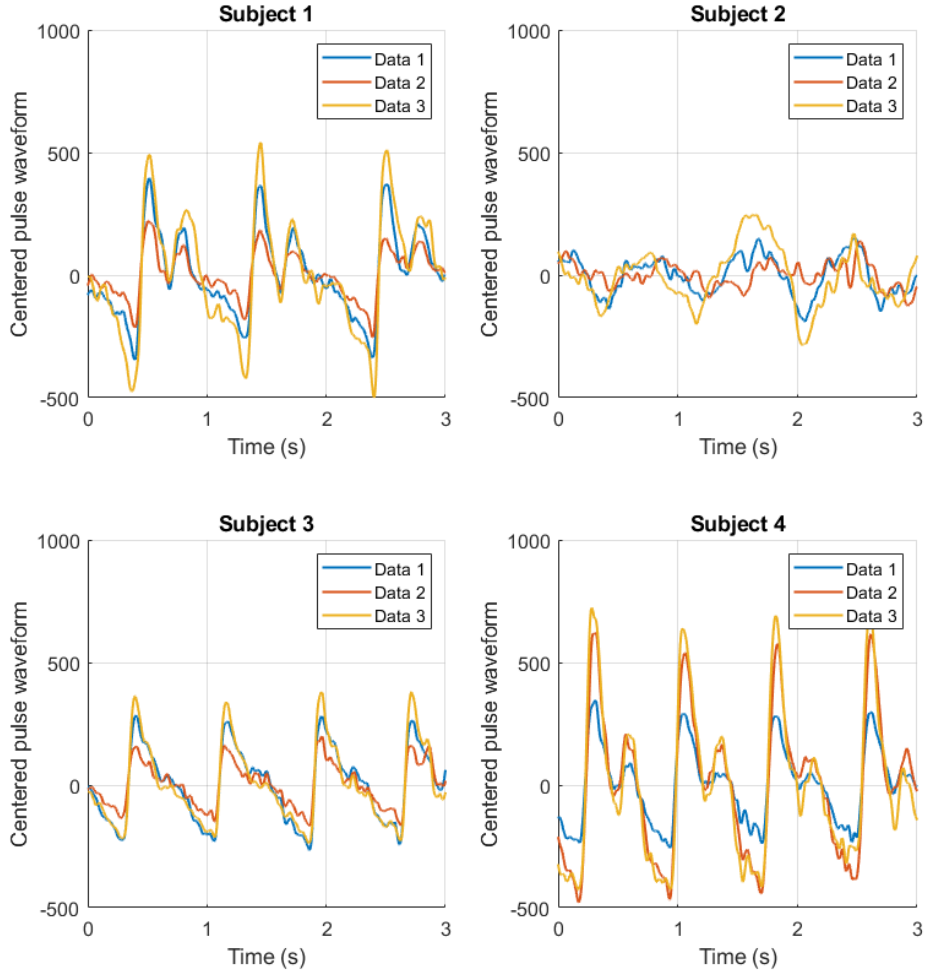

Figure 9.5 Example pulse waveform in the radial artery for each of the four subjects.

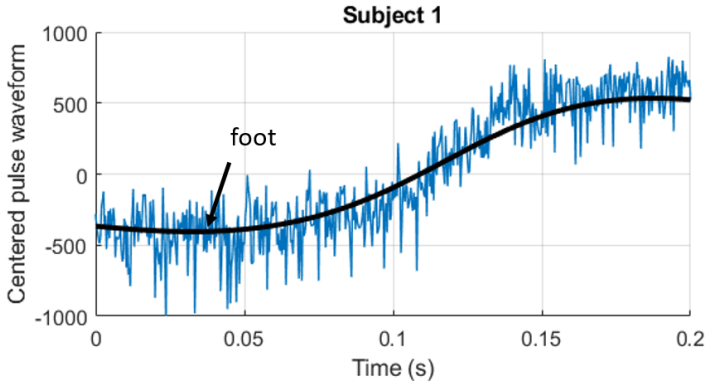

Figure 9.6 Single raw(blue) and filtered (black) pulse waveform in the radial artery for Subject 1. Note the flat shape of the foot just before systole.

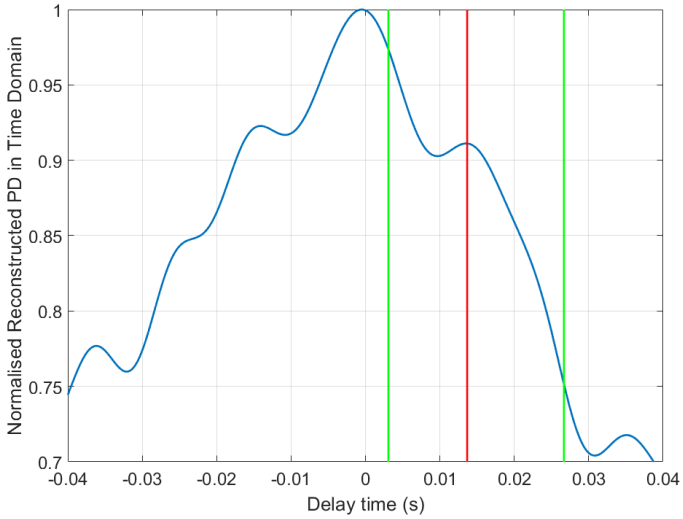

Figure 9.7 Normalised phase difference (PD) waveform reconstructed in the time domain. The time delay with the highest reconstructed phase difference within the expected range is the pulse transit time (PTT). The green lines represent the physiological boundaries of the expected PTT, and the red line shows the estimated PTT.

limited to between 1.5 m s^{-1} to 15 m s^{-1}.

The CoV for the foot-foot and phase difference methods are shown in Table 9.2. The foot-foot results were variable beat-to-beat, with a mean CoV of 13%, while the phase difference method had a lower CoV for each subject. For Subject 2, the foot-foot method was unable to track the feet of each waveform, giving a mean PWV of 2.2 m s^{-1}. The percentage of PWV calculations outside the expected PWV range is also given, with the foot-foot and phase difference methods calculating an average of 23.7% and 2.0% outside range. At the sensing distance of 40 mm, an error of one sample gives a relative PWV error of ± 0.1 m s^{-1}.

Table 9.2 Results of the foot-foot (F-F) and phase difference (PD) method for calculating PWV.

	Subject 1	Subject 2	Subject 3	Subject 4	Mean ±SD
F-F mean PWV (m s^{-1})	4.5	2.2	5.6	4.0	4.0 ±1.4
PD mean PWV (m s^{-1})	3.9	4.9	5.0	5.1	4.7 ±0.6
F-F CoV (%)	61	82	38	51	58.0 ±18.6
PD CoV (%)	37	3	22	18	20.0 ±14.0
F-F rejected data (%)	11	23	38	23	23.8 ±11.1
PD rejected data (%)	3	0	5	0	2.0 ±2.4

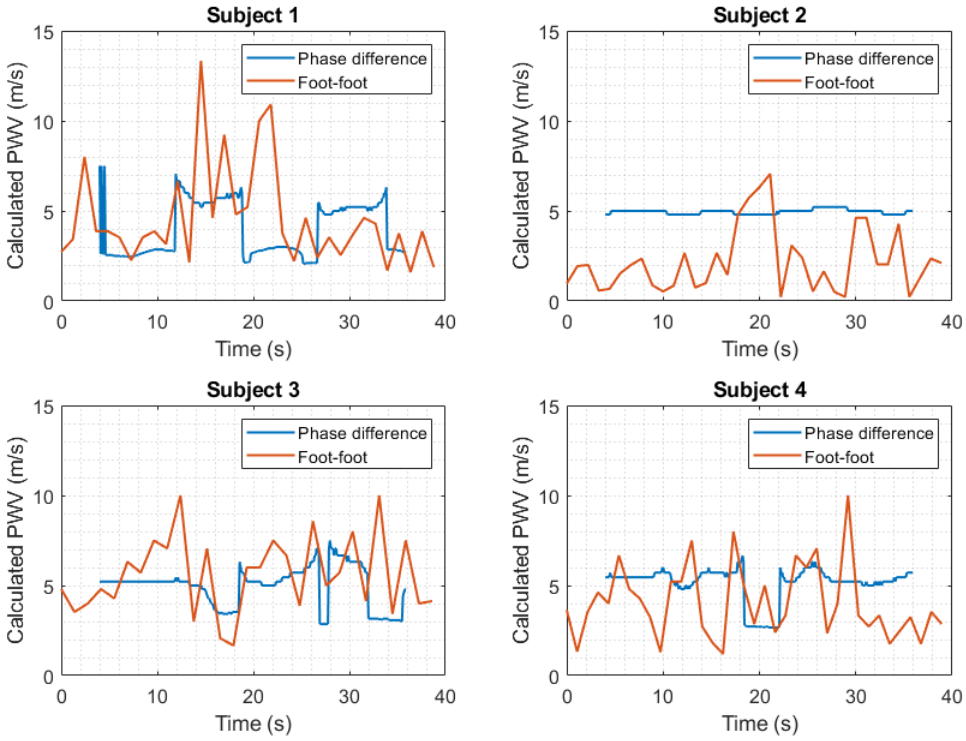

Figure 9.8 Calculated pulse wave velocity for each subject using the foot-foot and phase difference method.

9.4 DISCUSSION

The sensor developed in this chapter gave PWV results within the expected physiological range of 4.5 $\pm 1.2\,\mathrm{m\,s^{-1}}$ [Obeid et al. 2021]. The mean PWV calculated by the foot-foot method was 4.0 $\pm 1.4\,\mathrm{m\,s^{-1}}$. However this method had a high mean CoV for each subject (58%). The phase difference method returned a mean PWV calculation of 4.7 $\pm 0.6\,\mathrm{m\,s^{-1}}$, and a mean CoV of 20%. Thus, also with a much lower percentage of rejected data, the phase difference method gave better results than the foot-foot method when measuring local pulse wave velocity on the radial artery.

The main difficulty for the foot-foot method was identifying the position of the foot of each waveform. While the approximate foot of each arterial pulse waveform was simple to locate, determining the exact sample at which the foot occurred caused both the foot-foot and phase difference method to incorrectly measure PTT.

The signal from Subject 2 was difficult for identifying arterial pulse features and the foot-foot method failed to accuracy track PTT. However, as the shape of each waveform remained similar, the phase difference method retained consistent readings. This outcome shows the benefit of not relying on a single feature to track PTT, rather taking the waveform as a whole. Across each subject, the phase difference method had a lower CoV and had few calculations outside of physiological range. Thus, when measuring local PWV with noisy signals, the phase difference method produced more reliable results than the foot-foot method.

The cut-off frequency of the filter used to retain the arterial pulse harmonic frequencies required an increase of the cut-off frequency used in Chapter 8 (35 Hz), as the peak of the phase difference reconstruction was flattened, leading to varying PTT values. While the new cut-off frequency was heuristically chosen at 75 Hz, all recorded data was compared using the same settings. Further development of the method may further adjust filter settings to improve accuracy.

Increasing the filter cut-off frequency above 50 Hz introduced a peak centred at a PTT of zero seconds, and is suspected to be due to the 50 Hz mains noise present in the

signal. Only when the cut-off frequency increased above 75 Hz, did a second peak appear within the expected PTT range. The peak at zero remained, with the second peak varying in time for each of the subjects, This second peak was taken to be the calculated PTT, and could be readily filtered by an added algorithm. The second peak consistently appeared in all results, staying within the physiological bounds. It is likely that the peak centred at zero from the mains noise reconstructed with a FFT magnitude spike larger than the frequencies responsible for the actual PTT time domain peak.

A third peak would sometimes occur in the time domain reconstruction of the phase difference. At times this third peak would increase in amplitude above the second peak, and the algorithm would switch to this new peak as the PTT. This behaviour is evident in Figure 9.8, where the calculated PWV drops to $2\,\mathrm{m\,s^{-1}}$. The third peak is not always present in the reconstruction waveform, so was assumed to not be the actual calculated PTT.

The sensor was not validated against an invasive gold standard reference. However, the results are based on known pulse detection methods that have been validated against invasive methods. The calculated PWV is within the expected ranges, so the performance of the sensor is validated.

9.5 SUMMARY

This chapter developed a sensor to measure the local pulse wave velocity at the radial artery. The sensor, adapted from the designs in Chapters 4 and 7, measured across a 40 mm section of the radial artery at a sample rate of 3 kHz. The conventional foot-foot method of calculating the PWV gave unreliable results, with 13% of estimated PWV values outside the expected physiological range. The phase difference method gave more reliable results, with 2% of reading outside the physiological range. However, the phase difference method was sensitive to the filter cut-off frequency the method used, often jumping between PWV values.

The 3 kHz sampling rate was deemed sufficiently fast for calculating PTT across a

40 mm sensing distance. Thus, the use of PPG for measuring PWV local to an artery is a viable method.

Part IV

Non-invasive Estimation of Blood Glucose Concentration

Chapter 10

DESIGN OF A DISCRETE LED-LED SPECTROMETRIC GLUCOMETER

This chapter develops a discrete wavelength LED-LED spectrometric light-based sensor to measure in-vitro blood glucose concentrations. The sensor uses the LED-LED sensing method described in Chapter 3, with a total of six discrete wavelength LEDs used (660 nm, 850 nm, 940 nm, 1450 nm, 1550 nm, 1650 nm). Glucose concentration ranges of 0 $\mathrm{mmol\,l^{-1}}$ to 20 $\mathrm{mmol\,l^{-1}}$ in water and porcine blood are measured, via differential absorption of these wavelengths.

10.1 INTRODUCTION

Type 1 Diabetes is a metabolic disorder resulting from the inability of the body to regulate the concentration of glucose in the blood. The prevalence of diabetes worldwide is ever-increasing, with over 9.4% of the world population expected to be diagnosed with either Type 1 or Type 2 diabetes by 2030 [Ampofo and Boateng 2020]. Countries in Oceania have the highest age-standardised incidence rate (ASIR) [Liu et al. 2020]. Currently, individuals with diabetes need to use invasive methods, such as finger pricks, or continuous glucose monitors (CGM), to monitor blood glucose concentration. The discomfort and possible complications caused by these methods lead to reduced frequency of monitoring by patients, reducing the effectiveness of diabetes prevention [Chowdhury et al. 2013].

An alternative to the finger stick glucometer is a minimally invasive continuous glucose

monitor (CGM). The majority of CGMs require subcutaneous insertion of a filament for electro-chemical measurement of local interstitial glucose concentrations and require multiple calibrations each day. They are complex and have significant drift and dynamics [Zhou et al. 2018]. Futures in healthcare rely as much on enabling patient self-management as on new innovative technologies. A non-invasive glucose sensing method would facilitate more patient monitoring, reducing complications and improving quality of life.

Similar to pulse oximetry, other components in blood can be analysed using NIR spectroscopy. Wavelengths of light other than the traditional 660 nm and 940 nm are used to identify spectral fingerprints of components in blood. Continuous non-invasive glucose sensing has been a topic of research for over 20 years [Liu et al. 2005], including techniques such as near-infrared (NIR) spectroscopy, but as yet, there have been no commercialised products providing a solution. Products using NIR measurements have reported good correlation with blood glucose, but none were clinically acceptable [Nybacka 2016, Poddar et al. 2008, Smith 2017]. This chapter builds on the NIR spectroscopy background provided in Chapter 2 with the discrete wavelengths used in this project, and their rationale.

The main difficulty in non-invasive NIR detection is the weak absorption characteristics of glucose occurs in a spectral region dominated by absorption from water, haemoglobin and lipids [Amerov et al. 2004]. Conventional spectroscopy has been investigated through the wavelength range of 500 nm to 2000 nm with three main bands of interest: 2000 nm-2500 nm (combination overtone), 1400 nm-2000 nm(first overtone) and 750 nm-1400 nm (second overtone) [Yadav et al. 2015]. Yamakoshi and Yamakoshi [2006] developed a pulse glucometer using spectrometry from 900 nm to 1700 nm wavelengths. Through PLS methods, they gained accurate results from glucose measurement, but required further work on their instrumentation to take the sensor out of the laboratory [Yamakoshi et al. 2009].

Haxha et al used a 940 nm LED to monitor changes in glucose concentration [Haxha and Jhoja 2016]. In this region, haemoglobin is the dominant absorber, so any changes

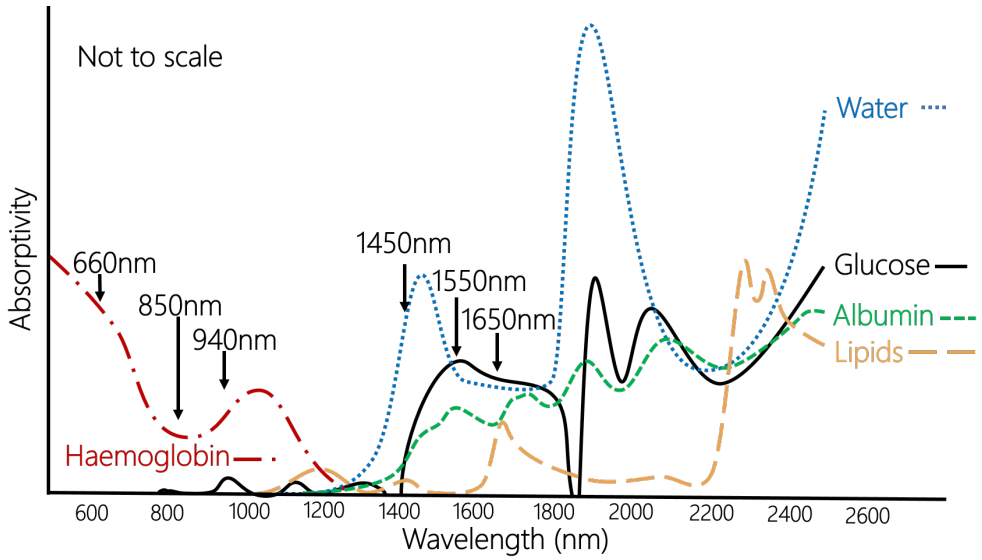

Figure 10.1 Absorption spectrum of the major light absorbers in the NIR range, not to scale. Derived from [Amerov et al. 2004, Yadav et al. 2015]

in blood oxygen concentration will skew the results [Bashkatov et al. 2005]. An LED emitting around 850 nm was used by Chan et al to isolate the isosbestic point of oxyhaemoglobin and de-oxyhaemoglobin at 800 nm [Chan et al. 2013]. At the isosbestic point, the absorption by oxyhaemoglobin and de-oxyhaemoglobin is equal, regardless of the oxygen saturation.

In the second absorption band, glucose has dominant absorption peaks at 1550 nm and 1650 nm [Jain et al. 2019]. Figure 10.1 shows the approximate absorption by glucose, water, lipids and albumin from 500 nm to 2000 nm, adapted from the coefficients identified in table 10.1. At 1450 nm absorption is dominated by water, meaning variations in concentrations of glucose and other blood constituents cause a minimal change in absorption at this wavelength. At 1550 nm and 1650 nm, glucose is the dominant absorber, so a rise in glucose concentration is expected to increase absorption at these wavelengths.

Table 10.1 gives the absorption coefficients of the 5 blood components of interest at each of the 6 wavelengths. The absorption and scattering coefficients of skin, as well as the depth of penetration into the tissue is also given. The light penetration depth does not take into account the entire optical path-length of each wavelength as it depends

on the LED emitter-detector spacing.

10.1.1 Beer-Lambert's Law

Beer Lambert's law describes the exponential attenuation of light travelling through a medium. The attenuation of light along a path length (d) results from the concentration of the solution (c) and how much light it absorbs (ϵ) [Mendelson 1992], yielding:

$$I_D = I_E e^{\epsilon c d} \tag{10.1}$$

Where,

I_D: Detected light intensity

I_E: Emitted light intensity

ϵ: Absorption coefficients

c: Concentration of molecules

d: Optical path length

This chapter develops an LED-LED based discrete reflectance glucometer to measure glucose concentration. Testing varying glucose concentrations in water and porcine blood provides a method for proof-of-concept testing, as the concentrations of glucose and other constituents can be controlled or known. Six different wavelength LEDs are utilised to isolate the spectral fingerprint of glucose from solution. Literature has investigated wavelengths at, or similar to the six developed here. However, none have used the digital LED-LED method of light detection, nor investigated both the first and second absorption band using these LED wavelengths.

Table 10.1 Optical properties of five main components in blood (water, glucose, albumin, lipids, haemoglobin) as well as tissue absorption and light penetration depth at 660 nm, 850 nm, 940 nm, 1450 nm,1550 nm, 1650 nm from literature

	Water (cm^{-1})					
	660nm	850nm	940nm	1450nm	1550nm	1650nm
Cao et al. [2013]	-	0.01	3	100	-	-
Altshuler et al. [2006]	-	0.05	0.5	40	20	6
Kraitl et al. [2005]	-	-	0.3	35	15	6
Kohl et al. [1995]	0.003	0.04	0.3	-	-	-
Amerov et al. [2004]	-	0.005	0.25	23.0	8.0	4.5
Maruo et al. [2006b]	-	-	-	29.0	10.0	5.0

	Glucose (cm^{-1})					
	660nm	850nm	940nm	1450nm	1550nm	1650nm
Kohl et al. [1995]	0.001	0.0015	0.002	-	-	-
Amerov et al. [2004]	-	-	-	-	5.06	7.19
Maruo et al. [2006b]	-	-	-	3.0	13.0	11.0

	Albumin (cm^{-1})					
	660nm	850nm	940nm	1450nm	1550nm	1650nm
Cao et al. [2013]	-	0.2	0.5	2.0	-	-
Maruo et al. [2006b]	-	-	-	4.0	7.0	5.0

	Lipids (cm^{-1})					
	660nm	850nm	940nm	1450nm	1550nm	1650nm
Cao et al. [2013]	-	0.06	0.03	0.5	-	-
Altshuler et al. [2006]	-	0.03	0.02	0.6	0.16	0.2
van Veen et al. [2004]	0.04	0.06	0.85	-	-	-
Maruo et al. [2006b]	-	-	-	2.0	1.0	1.0

	Haemoglobin (cm^{-1})					
	660nm	850nm	940nm	1450nm	1550nm	1650nm
Cao et al. [2013]	17	17	10	-	-	-
Scott Prahl [1998]	17.4	5.7	6.5	-	-	-

	Skin (Absorption plus Scattering) (cm^{-1})					
	660nm	850nm	940nm	1450nm	1550nm	1650nm
Wilson et al. [2015]	-	15	16	15	15	15
Bashkatov et al. [2005]	23.4	18.8	17.7	15.1	14.8	14.6

	Light penetration depth (mm)					
	660nm	850nm	940nm	1450nm	1550nm	1650nm
Ritz et al. [2001]	3.6	6.0	4.5	0.6	0.8	1.6
Bashkatov et al. [2005]	1.75	2.5	3	0.2	0.4	0.8

10.2 METHODS

To measure absorption of light at the various wavelengths, a sensor with 6 pairs of emitting and detecting LEDs was built. The digital LED-LED light detection method presented in Chapter 3 was used. The sensor was designed in a rosette shape to ensure the light path of each wavelength travelled through the same space, and is shown in Figure 10.2.

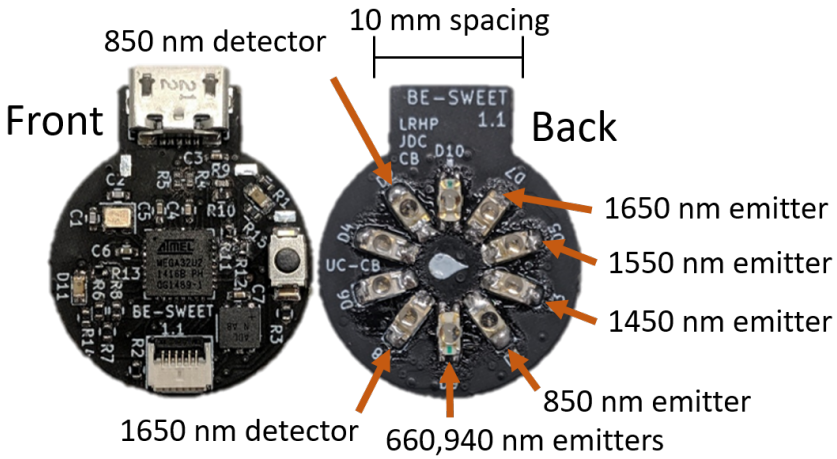

Figure 10.2 Diagram of the glucose sensor developed in this work. Each of the 6 wavelength has a dedicated sensing and emitting LED placed across from each other.

This chapter analyses the response of the sensor to glucose concentrations in-vitro. Glucose was added to solutions, exposing the sensor to a glucose concentration ranging from $0\,\mathrm{mmol\,l^{-1}}$ to $20\,\mathrm{mmol\,l^{-1}}$. Two different tests to detect changes in light absorption were conducted: adding glucose to de-ionised water; and fresh porcine blood. The target physiological range of blood glucose in a person is between $4\,\mathrm{mmol\,l^{-1}}$ to $8\,\mathrm{mmol\,l^{-1}}$. While blood glucose concentrations may climb above $20\,\mathrm{mmol\,l^{-1}}$ in hyperglycaemic patients, the range from $0\,\mathrm{mmol\,l^{-1}}$ to $20\,\mathrm{mmol\,l^{-1}}$ provides a physiologically relevant range to show a response to glucose.

10.2.1 Materials

The first sensor test used 40 litres of de-ionised water at $37\,^{\circ}\mathrm{C}$ inside an insulated container to minimise the effect of outside variables during testing. The container used

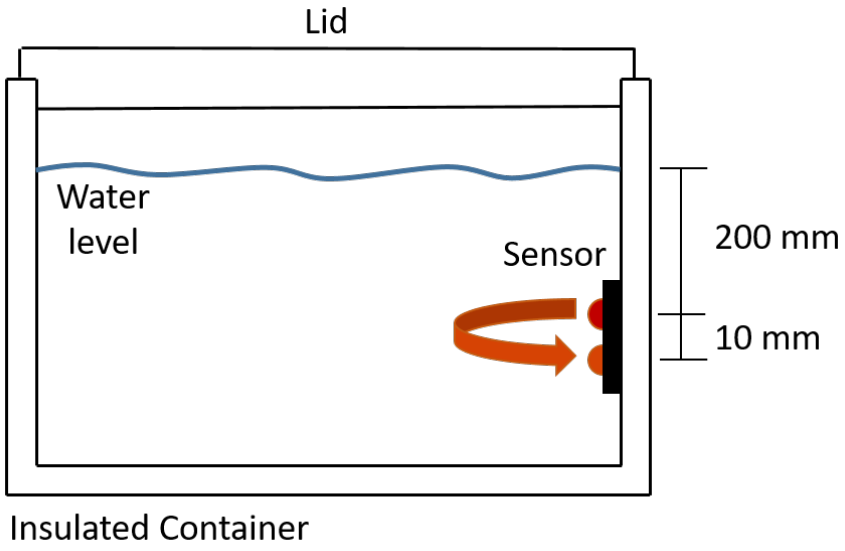

Figure 10.3 Experimental setup for water testing.

a lid to block ambient light from reaching the sensor, which was placed in a plastic housing 200 mm below the surface of the water, as shown in Figure 10.3.

The second test used two litres of pigs blood, with 1.8 g of EDTA per 1 l of pig blood added as an anticoagulant. The fresh pig blood was obtained from a local supplier not more than one hour after slaughter, and kept in an insulated container between 0 °C to 4 °C during transport and storage. The blood was partitioned into two portions for testing, 1.1 litre, and 0.9 litre. Testing of the 1.1 litre portion occurred three hours after obtaining the blood, and the 0.9 litre portion test occurred 48 hours later. The second test was conducted two days after the first to further reduce the blood glucose content as glucose continues to be consumed by the on-going metabolism of cellular constituents in blood [Nwosu and Nwani 2009]. The temperature of the blood remained between 2 °C to 8 °C during the waiting period and was brought to room temperature for testing.

An ACCU-CHEK Performa Glucometer was used to measure the blood glucose concentration throughout the sensor calibration test. Table 10.2 gives the test conditions and Figure 10.4 shows the setup for both tests. The sensor was mounted underneath the flask, in contact with the glass.

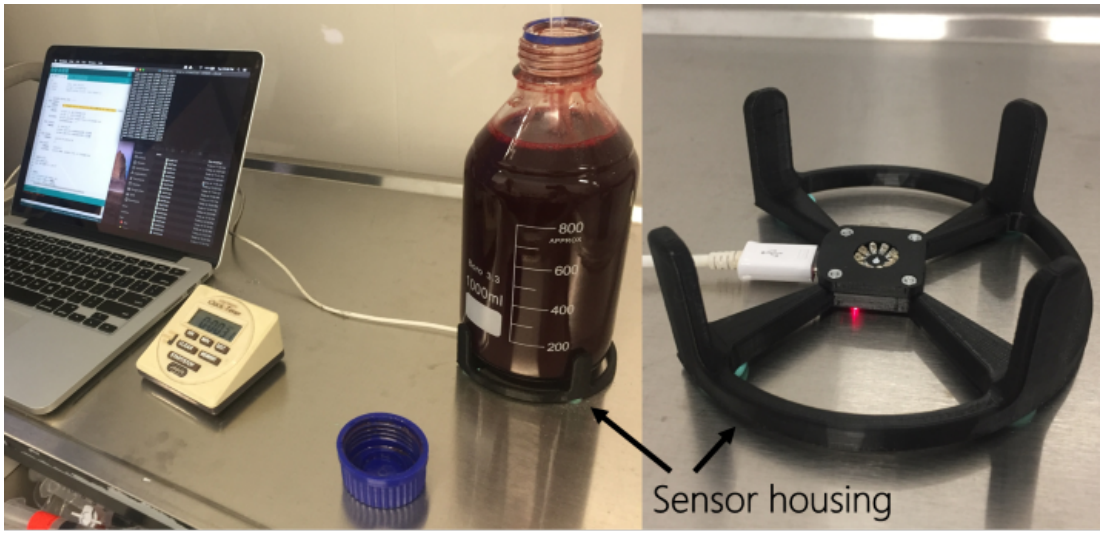

Figure 10.4 Experimental setup for pig blood testing.

Table 10.2 Experimental setup for testing the response of the senor to a range of glucose concentrations.

Test	Volume (l)	G_{start} ($mmol\,l^{-1}$)	G_{step} ($mmol\,l^{-1}$)	G_{end} $mmol\,l^{-1}$
Water	40.20	0	0.50	20.0
Blood 1	1.10	4.9	0.50	16.8
Blood 2	0.94	4.3	0.50	20.6

10.2.2 Procedures

Glucose was added to the 40 l of water in increments of 3.60 g to increase the concentration by $0.5\,mmol\,l^{-1}$ at each step. The concentration was increased from $0\,mmol\,l^{-1}$ up to $20\,mmol\,l^{-1}$.

Upon each addition of glucose, the water was stirred for 20 seconds and allowed to come to rest. Data was recorded over 30 seconds and the average LED voltage decay time was used for analysis. Each set of recording was conducted in a dark room with no light source other than the sensor.

The next step in testing the sensor's response to glucose was to add glucose to blood under the same conditions as the test in water. The first test with the pigs blood was conducted within 3 hours of obtaining the fresh blood with a volume of 1.1 litre and an initial blood glucose concentration of $4.9\,mmol\,l^{-1}$. The second test using the pigs blood was conducted 48 hours after the first, with a volume of 0.94 litre.

For the first and second test, 0.09 g and 0.08 g respectively of glucose powder was stirred into the blood for 30 seconds and allowed to settle. One minute of data was recorded and the average LED voltage decay time used for analysis.

10.2.3 Equipment

The LEDs used in the sensor were 660, 940 nm [SunLED 2017], 850 nm [Würth Electronic 2021], 1450 nm [Marktech 2018], 1550 nm [Marktech 2017a] and 1650 nm [Marktech 2017b]. The 660 nm and 940 nm LEDs are contained in the same package to minimise the footprint. Each emitting and detecting pair of LEDs are separated by 10 mm, with the path-length of all LEDs crossing at the centre of the rosette, as shown in Figure 10.2.

LEDs of wavelengths 660 nm, 850 nm and 940 nm were implemented to take advantage of the light absorption bands of glucose at 750 nm-1400 nm. The 1450 nm LED was chosen due to the peak absorption by water at this wavelength. LEDs at 1550 nm and 1650 nm were chosen as the absorption of lipids differ greatly between them, potentially allowing extraction of the lipid concentration and discrimination between lipids and glucose. Extracting lipids concentrations is also clinically useful.

An ATMEGA32U2 running at 16 MHz powers the emitting LEDs and also times the discharge of the reverse-biased sensing LED. Each wavelength LED was sampled sequentially to ensure no influence from other emitting wavelengths. The total sample rate of the sensor was 24 Hz to allow time for the LED voltage of the higher wavelength LEDs to decay to logic LOW on the microcontroller pin. Table 10.3 gives the power output, forward current and forward voltage of each LED. Due to the current source limit of the ATMEGA32U2 GPIO pins, the drive current of each LED was limited to 20 mA. At a forward current of 20 mA, the 660 nm LED has the highest radiant flux (8.3 mW) and the 1450 nm to 1650 nm LEDs have the lowest (0.8 mW).

Table 10.3 Electrical and optical characteristics of each LED wavelength tested.

	Wavelength (nm)					
	660	850	940	1450	1550	1650
Nominal I_f (mA)	20	20	20	50	50	50
$V_{forward}$ (V)	2.1	1.4	1.2	1.3	1.05	0.75
Radiant Flux (mW) (I_f =20 mA)	8.3	1.0	1.3	0.8	0.8	0.8
Radiant Intensity (mW m^{-2}) (I_f =20 mA)	21.3	2.5	3.3	2.0	2.0	2.0

10.2.4 Sensor output processing

The sensor returns the decay time of each of the six reverse biased LEDs using the digital LED-LED light detection method. Thus, all data presented in this chapter is a function of LED voltage discharge time. Data recorded for 30 seconds at each glucose concentration was averaged, and the mean used for analysis.

The displacement of water by glucose must be accounted for (displacement factor of 6.24) when calculating the absorption of light due to glucose [Amerov et al. 2004]. The relatively strong absorption properties of water in the NIR spectrum causes significant changes in total absorbance when glucose is added. Upon dissolution of glucose, water molecules are displaced from the optical path length. At wavelengths where water dominates absorption (1450 nm), the total absorbance is expected to drop with increasing glucose. At 1550 nm and 1650 nm, glucose is the dominant absorber of light, so even with displacement of water, the absorbance is expected to increase with glucose concentration. The combinations of these wavelengths and their differences in absorption of different primary elements of pulsatile blood allow better discrimination of these elements.

When calculating SpO_2, the units of light intensity is not needed as the detected light, I_D is normalised by the emitted light intensity, I_E, making the relative light absorption unitless. Thus, as the intensity units are not needed, the reflected light returning to the sensing LEDs in this chapter is represented by the LED voltage decay time.

10.2.5 Analysis

For both the water and porcine blood tests, the absorption of each wavelength of light by glucose was calculated. The range of glucose values will be plotted to analyse the change in absorption at each wavelength.

Compared to 1450 nm, the reflected light intensity at 1550 nm should increase with the addition of glucose. Thus, the ratio of 1450 nm and 1550 nm should increase, following the Beer-Lambert model. Absorption by 1650 nm is also expected to increase with glucose, but not as much as 1550 nm. Therefore, the ratios are plotted against a known glucose concentration.

The three main wavelength relationships of interest were between 1450 nm and 1550 nm, 1550 nm and 1560 nm and 940 nm and 850 nm. At 1450 nm and 1550 nm is the greatest difference between glucose absorbance coefficients and at 940 nm and 850 nm is the isosbestic point of haemoglobin and a limited absorbance by glucose. At 1650 nm and 1550 nm, there is a difference in absorption by albumin and lipids, as well as glucose.

For analysis of the wavelength ratios against changing glucose concentrations, the ratio responses were normalised. First, each ratio's response was divided by the maximum value to scale from 0-1. Next, the minimum value of each ratio was subtracted to centre the plot on zero.

10.3 RESULTS

10.3.1 Water Testing

Testing showed the predicted relationship between glucose levels and light absorption. Increases in absorption at 940 nm, 1550 nm and 1650 nm were recorded, while at 660 nm and 850 nm, a decrease in absorption was observed. Figure 10.5 plots the discharge time of each wavelength at increasing glucose levels. At 1450 nm and 850 nm, the data was very noisy with small upwards and downwards trends respectively over the range

of glucose. At 660 nm there was a slight decrease and at 940 nm, an increase. This increase is due to the slight absorption peak at 940 nm.

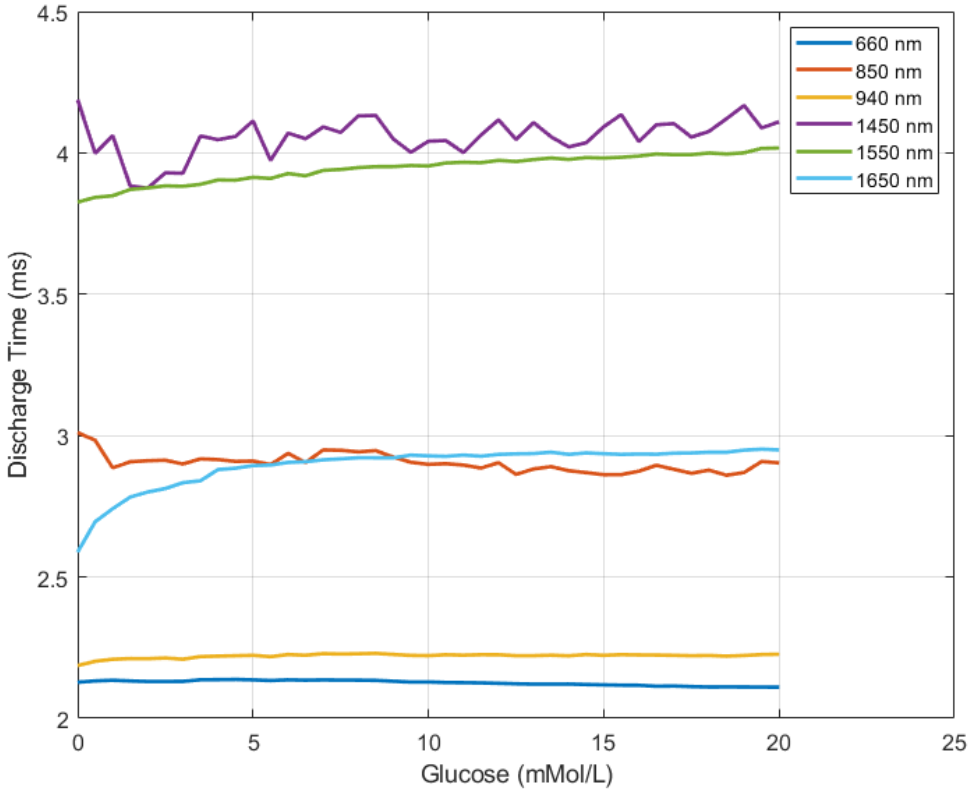

Figure 10.5 Change in LED discharge time in water with an increase in glucose concentration.

10.3.2 Porcine Blood Testing

Testing in blood gave different absorptions, compared to the water testing. Figure 10.6 shows at 1450 nm and 1650 nm there was decreased absorption with increasing glucose. This difference is represented in the change in absorption at 850 nm, as this wavelength represents the total haemoglobin count. Absorption at 1450 nm, 660 nm, 940 nm and 1650 nm were consistent between the two porcine blood tests.

10.3.3 Wavelength Ratios

In Figure 10.6, the noise variation in readings are present in all wavelengths. Taking the ratio of each wavelength pair removes the constant noise component during each

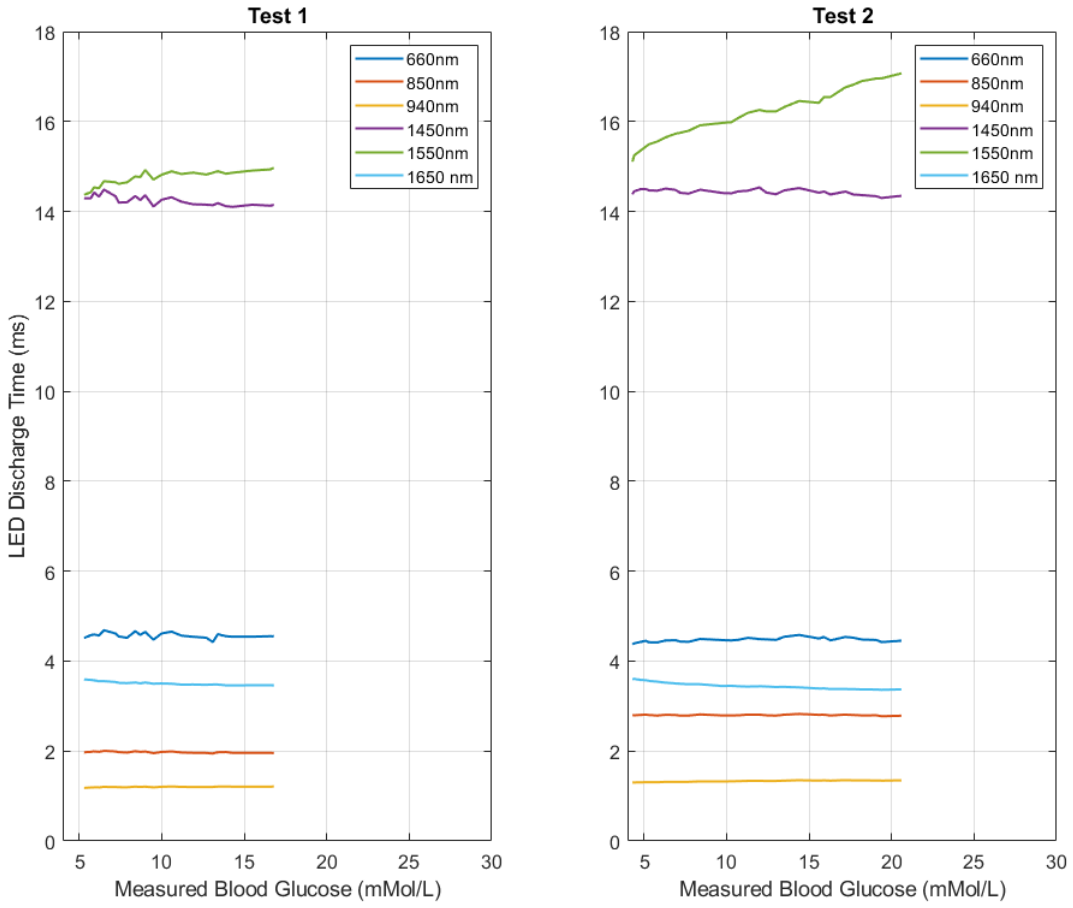

Figure 10.6 Change in LED discharge time in pigs blood with an increase in glucose concentration. A longer LED discharge time implies a higher amount of light absorption.

measurement such as ambient lighting.

Figure 10.7 plots each of the wavelength ratios against the measured glucose. Each response is normalised and centred at zero. The absorbance at 1650 nm has the largest decrease, so the ratio of 1550 nm to 1650 nm was also calculated ($R_{1550/1650}$). This ratio gives the greatest response to the normalised data, with $R_{1550/1450}$ second greatest. Ratio $R_{940/850}$ gives the lowest response to increasing glucose.

10.4 DISCUSSION

The sensor developed in this chapter showed a clear change in light absorption with increasing glucose values. Each wavelength tested increased, or decreased the amount

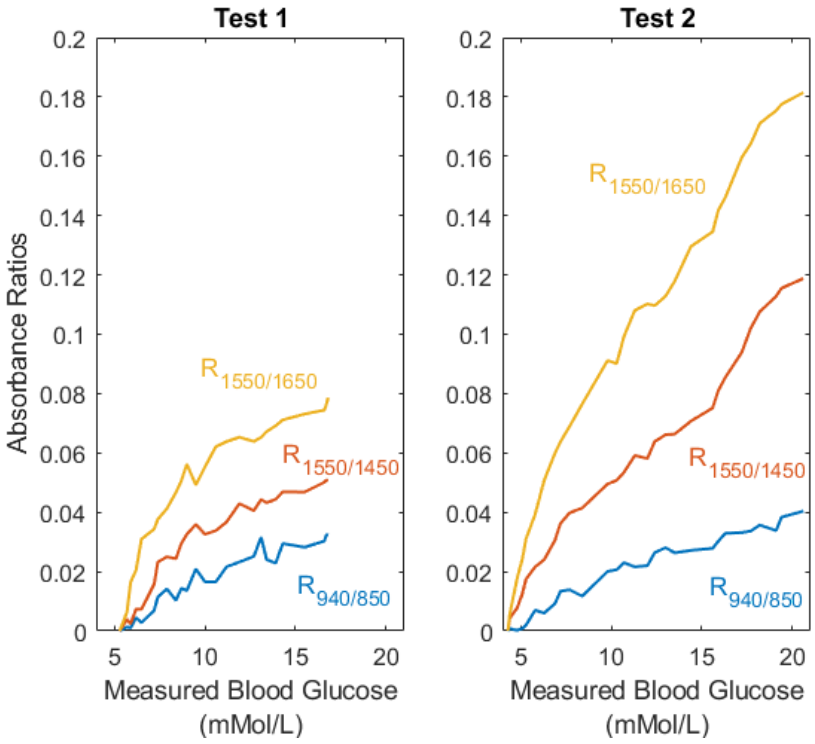

Figure 10.7 Normalised and centred absorbance ratios of $R_{1550/1650}$, $R_{1550/1450}$ and $R_{940/850}$ in pigs blood over an increasing glucose level.

of returned light in line with the absorption spectrum displayed in Figure 10.1. The ratio of $R_{1550/1650}$ gave the biggest change with glucose concentration, with a rapid change in absorption at lower blood glucose concentrations ($<10\,\mathrm{mmol\,l^{-1}}$), then a flattening off at higher concentrations ($>10\,\mathrm{mmol\,l^{-1}}$).

The 850 nm to 1650 nm LEDs returned a change in absorption due to glucose, and are recommended for further development. The 660 nm LED showed minimal change, but as the 660 nm and 940 nm LEDs are included in the same package, there is no point removing the LED from the circuit.

In water, the change in absorbance was solely due to the increase in glucose concentration and the displacement of water molecules. At 1650 nm and 1550 nm, the signal gave the greatest rise in absorption. The response at 1450 nm was expected to reduce due to the displacement of water. However, it remained noisy, slightly increasing with glucose level. This high variation is likely due to the minimal effect of water displacement due to glucose. The high absorption of light by water at 1450 nm means minimal

light entering the solution returned to the sensor.

The intensity of reflected light was much higher for 660 nm and 940 nm, as water and glucose absorb minimally at these wavelengths. Absorption of 660 nm and 940 nm light in the pig blood were much higher due to the presence of haemoglobin. It is also expected the glass of the flask reduced the amount of reflected light reaching the sensor as the LED discharge times for an empty flask were very similar to those with blood present for these wavelengths. The exact absorption by the glass is not further explored as the purpose of this test is to measure a change in absorption with increasing glucose concentrations, so a constant effect from glass does not affect the conclusions.

Testing in porcine blood yielded different absorption responses to testing in water. The presence of haemoglobin reduced the intensity of reflected light in the first absorption band and the presence of other lipids and albumin in the blood resulted in an opposite response to water at 1650 nm. At 1650 nm, glucose, water, albumin and lipids have similar absorption coefficients. As glucose displaces the other molecules from the optical path, the corresponding increase in absorption by glucose does not account for the reduced absorption by displacement of water and other components. Thus, the absorption in blood at 1650 nm decreases with increasing glucose levels. In contrast, the increased absorption from glucose at 1550 nm is more than the reduction in absorption from displacement, so the overall absorption at 1550 nm increases with increasing glucose concentration.

Ratios of absorbance at various wavelengths were calculated to test the response to glucose. The wavelength 1450 nm was chosen for testing as water is the primary absorber (Figure 10.1). By comparing the increasing absorbance at 1550 nm to the decreasing absorption at 1450 nm, the effect of glucose concentration can be seen. Water has minimal absorption in the first absorption band, so the ratio between 940 nm and 850 nm shows the relationship between glucose and haemoglobin. At the isosbestic point of haemoglobin (850 nm) the decrease in absorption is due to the displacement of haemoglobin and at 940 nm, the increase in absorption is from the increased absorption of glucose. This behaviour can also be seen at 660 nm as absorbance decreases with

increasing glucose. The ratio of 1650 nm to 1550 nm gave the largest change with increasing glucose in blood. Other than 1650 nm, all other wavelength absorptions were as expected.

This sensor design used emitting and detecting LEDs spaced by 10 mm. This large spacing resulted in long LED voltage discharge times of almost 20 ms per LED. As each of the LEDs need to be sampled sequentially to avoid interference, the possible sample rate was reduced to 24 Hz. This low sample rate did not matter for in-vitro testing in porcine blood, but future testing in-vivo on people requires a much faster sample rate. The next version of the glucose sensor will need to have a greatly reduced separation between emitting and detecting LEDs (4 mm) and a dedicated LED driver to emit light at a greater intensity than the current 20 mA GPIO pin limit to reduce the sensing LED discharge time.

Conventional pulse oximeters sample at a minimum rate of 200 Hz to remove mains line noise. To reach this goal sample rate, the total discharge time across the 6 LEDs must be less than 5 ms. A possible means to reduce the decay time is to measure the voltage decay waveform and predict the shape of the decay. Thus, a short measurement of 500 µs could be taken and the remaining 19.5 ms of the decay waveform predicted from a model equation.

10.5 SUMMARY

A sensor was developed to measure the light absorption by glucose in the NIR spectrum. The overall results provide initial proof of concept validation for this sensing approach. Using discrete spectroscopy at 660 nm, 850 nm, 940 nm, 1450 nm, 1550 nm and 1650 nm, varied responses were found through testing in both water and porcine blood. The results obtained can be explained by Beer Lambert's law as the only factor affecting absorbance is the change in glucose concentration. The glucose concentrations tested were within the expected physiological range of blood glucose concentrations.

Using LED-LED detection methods, the sensor integrates the reflected light intensity of

the six wavelengths. The ratio of $R_{940/850}$ increases with glucose due to the absorption peak at 940 nm and minimal change at the isosbestic point of haemoglobin (850 nm). In the first overtone, $R_{1550/1450}$ gives an increase in absorption because glucose is the dominant absorber at 1550 nm, while water is the only absorber at 1450 nm. The final ratio calculated was $R_{1550/1650}$ which gave the greatest rise due to the displacement of other absorbing molecules (lipids, albumin). Thus, the 660 nm LED is not needed for future work with this sensor.

Future work on the sensor will adapt the LED layout and sampling time to allow measurement of the blood pulse. This design change will be done using a model of the LED voltage decay using an ADC to estimate photocurrent as well as using an additional emitting LED of each wavelength to increase the emitted light intensity.

Chapter 11

A MODEL FOR LED LIGHT DETECTION USING AN ADC

The sensor developed in Chapter 10 showed a relationship between glucose concentration and light absorption at the wavelengths tested. This chapter develops a model for the LED voltage decay waveform to enable faster sampling rates using the ADC method of sensing. LED wavelengths 1450 nm and 1550 nm are used to validate the model.

11.1 INTRODUCTION

This chapter develops a model for the measurement of light using just a microcontroller with an on-board ADC, and an LED acting as a photodiode. A model is necessary for three reasons. First, a sensor sample rate of >200 Hz is recommended [Kennedy 2015]. Thus, measuring 6 different wavelength LEDs sequentially at 200 Hz allocates only 800 µs to each LED. For the wavelength LEDs <1000 nm, this is not a problem. However, the LEDs with wavelength >1000 nm can take up to 5 ms to decay. Secondly, the impedance of the LED acting as a photodiode is close the impedance of the microcontroller input pins, so the pin impedance has a significant effect on the measured voltage. Third, during the sensing process, the LED acting as a photodiode is transitioning from photoconductive to photovoltaic mode. This model can then be solved for the photocurrent, I_p, which is proportional to the incident light on the sensing LED.

Figure 11.1 shows the equivalent circuit for a photodiode [Jau-Ji Jou et al. 2002, Jiang

and Yu 1998]. A photodiode can be represented by a current source in parallel with an ideal diode, where the current source represents the photocurrent generated by incident light and the diode represents the P-N junction. The junction capacitance (C_j) ranging 1 nF-100 nF [Gonçalves et al. 2013] and shunt resistance (R_{sh}) 1 MΩ-100 GΩ [Thompson and Larason 2001] determine the voltage decay time constant of the diode [Hamamatsu 2021]. The right side of the circuit in Figure 11.1 represents the equivalent impedance of the microcontroller pin the photodiode is connected to (Z_{pin}). The series resistance (10 Ω-1 kΩ) of the photodiode results from the physical circuit contacts and is minimal compared to the shunt resistance.

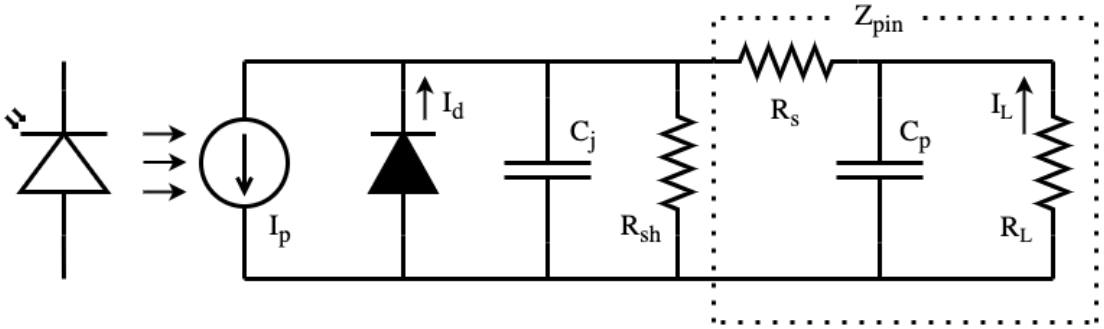

Figure 11.1 Equivalent circuit of a photodiode under incident light: consisting of the photocurrent (I_p), p-n diode junction current (I_d), junction capacitance (R_j), shunt resistance (R_{sh}) and the impedance (Z_{pin}) of the μC pin the photodiode connects to. Z_{pin} consists of the series and load resistance (R_s, R_l), and the microcontroller pin capacitance (C_p).

The photodiode/LED can operate in either photovoltaic, or photoconductive mode. In photoconductive mode, a constant reverse bias is applied to the diode's P-N junction. This reverse bias reduces the inherent capacitance of the diode, allowing faster response times, but also introducing dark current (I_{dark}) into the signal, reducing accuracy in low light conditions. In a reverse bias condition, the depletion width of the LED junction is increased, reducing the effective junction capacitance [Hamamatsu 2021, Kowalczyk and Siuzdak 2017, Meneghini et al. 2010]. In photovoltaic mode, no reverse bias is applied to the photodiode, making the sensor better suited for low light applications as the dark current is much reduced [Hamamatsu 2021]. This trade off is a greatly reduced response time caused by the increased junction capacitance.

Photodiodes are generally operated in either photoconductive or photovoltaic modes.

However, this proposed method transitions between the two modes. At a reverse bias of 3.3 V, the LED is operating under photoconductive mode, but as the pin discharges, the reverse bias voltage across the LED reduces, transitioning the LED closer to photovoltaic mode (no reverse bias). This reduction in reverse bias reduces the effect of dark current towards the end of the discharge cycle. Unless under high incident light intensities, the dark current is assumed to be a constant as the LED remains at a small reverse bias.

In many settings for electronics design, it is assumed the input impedance for a microcontroller pin is near infinite and no current passes through it. However, this assumption is not true for microcontrollers, as there are limitations on the input impedance [NXP Semiconductors 2020a]. Thus, the model for the photodiode must incorporate the influence of the connected microcontroller GPIO pin.

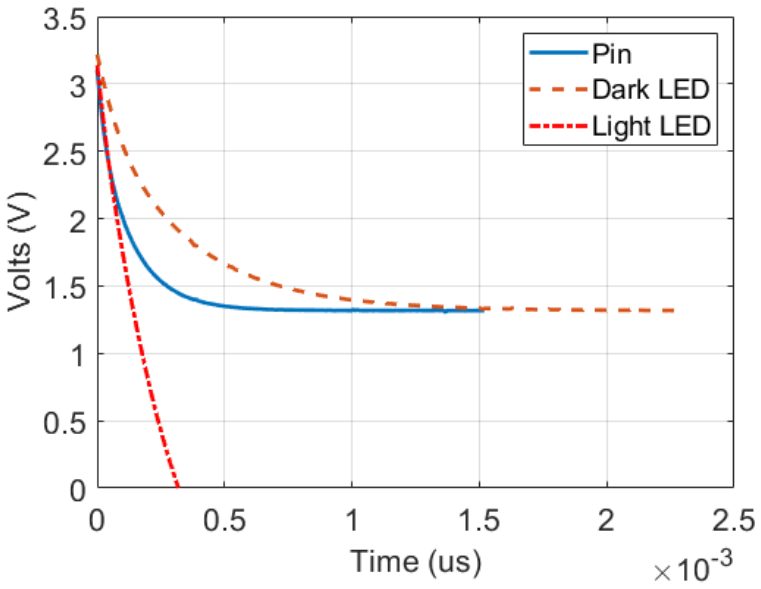

Figure 11.2 Ranges in discharge times of the LED and microcontroller pin under zero incident light (dashed orange), and high incident light intensities (dot-dashed red), as well as the pin disconnected from the LED (blue).

Figure 11.2 shows the voltage decay waveform of a pin without an LED connected to it transitions from being pulled to V_{cc} to HiZ. The voltage decays to the resting voltage created by the internal pullup and pulldown resistors (1.3 V in this case). When connecting the LED to the GPIO pin, the decay time constant is increased, or decreased,

depending of the incident light. As the discharge time of the pin has a similar time constant (τ) compared to the pin connected to the LED, the pin model must be included in the calculation of discharge time.

This chapter will cover the development of a model for the LED voltage decay waveform. The model will be able to track the decay waveform, and calculate the generated photocurrent (I_P). Decay data under zero incident light is used to calibrate the model. Once the model has been calibrated, the fit of the model will be compared to at 500 µs to assess the viability of the model-based approach and resulting decay rate estimation.

11.2 METHODS

The model presented in this chapter provides a solution to the low sampling rate of the sensor. If the microcontroller's on-board ADC can sample the voltage across the LED for a short time (500 µs), then predict the rest of the voltage decay using the model, the sample rate would be increased to 2 kHz for a single LED. For long LED decay times, the model provides a method to replace the timing method to maintain a fast sample rate. The voltage decay is recorded over 3 ms and the model fit to the first 500 µs. The fit of the model generated on the first 500 µs is then compared to the full 3 ms of data.

The response of the tested LEDs to incident light of the same wavelength was tested. The test setup involved placing the LEDs 5 mm away from a mirror inside a cabinet with approximately zero ambient light as shown in Figure 11.3. Tests were conducted at light intensities increasing from 0% to 100% emitter light intensity (0-2 $\mathrm{mW\,m^{-2}}$) in 10% increments. The response of the LED to incident light is expected to be linear.

The mirror used is transparent to visible light, but may be opaque in the NIR range. However, this chapter is measuring a proportional change in generated photocurrent, so a constant absorption by the glass would only provide an absorption offset at each emitter intensity.

An additional metric tested was the effect of LED emitter-detector separation on the generated photocurrent. Seven sensing LEDs of the same wavelength were used on

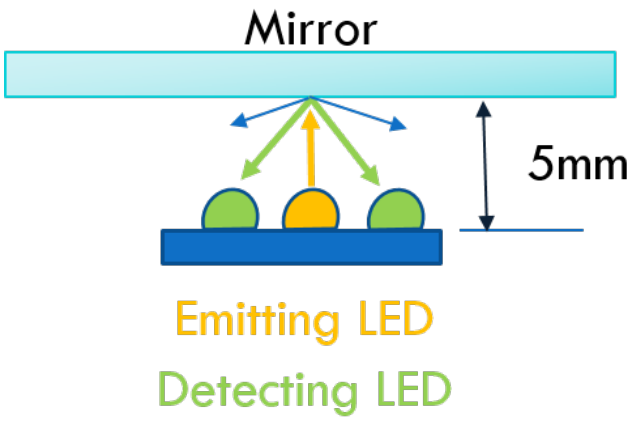

Figure 11.3 Experimental test setup, including the emitting and detecting LEDs 5 mm away from a mirror.

a sensing board, surrounding a single emitting LED. Each sensing LED is a different distance from the emitter.

11.2.1 Materials

Two different wavelength LEDs were analysed with this model: 1450 nm (Marktech, USA) and 1550 nm (Marktech, USA). The 1450 nm and 1550 nm LEDs have a nominal drive current of 50 mA [Marktech 2017a, 2018]. These two wavelengths were chosen as they were expected to give the greatest response to changing glucose, as identified in Chapter 10.

11.2.2 Equipment

Testing the 1450 nm and 1550 nm LEDs involved development of a test board for each LED. However, the entire approach and modelling are generalisable to any relevant wavelength LED. The 1550 nm LED sensing board is shown in Figure 11.4, with the 1450 nm LED sensing board identically set up. These boards connect to the SvO_2 sensor developed in Chapter 4, but use 7 LEDs of the same wavelength LEDs at separate distances, surrounding a central emitting LED.

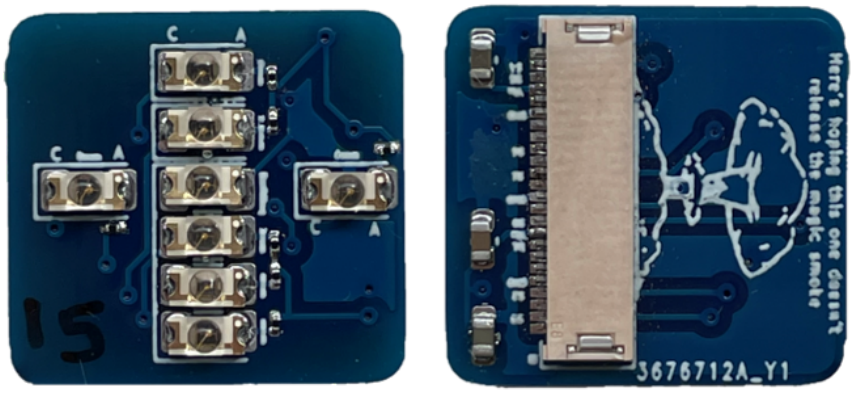

Figure 11.4 LED distance calibration board for the 1550 nm wavelength LEDs. 7 sensing LEDs surround a central emitting LED at different sensing distances.

This new sensing board has a single emitting LED at the centre, with detecting LEDs spaced vertically and horizontally at separate distances. The vertical sensing distances included 2 mm, 2.5 mm, 4 mm, 5 mm, 6 mm (V2, V2.5, V4, V5, V6). The horizontal spacing consisted of 5 mm and 6 mm (H5, H6) to investigate whether the orientation of the sensing LED to the emitter affects the light detection. The layout of each LED is shown in Figure 11.5.

The microcontroller records the voltage decay across each LED at a sample rate of 64 kHz, sending the decay waveforms of all 7 LEDs to the PC via serial, and the Arduino serial monitor was used to record the incoming serial data.

11.2.3 Sensor output processing

The model developed in this chapter represents the voltage-time relationship of the microcontroller pin and LED under incident light, allowing the generated photocurrent to be calculated. The circuit in Figure 11.6 represents the LED during the sensing cycle. This model is a combination of the photodiode equivalent circuit and the high impedance mode of the ADC pin on a microcontroller.

The LED model section contains the current source (I_p), junction capacitance (C_j), shunt resistance (R_{sh}). The ADC pin model on the left hand side includes a voltage

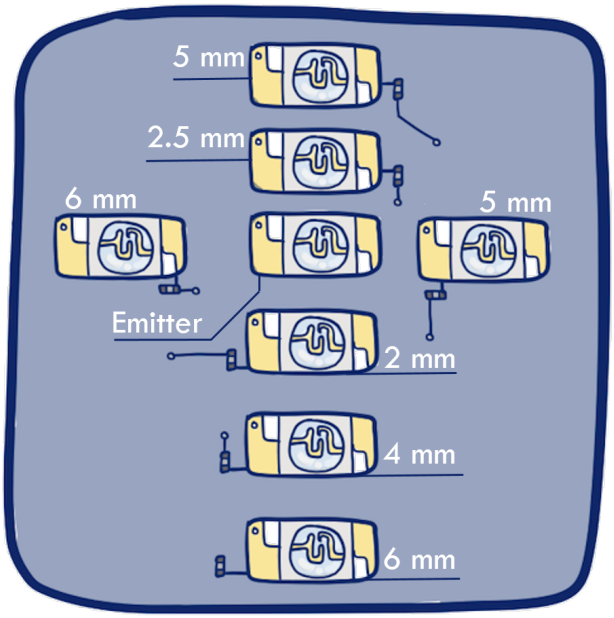

Figure 11.5 Layout of the emitting LED, and seven sensing LEDs used for validating the model.

source at V_{cc} (3.3 V), R_{pu} and R_{pd} as the pullup and pulldown resistors, R_s is the ADC pin input impedance and C_p is the internal capacitance of the microcontroller pin. The model can be solved to determine the input voltage to the ADC pin at the node V_2.

Connecting the LED to the pin circuit increases the decay time constant (τ), as seen in Figure 11.2. As the input resistance (R_s) and shunt resistance (R_{sh}) are an order of magnitude larger than the pulldown resistor (R_{pd}), the voltage divider remains the same. The method described in [Thompson and Larason 2001] was used to calculate the shunt resistance of each LED. This method measures the leakage current through the reverse biased LED in the voltage range of -50 mV to 50 mV. The slope of this current-voltage relationship is equivalent to the shunt resistance.

From the equivalent circuit model of Figure 11.6, the Laplace domain representation of the model for V_2 is given, where the voltages V_{C_p} and V_{C_j} represent the initial conditions across C_p and C_j, respectively:

$$V_2(s) = \frac{a_1 s^2 + a_2 s + a_3}{s(b_1 s^2 + b_2 s + b_3)} \tag{11.1}$$

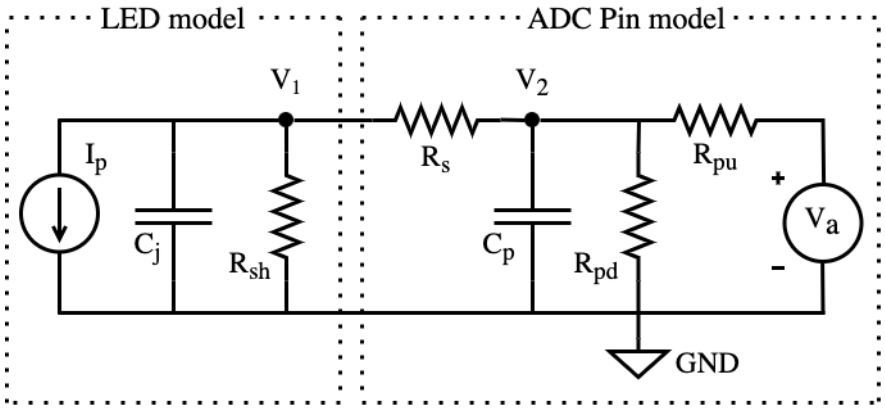

Figure 11.6 Equivalent circuit of a reverse biased led detecting light. R_{pu} and R_{pd} are the pullup and pulldown resistors, C_{pin} is the microcontroller pin input capacitance, R_s is the input ADC resistance, R_{sh} is the led shunt resistance, C_j is the led junction capacitance and I_p is the generated photocurrent. V_a is V_{cc} (3.3 V), V_1 and V_2 are the nodal voltages solved for.

Where,

$$a_1\colon\ C_pC_jR_{pu}R_{pd}R_sR_{sh}V_{C_p}$$

$$a_2\colon\ C_pR_{pu}R_{pd}R_sV_{C_p} + C_pR_{pu}R_{pd}R_{sh}V_{C_p} + C_jR_{pu}R_{pd}R_{sh}V_{C_j} + C_jR_{pd}R_sR_{sh}V_a$$

$$a_3\colon\ R_sR_{pd}V_a + R_{sh}R_{pd}V_a - (I_{dark} + I_p)R_{pu}R_{pd}R_{sh}$$

$$b_1\colon\ C_pC_jR_{pu}R_{pd}R_sR_{sh}$$

$$b_2\colon\ C_pR_{pu}R_{pd}R_s + C_pR_{pu}R_{pd}R_{sh} + C_jR_{pu}R_{pd}R_{sh} + C_jR_{pu}R_sR_{sh} + C_jR_sR_{pd}R_{sh}$$

$$b_3\colon\ R_{pu}R_{pd} + R_{pu}R_s + R_{pu}R_{sh} + R_sR_{pd} + R_{sh}R_{pd}$$

Inverse Laplace of Equation 11.1 yields the time domain voltage representation of the model at node V_2:

$$V_2(t) = \alpha_1 e^{\beta_1 t} + \alpha_2 e^{\beta_2 t} + \alpha_3 \tag{11.2}$$

Where,

$$\alpha_1 = \frac{(a_1 - \frac{a_3 b_1}{b_3})(b_2 + \sqrt{b_2^2 - 4b_1 b_3}) - 2b_1(a_2 - \frac{a_3 b_2}{b_3})}{2b_1\sqrt{b_2^2 - 4b_1 b_3}} \tag{11.3}$$

$$\alpha_2 = \frac{(a_1 - \frac{a_3 b_1}{b_3})(-b_2 + \sqrt{b_2^2 - 4b_1 b_3}) + 2b_1(a_2 - \frac{a_3 b_2}{b_3})}{2b_1\sqrt{b_2^2 - 4b_1 b_3}} \tag{11.4}$$

$$\alpha_3 = \frac{a_3}{b_3} \tag{11.5}$$

$$\beta_1 = \frac{-b_2 - \sqrt{b_2^2 - 4b_1 b_3}}{2b_1} \tag{11.6}$$

$$\beta_2 = \frac{b_2 - \sqrt{b_2^2 - 4b_1 b_3}}{2b_1} \tag{11.7}$$

Therefore, the time domain response of the system is the sum of two exponential decays with a voltage offset. The model assumes that at zero incident light the only current flowing through the LED is the dark current present in the diode under reverse bias conditions (I_{dark}), and is accounted for by setting the calibration measurement to zero.

Each component of the model must be identified to calculate photocurrent as every LED has different parameter values (C_j, R_{sh} and R_s). Once these parameters are calculated through the calibration process, the shape of the voltage decay across the LED under varying light levels can be used to calculate photocurrent.

11.2.3.1 Solving for Cpin, Rpu, Rpd

Before the LED is connected to the Teensy 4.0, the characteristics of the Teensy's GPIO pin musts first be found. By reverse biasing the pin without an LED, the voltage decay curve provides information about the values for C_{pin}, R_{pu} an R_{pd}. The equivalent circuit

for the ADC pin model in Figure 11.6 assumes an open circuit between V_1 and GND. The relationship between the time constant (τ) and the resistance and capacitance values, where R_{eq} is the equivalent resistance of the pullup and pulldown resistors is given:

$$\tau = R_{eq} \times C_{pin} \tag{11.8}$$

Where,

$$R_{eq} = \frac{R_{pu} R_{pd}}{R_{pu} + R_{pd}} \tag{11.9}$$

Figure 11.7 shows the decay times of the reverse biased Teensy 4.0 GPIO pins with no LEDs connected (orange) and with the cathode of the 1450 nm and 1550 nm LEDs connected (blue). Two different wavelength LEDs are shown in this analysis as they were identified in Chapter 10 to be the most likely to show a change in absorption in the presence of glucose. The orange dashed lines show the decay curve under near zero incident light and the dashed red line shows the decay curve under high incident light, where the model's double exponential shape is clear. Using the time constant of the pin voltage decay with no LED connected gives a time constant of 500 µs. Assuming a pin capacitance of 1.5 pF to 2 pF gives an R_{eq} value of 250 MΩ to 333 MΩ [NXP Semiconductors 2020a].

Using the floating voltage of the GPIO pin at V_1 in Figure 11.6, a voltage divider is generated between R_{pu} and R_{pd}. With V_{cc} of 3.3 V and a GPIO pin floating voltage of 1.3 V, the voltage divider ratio is 0.4, giving the relationship between R_{pu} and R_{pd}:

$$1.3V = 3.3V \frac{R_{pd}}{R_{pu} + R_{pd}} \tag{11.10}$$

$$0.4 = \frac{R_{pd}}{R_{pu} + R_{pd}} \tag{11.11}$$

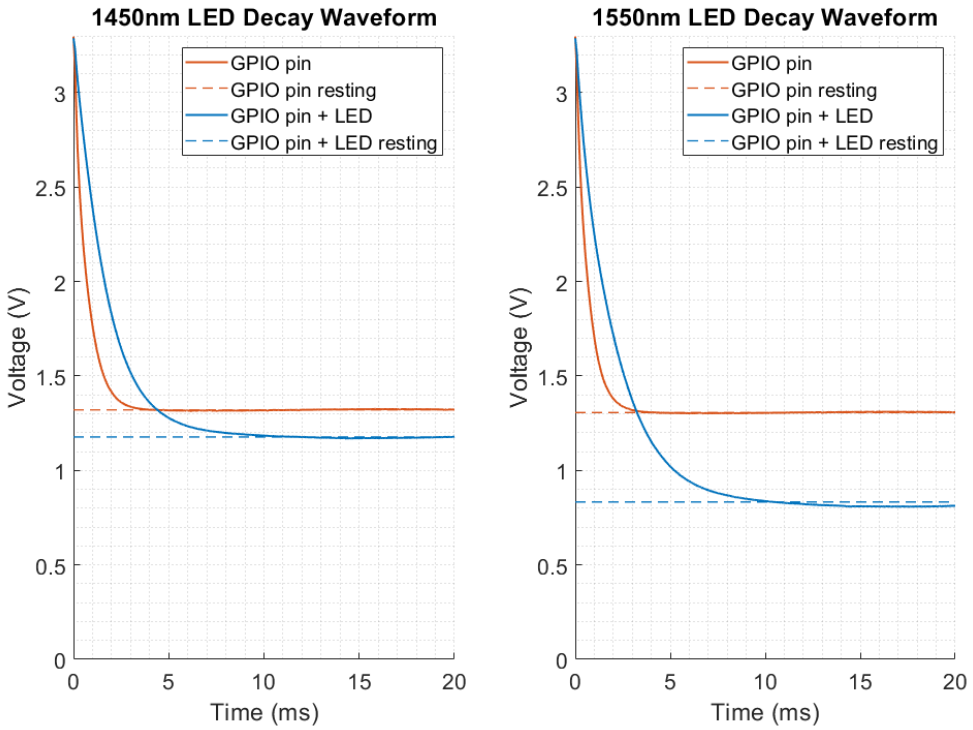

Figure 11.7 Voltage decay waveforms for the Teensy 4.0 GPIO pins (orange), and the GPIO pin with the 1450 nm and 1550 nm LEDs connected to their respective GPIO pin.

$$R_{pu} = 1.5R_{pd} \tag{11.12}$$

Using the Req value range of 250 MΩ to 333 MΩ, combining Equations 11.9 and 11.12 gives a value range of 410 MΩ to 550 MΩ for R_{pd} and 630 MΩ to 850 MΩ for R_{pu}.

11.2.3.2 Solving for Rsh

The shunt resistance of the LED is defined to be the inverse slope of the photodiode I-V curve at 0 V. An alternative to measuring the current at 0 V is to measure the current at ± 10 mV and fit a slope between the two readings [Thompson and Larason 2001]. Using Ohm's law, the gradient of the fit between ± 25 mV is the shunt resistance. The anodes and cathodes of each wavelength LED in the developed sensor was calculated using this method. Figure 11.8 shows the current-voltage relationship used to calculate the shunt resistance of both the 1450 nm and 1550 nm LED.

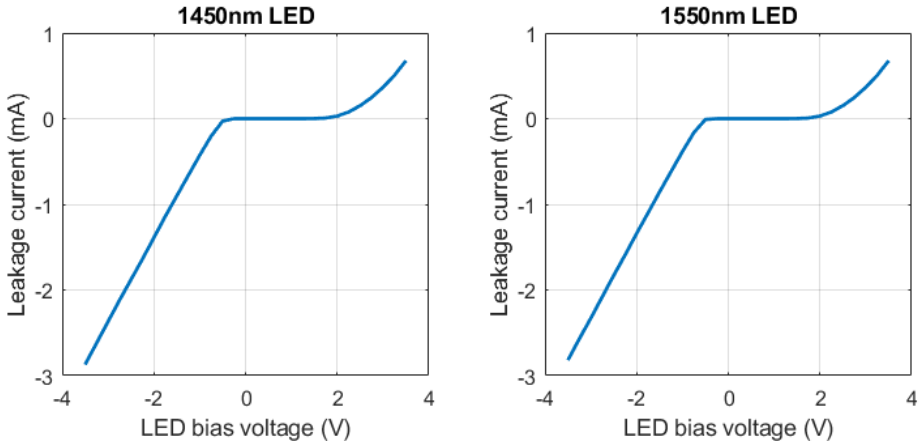

Figure 11.8 Current-voltage relationship for a reverse biased LED. The gradient between the -0.25 V to 0.25 V range gives the LED shunt resistance.

11.2.3.3 Solve for Rs

The voltage of the GPIO pin under zero reverse bias and zero incident light is the combination of the resistances creating a resistor divider between V_{cc} and ground. The relationship between V_1 and V_{cc} is used to calculate R_s:

$$R_s = \frac{V_1 R_{pu} R_{pd}}{R_{pd} V_{cc} - V_1 (R_{pu} + R_{pd})} - R_{sh} \tag{11.13}$$

The voltage measured at V_1 is lower than the voltage used to calculate R_{pu} and R_{pd} (1.3 V) due to the additional resistors in parallel with R_{pd}.

11.2.3.4 Solve for VCp and VCj

V_{C_p} and V_{C_j} are the initial condition voltages across C_{pin} and C_j respectively. These voltages can be calculated once all resistor values are calculated as the capacitors do not impact steady state voltages. When calibrating the decay curve under near zero light conditions, I_p is assumed to be 0. The matrix used to solve for V_{C_p} and V_{C_j} is

given:

$$\begin{bmatrix} \frac{1}{R_{pu}} + \frac{1}{R_{pd}} + \frac{1}{R_s} & -\frac{1}{R_s} \\ \frac{1}{R_s} & -\frac{1}{R_s} - \frac{1}{R_{sh}} \end{bmatrix} \cdot \begin{bmatrix} V_1 \\ V_2 \end{bmatrix} = \begin{bmatrix} \frac{V_a}{R_{pu}} \\ I_p \end{bmatrix} \tag{11.14}$$

11.2.3.5 Solve for Cj

The LED junction capacitance (C_j) can be solved using the decay time of the pin and LED under near zero light conditions. However, the junction capacitance of an LED varies with reverse bias so the calculation here is only an approximation [Hamamatsu 2021]. Using an equation based off the RC decay presented in Equation 11.8 to calculate C_j gives:

$$C_j = \frac{\tau}{\frac{R_s R_{sh}}{R_s + R_{sh}}} \tag{11.15}$$

After fitting the model to the decay with near zero incident light conditions, the response of each LED to varying light intensities was assessed. For a perfect model fit, the I_p calculated at 500 µs and 3 ms should be the same.

11.2.4 Analysis

The performance of the ADC to track the voltage decay will be analysed by comparing the mean decay waveform to 400 raw decay waveforms. The error in the ADC measurement will be represented by the standard deviation.

The model decay of each LED under near zero incident light will be compared to the recorded voltage decay. The RMSE between the model and recorded voltage decay will indicate the outcome of the model. The spacing of each sensing LED from the emitter will be assessed. It is assumed that the generated I_p will decrease with distance from the emitting LED.

The calculated I_p of each LED at 500 µs will be compared to the calculated I_p at 3 ms. This 3 ms time is assumed to the LED steady state voltage after decaying. This relationship will be represented as the gradient of the I_p at 500 µs vs 3 ms across the range of emitter light intensities. A gradient of 1 would indicate zero error between the calculated I_p at each point in time. A gradient greater, or, less than 1 indicates an error in the model at calculating I_p. However, if this gradient is constant, then the error in the model is a linear offset than can be accounted for in calibration. Assuming the offset will is linear allows the ratio of the "AC" to "DC" components in pulse oximetry to remove this offset. The R^2 will be used to analyse the gradient fit.

11.3 RESULTS

The results of fitting the model to the Teensy 4 GPIO pin as well as the dark voltage discharge data is shown in Figure 11.9. The microcontroller GPIO pin decay waveforms were consistent across each pin tested, with a resting voltage of 1.312 V $\pm$0.007 V. Connecting LEDs to the circuit reduced the resting voltage. The parameters fit to the model track to the fit the final resting voltage of the GPIO pin and LED as shown in the green decay waveform.

Figure 11.10 shows the noise levels of the 12-bit Teensy 4.0 ADC across 400 voltage decay waveforms under constant incident light. The mean decay waveforms is plotted in black.

The decay waveforms of the seven 1450 nm and 1550 nm LEDs were measured under increasing emitting LED light intensity. Figures 11.11 and 11.12 show the calculated photocurrent (I_p) for the 1450 nm and 1550 nm LEDs respectively. The sensing 1450 nm LEDs generated a photocurrent (I_p) in the range of 0 µA to 3.7 µA, with the closer the LED to the emitter, the higher the generated I_p at each emitter intensity. The sensing 1550 nm LEDs generated an I_p in the range of 0 nA to 130 nA. However, for the 1550 nm LEDs, the distance from the emitting LED did not solely determine the generated I_p as the V2 and V5 give higher than expected I_p. All seven LEDs across both wavelengths

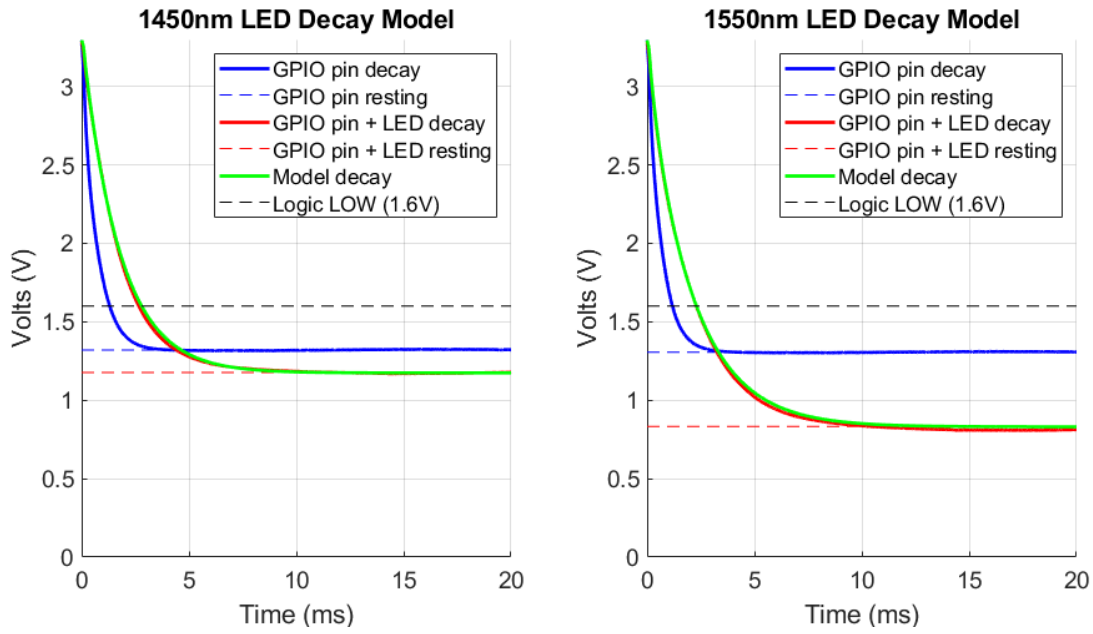

Figure 11.9 Voltage decay curves for the two tested LEDs. The blue decay plot is the voltage decay of the Teensy 4 GPIO pin with no LED connected. The red plot is the voltage decay of the GPIO pin with the LED connected and the green plot is the model fit to the decay data.

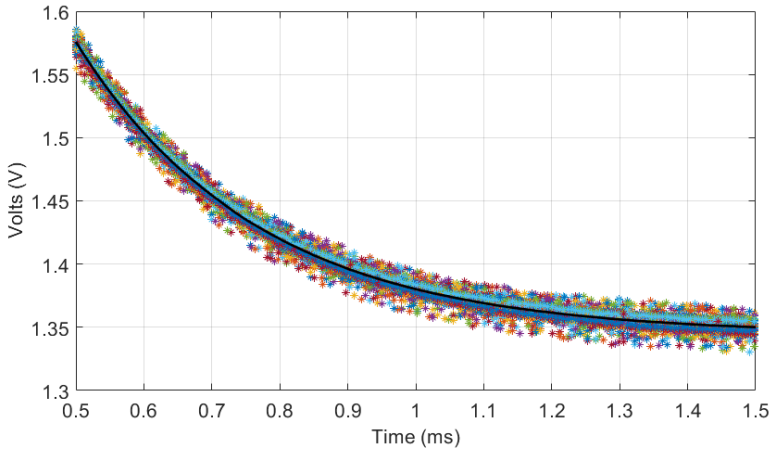

Figure 11.10 Noise levels of the 12-bit ADC measuring decay under zero incident light and the mean decay curve (black). Time shown from 0.5 ms to show the noise at the settling voltage.

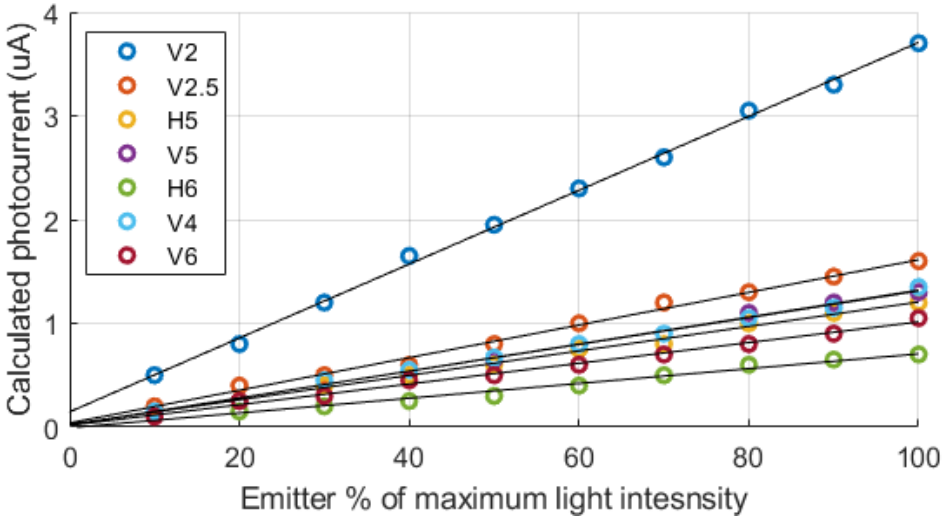

Figure 11.11 Calculated photocurrent for each of the seven 1450 nm LEDs under varying emitting LED intensity. The emitting 1450 nm LED radiant intensity increased from 0 mW m^{-2} to 2 mW m^{-2} in 10% increments. The vertical and horizontal LEDs are represented by V2-V6, and H5-H6 respectively.

returned an $R^2 > 0.99$.

Table 11.1 shows the relationship between the calculated I_p at 500 µs, and 3 ms. Each of the seven LEDs returns a positive gradient, with an $R^2 > 0.97$, showing a linear error between the I_p calculated at each time. Thus, the linear error in the I_p calculated at 500 µs can be calibrated for to calculate the I_p at 3 ms.

Table 11.1 Gradient of the relationship between the I_p calculated at 500 µs, and 3 ms.

	V2	V2.5	H5	V5	H6	V4	V6
mean gradient	4.3	2.8	5.2	4.6	3.4	3.0	2.8
1450 nm R^2	0.99	0.98	0.99	0.99	0.98	0.99	0.99
1550 nm R^2	0.99	0.99	0.97	0.98	0.98	0.99	0.98

11.4 DISCUSSION

The proposed model demonstrates a linear relationship between the photocurrent induced in an LED acting as a photodiode when directly attached to the pin of a microcontroller and incident light at varying intensities. The linear relationship between the emitter and each detector for both wavelengths tested is linear, with all LEDs returning an $R^2 > 0.99$. Thus, providing an accurate measure of incident light for use in the

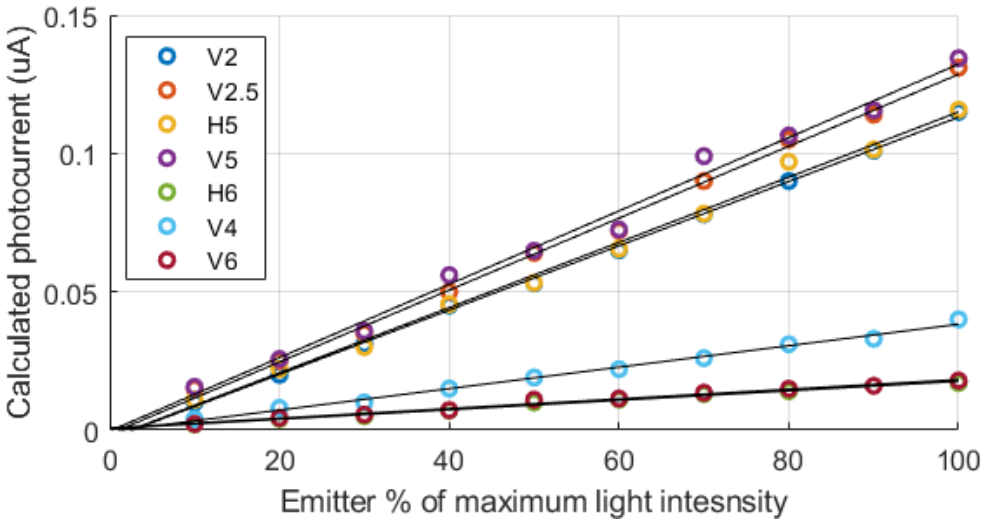

Figure 11.12 Calculated photocurrent for each of the seven 1550 nm LEDs under varying emitting LED intensity. The emitting 1550 nm LED radiant intensity increased from 0 mW m^{-2} to 2 mW m^{-2} in 10% increments. The vertical and horizontal LEDs are represented by V2-V6, and H5-H6 respectively.

CGM sensor. The units of the measurement are removed, as the ratio of the AC to DC is taken when measuring pulsatile data, so only the linear relationship is required for accurate measurements.

Using the calculated photocurrent at 500 µs to predict the photocurrent calculated at 3 ms had a linear relationship, with the worst fit having an R^2 of 0.97. Thus, while the model does have errors in prediction, this error is linear and can be accounted for with calibration.

Either the ADC sensing method, or timing to a threshold voltage can be used to determine incident light. The timing method is the simpler option, but requires a fast microcontroller clock and has a variable sample rate which can result in sampling rates in the region of 50 Hz. The ADC method requires an additional component (ADC), but is more accurate and you can generate a much faster and fixed sample rate as the sensor does not have to wait for the voltage across the LED to decay past the threshold voltage.

Figure 11.10 shows the final stages of decay of the LED under zero incident light. The variance is due to the resolution of the ADC. As the Teensy 4.0 ADC has a resolution of

800 µV, the resolution limit of the ADC is clearly reached. Using an external ADC to the Teensy 4.0, such as a 16 or 24 bit ADC would increase the accuracy of the sensor.

At high light intensities, the decayed voltage at the pin reaches zero, transitioning from photoconductive sensing to photovoltaic. This change means the dark current at high incident light intensities is reduced, while the response times at low incident light levels remain faster due to the reverse bias. A reduction in dark current (I_{dark}) could be be an additional reason for the reduction in the data-set variance at higher intensities. This model assumes the dark current is constant at every light intensity and can explain the slight drop in the calculated current in Figures 11.11 and 11.12 at high light intensities. To detect at higher light intensities may require an adaptive (I_{dark}) value to maintain a linear response to incident light.

Unlike photodiodes, LED datasheets do not give important values, such as shunt resistance [Kowalczyk and Siuzdak 2017]. Unless the I-V curve method described by Thompson and Larason [2001] can be used to measure the shunt resistance, the range for R_{sh} is one of the large unknowns. The dark current (I_{dark}) is also not given, but is generally in the pA range.

The calculated photocurrent calculated ranged from 0 µA to 3.7 µA. This result shows the sensor comprising just a microcontroller (Teensy 4.0), an LED, and the model presented are capable of low light measurement. The 1450 nm LED gave expected results for generated I_p at each distance from the emitting LED. However, the 1550 nm sensing results gave skewed results, biasing one side of the emitting LED (V2.5, V5 mm), compared to the other side (V2,V4, V5 mm). This discrepancy is likely due to the emitting LED being mounted at an angle facing the V2 and V5 LEDs. The horizontal LEDs, H5, H6 give results as expected, further showing the bias of the emitting 1550 nm LED to one side of the sensing board.

While the Teensy 4.0, and the 1450 nm and 1450 nm LEDs were chosen for validation of the model, the model can extend to other microcontrollers and LEDs. The pin decay section of the model is adjustable to whichever ADC is used and the model should capture the changing junction capacitance and shunt resistance of different chemistry

LEDs.

11.5 SUMMARY

This chapter developed a model for the discharge of an LED under reverse bias and while connected to a microcontroller's inbuilt ADC pin. This model allows fast, simple detection of incident light with a fixed sample time of 500 µs, compared to a threshold crossing timing method which has can take up to 10 ms to wait for the voltage to decay. The calculated photocurrent ranged from 0 µA to 3.7 µA across an emission range of 0-2 $\mathrm{mW\,m^{-2}}$ radiant intensity.

Thus, a new sensor can be developed to use an ADC to increase the sample rate of the sensor to be usable for in-vivo trials. To improve reading accuracy, an ADC with higher resolution than the in-buit 12-bit Teensy 4.0 ADC is needed. Using a 24-bit ADC that can sample all six wavelength LEDs should be implemented in the next sensor.

Chapter 12

VALIDATION OF A NON-INVASIVE CONTINUOUS GLUCOSE MONITOR

This chapter covers the validation of a non-invasive NIR discrete glucometer. Chapters 10 and 11 developed the proof of concept hardware and model for the sensor. The sensor presented in this chapter was designed for use in-vivo, measuring blood glucose concentrations (BGC) for both adults and babies. A pilot clinical trial in adults was conducted, as well as a clinical trial in the neonatal intensive care unit (NICU).

12.1 INTRODUCTION

Measuring blood glucose in the NICU is critical to analysis and treatment of hyperglycaemia and hypoglycaemia, with up to 30% of neonates at risk of low blood glucose [McKinlay et al. 2017a], and 15% formally diagnosed [McKinlay et al. 2015], which is up to 8-9000 babies per year in New Zealand. While hyperglycaemia should also be avoided, neonatal hypoglycaemia can cause permanent brain damage, or death [Spitzer et al. 1984]. Equally, hyperglycaemia can have negative outcomes on pre-term infants, including mortality, but control is very hard as very small blood volumes limit blood glucose testing [Dickson et al. 2013, 2017, Knopp nee Dickson]. In both cases, current methods of diagnosis from blood glucose measurements require blood samples to be taken, often hours apart, so key low or high values may be missed [Signal et al. 2012b].

Treatment of hypoglycaemia in the neonate is often dependent on the their birth-weight, and gestational age. For late pre-term and term babies, this involves repeated, painful

blood tests [Harris et al. 2013], and if the blood glucose concentration remains low, admission to the NICU is common [Vain and Chiarelli 2021]. Using a CGM would potentially improve glycaemic management and hypoglycaemia detection, while requiring fewer blood samples. To date, no continuous glucose monitor (CGM) has regulatory approval for use in infants, and there are concerns about the accuracy of these devices at the low blood glucose range seen in babies [McKinlay et al. 2017b].

Invasive, continuous glucose monitors have been investigated for use in the NICU [Harris et al. 2010, Signal et al. 2012a]. However, these sensors still require invasive calibration measurements, and themselves are invasive. Using a non-invasive NIR glucometer would provide the benefits of the CGM in glycaemic control, while reducing the need for additionally invasive blood sampling.

This chapter focuses on the design and validation of a discrete LED-LED NIR spectrometer for use in glucose monitoring in the NICU. The sensor designed in Chapter 10 has been adapted to use the model designed in Chapter 11, using an external ADC to track the LED voltage decay waveforms. The waveforms will be retrospectively analysed and fit to a physiological model, which will be compared to the paired clinical blood glucose measurement. Pairs of NIR and standard blood glucose measurements outcomes will provide proof-of concept outcomes for the use of this sensor in a neonatal cohort, as well as evidence for its extrapolation to other cohorts via the adult clinical testing implemented.

12.2 METHODS

To validate the sensor's ability to measure blood glucose, a wide range of concentrations must be tested. A pilot trial was run in healthy adults to measure the expected adult range of blood glucose from $4.0\,\mathrm{mmol\,l^{-1}}$ to $10.0\,\mathrm{mmol\,l^{-1}}$ [Frier et al. 2011, Kovatchev 2018]. Conducting a trial in the neonatal ICU provides blood glucose concentrations ranging $2\,\mathrm{mmol\,l^{-1}}$ to $5\,\mathrm{mmol\,l^{-1}}$ [McKinlay et al. 2015]. Combining these two trials covers a range of $2.0\,\mathrm{mmol\,l^{-1}}$ to $8.0\,\mathrm{mmol\,l^{-1}}$. While this range does not cover more

extreme hyperglycaemia in adults, further trials can assess these ranges, where accuracy has less impact on clinical decisions [Clarke 2005].

12.2.1 Pilot trial protocol

A pilot trial with adults was initially run to test the proof of concept sensor. The trial consisted of an OGTT to cause a change in blood glucose concentrations. Subjects are required to have not eaten for 12 hours (overnight), to ensure blood glucose concentrations are at fasting level. The goal of this trial is to take measurements with a reference finger stick glucometer as well as the light-based NIR reflectance glucometer. Before the trial begins, an initial glucose measurement is taken to read the fasting level blood glucose. To commence the test after the basal blood glucose measurement, a 330 ml can of Coca Cola, containing 35 g of sucrose (17.5 g glucose), is drunk and a timer started. The timeline for the entire test, including measurements is given in Figure 12.1.

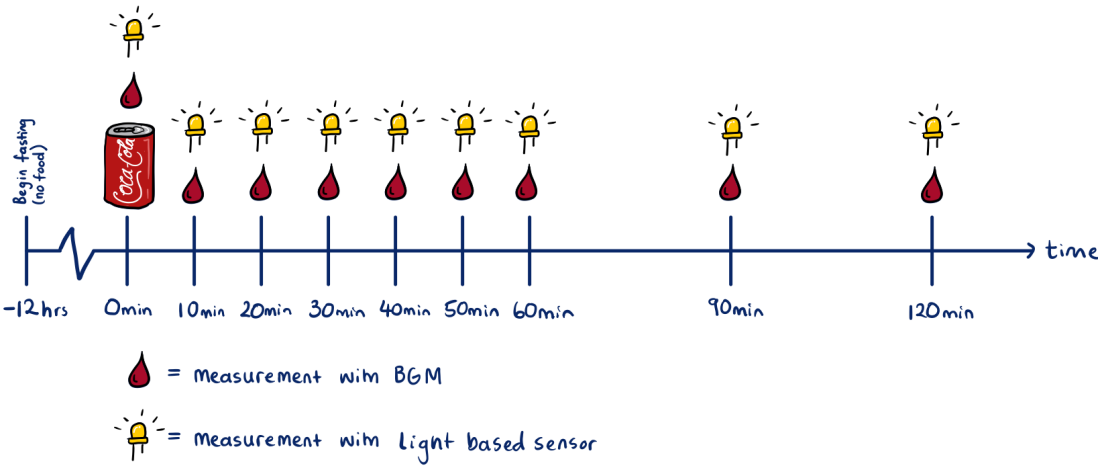

Figure 12.1 Trial timeline for the adult pilot trial.

Three sites are measured with the light-based sensor, the carotid artery, palm, and finger tip. Measuring at the carotid artery places the sensor over a major artery, compared to the capillaries in the palm and finger, giving a range of sensing sites. The user interface designed in Figure 12.2 records the subject number, reference blood glucose value, and measurement site.

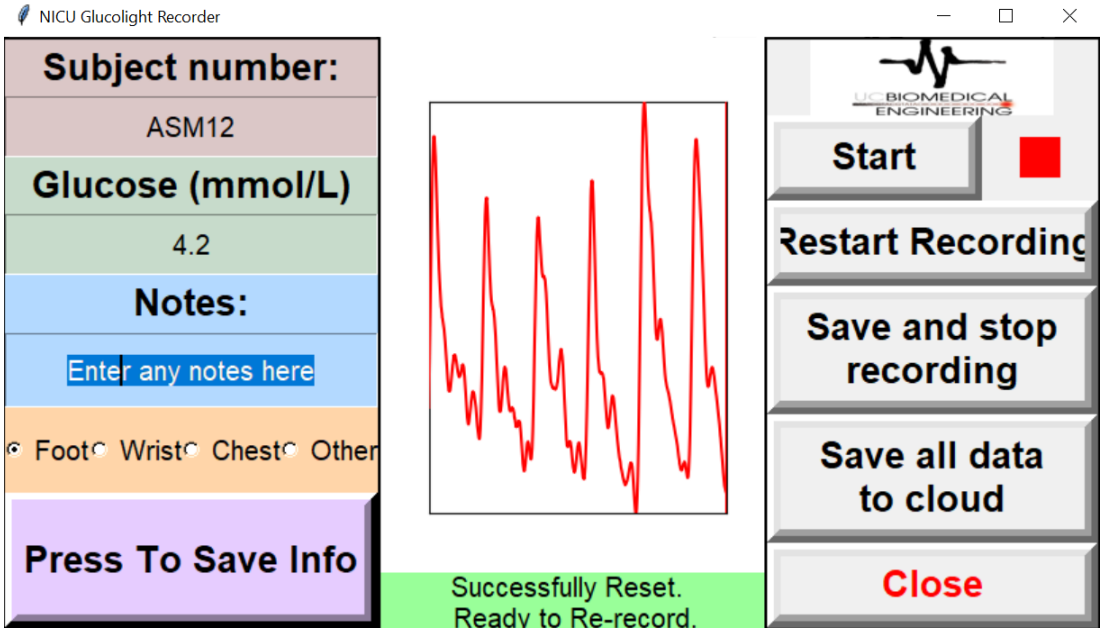

Figure 12.2 User interface used for the pilot adult trial and the NICU trial.

Once the sensor has been placed on the site, and the plot shows a pulsatile waveform, the start button is pressed, recording for 30 seconds. After recording data, the user has the option to save locally, or to send the data to a git repository stored local to the University of Canterbury for secure storage.

12.2.1.1 Adult Subjects

This study uses data obtained from participants between 18-40 years old, with no diagnosed haematological conditions, no disease affecting blood sugar regulation except diabetes or pre-diabetes, and are not smokers. During the two hour long trial, the subjects are required to be seated, and not consume any food or water. Table 12.1 shows the subject demographics. This study was approved by the Human Ethics Committee, University of Canterbury (HEC2019/153) and informed consent was obtained from each participant prior to the experiment.

Table 12.1 Light based continuous glucose monitor adult pilot trial subject demographics. Data is shown in median [IQR] where appropriate.

Subjects	5
Age (years)	25 [22-28]
Sex (M/F)	3/2
Ethnicity (Maori/ NZ European/ other)	1/4/0

12.2.2 NICU trial protocol

The NICU study consisted of an observational cross-sectional methods comparison study in neonates. Following written, informed parental consent, the light-based glucose sensor was held against the neonate's skin for approximately 30 seconds, at three sites (foot, wrist and chest). Immediately before this measurement, a standard clinical BGC measurement was performed as part of standard care. No additional blood sampling was performed in the study, as standard clinical BGC measurements triggered NIR sensor measurements. The NICU study schedule is given in Figure 12.3.

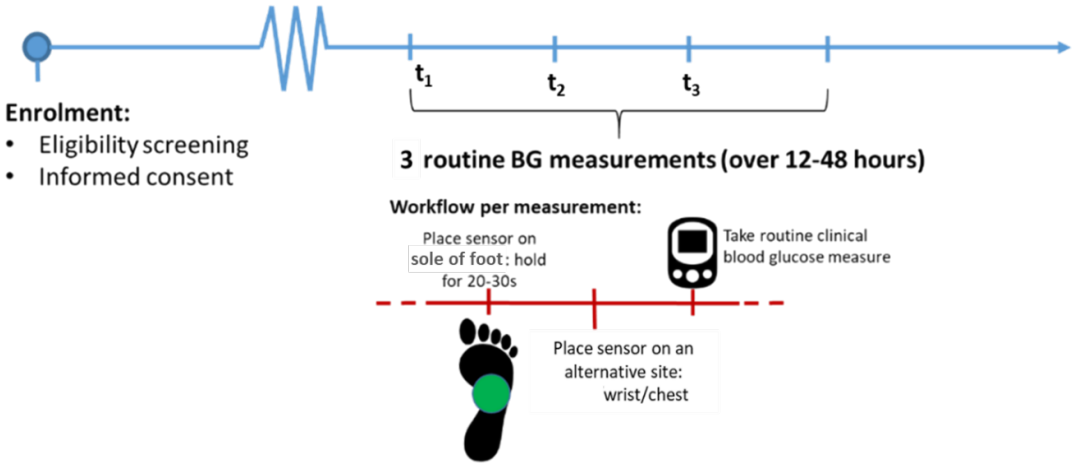

Figure 12.3 Trial timeline for the NICU trial.

12.2.2.1 NICU Subjects

The inclusion criteria for this study included neonates born at ≥34 weeks gestation at risk of hypoglycemia, or undergoing clinical BGC monitoring, recruited from the NICU and postnatal wards. The planned sample size is 20-30 neonates recruited across two hospitals, Auckland Hospital, and Middlemore Hospital.

Exclusion criteria include: skin irritation/infection on feet/hands/chest; neonates in isolation due to infection risk; neonates who are critically unwell; and a patient who has a parent or whanau with suspected COVID19. Enrolment in this trial does not affect, or limit eligibility of the neonate to participate in other trials.

Table 12.2 shows the demographics of the neonates recruited for the trial. Note, skin colour is recorded due to the applicability to NIR light based sensing, and is quantified using the Fitzpatrick Scale [Sachdeva 2009].

Table 12.2 Light based continuous glucose monitor NICU trial patient demographics. Data is shown in median [IQR] where appropriate.

Patients	22
Hospital (Auckland/Middlemore)	15/7
Gestational age (wk + day)	38+4 [37+4, 39+5]
Sex (M/F)	10/12
Birth-weight (g)	3302 [2686, 3806]
Customised Birth-weight Centile (%)	24.5 [8.5, 81.0]
Skin Colour (1-6)	2/11/7/1/1

12.2.3 Equipment

The model developed in Chapter 11 showed good results for increasing the sampling rate, while tracking the LED voltage decay with an ADC. However, at low light levels, the resolution of the Teensy 4.0 inbuilt 12-bit ADC was too low. Thus, an external ADC has been implemented on the new board.

The sensor presented in Chapter 10 used six different wavelength LEDs spaced with 10 mm between emitting and sensing LEDs. An additional arrangement between LEDs was presented in Chapter 4, placing the LEDs in a grid with the sensing LED of each wavelength surrounded two emitting LEDs spaced 5 mm apart. The final LED arrangement used in this chapter is the same as the $SjvO_2$ sensor, except with 4 mm between emitting and detecting LEDs. The design of the circuit board is shown in Figure 12.4. For each wavelength measured, a sensing LED has two emitting LEDs separated by 4 mm.

To reduce noise in the circuit, the emitting and sensing boards presented in Chapter 4

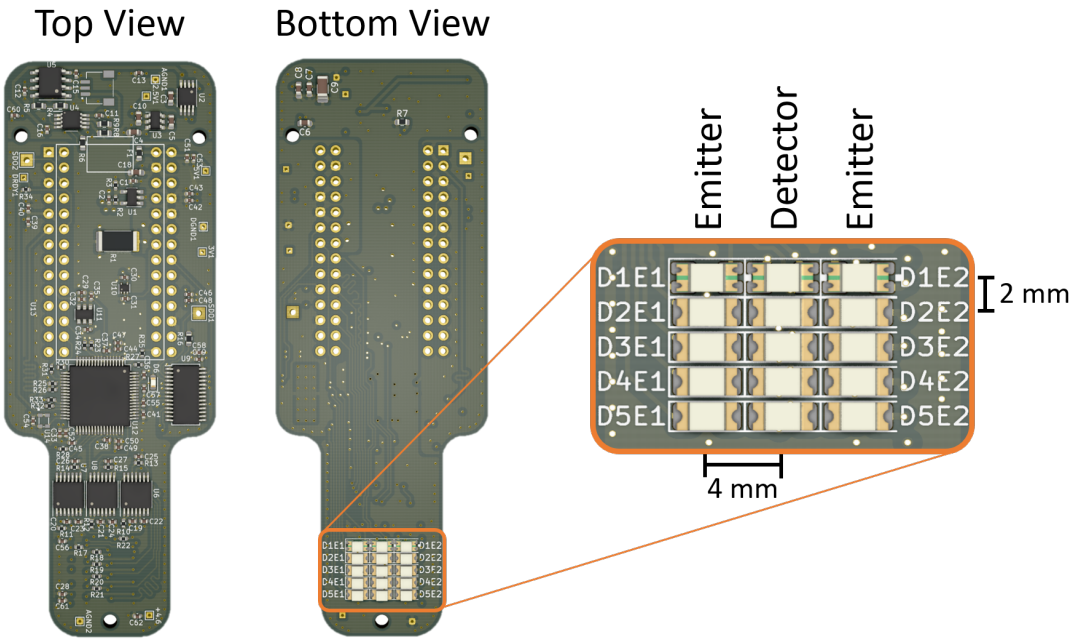

Figure 12.4 Design of the circuit board for use in the NICU. Each detector LED has two emitting LEDs of the same wavelength separated by 4 mm. LED D1 contains the wavelengths 660 nm and 940 nm, while D2-D5 contain wavelenths 850 nm,1450 nm,1550 nm,1650 nm respectively.

were combined onto one board. This combination removes the need for an FPC cable. However, as all hardware is on a single board, the LEDs has to be placed separately to the remainder of the components. To ensure the LEDs can be placed on a neonatal wrist, the width of the circuit board at the LEDs was limited to 20 mm, and the total sensing area of the LED matrix is 8x10 mm.

12.2.3.1 Component choice

Many of the sensor components presented in Chapter 4 are retained in this design, including: the Teensy 4.0; all LEDs; the 57 mA constant current LED driver; and the right leg driver (RLD) circuit. However, the RLD circuit is not used in either of the two trials, so the components were not populated on the circuit board.

The AD7768BSTZ 24 bit ADC is used in this project to monitor the LED decay voltage at 33 kHz [Analog Devices 2016]. This ADC has the capacity to simultaneously read eight channels, of which this sensor uses six, one for each sensing LED. To reduce the

noise present in the analogue signal, hardware filtering was included. Three rail-rail quad opamp AD8608s were chosen to filter the six inputs from the sensing LEDs [Analog Devices 2017]. The first opamp forms a voltage follower to create a high impedance path between the LED and ADC, while the second creates a 5 kHz cutoff (F_c) lowpass RC filter, given:

$$F_c = \frac{1}{2\pi RC} \tag{12.1}$$

Thus, the combination of a 95 Ω resister, with a 330 nF capacitor creates this 5 kHz cutoff frequency.

12.2.3.2 Design considerations for the NICU

The sensor must be capable of being sanitised between each patient. Thus, the housing was designed to be splash proof, and wet alcohol wipes can be used between each test. This splash proof design was implemented using a 3D printed housing with rubber grommets set between each of the attachment points. The LEDs were separated from the skin by an optically clear, anti static plastic screen designed for overhead projectors. This screen provides a moisture barrier, while retaining optical clarity for sensing.

Figure 12.5 shows the design of the housing for the NICU sensor. As the sensor has the emitting and detecting LEDs located on the bottom of the board, the bottom of the housing must be flat to ensure flush placement on sites, such as the carotid artery, or chest.

12.2.4 Sensor output processing

The raw pulsatile data must first be processed before calculating blood glucose concentration. The data flow is shown in Figure 12.6, where the raw LED voltage decay waveform gets processed using the ADC decay method presented in Chapter 11. The "AC" and "DC" components of the signal were calculated using the rolling RMS method

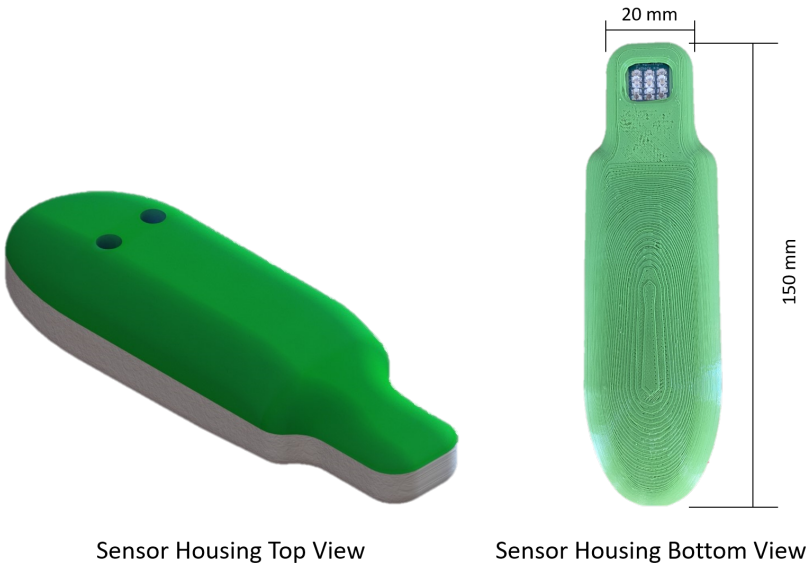

Figure 12.5 Design of the sensor housing. The ergonomic grip is flat along the bottom to ensure flush placement on the measuring site.

as the peaks and troughs were too difficult accurately identify. The AC/DC ratio of each wavelength are then used in the absorption model to get the model predicted glucose concentration. Passing the data through a calibration equation returns the calculated blood glucose concentration.

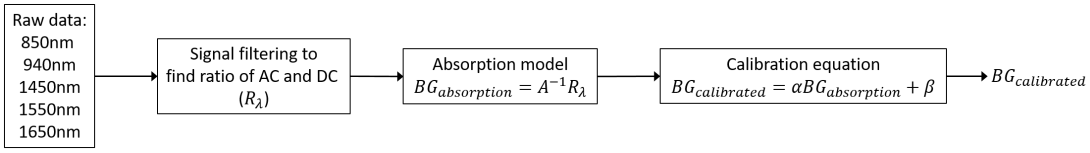

Figure 12.6 Processing flow of the recorded arterial pulse waveform at each LED wavelength measured.

The absorption model was developed to use light absorption from the 850 nm, 940 nm, 1450 nm, 1550 nm, 1650 nm wavelength LEDs. The 660 nm wavelength data was not included due to its minimal glucose absorption band [Amerov et al. 2004]. The components analysed in this model include: water (W), glucose (G), albumin (A), lipids (L), and tissue (T). This absorption model was developed based on Beer-Lambert's law, as

described in Chapter 10, and defined:

$$I_D = I_E e^{A_\lambda C} \tag{12.2}$$

Where,

I_E: LED voltage decay time under maximum incident light intensity from the emitting LEDs.

I_D: LED voltage decay time under varying incident light intensity reflected from tissue.

A_λ: Combined absorption coefficient ϵ_λ, and optical path-length, d_λ

C: Concentration of each component

The absorption coefficient of glucose must account for the displacement of water (f_g^w) at each wavelength. Thus, each new glucose absorption coefficient (ϵ'_{G_λ}) takes the form:

$$\epsilon'_{G_\lambda} = \epsilon_{G_\lambda} - \epsilon_{W_\lambda} \times f_g^w \tag{12.3}$$

Rearranging Equation 12.2 to solve for the absorption for an individual wavelength gives:

$$\ln\left(\frac{I_D}{I_E}\right) = A_\lambda C \tag{12.4}$$

The LED voltage decay time under maximum light intensity is considered to be I_E, and the LED voltage decay when placed on the tissue is I_D. The voltage decay time from each detecting LED was normalised by dividing by I_E.

Using the principles of pulse oximetry, the ratio of the AC and DC components of the pulsatile waveform at each wavelength were calculated. This ratio is denoted as

R_λ. Combining the combined absorption coefficients and path-length each wavelength travels, with the concentration of each component gives:

$$R_\lambda = A_\lambda C \tag{12.5}$$

Thus, including the five measured wavelengths:

$$\begin{bmatrix} R_{850} \\ R_{940} \\ R_{1450} \\ R_{1550} \\ R_{1650} \end{bmatrix} = \begin{bmatrix} A_{850W} & A_{850G} & A_{850A} & A_{850L} & A_{850T} \\ A_{940W} & A_{940G} & A_{940A} & A_{940L} & A_{940T} \\ A_{1450W} & A_{1450G} & A_{1450A} & A_{1450L} & A_{1450T} \\ A_{1550W} & A_{1550G} & A_{1550A} & A_{1550L} & A_{1550T} \\ A_{1650W} & A_{1650G} & A_{1650A} & A_{1650L} & A_{1650T} \end{bmatrix} \begin{bmatrix} C_W \\ C_G \\ C_A \\ C_L \\ C_T \end{bmatrix} \tag{12.6}$$

Equation 12.6 is then rearranged to solve for the physiological concentration of each component:

$$\begin{bmatrix} C_W \\ C_G \\ C_A \\ C_L \\ C_T \end{bmatrix} = \begin{bmatrix} A_{850W} & A_{850G} & A_{850A} & A_{850L} & A_{850T} \\ A_{940W} & A_{940G} & A_{940A} & A_{940L} & A_{940T} \\ A_{1450W} & A_{1450G} & A_{1450A} & A_{1450L} & A_{1450T} \\ A_{1550W} & A_{1550G} & A_{1550A} & A_{1550L} & A_{1550T} \\ A_{1650W} & A_{1650G} & A_{1650A} & A_{1650L} & A_{1650T} \end{bmatrix}^{-1} \begin{bmatrix} R_{850} \\ R_{940} \\ R_{1450} \\ R_{1550} \\ R_{1650} \end{bmatrix} \tag{12.7}$$

The result of solving this series of equations using the inverted equation returns a glucose concentration in $\mathrm{mg\,dl^{-1}}$. A conversion factor of 18.018 is used to convert to $\mathrm{mmol\,l^{-1}}$.

Table 12.3 gives the absorption coefficients for each wavelength, adapted from [Altshuler et al. 2006, Cao et al. 2013, Kohl et al. 1995, Maruo et al. 2006a, b]. The model includes absorption for water glucose, albumin, lipids, and tissue. The tissue component accounts for the remaining components in blood. The results of each measurement is then compared to the reference finger prick measurement taken at the same point in

time, and plotted in a Clarke Error Grid (CEG) for analysis.

Table 12.3 Absorption coefficients of blood components at each wavelength measured.

	Wavelength (nm)				
Absorption (ϵ) (cm^{-1})	850	940	1450	1550	1650
Water	0.05	0.5	40	20	6
Glucose	0.0015	0.002	4	14	1
Albumin	0.4	1	4	7	5
Lipids	0.8	0.1	2	2	2
Tissue	15	16	15	15	15

Similar to the raw output of the pulse oximeter ratio equation, the result of Equation 12.7 requires a calibration equation. An absorption model does not account for additional impacts on light absorption, such as light reflection, ambient lighting, and sensor error. Additional absorption and scattering is still expected to be present at zero glucose in the blood, so will create result in a non-zero crossing of the absorption model. Thus, a linear calibration model will be created to adjust for the non-zero offset, as given:

$$BG_{calibrated} = \alpha BG_{absorption} + \beta \tag{12.8}$$

Where,

α: calibrated gradient

β: calibrated absorption offset

K-fold cross-validation is used to calibrate the linear model. Cross-validation is a re-sampling method which uses different portions of the data-set to train, then test a model. The goal of the calibration is to test the ability of the calibration to predict data which wasn't used to train the model. K-fold cross-validation uses K sections of equally sized training and testing sets. For example, 10-fold cross-validation randomly separates a data-set of 200 samples into 10 sets of 20.

Each set of 20 data points is then used as a test set of the calibration, where the remaining 180 out of the 200 data points are used to train the model. The RMSE of each

test set between the reference BGC and calibrated BGC is calculated for comparison. After each of the models have been fit to the split data, the mean coefficients from each fit are used for the final calibration equation. The calibrated blood glucose calculation is then compared to the reference blood glucose for analysis.

Conventional parameter fitting for a linear model minimises the error between each data point and the line of best fit. While this method will return a valid calibration, the parameter fitting assumes the x-data to be truly accurate. However, the reference glucose measurements themselves have error. Thus, TLS is used to calculate the line of best fit. This method optimises the perpendicular distance between the data point and the linear line of best fit, accounting for error in both the x and y-axis [Golub and van Loan 1980]. The GMD fitting method is often used instead of TLS as it is scale invariant. However, as the reference and estimated glucose are on the same scale, the TLS method is used in this chapter.

The coefficient of determination, R^2, calculates the difference between how the y-axis error from the line of best fit is compared to the y-axis error to the mean. Similar to TLS fitting, the error in the reference measurement must also be accounted for [Lam et al. 2020]. Thus, a TLS coefficient of determination will also be presented. This R^2_{TLS} measures the error perpendicular to the line of best fit.

12.2.5 Analysis

Blood glucose was assessed in both adults and neonates, providing a range in glucose between $2.2\,\mathrm{mmol\,l^{-1}}$ to $8.0\,\mathrm{mmol\,l^{-1}}$. The results from both trials will be included together in a CEG, as well as Bland-Altman analysis. The average reading from each of the three sites is also presented.

Data exclusion criteria was included to remove noisy data. A rolling RMS window of the pulsatile data is used to threshold the noise level. If the RMS of the pulsatile waveform from one of the waveforms exceeds this threshold, the section of data is excluded from the analysis. This increase in RMS is often due to motion artefacts

introduced by movement of the neonate. The exclusion criteria will be run at three different noise thresholds to demonstrate the effect of each threshold.

The performance of the k-fold cross validation will be assessed using the RMSE at each step of calibration. A larger range in RMSE indicates a poor fit to the data. The mean and standard deviation of the α and β values will also be presented.

The primary outcome of these trials is the proportion of predicted BGC measurements with a MARD <20% compared to the reference method. MARD will be calculated overall, and by skin site and at lower ($<3.5\,\mathrm{mmol\,l^{-1}}$) and higher ($\geq 3.5\,\mathrm{mmol\,l^{-1}}$) BGC [Rodbard 2014]. MARD gives the average percentage difference between the experimental and testing device. Invasive glucometers have a MARD of 5-10%, while a MARD of 15% would be deemed very good for a non-invasive system [Smith 2017]. However, the CEG indicates a MARD of 20% is within clinical accuracy requirements.

12.3 RESULTS

In total, 27 subjects were tested, with 22 neonates, and 5 adults. A combined 290 measurements were taken across the three sites: foot, wrist, and chest for neonates, and finger, palm, and carotid artery for adults. Each invasive glucose measurement was paired with measurements at each of the three sites.

The RMS thresholding determined 117 measurements did not record a pulse for data analysis. This percentage of lost data, 43%, was generally recorded at the early stages of the trial as each user learnt how to best apply the sensor. Thus they declined with practice with the device.

Figure 12.7 plots the reference glucose reading against the raw output of the absorption model. The mean RMSE from each of the the 10-fold cross validation calibrations was $1.6\ \pm 0.4\,\mathrm{mmol\,l^{-1}}$, indicating a consistent linear calibration model. The model is given:

$$BG_{calibrated} = 1.32(\pm 0.06)BG_{absorption} - 1.25(\pm 0.27) \tag{12.9}$$

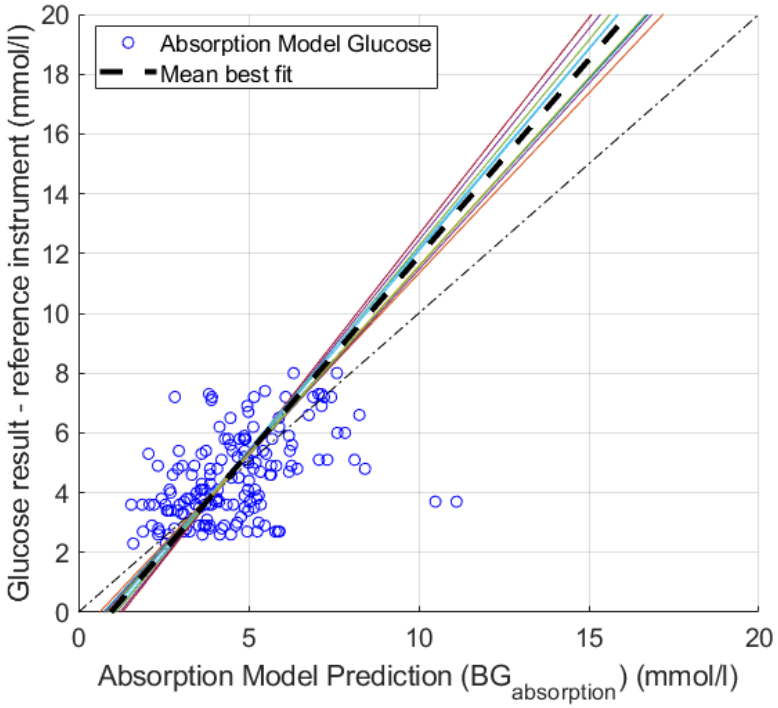

Figure 12.7 K-fold cross validation method for calibrating the raw output from the absorption model.

Figure 12.8 plots the CEG generated from the neonatal data (blue) and adult data (red). The error grid contains 62% percent in Zone A, 31% in Zone B, 6% in Zone C, and 1% in Zone D. The sensor shows a greater spread in estimated BGC in adults, compared to neonates, with the two neonate readings clear outliers. The R^2 of the calibrated estimated blood glucose concentration compared to the reference is 0.33. Table 12.4 shows the results from the CEG analysis.

The effect of different noise thresholds on the sensor calibration is shown in Figure 12.9, with the results shown in Table 12.4.

The Bland Altman analysis is shown in Figure 12.10, demonstrating an overestimation of blood glucose concentration for the neonates, and an under estimation for adults. The mean difference between the light-based and reference measurements was -0.21 $\mathrm{mmol\,l^{-1}}$.

The calculated light-based glucose values were separated into each recording site, with

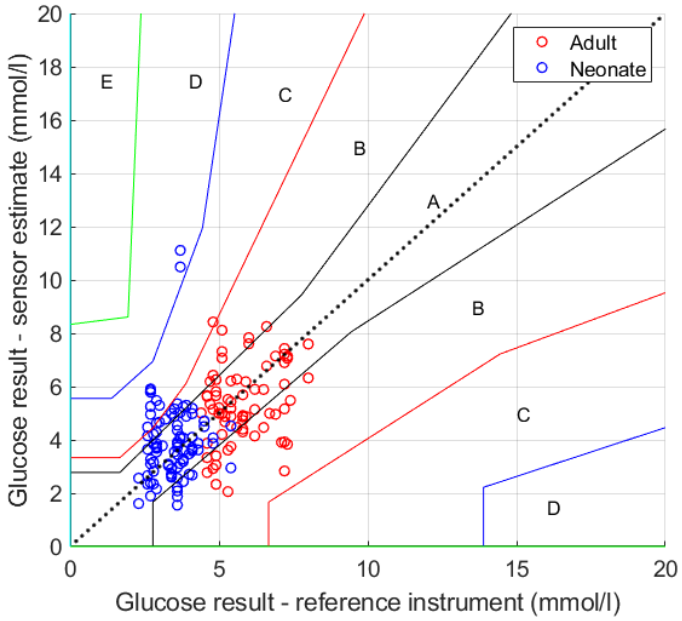

Figure 12.8 Clarke Error grid for the calculated light-based glucose sensor compared to a reference glucometer measurement after calibrating for reflectance at zero glucose, with an $R^2 = 0.33$. The blue data is recorded from neonates, and the red data from adults.

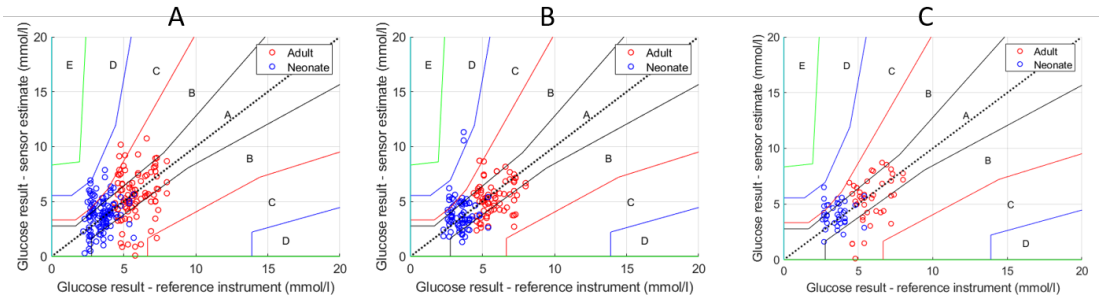

Figure 12.9 Clarke Error grid for the calculated light-based glucose sensor compared to a reference glucometer measurement at three different noise threshold levels of the total 290 estimated glucose values. CEG A plots 210/290, CEG C plots 149/290, CEG C plots 78/290.

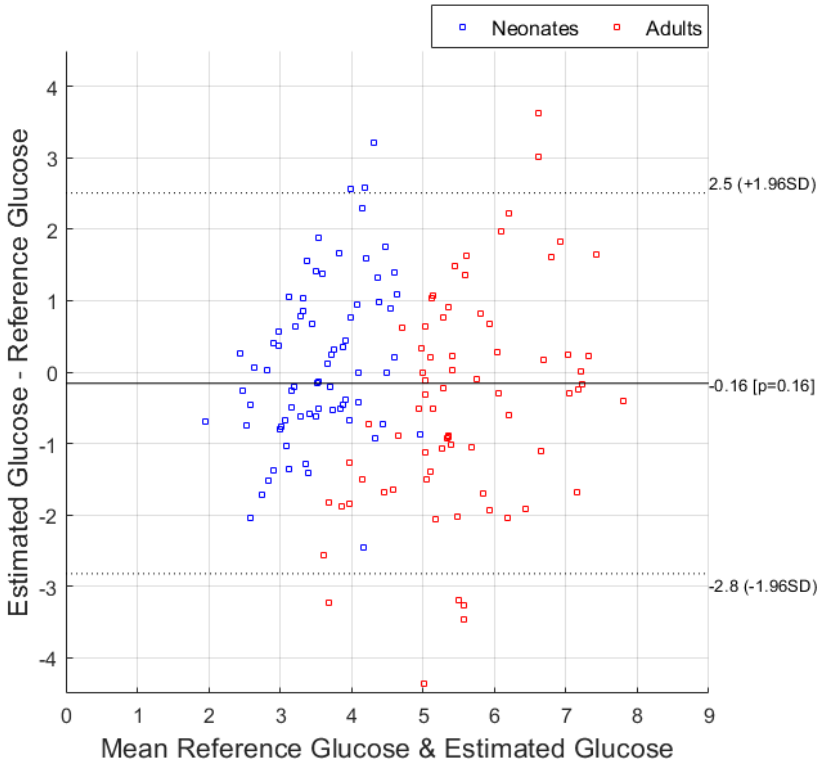

Figure 12.10 Bland Altman plot for the calculated light-based glucose sensor compared to a reference glucometer measurement. The blue data is recorded from neonates, and the red data from adults.

Table 12.4 Combined results from the adult and NICU trial.

	Total Reads	RMSE ($\mathrm{mmol\,l^{-1}}$)	MARD $<3.5\,\mathrm{mmol\,l^{-1}}$	MARD $\geq 3.5\,\mathrm{mmol\,l^{-1}}$	R^2	R^2_{TLS}
Foot	50	1.6	24	25	-1.2	0.71
Wrist	63	2.0	28	29	-0.43	0.73
Chest	47	1.9	33	21	-0.62	0.73
Average of three sites	52	1.2	15	31	0.47	0.77
Threshold A	210	1.9	28	52	0.18	0.72
Threshold B	167	1.0	24	40	0.33	0.71
Threshold C	78	1.0	24	40	0.34	0.73

the foot and finger, wrist and palm, and chest and neck plotted for the neonate and adult respectively. Figure 12.11 shows these three site plots, as well as the mean across the recorded sites for each invasive reference measurement taken. The CEG showing the mean estimations contained 85% in Zone A, 11% in Zone B, and 4% in Zone C.

The CEG containing the foot and finger data had the lowest MARD of 25%, representing the best fit of each of the sites. However, the adults' thumb had the greatest variation of the three sites, excluding the two outliers in the neonatal wrist data. The combined average has much reduced variation, leading to an R^2 of 0.47.

12.4 DISCUSSION

The calculated glucose concentration using the light-based sensor gave a positive correlation to the measured reference, with an R^2 of 0.33. This R^2 improved to 0.47 when taking the average measurement at the measured sites for each invasive reference measurement. However, these values are likely influenced by the outliers present in the neonate wrist data. The R^2_{TLS} of the mean data returned a value of 0.77. This R^2_{TLS} is expected to be higher than the conventional R^2 as the perpendicular distance to the best fit line. rather than the y distance is taken.

The measured range of $2.2\,\mathrm{mmol\,l^{-1}}$ to $8.0\,\mathrm{mmol\,l^{-1}}$ provided a spectrum covering the healthy range, $4.0\,\mathrm{mmol\,l^{-1}}$ to $8.0\,\mathrm{mmol\,l^{-1}}$, while also covering concentrations that would indicate hypoglycaemia. An advantage of conducting the NICU trial was the

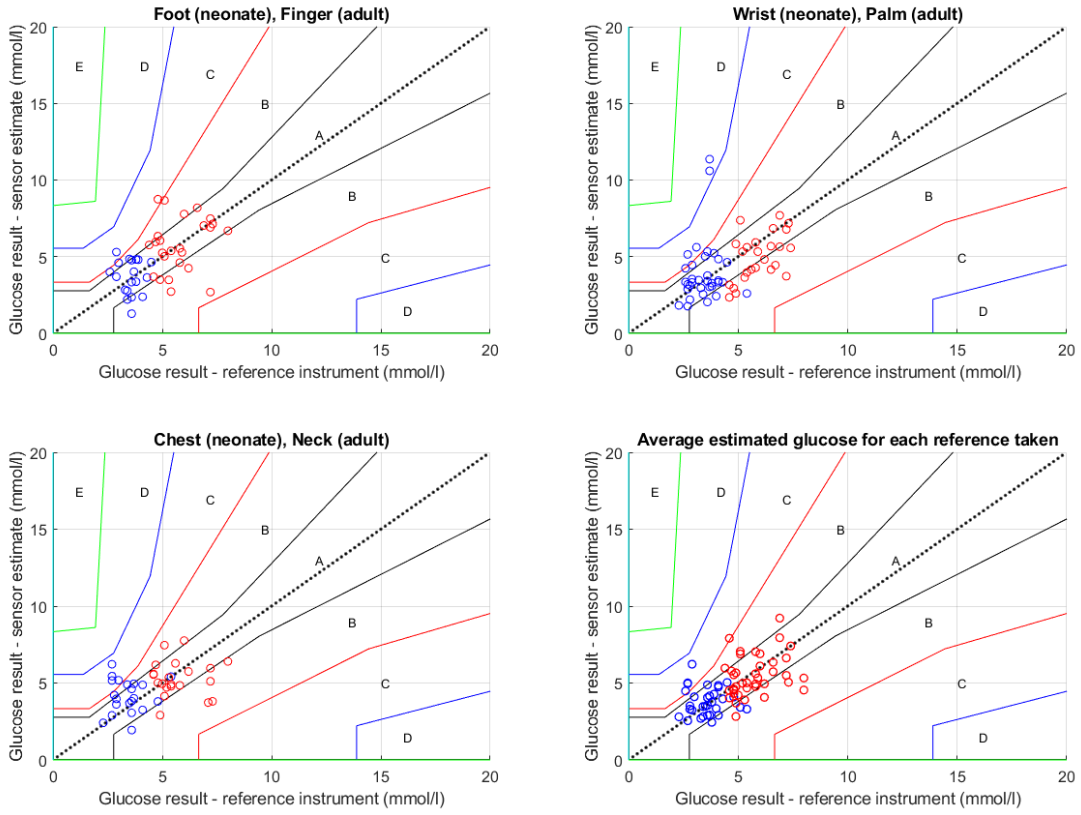

Figure 12.11 Clarke Error grid for the calculated light-based glucose sensor compared to a reference glucometer measurement separated into the recorded sites. The bottom right CEG plots the average of each site for each invasive reference taken, with an $R^2 = 0.47$. The blue data is recorded from neonates, and the red data from adults.

ability to gain access to these low glucose concentrations, which are not feasible to induce in adults without rising hypoglycaemia. However, this range needs to extend further into the hyperglycaemia range to give a true reading of the model fit. Equally, as seen in a CEG, accuracy is less important in how it impacts clinical decisions at these higher BGC levels.

The goal MARD for the sensor was a 20% error across the full range of measured glucose. While the raw output from the model only generated a MARD of 28% across the measured range, the MARD at the foot demonstrated a MARD of 24% $<3.5\,\mathrm{mmol\,l^{-1}}$ and 25% $\geq 3.5\,\mathrm{mmol\,l^{-1}}$. While these individual MARD values did not reach the goal 20%, taking the average read from each site returned an overall MARD of 19%, achieving the set goal.

The R^2 value calculated at each of the sites returned a negative value. This means that fitting to the mean of the data points returns less error than to the line of best fit. This often occurs when data is clustered, and outliers skew the line of best fit. Taking the R^2_{TLS} is a better metric as it captures the error perpendicular to the model, not just the y-axis, especially with variability in the reference measurements.

The oral glucose tolerance test is a simple test to indicate whether a sensor is capable of tracking changing glucose concentration. However, ingesting the glucose required for the test has been known to cause changes in core and surface temperature, peripheral perfusion, skin hydration, enzyme levels, and many others [Smith 2017]. As these factors also exhibit changes with glucose concentration, a sensor may instead be tracking these parameters.

While the adult trial method involved an OGTT, the NICU trial involved random time sampling, avoiding the potential correlation to different parameters than glucose. Three different sensors were used across both trials. Using these different sensors reduces the risk of each reading being senor dependent.

The data recorded from the neonates shows a smaller spread than the adults, with a higher spread at lower blood glucose concentrations. This spread is not ideal as

accuracy at lower glucose concentrations is critical to diagnosing, and treating hypoglycaemia. To account for the difference in spread between adults and neonates, separate calibrations may be required. This difference in spread is likely due to the different physiological parameters of the neonatal skin, such as, neonatal skin dermal thickness being only 60% that of adults [Fox 2011].

The influence of the RMS noise threshold for the AC component was evident in Figure 12.9. Each level of thresholding returned an increasing R^2, although the thresholding B plot further shown in Figure 12.8 was likely influenced by the two outliers in the D region. Each plot is 12.9 shows different spread data as the calibration algorithm had a different amount of data for training and testing. When calibrating using k-means clustering, the lowest noise threshold with 78 data points only had 70 data points to train and 7-8 for testing. Thus, the lower noise threshold likely requires more data before using that getting a reliable calibration.

Each site recorded gave a different spread of estimated glucose concentrations, with the neonatal foot, and adult finger having the highest correlation, but also a greater spread. The palm and wrist show promise. However, the wrist of a neonate is difficult to measure due to motion artefacts. These are the conventional sites of measurements for pulse oximeters in both neonates and adults, and will be the future site for measurements when analysing pulse glucometry. If the sensor is used without the need for finding a pulse, then the other sites may be an option, allowing incorporation of the sensor into devices such as smart watches.

Figure 12.11 plots the glucose estimation from each of the three sites, with the average at each site plotted in the bottom right figure. This average is much smoother than the raw data, implying that taking the average reading over time would reduce the error. Conventional CGMs also take the average over many readings, making this a viable method to improve sensing accuracy.

The correlation plot has a y-crossing above zero. The total least squares method was used to calculate the linear fit, as this method assumes both the light-based sensor, and the reference measurements both contain errors [Golub and van Loan 1980]. A

positive non-zero y-axis crossing point is expected due to the model not accounting for absorption in the blood or tissue influencing the returning light intensity.

Changes in glucose concentration for a person living with diabetes ranges from $2\,\mathrm{mmol\,l^{-1}}$ to $20\,\mathrm{mmol\,l^{-1}}$. While the measurements are in $\mathrm{mmol\,l^{-1}}$, there is still an order of magnitude difference across the physiological range, as shown in Chapter 10 with a clear change in absorption across this range. It is expected that in-vivo testing would have higher noise levels due to the additional interference from other molecules, as shown in the higher noise levels present in the NICU and adult testing data.

12.5 SUMMARY

This chapter covered the validation of a non-invasive, discrete NIR spectrometric glucometer through two trials, one in adults, and the other in the NICU with neonates. The sensor gave a positive, but weak correlation of $R^2 = 0.34$. Data from the neonatal foot and adult finger returned the most consistent MARD values (24% at $<3.5\,\mathrm{mmol\,l^{-1}}$ and 25% at $\geq 3.5\,\mathrm{mmol\,l^{-1}}$), and taking the average recording at each site for a reference glucose measurement achieved the 20% goal with a 19% MARD. A large portion data was unable to measure pulsatile data. However, user training and experience reduced the amount of lost data.

The results suggest there is still a way to go before the sensor is ready for any clinical use, especially at low BGC. Improvements may include calibrations to each individual, possibly daily with invasive measurements. Additional testing is needed in adults at a higher glucose range than presented in this trial. This higher range will provide greater insight into the accuracy of the model and the calibrated best fit.

The sensor shows promise for non-invasive glucose measurement, especially with an improved model and data averaging. Non-invasive glucose measurements and their algorithms can play a significant role in monitoring hypoglycaemia in neonates, as well as providing a pain free monitoring method for adults.

Chapter 13

CONCLUSIONS

The aim of this thesis was to develop non-invasive, optical methods of monitoring important dynamic physiological variables, venous oxygen saturation, pulse wave velocity, and blood glucose concentration. These goal measurements assess key metrics needed to provide better care. The thesis achieved this goal, with each key measurement validated against gold standard reference measurements (BGC), or where this was not possible, against literature values ($SpjvO_2$ and PWV).

Achieving the aim of this thesis required development of a non-invasive reflectance photoplethysmograph (PPG) sensor capable of using multiple different wavelength LEDs to both emit and detect the returning light. This novel sensor provides discrete wavelength spectroscopy using LEDs of different wavelengths. The digital method of sensing lowers the complexity and cost of pulse oximeter design. A model was developed for the voltage decay of the reverse biased LED under varying light conditions, using an ADC to increase the sensor sample rate. This ADC method of detection is a novel adaption of the conventional digital timing method of voltage decay.

The sensor developed was successfully adapted to measure the jugular venous pulse (JVP), as well as estimate the jugular venous oxygen saturation. A study of 15 subjects all returned a visible JVP, allowing the estimation of oxygen saturation, with a mean $SpjvO_2$ of 82.4 $\pm$5.2%. The novel contribution of this sensor is the contribution of a non-invasive central venous oxygen saturation measurement. An adapted pulse oximeter calibration equation was also used to estimate $SpjvO_2$ from the breathing induced pulse in the neck. While the senor did estimate $SpjvO_2$ in the higher range, this was expected

as the healthy test subjects were at rest, lying supine, where the brain would consume minimal additional oxygen.

A sensor capable of sampling the pulse at two points local to an artery using PPG signals was developed. This sensor sampled at 3 kHz to measure the PWV in the artery. A signal processing method of calculating PWV using the phase difference across multiple beats improved the results of the sensor (SD of $\pm 0.6\,\mathrm{m\,s^{-1}}$, and CoV of 20%), compared to the gold standard "foot-foot" method (SD of $\pm 1.2\,\mathrm{m\,s^{-1}}$, and CoV of 58%). The phase difference method performs better under high noise levels, and when the features of the arterial pulse waveform are difficult to identify. The novel contribution of this sensor included the ability to measure the arterial pulse waveform using an array of LEDs placed over either the carotid artery, or radial artery.

The final sensor developed used six different wavelength LEDs to isolate the spectral fingerprint of glucose in blood. Initial testing in porcine blood showed a clear relationship between the LED light absorption and BGC. A subsequently improved version of the sensor used, novel, discrete spectrometry with the ADC sensing method to estimate the BGC in humans. Trials conducted in adults and neonates returned a MARD of 19%, achieving the goal of developing a sensor with a MARD <20%. The sensor is a novel contribution towards non-invasive NIR measurement, both in adults and neonates.

Chapter 14

FUTURE WORK

The overall goal of this thesis was dedicated to developing a sensor capable to detecting light using the LED-LED detection method for the use in biomedical applications. There is much work to be done to improve the accuracy of the sensor for each of the applications presented in this thesis:

14.1 SENSOR DESIGN

In early versions of the sensor, the accuracy was proportional to the clock speed of the microcontroller timing the voltage decay of the reverse biased LED. However, the current microcontroller using the digital timing method is the ARM Cortex-M7, running at 600 MHz, and is currently one of the fastest consumer microcontrollers available. The accuracy the sensor is likely no longer proportional to the sample rate, and thus, possible improvements to the sensor outside of the microcontroller include:

- A dedicated pulse oximeter LED driver to reduce voltage jitter on the emitting LED. The current LED driver is designed for consumer products, rather than precision LED driving, so replacing the driver would reduce noise introduced by the emitting LED.

- The ADC method uses a 24-bit ADC capable of sampling at 33 kHz, giving fewer than 10 voltage reads during high light intensities. While the accuracy of the ADC is sufficient, a higher sample rate ADC with a 16-bit resolution would provide a

more useful output as the ADC can sample more points along the LED decay waveform.

- The emitter-detector separation varied throughout the thesis, ranging from 2 mm to 10 mm. For the 1450 nm to 1650 nm LEDs, the smaller the separation, the better, with the 2 mm spacing returning the largest response to incident light. Thus, future LED layout could utilise a spacing of 2 mm for the 1450 nm to 1650 nm LEDs, and a greater separation for the 660 nm to 940 nm LEDs due to the reduced absorption at these wavelengths.

14.2 VENOUS OXYGEN SENSING

The venous oxygen sensor returned $SpjvO_2$ values in the expected physiological range when compared to literature. However, the sensor requires a validation against the gold standard venous bulb catheter measured SvO_2. The sensor returned clear JVP waveforms. However, converting the sensor to a small patch that could be taped over the EJV would reduce motion artefacts, and the external pressure applied by the sensor, reducing the risk of collapsing the vein. Using the breathing induced pulsatile signal appears to have more potential than the JVP directly. As the use case of the sensor is likely in the hospital, the respiratory rate would also be of use.

14.3 PULSE WAVE VELOCITY SENSING

Literature has not yet been able to develop a PWV sensor capable of simple, reliable measurement of PWV. The sensor developed in this thesis would require improvements to return more viable results. Migrating the LED driver board and sensor board to a single board would reduce the noise coupled into the circuit. The middle sensing LED did not return usable results on either of the two sensors, so only the LEDs placed at the edges of the sensor are required for sensing. The separation between the two sensing sites could increase from 40 mm to 50 mm, giving a 20% increase in PTT. Validation against gold standard measurements, either invasively, or through Doppler ultrasound.

14.4 NON-INVASIVE GLUCOSE SENSING

The discrete LED-LED spectrometer showed a clear change in light absorption, proportional to glucose concentration. However, in-vivo testing in humans highlighted key improvements.

- Over 40% of the reads across the adult and neonatal trial did not return a pulsatile signal. This rate improved with further training and understanding of how the sensor worked. Thus, the sensor needs to remove the user variability, likely by being attached to the skin, rather than held on by the user, as the user introduces additional pressure and motion artefacts. A sensor similar to a conventional pulse oximeter finger-clip would reduce this error, although a smart watch style sensor would be more friendly at a trade off of lower pulsatile signal strength.
- The sensor had to use the RMS method of calculating the AC component of the signal. Reducing the LED emitter-detector separation would increase the amount of light returning to the sensor, potentially improving the pulsatile signal.
- There is the potential that the sensor may not need to read the pulsatile signal. Many NIR glucose sensors look at the interstitial glucose concentration, similar to conventional CGMs. Removing the need for an arterial pulse allows a greater range in sensor placement, such as the upper arm, or wrist.

Appendix A

VENOUS OXYGEN SENSING

A.1 DRIVE BOARD AND SENSE BOARD SCHEMATICS

The KiCad schematic files are included here. All design files including the Schematics, Gerber files, Arduino code, and STL files can be found online at an Open Science Framework repository:

https://doi.org/10.17605/OSF.IO/VA3JW

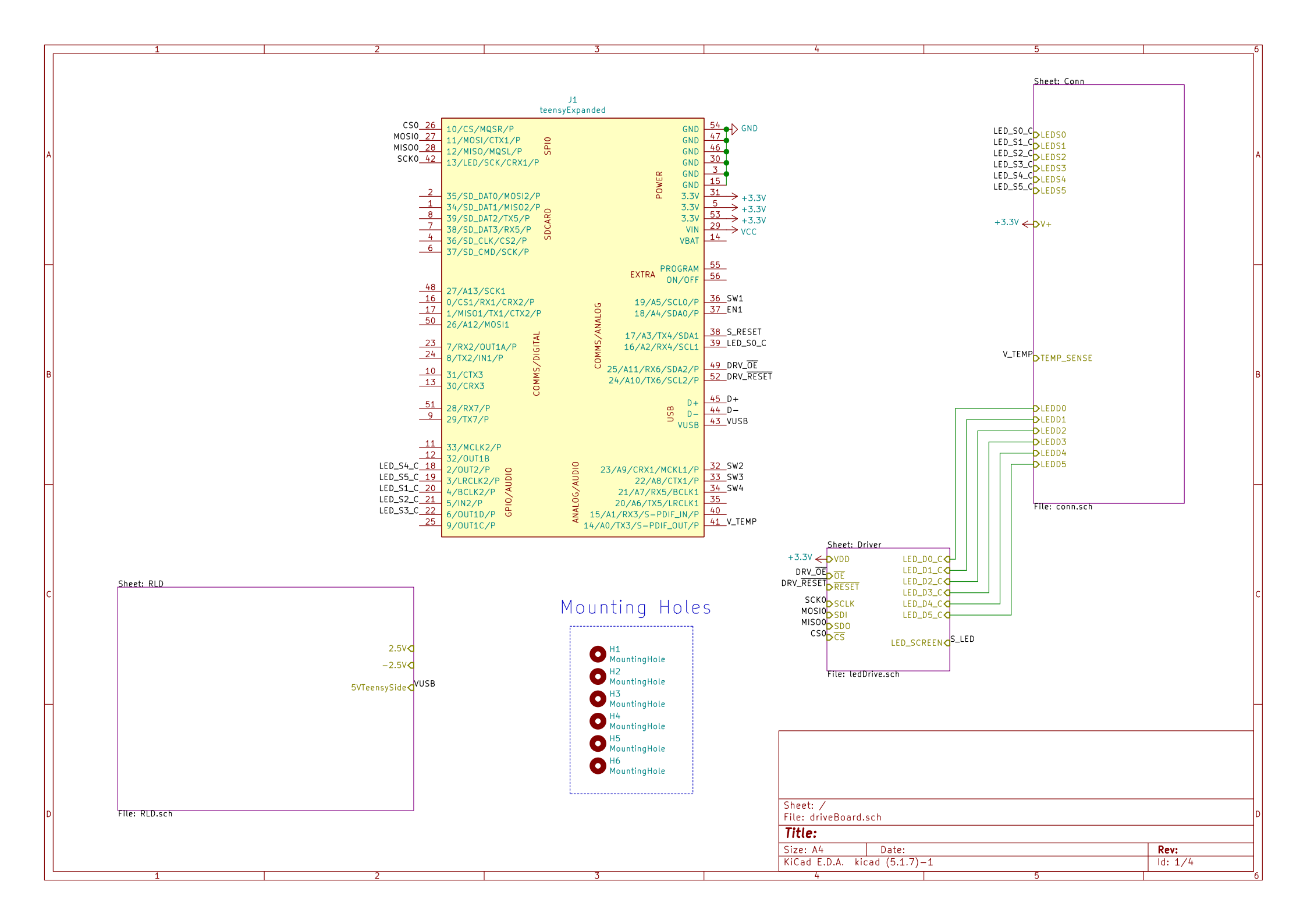
J1
teensyExpanded
CS0 26
MOSI0 27
MISO0 28
SCK0 42
SPI0
10/CS/MQSR/P
11/MOSI/CTX1/P
12/MISO/MQSL/P
13/LED/SCK/CRX1/P
2
1
8
7
4
6
SDCARD
35/SD_DAT0/MOSI2/P
34/SD_DAT1/MISO2/P
39/SD_DAT2/TX5/P
38/SD_DAT3/RX5/P
36/SD_CLK/CS2/P
37/SD_CMD/SCK/P
48
16
17
50
23
24
10
13
51
9
11
12
LED_S4_C 18
LED_S5_C 19
LED_S1_C 20
LED_S2_C 21
LED_S3_C 22
25
COMMS/DIGITAL
27/A13/SCK1
0/CS1/RX1/CRX2/P
1/MISO1/TX1/CTX2/P
26/A12/MOSI1
7/RX2/OUT1A/P
8/TX2/IN1/P
31/CTX3
30/CRX3
28/RX7/P
29/TX7/P
33/MCLK2/P
32/OUT1B
2/OUT2/P
3/LRCLK2/P
4/BCLK2/P
5/IN2/P
6/OUT1D/P
9/OUT1C/P
GPIO/AUDIO
POWER
GND 54
GND 47
GND 46
GND 30
GND 3
GND 15
3.3V 31
3.3V 5
3.3V 53
VIN 29
VBAT 14
GND
+3.3V
+3.3V
+3.3V
VCC
EXTRA
PROGRAM 55
ON/OFF 56
COMMS/ANALOG
19/A5/SCL0/P 36 SW1
18/A4/SDA0/P 37 EN1
17/A3/TX4/SDA1 38 S_RESET
16/A2/RX4/SCL1 39 LED_S0_C
25/A11/RX6/SDA2/P 49 DRV_OE
24/A10/TX6/SCL2/P 52 DRV_RESET
USB
D+ 45 D+
D− 44 D−
VUSB 43 VUSB
ANALOG/AUDIO
23/A9/CRX1/MCKL1/P 32 SW2
22/A8/CTX1/P 33 SW3
21/A7/RX5/BCLK1 34 SW4
20/A6/TX5/LRCLK1 35
15/A1/RX3/S-PDIF_IN/P 40
14/A0/TX3/S-PDIF_OUT/P 41 V_TEMP
Sheet: Conn
LED_S0_C LEDS0
LED_S1_C LEDS1
LED_S2_C LEDS2
LED_S3_C LEDS3
LED_S4_C LEDS4
LED_S5_C LEDS5
+3.3V V+
V_TEMP TEMP_SENSE
LEDD0
LEDD1
LEDD2
LEDD3
LEDD4
LEDD5
File: conn.sch
Sheet: Driver
+3.3V VDD
DRV_OE OE
DRV_RESET RESET
SCK0 SCLK
MOSI0 SDI
MISO0 SDO
CS0 CS
LED_D0_C
LED_D1_C
LED_D2_C
LED_D3_C
LED_D4_C
LED_D5_C
LED_SCREEN S_LED
File: ledDrive.sch
Sheet: RLD
2.5V
−2.5V
5VTeensySide VUSB
File: RLD.sch
Mounting Holes
H1 MountingHole
H2 MountingHole
H3 MountingHole
H4 MountingHole
H5 MountingHole
H6 MountingHole
Sheet: /
File: driveBoard.sch
Title:
Size: A4
Date:
Rev:
KiCad E.D.A. kicad (5.1.7)-1
Id: 1/4

Decoupling Capacitors

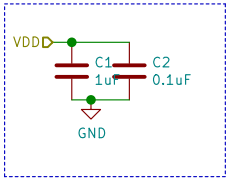

LED Driver

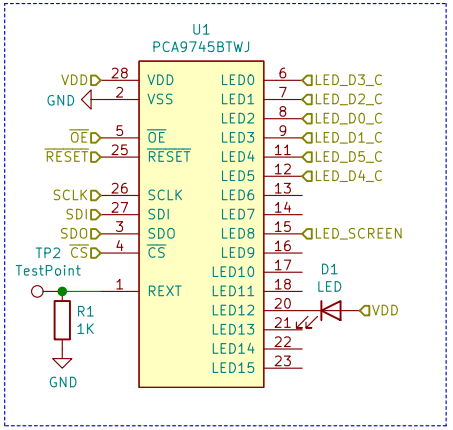

Sheet: /Driver/ File: ledDrive.sch		
Title:		
Size: A4	Date:	**Rev:**
KiCad E.D.A. kicad (5.1.7)-1		Id: 2/4

Electrodes

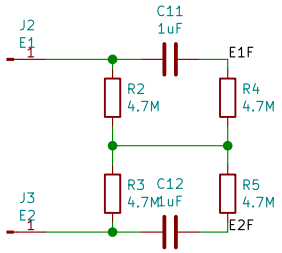

Right Leg Driver

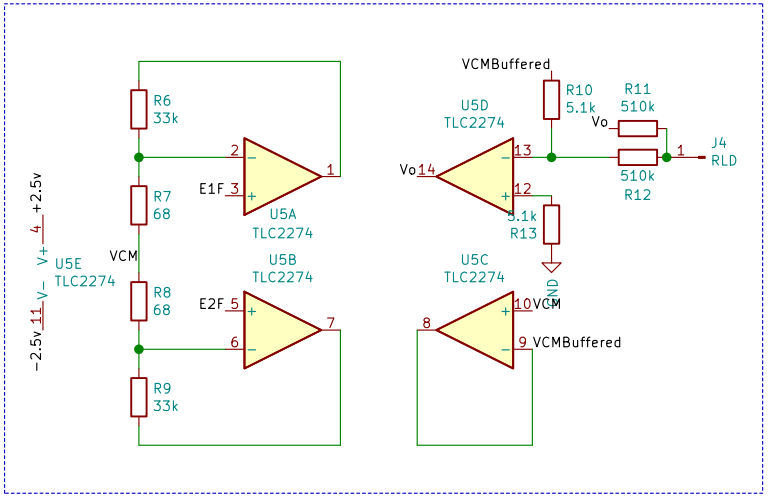

Regulators

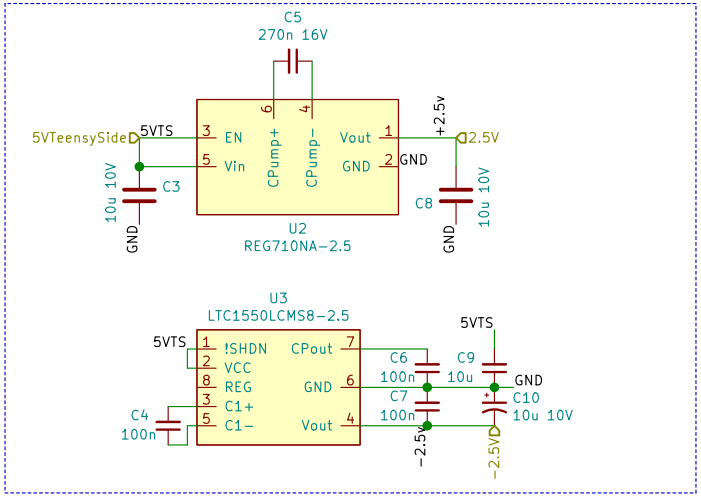

Decoupling Capacitors

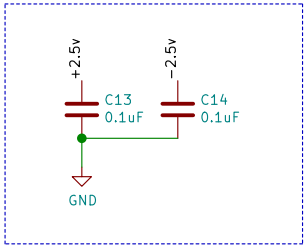

Test Points

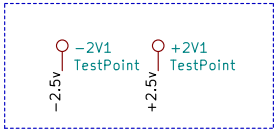

Sheet: /RLD/ File: RLD.sch		
Title:		
Size: A4	Date:	**Rev:**
KiCad E.D.A. kicad (5.1.7)−1		Id: 3/4

Fuse

FPC Connector

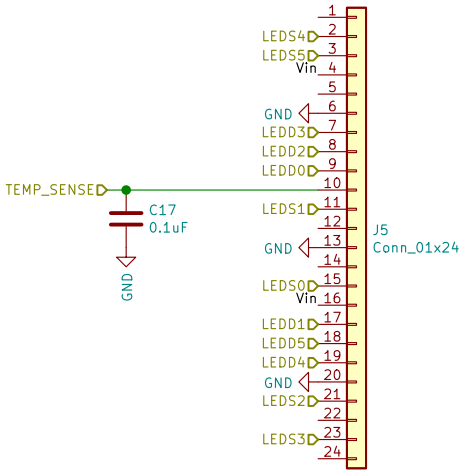

Decoupling Capacitors

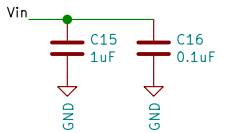

Sheet: /Conn/ File: conn.sch		
Title:		
Size: A4	Date:	**Rev:**
KiCad E.D.A. kicad (5.1.7)-1		Id: 4/4

FPC Cable

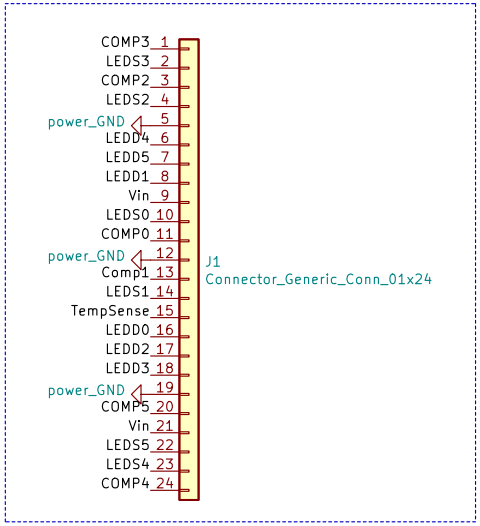

Detecting LEDs

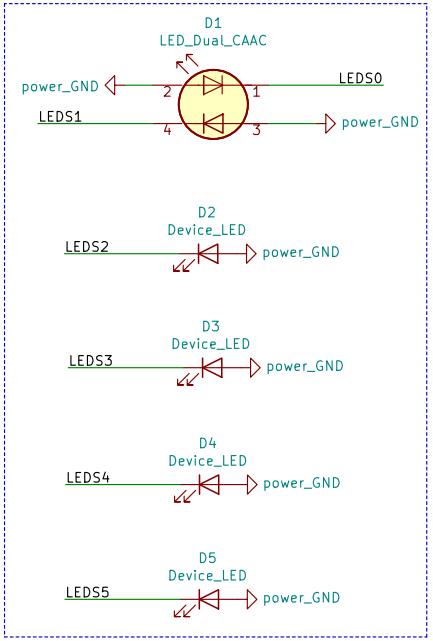

Emitting LEDs

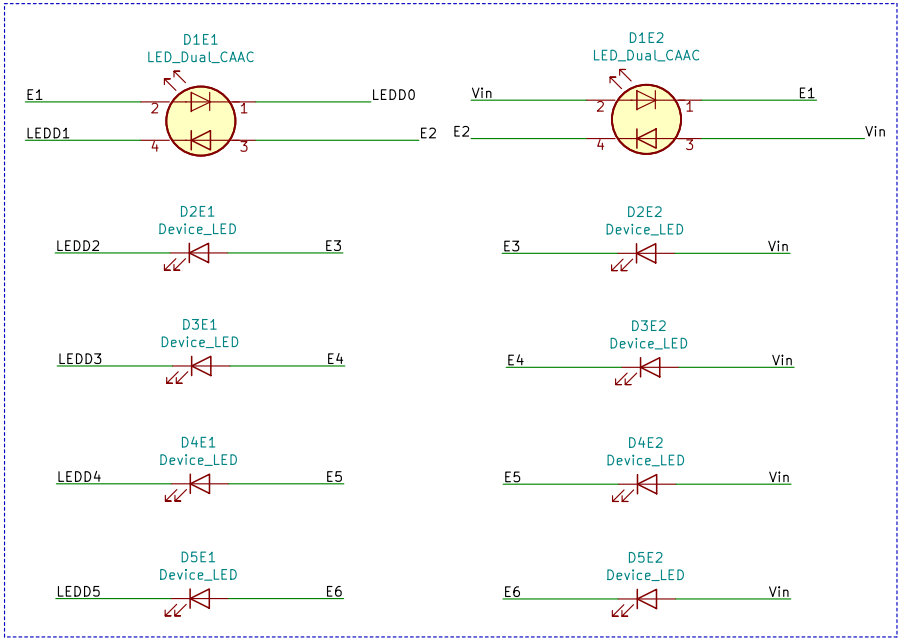

Temperature Sensor

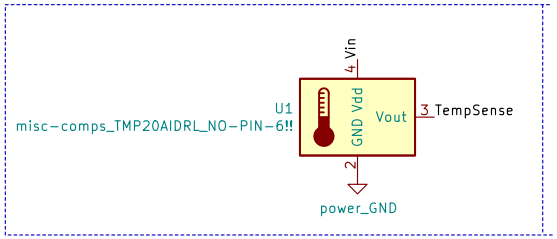

Decoupling Capacitors

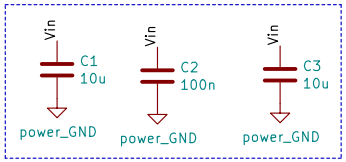

Sheet: /		
File: led-pcb-1.sch		
Title:		
Size: A4	Date:	**Rev:**
KiCad E.D.A. kicad (5.1.7)-1		Id: 1/1

Table A.1 BOM for the LED drive board and the LED sense board.

Designator	Component	Num	Unit Cost ($USD)	Tot Cost ($USD)	Source of Materials
Driver board					
J1-1	Teensy 4.0	1	$19.95	$19.95	PJRC
J1-2	Teensy 4.0 hat	1	$6.30	$6.30	OshPark
J2,J3,J4	1 pos header	3	$0.05	$0.15	Digi-Key
J5	24 pin FPC	1	$1.58	$1.58	Digi-Key
J6	14 pos header	2	$1.08	$2.16	Digi-Key
H7	2 pos header	1	$0.21	$0.21	Digi-Key
H8	5" FPC cable	1	$5.99	$5.99	Digi-Key
F1	200 mA Fuse	1	$0.73	$0.73	Digi-Key
U1	LED driver	1	$3.32	$3.32	Digi-Key
U2	2.5V regulator	1	$1.74	$1.74	Digi-Key
U3	-2.5V regulator	1	$6.45	$6.45	Digi-Key
U5	Quad op-amp	1	$2.60	$2.60	Digi-Key
R1	Resistor 1 kΩ	1	$0.10	$0.10	Digi-Key
R2,R3,R4,R5	Resistor 4.7 MΩ	4	$0.17	$0.68	Digi-Key
R7,R8	Resistor 68 Ω	2	$0.11	$0.22	Digi-Key
R6,R9	Resistor 33 kΩ	2	$0.25	$0.50	Digi-Key
R10,R13	Resistor 5.1 kΩ	2	$0.11	$0.22	Digi-Key
R11.R12	Resistor 510 kΩ	2	$0.11	$0.22	Digi-Key
C2,C4,C6,C7,C13, C14,C16,C17	Cap 100 nF 16 V	8	$0.11	$0.88	Digi-Key
C1,C11,C12,C15	Cap 1 µF 6.3 V	4	$0.11	$0.44	Digi-Key
C3,C8,C9	Cap 10 µF 10 V	3	$0.11	$0.33	Digi-Key
C5	Cap 270 nF 16 V	1	$0.28	$0.28	Digi-Key
C10	Cap 10 µF 10 V	1	$0.38	$0.38	Digi-Key
Total Driver Board Cost:				$56	
Sensor board					
J1	24 pin FPC	1	$1.58	$1.58	Digi-Key
U1	Temp sensor	1	$1.48	$1.48	Digi-Key
D1	LED (660,940nm)	3	$1.48	$4.44	Digi-Key
D2	LED (850nm)	3	$0.33	$0.99	Digi-Key
D3	LED (1450nm)	3	$22.25	$66.74	Digi-Key
D4	LED (1550nm)	3	$13.79	$41.37	Digi-Key
D5	LED (1650nm)	3	$22.25	$66.74	Digi-Key
C1,C3	Cap 10 µF	1	$0.35	$0.7	Digi-Key
C2	Cap 100 nF	1	$0.11	$0.11	Digi-Key
E1,E2,RLD	99.99% Silver Electrodes 1 mm	60 mm	$8.30	$0.5	Regal
Total Sense Board Cost:				$184	
PCBway PCB (5 of each board):				$20	
3D Printing Cost (16 g)				$1	
Total Cost:				$261	
Total Cost without specialist LEDs:				$86	

Appendix B

CO-AUTHORSHIP FORMS

The co-authorship forms are included below.

UNIVERSITY OF CANTERBURY
Te Whare Wānanga o Waitaha
CHRISTCHURCH NEW ZEALAND

Deputy Vice-Chancellor's Office
Postgraduate Research Office

Co-Authorship Form

This form is to accompany the submission of any thesis that contains research reported in co-authored work that has been published, accepted for publication, or submitted for publication. A copy of this form should be included for each co-authored work that is included in the thesis. Completed forms should be included at the front (after the thesis abstract) of each copy of the thesis submitted for examination and library deposit.

Please indicate the chapter/section/pages of this thesis that are extracted from co-authored work and provide details of the publication or submission from the extract comes:

Chapter in thesis: 4

Publication type: Journal (submitted)

*Publication: **J. D. Campbell**, L R Mckenzie, C. G. Pretty, P. Bones, and J. G. Chase, "Digital Sensing LED Emission and Detection Array for Pulse Oximetry" Submitted to HardwareX*

Please detail the nature and extent (%) of contribution by the candidate:

90%

The candidate developed the hypothesis, method and software, conducted the trials, analysed the data, and wrote the article.

The candidate worked with a co-author on the circuit design, and producing the hardware. Co-authors also provided help in discussing the methods, results, and editing

Certification by Co-authors:

If there is more than one co-author then a single co-author can sign on behalf of all

The undersigned certifies that:

- The above statement correctly reflects the nature and extent of the Doctoral candidate's contribution to this co-authored work
- In cases where the candidate was the lead author of the co-authored work he or she wrote the text

Name: *Chris Pretty* Signature: *Chris Pretty* Date: *09/12/2021*

UNIVERSITY OF CANTERBURY
Te Whare Wānanga o Waitaha
CHRISTCHURCH NEW ZEALAND

Deputy Vice-Chancellor's Office
Postgraduate Research Office

Co-Authorship Form

This form is to accompany the submission of any thesis that contains research reported in co-authored work that has been published, accepted for publication, or submitted for publication. A copy of this form should be included for each co-authored work that is included in the thesis. Completed forms should be included at the front (after the thesis abstract) of each copy of the thesis submitted for examination and library deposit.

Please indicate the chapter/section/pages of this thesis that are extracted from co-authored work and provide details of the publication or submission from the extract comes:

Chapter in thesis: 5

Publication type: Conference

*Publication: **J. Campbell**, C. Pretty, G. Chase, and P. J. Bones, "A Robust Method of a Peak Detection in Noisy PPG Signals Using a Structure of IIR Filters," in 2018 14th IEEE\ASME International Conference on Mechatronic and Embedded Systems and Applications (MESA), Oulu, Finland, Jul. 2018, vol. 14}*

Please detail the nature and extent (%) of contribution by the candidate:

90%

The candidate developed the hypothesis, method and software, conducted the trials, analysed the data, and wrote the article.

Co-authors also provided help in discussing the methods, algorithm design, results, and editing

Certification by Co-authors:

If there is more than one co-author then a single co-author can sign on behalf of all

The undersigned certifies that:

- The above statement correctly reflects the nature and extent of the Doctoral candidate's contribution to this co-authored work
- In cases where the candidate was the lead author of the co-authored work he or she wrote the text

Name: Chris Pretty Signature: Chris Pretty Date: 09/12/2021

UNIVERSITY OF CANTERBURY
Te Whare Wānanga o Waitaha
CHRISTCHURCH NEW ZEALAND

Deputy Vice-Chancellor's Office
Postgraduate Research Office

Co-Authorship Form

This form is to accompany the submission of any thesis that contains research reported in co-authored work that has been published, accepted for publication, or submitted for publication. A copy of this form should be included for each co-authored work that is included in the thesis. Completed forms should be included at the front (after the thesis abstract) of each copy of the thesis submitted for examination and library deposit.

Please indicate the chapter/section/pages of this thesis that are extracted from co-authored work and provide details of the publication or submission from the extract comes:

Chapter in thesis: 5

Publication type: Conference

*Publication: **J. Campbell**, C. Pretty, J. G. Chase, and P. J. Bones, "Near-Real-Time Detection of Pulse Oximeter PPG Peaks Using Wavelet Decomposition," in 10th IFAC Symposium on Biological and Medical Systems, Sao Paulo, Brazil, Sep. 2018, pp. 181–186.*

Please detail the nature and extent (%) of contribution by the candidate:

90\%

The candidate developed the hypothesis, method and software, conducted the trials, analysed the data, and wrote the article.

Co-authors also provided help in discussing the methods, algorithm design, results, and editing

Certification by Co-authors:

If there is more than one co-author then a single co-author can sign on behalf of all

The undersigned certifies that:

- The above statement correctly reflects the nature and extent of the Doctoral candidate's contribution to this co-authored work
- In cases where the candidate was the lead author of the co-authored work he or she wrote the text

Name: Chris Pretty Signature: Chris Pretty Date: 09/12/2021

UNIVERSITY OF CANTERBURY
Te Whare Wānanga o Waitaha
CHRISTCHURCH NEW ZEALAND

Deputy Vice-Chancellor's Office
Postgraduate Research Office

Co-Authorship Form

This form is to accompany the submission of any thesis that contains research reported in co-authored work that has been published, accepted for publication, or submitted for publication. A copy of this form should be included for each co-authored work that is included in the thesis. Completed forms should be included at the front (after the thesis abstract) of each copy of the thesis submitted for examination and library deposit.

Please indicate the chapter/section/pages of this thesis that are extracted from co-authored work and provide details of the publication or submission from the extract comes:

Chapter in thesis: 7

Publication type: Conference

*Publication: **J. D. Campbell**, L. Holder-Pearson, C. G. Pretty, P. Bones, and J. G. Chase, "Pulse Wave Velocity Measurement in the Carotid Artery Using an LED-LED Array Pulse Oximeter," in 21st IFAC World Congress, 2020, vol. 53*

Please detail the nature and extent (%) of contribution by the candidate:

80\%

The candidate developed the hypothesis, method and software, conducted the trials, analysed the data, and wrote the article.

The candidate worked with a co-author on the circuit design, and producing the hardware, and an additional co-author on the algorithm design.

Co-authors also provided help in discussing the methods, results, and editing

Certification by Co-authors:

If there is more than one co-author then a single co-author can sign on behalf of all

The undersigned certifies that:

- The above statement correctly reflects the nature and extent of the Doctoral candidate's contribution to this co-authored work
- In cases where the candidate was the lead author of the co-authored work he or she wrote the text

Name: Chris Pretty Signature: Chris Pretty Date: 09/12/2021

UNIVERSITY OF CANTERBURY
Te Whare Wānanga o Waitaha
CHRISTCHURCH NEW ZEALAND

Deputy Vice-Chancellor's Office
Postgraduate Research Office

Co-Authorship Form

This form is to accompany the submission of any thesis that contains research reported in co-authored work that has been published, accepted for publication, or submitted for publication. A copy of this form should be included for each co-authored work that is included in the thesis. Completed forms should be included at the front (after the thesis abstract) of each copy of the thesis submitted for examination and library deposit.

Please indicate the chapter/section/pages of this thesis that are extracted from co-authored work and provide details of the publication or submission from the extract comes:

Chapter in thesis: 8

Publication type: Journal (submitted)

Publication: J. D. Campbell, C. G. Pretty ,Rachel Smith, P. Bones, and J. G. Chase Peripheral Pulse Wave Velocity Measurement with the Phase Difference Method, Submitted to Biomedical Signal Processing and Control.

Please detail the nature and extent (%) of contribution by the candidate:

80%

The candidate developed the hypothesis, method and software, analysed the data, and wrote the article.

A co-author provided the gold standard reference algorithm and data for validations of the methods.

Additional co-authors provided help in discussing the methods, algorithm design, results, and editing.

Certification by Co-authors:

If there is more than one co-author then a single co-author can sign on behalf of all

The undersigned certifies that:

- The above statement correctly reflects the nature and extent of the Doctoral candidate's contribution to this co-authored work
- In cases where the candidate was the lead author of the co-authored work he or she wrote the text

Name: Chris Pretty Signature: Chris Pretty Date: 09/12/2021

UNIVERSITY OF CANTERBURY
Te Whare Wānanga o Waitaha
CHRISTCHURCH NEW ZEALAND

Deputy Vice-Chancellor's Office
Postgraduate Research Office

Co-Authorship Form

This form is to accompany the submission of any thesis that contains research reported in co-authored work that has been published, accepted for publication, or submitted for publication. A copy of this form should be included for each co-authored work that is included in the thesis. Completed forms should be included at the front (after the thesis abstract) of each copy of the thesis submitted for examination and library deposit.

Please indicate the chapter/section/pages of this thesis that are extracted from co-authored work and provide details of the publication or submission from the extract comes:

Chapter in thesis: 10

Publication type: Conference

*Publication: **J. D. Campbell**, L. Holder-Pearson, C. G. Pretty, P. Bones, and J. G. Chase, "Pulse Wave Velocity Measurement in the Carotid Artery Using an LED-LED Array Pulse Oximeter," in 21st IFAC World Congress, 2020, vol. 53*

Please detail the nature and extent (%) of contribution by the candidate:

80%

The candidate developed the hypothesis, method and software, analysed the data, and wrote the article.

A co-author helped conduct the trial and another helped design the sensing hardware.

Additional co-authors provided help in discussing the methods, algorithm design, results, and editing.

Certification by Co-authors:

If there is more than one co-author then a single co-author can sign on behalf of all

The undersigned certifies that:

- The above statement correctly reflects the nature and extent of the Doctoral candidate's contribution to this co-authored work
- In cases where the candidate was the lead author of the co-authored work he or she wrote the text

Name: *Chris Pretty* Signature: *Chris Pretty* Date: *09/12/2021*

UNIVERSITY OF CANTERBURY
Te Whare Wānanga o Waitaha
CHRISTCHURCH NEW ZEALAND

Deputy Vice-Chancellor's Office
Postgraduate Research Office

Co-Authorship Form

This form is to accompany the submission of any thesis that contains research reported in co-authored work that has been published, accepted for publication, or submitted for publication. A copy of this form should be included for each co-authored work that is included in the thesis. Completed forms should be included at the front (after the thesis abstract) of each copy of the thesis submitted for examination and library deposit.

Please indicate the chapter/section/pages of this thesis that are extracted from co-authored work and provide details of the publication or submission from the extract comes:

Chapter in thesis: 11

Publication type: Conference

*Publication: **J. Campbell**, C. G. Pretty, J. Knopp, P. Bones, and J. G. Chase, "A model for the digital method of measuring LED incident photocurrent," in ASME 2021 International Design Engineering Technical Conferences \& Computers and Information in Engineering Conference, Online, Virtual, 2021, p. 9.*

Please detail the nature and extent (%) of contribution by the candidate:

90%

The candidate developed the hypothesis, method and software, conducted the trials, analysed the data, and wrote the article.

A co-author helped design the concept of the algorithm.

Co-authors also provided help in discussing the methods, algorithm design, results, and editing

Certification by Co-authors:

If there is more than one co-author then a single co-author can sign on behalf of all

The undersigned certifies that:

- The above statement correctly reflects the nature and extent of the Doctoral candidate's contribution to this co-authored work
- In cases where the candidate was the lead author of the co-authored work he or she wrote the text

Name: *Chris Pretty* Signature: *Chris Pretty* Date: *09/12/2021*

REFERENCES

Abd Rahim, I.M., Abdul Rahim, H., Ghazali, R., Ismail, R. and Omar, J. (2016), 'Glucose Detection In Blood Using Near-Infrared Spectroscopy: Significant Wavelength For Glucose Detection', *Jurnal Teknologi*, Vol. 78, No. 7-4.

Abdallah, O. and Bolz, A. (2011), 'Adaptive filtering by non-invasive vital signals monitoring and diseases diagnosis', In L. Garcia Morales (editor), *Adaptive Filtering Applications*, InTech.

Abdallah, O., Schoenegg, M. and Bolz, A. (2007), 'Comparison between Different Pulse Hemometer Sensors by Monitoring Fractional Oxygen Saturation of Hemoglobin', In R. Magjarevic and J.H. Nagel (editors), *World Congress on Medical Physics and Biomedical Engineering 2006*, Vol. 14, pp. 668–671, Springer Berlin Heidelberg, Berlin, Heidelberg.

Abdulkareem, M.B. (2018), 'Design and Development of Multimodal Medical Image Fusion using Discrete Wavelet Transform', In *2018 Second International Conference on Inventive Communication and Computational Technologies (ICICCT)*, pp. 1629–1633.

Aboy, M., McNames, J., Throng, T., Tsunami, D., Ellenby, M.S. and Goldstein, B. (2005), 'An automatic beat detection algorithm for pressure signals', *IEEE Transactions on Biomedical Engineering*, Vol. 52, No. 10, pp. 1662–1670.

Achakri, H., Rachev, A., Stergiopulos, N. and Meister, J.J. (1994), 'A theoretical investigation of low frequency diameter oscillations of muscular arteries', *Annals of biomedical engineering*, Vol. 22, No. 3, pp. 253–263.

Alian, A.A. and Shelley, K.H. (2014), 'Photoplethysmography', *Best Practice & Research Clinical Anaesthesiology*, Vol. 28, No. 4, pp. 395–406.

Allen, J. (2007), 'Photoplethysmography and its application in clinical physiological measurement', *Physiological Measurement*, Vol. 28, No. 3, pp. R1–R39.

Allwood, M.J. and Burry, H.S. (1954), 'The effect of local temperature on blood flow in the human foot', *The Journal of Physiology*, Vol. 124, No. 2, pp. 345–357.

Altshuler, G.B., Anderson, R.R. and Manstein, D. (2006), 'Method and apparatus for the selective targeting of lipid-rich tissues', Jun.

Amelard, R., Robertson, A.D., Patterson, C.A., Heigold, H., Saarikoski, E. and Hughson, R.L. (2021), 'Optical Hemodynamic Imaging of Jugular Venous Dynamics During Altered Central Venous Pressure', *arXiv:2007.11527 [physics]*, arXiv: 2007.11527.

Amerov, A.K., Chen, J. and Arnold, M.A. (2004), 'Molar Absorptivities of Glucose and other Biological Molecules in Aqueous Solutions over the First Overtone and Combination Regions of the Near-Infrared Spectrum', *Applied Spectroscopy*, Vol. 58, No. 10, pp. 1195–1204.

Amir, O., Weinstein, D., Zilberman, S., Less, M., Perl-Treves, D., Primack, H., Weinstein, A., Gabis, E., Fikhte, B. and Karasik, A. (2007), 'Continuous Noninvasive Glucose Monitoring Technology Based on Occlusion Spectroscopy', *Journal of Diabetes Science and Technology*, Vol. 1, No. 4, pp. 463–469.

Ampofo, A.G. and Boateng, E.B. (2020), 'Beyond 2020: Modelling obesity and diabetes prevalence', *Diabetes Research and Clinical Practice*, Vol. 167, p. 108362.

Analog Devices (2016), 'AD7768/AD7768-4 Datasheet', .

Analog Devices (2017), 'AD8605_8606_8608.pdf', .

Aniagyei-Mensah, G. (2014), *Noninvasive Detection of Central Venous Waveform Using Photoplethysmography*, Master's thesis, University of Ottowa, Ottowa, Canada.

Aronson, D. (2008), 'Hyperglycemia and the Pathobiology of Diabetic Complications', In E. Fisman and A. Tenenbaum (editors), *Advances In Cardiology*, Vol. 45, pp. 1–16, KARGER, Basel, iSSN: 0065-2326.

Ashraf, R., Ahmed, M., Jabbar, S., Khalid, S., Ahmad, A., Din, S. and Jeon, G. (2018), 'Content Based Image Retrieval by Using Color Descriptor and Discrete Wavelet Transform', *Journal of Medical Systems*, Vol. 42, No. 3, p. 44.

Atlas Writing Group (2021), 'European Society of Cardiology: Cardiovascular Disease Statistics 2019', *European Heart Journal*, Vol. 41, No. 1, pp. 12–85.

Auseon, A., Tran, T., Garcia, A., Hardy, C., Valavalkar, P., Moeschberger, M. and Raman, S. (2007), 'Aortic Pathophysiology by Cardiovascular Magnetic Resonance in Patients with Clinical Suspicion of Coronary Artery Disease', *Journal of Cardiovascular Magnetic Resonance*, Vol. 9, No. 1, pp. 43–48.

Baig, S., Muhammad Asif, H., Umer, T., Mumtaz, S., Shafiq, M. and Choi, J.G. (2018), 'High Data Rate Discrete Wavelet Transform-Based PLC-VLC Design for 5G Communication Systems', *IEEE Access*, Vol. 6, pp. 52490–52499, conference Name: IEEE Access.

Baker, W.B., Parthasarathy, A.B., Busch, D.R., Mesquita, R.C., Greenberg, J.H. and Yodh, A.G. (2014), 'Modified Beer-Lambert law for blood flow', *Biomedical Optics Express*, Vol. 5, No. 11, p. 4053.

Balmer, J., Pretty, C., Kamoi, S., Davidson, S., Pironet, A., Desaive, T., Shaw, G.M. and Chase, J.G. (2017), 'Electrocardiogram R-wave is an Unreliable Indicator of Pulse Wave Initialization', *IFAC-PapersOnLine*, Vol. 50, No. 1, pp. 856–861.

Balmer, J., Pretty, C., Amies, A., Desaive, T. and Chase, J.G. (2018a), 'Accurate dicrotic notch detection using adaptive shear transforms', *IFAC-PapersOnLine*, Vol. 51, No. 27, pp. 74–79.

Balmer, J., Pretty, C., Davidson, S., Desaive, T., Kamoi, S., Pironet, A., Morimont, P., Janssen, N., Lambermont, B., Shaw, G.M. and Chase, J.G. (2018b), 'Pre-ejection period, the reason why the electrocardiogram Q-wave is an unreliable indicator of pulse wave initialization', *Physiological Measurement*, Vol. 39, No. 9.

Balmer, J., Pretty, C.G., Davidson, S., Mehta-Wilson, T., Desaive, T., Smith, R., Shaw, G.M. and Chase, J.G. (2020), 'Clinically applicable model-based method, for physiologically accurate flow waveform and stroke volume estimation', *Computer Methods and Programs in Biomedicine*, Vol. 185, p. 105125.

Barker, S.J., Tremper, K. and Hyatt, J. (1989), 'Effects of MetHemoglobin on Pulse Oximetry and Mixed Venous Oximetry.', *Anesthesiology*, Vol. 70, pp. 112–117.

Bashkatov, A.N., Genina, E.A., Kochubey, V.I. and Tuchin, V.V. (2005), 'Optical properties of human skin, subcutaneous and mucous tissues in the wavelength range from 400 to 2000 nm', *Journal of Physics D: Applied Physics*, Vol. 38, No. 15, pp. 2543–2555.

Baumgartner, H., Kylmanen, K., Kantamaa, O., Karha, P. and Ikonen, E. (2018), 'LED based reference for wavelength and relative intensity', *Journal of Physics: Conference Series*, Vol. 972, p. 012010.

Beck, R.W., Brown, S.A., Lum, J.W. and Kovatchev, B.P. (2020), 'Nonadjunctive Use of Continuous Glucose Monitoring: The End of Fingersticks?', *Diabetes Technology & Therapeutics*, Vol. 22, No. 2, pp. 67–68.

Bein, B., Meybohm, P., Cavus, E., Renner, J., Tonner, P.H., Steinfath, M., Scholz, J. and Doerges, V. (2007), 'The Reliability of Pulse Contour-Derived Cardiac Output During Hemorrhage and After Vasopressor Administration', *Anesthesia & Analgesia*, Vol. 105, No. 1, pp. 107–113.

Bertram, C., Gow, B. and Greenwald, S. (1997), 'Comparison of different methods for the determination of the true wave propagation coefficient, in rubber tubes and the canine thoracic aorta', *Medical Engineering & Physics*, Vol. 19, No. 3, pp. 212–222.

Bewick, V., Cheek, L. and Ball, J. (2003), 'Statistics review 7: Correlation and regression', *Critical Care*, Vol. 7, No. 6, p. 451.

Bhardwaj, A., Bhagat, H. and Grover, V. (2015), 'Jugular venous oximetry', *Journal of Neuroanaesthesiology and Critical Care*, Vol. 02, No. 03, pp. 225–231.

Bistrian, B.R. (2001), 'Hyperglycemia and Infection: Which is the Chicken and Which is the Egg?', *Journal of Parenteral and Enteral Nutrition*, Vol. 25, No. 4, pp. 180–181.

Bland, J.M. and Altman, D.G. (1986), 'Statistical methods for assessing agreement between two methods of clinical measurement', *The Lancet*, Vol. 327, pp. 307–310.

Boland, E., Monsod, T., Delucia, M., Brandt, C.A., Fernando, S. and Tamborlane, W.V. (2001), 'Limitations of Conventional Methods of Self-Monitoring of Blood Glucose', *Diabetes Care*, Vol. 24, No. 11, p. 5.

Bommer, C., Sagalova, V., Heesemann, E., Manne-Goehler, J., Atun, R., Bärnighausen, T., Davies, J. and Vollmer, S. (2018), 'Global Economic Burden of Diabetes in Adults: Projections From 2015 to 2030', *Diabetes Care*, Vol. 41, No. 5, pp. 963–970.

Boscari, F., Galasso, S., Acciaroli, G., Facchinetti, A., Marescotti, M., Avogaro, A. and Bruttomesso, D. (2018), 'Head-to-head comparison of the accuracy of Abbott FreeStyle Libre and Dexcom G5 mobile', *Nutrition, Metabolism and Cardiovascular Diseases*, Vol. 28, No. 4, pp. 425–427.

Boughton, C.K., Tripyla, A., Hartnell, S., Daly, A., Herzig, D., Wilinska, M.E., Czerlau, C., Fry, A., Bally, L. and Hovorka, R. (2021), 'Fully automated closed-loop glucose control compared with standard insulin therapy in adults with type 2 diabetes requiring dialysis: an open-label, randomized crossover trial', *Nature Medicine*, Vol. 27, No. 8, pp. 1471–1476.

Boutouyrie, P. and Vermeersch, S. (2010), 'Determinants of pulse wave velocity in healthy people and in the presence of cardiovascular risk factors: establishing normal and reference values', *European Heart Journal*, Vol. 31, No. 19, pp. 2338–2350.

Boutouyrie, P., Briet, M., Collin, C., Vermeersch, S. and Pannier, B. (2009), 'Assessment of pulse wave velocity', *Artery Research*, Vol. 3, No. 1, pp. 3–8.

Bozkurt, A. and Onaral, B. (2004), 'Safety assessment of near infrared light emitting diodes for diffuse optical measurements', *BioMedical Engineering OnLine*, Vol. 3, p. 9.

BPAC (2021), 'Initiating insulin for people with type 2 diabetes', Article, bpac.

Branco, R.G., Garcia, P.C.R., Piva, J.P., Casartelli, C.H., Seibel, V. and Tasker, R.C. (2005), 'Glucose level and risk of mortality in pediatric septic shock', *Pediatric Critical Care Medicine*, Vol. 6, No. 4, pp. 470–472.

Butlin, M. and Qasem, A. (2016), 'Large Artery Stiffness Assessment Using SphygmoCor Technology', *Pulse*, Vol. 4, No. 4, pp. 180–192.

Calabia, J., Torguet, P., Garcia, M., Garcia, I., Martin, N., Guasch, B., Faur, D. and Vallés, M. (2011), 'Doppler ultrasound in the measurement of pulse wave velocity: agreement with the Complior method', *Cardiovascular Ultrasound*, Vol. 9, No. 1, p. 13.

Campbell, J.D., Holder-Pearson, L., Pretty, C.G., Bones, P. and Chase, J.G. (2020), 'Pulse Wave Velocity Measurement in the Carotid Artery Using an LED-LED Array Pulse Oximeter', In *21st IFAC World Congress*, Vol. 53, pp. 16031–16036.

Cao, Q., Zhegalova, N.G., Wang, S.T., Akers, W.J. and Berezin, M.Y. (2013), 'Multispectral imaging in the extended near-infrared window based on endogenous chromophores', *Journal of Biomedical Optics*, Vol. 18, No. 10, p. 101318.

Chan, E.D., Chan, M.M. and Chan, M.M. (2013), 'Pulse oximetry: Understanding its basic principles facilitates appreciation of its limitations', *Respiratory Medicine*, Vol. 107, No. 6, pp. 789–799.

Chan, F.C.D. (2002), *Non-invasive venous oximetry through venous blood volume modulation*, PhD, Fang-Chiat Daniel Chan.

Chan, F.C.D., Hayes, M.J. and Smith, P.R. (2007), 'Venous pulse oximetry', Aug.

Chase, J.G., Preiser, J.C., Dickson, J.L., Pironet, A., Chiew, Y.S., Pretty, C.G., Shaw, G.M., Benyo, B., Moeller, K., Safaei, S., Tawhai, M., Hunter, P. and Desaive, T. (2018), 'Next-generation, personalised, model-based critical care medicine: a state-of-the art review of in silico virtual patient models, methods, and cohorts, and how to validation them', *BioMedical Engineering OnLine*, Vol. 17, No. 1, p. 24.

Chase, J.G., Benyo, B. and Desaive, T. (2019), 'Glycemic control in the intensive care unit: A control systems perspective', *Annual Reviews in Control*, Vol. 48, pp. 359–368.

Chiaco, J., Parikh, N.I. and Fergusson, D.J. (2013), 'The jugular venous pressure revisited', *Cleveland Clinic journal of medicine*, Vol. 80, No. 10, pp. 638–644.

Chico, A., Vidal-Rios, P., Subira, M. and Novials, A. (2003), 'The Continuous Glucose Monitoring System Is Useful for Detecting Unrecognized Hypoglycemias in Patients With Type 1 and Type 2 Diabetes but Is Not Better Than Frequent Capillary Glucose Measurements for Improving Metabolic Control', *Diabetes Care*, Vol. 26, No. 4, pp. 1153–1157.

Chowdhury, K., Srivastava, A., Sharma, D.N. and Sharma, D.S. (2013), 'Challenges & Countermeasures in Optical Noninvasive Blood Glucose Detection', *International Journal of Innovative Research in Science, Engineering and Technology*, Vol. 2, No. 1, p. 6.

Chung, S.C. and Sun, C.C. (2016), 'Signal-enhancement reflective pulse oximeter with Fresnel lens', *Optics Communications*, Vol. 375, pp. 9–14.

Clarke, W.L. (2005), 'The Original Clarke Error Grid Analysis (EGA)', *Diabetes Technology & Therapeutics*, Vol. 7, No. 5, pp. 776–779.

Cloete, G., Fourie, P.R. and Scheffer, C. (2013), 'Development and testing of an artificial arterial and venous pulse oximeter', In *Engineering in Medicine and Biology Society (EMBC), 2013 35th Annual International Conference of the IEEE*, IEEE, pp. 4042–4045.

Colquhoun, D.A., Tucker-Schwartz, J.M., Durieux, M.E. and Thiele, R.H. (2012), 'Non-invasive estimation of jugular venous oxygen saturation: a comparison between near infrared spectroscopy and transcutaneous venous oximetry', *Journal of Clinical Monitoring and Computing*, Vol. 26, No. 2, pp. 91–98.

Critchley, J.A., Carey, I.M., Harris, T., DeWilde, S., Hosking, F.J. and Cook, D.G. (2018), 'Glycemic Control and Risk of Infections Among People With Type 1 or Type 2 Diabetes in a Large Primary Care Cohort Study', *Diabetes Care*, Vol. 41, No. 10, pp. 2127–2135.

Daly, S.M. and Leahy, M.J. (2013), 'Go with the flow: A review of methods and advancements in blood flow imaging', *Journal of Biophotonics*, Vol. 6, No. 3, pp. 217–255.

Danne, T., Nimri, R., Battelino, T. and Weinzimer, S.A. (2017), 'International Consensus on Use of Continuous Glucose Monitoring', *Diabetes Care*, Vol. 40, No. 12, pp. 1631–1640.

Darwich, M.A., Langevin, F. and Darwich, K. (2015), 'Local Pulse Wave Velocity Estimation in the Carotids Using Dynamic MR Sequences', *Journal of Biomedical Science and Engineering*, Vol. 08, No. 04, pp. 227–236.

Dassel, A.C.M., Graaff, R., Aardema, M., Zijlstra, W.G. and Aarnoudse, J.G. (1997), 'Effect of location of the sensor on reflectance pulse oximetry', *BJOG: An International Journal of Obstetrics & Gynaecology*, Vol. 104, No. 8, pp. 910–916.

Davidson, S. (2017), *Real-Time, Non-Additionally Invasive Metrics of Cardiovascular Performance in Critical Care: A Model-Based Framework*, PhD, University of Canterbury, Christchurch, New Zealand.

(DCCT)/(EDIC) Study Research Group (2016), 'Intensive Diabetes Treatment and Cardiovascular Outcomes in Type 1 Diabetes: The DCCT/EDIC Study 30-Year Follow-up', *Diabetes Care*, Vol. 39, No. 5, pp. 686–693.

De Santis, F., Ferrara, M. and Neitzert, H.C. (2006), 'Optical in situ characterization of isotactic polypropylene crystallization using an LED array in avalanche-photoreceiver mode', *IEEE Transactions on Instrumentation and Measurement*, Vol. 55, No. 1, pp. 123–127, conference Name: IEEE Transactions on Instrumentation and Measurement.

Desaive, T., Horikawa, O., Ortiz, J.P. and Chase, J.G. (2019), 'Model-based management of cardiovascular failure: Where medicine and control systems converge', *Annual Reviews in Control*, Vol. 48, pp. 383–391.

Diabetes Control and Complications Trial Research Group (1994), 'Effect of intensive diabetes treatment on the development and progression of long-term complications in adolescents with insulin-dependent diabetes mellitus: Diabetes Control and Complications Trial', *The Journal of Pediatrics*, Vol. 125, No. 2, pp. 177–188.

Dickson, J.L., Le Compte, A.J., Floyd, R.P., Geoffrey Chase, J., Lynn, A. and Shaw, G.M. (2013), 'Development and optimisation of stochastic targeted (STAR) glycaemic control for pre-term infants in neonatal intensive care', *Biomedical Signal Processing and Control*, Vol. 8, No. 2, pp. 215–221.

Dickson, J.L., Stewart, K.W., Pretty, C.G., Flechet, M., Desaive, T., Penning, S., Lambermont, B.C., Benyo, B., Shaw, G.M. and Chase, J.G. (2018), 'Generalisability of a Virtual Trials Method for Glycaemic Control in Intensive Care', *IEEE Transactions on Biomedical Engineering*, Vol. 65, No. 7, pp. 1543–1553.

Dickson, J., Pretty, C., Alsweiler, J., Lynn, A. and Chase, J. (2017), 'Insulin Kinetics and the Neonatal Intensive Care InsulinNutritionGlucose (NICING) Model', *Mathematical Biosciences*, Vol. 284, pp. 61–70.

Echiadis, A.S., Crabtree, V.P., Bence, J., Hadjinikolaou, L., Alexiou, C., Spyt, T.J. and Hu, S. (2007), 'Non-invasive measurement of peripheral venous oxygen saturation using a new venous oximetry method: evaluation during bypass in heart surgery', *Physiological Measurement*, Vol. 28, No. 8, pp. 897–911.

Elgendi, M. (2012), 'On the Analysis of Fingertip Photoplethysmogram Signals', *Current Cardiology Reviews*, Vol. 8, No. 1, pp. 14–25.

Ellahham, S. (2010), 'Insulin therapy in critically ill patients', *Vascular Health and Risk Management*, p. 1089.

Fabian, V., Matera, L., Bayerova, K., Havlik, J., Kremen, V., Pudil, J., Sajgalik, P. and Zemanek, D. (2019), 'Noninvasive Assessment of Aortic Pulse Wave Velocity by the Brachial Occlusion-Cuff Technique: Comparative Study', *Sensors*, Vol. 19, No. 16, p. 3467.

Fingar, M. and Podraj, P. (2018), 'A wavelet-based decomposition method for a robust extraction of pulse rate from video recordings', *PeerJ*, Vol. 6, p. e5859.

Flewelling, R. (2000), 'Oximetry and Pulse Oximetry', *Medical Instruments and Devices*.

Fokkert, M.J., Dijk, P.R.v., Edens, M.A., Abbes, S., Jong, D.d., Slingerland, R.J. and Bilo, H.J.G. (2017), 'Performance of the FreeStyle Libre Flash glucose monitoring system in patients with type 1 and 2 diabetes mellitus', *BMJ Open Diabetes Research and Care*, Vol. 5, No. 1, p. e000320, publisher: BMJ.

Forlenza, G.P., Nathan, B.M., Moran, A., Dunn, T.B., Beilman, G.J., Pruett, T.L., Kovatchev, B.P. and Bellin, M.D. (2016), 'Accuracy of Continuous Glucose Monitoring in Patients After Total Pancreatectomy with Islet Autotransplantation', *Diabetes Technology and Therapeutics*, Vol. 18, No. 8, pp. 455–463, publisher: Mary Ann Liebert Inc.

Fortune, B.C., Stewart, A., Hansenne, E., McKenzie, L., Chatfield, L. and Pretty, C.G. (2017), 'Design and testing of a low-cost electromyogram that uses a right leg driver circuit', In *2017 24th International Conference on Mechatronics and Machine Vision in Practice (M2VIP)*, IEEE, Auckland, pp. 1–6.

Fortune, B.C., Pretty, C.G., Chatfield, L.T., McKenzie, L.R. and Hayes, M.P. (2019), 'Low-cost active electromyography', *HardwareX*, Vol. 6, p. e00085.

Fortune, B.C., Pretty, C.G., Cameron, C.J., McKenzie, L.R., Chatfield, L.T. and Hayes, M.P. (2021), 'Electrodeskin impedance imbalance measured in the frequency domain', *Biomedical Signal Processing and Control*, Vol. 63, p. 102202.

Fox, M.D. (2011), 'Wound Care in the Neonatal Intensive Care Unit', *N ETWORK*, Vol. 30, No. 5, p. 13.

Fozzard, H., Haber, E., Jennings, R. and Katz, A. (1986), *The heart and cardiovascular system*, Raven Press, New York, (NY) USA.

Frier, B.M., Schernthaner, G. and Heller, S.R. (2011), 'Hypoglycemia and Cardiovascular Risks', *Diabetes Care*, Vol. 34, No. Supplement_2, pp. S132–S137.

Gayathri, B., Sruthi, K. and Menon, K.A.U. (2017), 'Non-invasive blood glucose monitoring using near infrared spectroscopy', In *2017 International Conference on Communication and Signal Processing (ICCSP)*, IEEE, CHENNAI, India, pp. 1139–1142.

Ghuysen, A., Lambermont, B., Kolh, P., Tchana-Sato, V., Magis, D., Gerard, P., Mommens, V., Janssen, N., Desaive, T. and D'Orio, V. (2008), 'Alteration of right ventricular-pulmonary vascular coupling in a porcine model of progressive pressure overloading', *Shock*, Vol. 29, No. 2, pp. 197–204.

Gingras, V., Taleb, N., RoyFleming, A., Legault, L. and RabasaLhoret, R. (2018), 'The challenges of achieving postprandial glucose control using closedloop systems in patients with type 1 diabetes', *Diabetes, Obesity and Metabolism*, Vol. 20, No. 2, pp. 245–256.

Girardin, C.M., Huot, C., Gonthier, M. and Delvin, E. (2009), 'Continuous glucose monitoring: A review of biochemical perspectives and clinical use in type 1 diabetes', *Clinical Biochemistry*, Vol. 42, No. 3, pp. 136–142.

Goelz, H., Jones, R.D. and Bones, P.J. (2000), 'Wavelet Analysis of Transient Biomedical Signals and Its Application to Detection of Epileptiform Activity in the ECG', *Clinical Electroencephalography*, Vol. 31, No. 4.

Goldman, J.M., Petterson, M.T., Kopotic, R.J. and Barker, S.J. (2000), 'Masimo signal extraction pulse oximetry', *Journal of clinical monitoring and computing*, Vol. 16, No. 7, pp. 475–483.

Golub, G.H. and van Loan, C.F. (1980), 'An Analysis of the Total Least Squares Problem', *SIAM Journal on Numerical Analysis*, Vol. 17, No. 6, pp. 883–893.

Gonçalves, D., Fernandes, L.M., Louro, P., Vieira, M. and Fantoni, A. (2013), 'Measurement of Photo Capacitance in Amorphous Silicon Photodiodes', In L.M. Camarinha-Matos, S. Tomic and P. Graça (editors), *Technological Innovation for the Internet of Things*, Vol. 394, pp. 547–554, Springer Berlin Heidelberg, Berlin, Heidelberg.

Greenhalgh, D.G., Lawless, M.B., Chew, B.B., Crone, W.A., Fein, M.E. and Palmieri, T.L. (2004), 'Temperature Threshold for Burn Injury: An Oximeter Safety Study:', *Journal of Burn Care & Rehabilitation*, Vol. 25, No. 5, pp. 411–415.

Greenhalgh, T., Knight, M., Inada-Kim, M., Fulop, N.J., Leach, J. and Vindrola-Padros, C. (2021), 'Remote management of covid-19 using home pulse oximetry and virtual ward support', *BMJ*, p. n677.

Guo, D.X., Shang, Y.Z., Peng, R., Yong, S.S. and Wang, X.A. (2015), 'Non-invasive Blood Glucose Measurement Based on NIR Spectrums and Double ANN Analysis', *Journal of Biosciences and Medicines*, Vol. 03, No. 06, pp. 42–48.

Gurovich, A.N. and Braith, R.W. (2011), 'Pulse wave analysis and pulse wave velocity techniques: are they ready for the clinic?', *Hypertension Research*, Vol. 34, No. 2, pp. 166–169.

Guyton, A. and Hall, J. (2006), *Textbook of Medical Physiology*, Elsevier, Amsterdam, 11th ed.

Ham, W.T., Mueller, H.A. and Sliney, D.H. (1976), 'Retinal sensitivity to damage from short wavelength light', *Nature*, Vol. 260, No. 5547, pp. 153–155.

Hamamatsu (2021), 'Si Photodiodes Handbook', .

Hampson, N.B., Scott, K.L. and Zmaeff, J.L. (2006), 'Carboxyhemoglobin measurement by hospitals: Implications for the diagnosis of carbon monoxide poisoning', *The Journal of Emergency Medicine*, Vol. 31, No. 1, pp. 13–16.

Han, G., Chen, S., Wang, X., Wang, J., Wang, H. and Zhao, Z. (2021), 'Noninvasive blood glucose sensing by near-infrared spectroscopy based on PLSR combines SAE deep neural network approach', *Infrared Physics & Technology*, Vol. 113, p. 103620.

Harris, D.L., Battin, M.R., Weston, P.J. and Harding, J.E. (2010), 'Continuous Glucose Monitoring in Newborn Babies at Risk of Hypoglycemia', *The Journal of Pediatrics*, Vol. 157, No. 2, pp. 198–202.e1.

Harris, D.L., Weston, P.J., Signal, M., Chase, J.G. and Harding, J.E. (2013), 'Dextrose gel for neonatal hypoglycaemia (the Sugar Babies Study): a randomised, double-blind, placebo-controlled trial', *The Lancet*, Vol. 382, No. 9910, pp. 2077–2083.

Harris, D.L., Alsweiler, J.M., Ansell, J.M., Gamble, G.D., Thompson, B. and Hess, R. (2016), 'Outcome at 2 Years after Dextrose Gel Treatment for Neonatal Hypoglycemia: Follow-Up of a Randomized Trial', *The Journal of Pediatrics*, Vol. 170, pp. 54–59.e2.

Haxha, S. and Jhoja, J. (2016), 'Optical Based Noninvasive Glucose Monitoring Sensor Prototype', *IEEE Photonics Journal*, Vol. 8, No. 6, pp. 1–11.

Hayward, R.A., Reaven, P.D., Wiitala, W.L., Bahn, G.D., Reda, D.J., Ge, L., McCarren, M., Duckworth, W.C. and Emanuele, N.V. (2015), 'Follow-up of Glycemic Control and Cardiovascular Outcomes in Type 2 Diabetes', *New England Journal of Medicine*, Vol. 372, No. 23, pp. 2197–2206.

He, Z.H. and Zhu, G.S. (2010), 'Variation of Absorption Coefficient of Glucose Water in Consideration of Water Displacement', *Advanced Materials Research*, Vol. 159, pp. 358–362.

Heinemann, L. (2018), 'Continuous Glucose Monitoring (CGM) or Blood Glucose Monitoring (BGM): Interactions and Implications', *Journal of Diabetes Science and Technology*, Vol. 12, No. 4, pp. 873–879.

Heinemann, L., Schoemaker, M., Schmelzeisen-Redecker, G., Hinzmann, R., Kassab, A., Freckmann, G., Reiterer, F. and Del Re, L. (2020), 'Benefits and Limitations of MARD as a Performance Parameter for Continuous Glucose Monitoring in the Interstitial Space', *Journal of Diabetes Science and Technology*, Vol. 14, No. 1, pp. 135–150.

Hellström, W., Forssell, L., Morsing, E., Sävman, K. and Ley, D. (2020), 'Neonatal clinical blood sampling led to major blood loss and was associated with bronchopulmonary dysplasia', *Acta Paediatrica*, Vol. 109, No. 4, pp. 679–687.

Hermeling, E. (2009), *Local Pulse Wave Velocity Determination: The arterial distension waveform from foot to crest*, PhD, College van Decanen.

Hermeling, E., Reesink, K.D., Reneman, R.S. and Hoeks, A.P. (2007), 'Measurement of Local Pulse Wave Velocity: Effects of Signal Processing on Precision', *Ultrasound in Medicine & Biology*, Vol. 33, No. 5, pp. 774–781.

Hertzman, A. (1938), 'The blood supply of various skin areas as estimated by the photoelectric plethysmograph.', *Experimental Biology*, Vol. 38.

Holden, E. and Newmark, N.J. (1871), *The Sphygmograph and the Physiology of the Circulation*, William Wood & Co., New York.

Horman, K., Mayzel, Y., Gal, A., Bahartan, K., Drexler, A. and Lin, t. (2016), 'Performance and User Experience Evaluation of a Non-Invasive Glucose Monitoring Device', *International Journal of Diabetes & Metabolic Disorders*, Vol. 1, No. 2.

Hsu, Y.P. and Young, D.J. (2014), 'Skin-Coupled Personal Wearable Ambulatory Pulse Wave Velocity Monitoring System Using Microelectromechanical Sensors', *IEEE Sensors Journal*, Vol. 14, No. 10, pp. 3490–3497.

Huckvale, K., Adomaviciute, S., Prieto, J.T., Leow, M.K.S. and Car, J. (2015), 'Smartphone apps for calculating insulin dose: a systematic assessment', *BMC Medicine*, Vol. 13, No. 1, p. 106.

ICNIRP (2013), 'ICNIRP Guidelines on Limits of Exposure to Incoherent Visible and Infrared Radiation', *Health Physics*, Vol. 105, No. 1, pp. 74–96.

ICNIRP (2020), 'Light-Emitting Diodes (LEDS): Implications for Safety', *Health Physics*, Vol. 118, No. 5, pp. 549–561.

Intengan, H.D. and Schiffrin, E.L. (2000), 'Structure and Mechanical Properties of Resistance Arteries in Hypertension: Role of Adhesion Molecules and Extracellular Matrix Determinants', *Hypertension*, Vol. 36, No. 3, pp. 312–318.

Jain, P., Maddila, R. and Joshi, A.M. (2019), 'A precise non-invasive blood glucose measurement system using NIR spectroscopy and Hubers regression model', *Optical and Quantum Electronics*, Vol. 51, No. 2, p. 51.

Jani, M., Lunder, M. and abovi, M. (2014), 'Arterial Stiffness and Cardiovascular Therapy', *BioMed Research International*, Vol. 2014, pp. 1–11.

Jau-Ji Jou, Cheng-Kuang Liu, Chien-Mei Hsiao, Huang-Hsiang Lin and Hsiu-Chih Lee (2002), 'Time-delay circuit model of high-speed p-i-n photodiodes', *IEEE Photonics Technology Letters*, Vol. 14, No. 4, pp. 525–527.

Jeon, K.J., Hwang, I.D., Hahn, S. and Yoon, G. (2006), 'Comparison between transmittance and reflectance measurements in glucose determination using near infrared spectroscopy', *Journal of Biomedical Optics*, Vol. 11, No. 1, p. 014022.

Jeong, H., Jeong, S., Lim, H.J., Lee, J. and Yoo, K.Y. (2012), 'Cerebral Oxygen Saturation Measured by Near-infrared Spectroscopy and Jugular Venous Bulb Oxygen Saturation during Arthroscopic Shoulder Surgery in Beach Chair Position under Sevoflurane-Nitrous Oxide or Propofol-Remifentanil Anesthesia:', *Anesthesiology*, Vol. 116, No. 5, pp. 1047–1056.

Jiang, H. and Yu, P. (1998), 'Equivalent circuit analysis of harmonic distortions in photodiode', *IEEE Photonics Technology Letters*, Vol. 10, No. 11, pp. 1608–1610.

Jianwen Luo, Li, R.X. and Konofagou, E.E. (2012), 'Pulse wave imaging of the human carotid artery: an in vivo feasibility study', *IEEE Transactions on Ultrasonics, Ferroelectrics and Frequency Control*, Vol. 59, No. 1, pp. 174–181.

Jing, X., Chen, J., Dong, Y., Han, D., Zhao, H., Wang, X., Gao, F., Li, C., Cui, Z., Liu, Y. and Ma, J. (2018), 'Related factors of quality of life of type 2 diabetes patients: a systematic review and meta-analysis', *Health and Quality of Life Outcomes*, Vol. 16.

Joseph, G., Joseph, A., Titus, G., Thomas, R.M. and Jose, D. (2014), 'Photoplethysmogram (PPG) signal analysis and wavelet de-noising', In *Emerging Research Areas: Magnetics, Machines and Drives (AICERA/iCMMD), 2014 Annual International Conference on*, IEEE, pp. 1–5.

Jubran, A. (1999), 'Pulse Oximetry', *Critical Care*, Vol. 3, pp. 11–17.

Kadoglou, N.P., Papadakis, I., Moulakakis, K.G., Ikonomidis, I., Alepaki, M., Moustardas, P., Lampropoulos, S., Karakitsos, P., Lekakis, J. and Liapis, C.D. (2012), 'Arterial stiffness and novel biomarkers in patients with abdominal aortic aneurysms', *Regulatory Peptides*, Vol. 179, No. 1-3, pp. 50–54.

Kamat, V. and others (2002), 'Pulse oximetry - emirical calibrations', *Indian J. Anaesth*, Vol. 46, No. 4, pp. 261–268.

Kamoi, S., Pretty, C., Balmer, J., Davidson, S., Pironet, A., Desaive, T., Shaw, G.M. and Chase, J.G. (2017), 'Improved pressure contour analysis for estimating cardiac stroke volume using pulse wave velocity measurement', *BioMedical Engineering OnLine*, Vol. 16, No. 1.

Karlen, W., Ansermino, J.M. and Dumont, G. (2012), 'Adaptive pulse segmentation and artifact detection in photoplethysmography for mobile applications', In *Engineering in Medicine and Biology Society (EMBC), 2012 Annual International Conference of the IEEE*, IEEE, pp. 3131–3134.

Kasahara, R., Kino, S., Soyama, S. and Matsuura, Y. (2018), 'Unsupervised calibration for noninvasive glucose-monitoring devices using mid-infrared spectroscopy', *Journal of Innovative Optical Health Sciences*, Vol. 11, No. 06, p. 1850038.

Kasambe, P. and Rathod, S. (2015), 'VLSI Wavelet Based Denoising of PPG Signal', *Procedia Computer Science*, Vol. 49, pp. 282–288.

Kato, N., Cui, J. and Kato, M. (2013), 'Structured selfmonitoring of blood glucose reduces glycated hemoglobin in insulintreated diabetes', *Journal of Diabetes Investigation*, Vol. 4, No. 5, pp. 450–453.

Kaufman, F.R., Gibson, L.C., Halvorson, M., Carpenter, S., Fisher, L.K. and Pitukcheewanont, P. (2001), 'A Pilot Study of the Continuous Glucose Monitoring System: Clinical decisions and glycemic control after its use in pediatric type 1 diabetic subjects', *Diabetes Care*, Vol. 24, No. 12, pp. 2030–2034.

Kazune, S., Grabovskis, A., Strike, E. and Vanags, I. (2014), 'Arterial Stiffness Measured by Pulse Wave Velocity in Patients with Early Sepsis', *Proceedings of the Latvian Academy of Sciences. Section B. Natural, Exact, and Applied Sciences.*, Vol. 68, No. 5-6, pp. 237–241.

Kennedy, S.M. (2015), 'An introduction to pulse oximeters: Equations and theory', *University of Wisconsin-Madison*, Vol. 20.

Khan, M. (2016), *Non-invasive monitoring of peripheral oxygen extraction and perfusion using photoplethysmography.*, PhD, University of Canterbury, Christchurch, New Zealand.

Khan, M., Pretty, C., Amies, A., Elliot, R., Shaw, G. and Chase, G. (2015a), 'Investigating the Effects of Temperature on Photoplethysmography', In *IFAC*, pp. 360–365.

Khan, M., Pretty, C.G., Amies, A.C., Elliott, R.B., Suhaimi, F.M., Shaw, G.M. and Chase, J.G. (2015b), 'Peripheral venous blood oxygen saturation can be non-invasively estimated using photoplethysmography', In *2015 37th Annual International Conference of the IEEE Engineering in Medicine and Biology Society (EMBC)*, IEEE, Milan, pp. 6405–6408.

Khan, M., Pretty, C.G., Amies, A.C., Elliott, R., Chiew, Y.S., Shaw, G.M. and Chase, J.G. (2016), 'Analysing the effects of cold, normal, and warm digits on transmittance pulse oximetry', *Biomedical Signal Processing and Control*, Vol. 26, pp. 34–41.

Khan, M., Pretty, C.G., Amies, A.C., Balmer, J., Banna, H.E., Shaw, G.M. and Chase, J.G. (2017), 'Proof of concept non-invasive estimation of peripheral venous oxygen saturation', *Biomedical engineering online*, Vol. 16, No. 1, p. 60.

Khan, Y., Han, D., Pierre, A., Ting, J., Wang, X., Lochner, C.M., Bovo, G., Yaacobi-Gross, N., Newsome, C., Wilson, R. and Arias, A.C. (2018), 'A flexible organic reflectance oximeter array', *Proceedings of the National Academy of Sciences*, Vol. 115, No. 47, pp. E11015–E11024.

Kim, E.J., Park, C.G., Park, J.S., Suh, S.Y., Choi, C.U., Kim, J.W., Kim, S.H., Lim, H.E., Rha, S.W., Seo, H.S. and Oh, D.J. (2007), 'Relationship between blood pressure parameters and pulse wave velocity in normotensive and hypertensive subjects: invasive study', *Journal of Human Hypertension*, Vol. 21, No. 2, pp. 141–148.

King, A.B., Kuroda, A., Matsuhisa, M. and Hobbs, T. (2016), 'A Review of Insulin-Dosing Formulas for Continuous Subcutaneous Insulin Infusion (CSII) for Adults with Type 1 Diabetes', *Current Diabetes Reports*, Vol. 16, No. 9, p. 83.

Klonoff, D.C., Ahn, D. and Drincic, A. (2017), 'Continuous glucose monitoring: A review of the technology and clinical use', *Diabetes Research and Clinical Practice*, Vol. 133, pp. 178–192.

Knopp (nee Dickson), J.L., Lynn, A.M., Shaw, G.M. and Chase, J.G. (2019), 'Safe and effective glycaemic control in premature infants: observational clinical results from the computerised STAR-GRYPHON protocol', *Archives of Disease in Childhood - Fetal and Neonatal Edition*, Vol. 104, No. 2, pp. F205–F211.

Kohl, M., Essenpreis, M. and Cope, M. (1995), 'The influence of glucose concentration upon the transport of light in tissue simulating phantoms', *Physics in Medicine and Biology*, Vol. 40, No. 7, pp. 1267–1287.

Kovatchev, B. (2018), 'Automated closed-loop control of diabetes: the artificial pancreas', *Bioelectronic Medicine*, Vol. 4, No. 1, p. 14.

Kowalczyk, M. and Siuzdak, J. (2017), 'Photo-reception properties of common LEDs', *Opto-Electronics Review*, Vol. 25, No. 3, pp. 222–228.

Kraitl, J., Ewald, H. and Gehring, H. (2005), 'An optical device to measure blood components by a photoplethysmographic method', *Journal of Optics A: Pure and Applied Optics*, Vol. 7, No. 6, pp. S318–S324.

Ku, D.N. (1997), 'Blood flow in arteries', *Annual Review of Fluid Mechanics*, Vol. 29, p. 36.

Lam, N., Docherty, P.D., Murray, R., Chase, J.G. and Morenga, L.T. (2020), 'Using the Adapted Levenberg-Marquardt method to determine the validity of ignoring insulin and glucose data that is affected by mixing', *IFAC-PapersOnLine*, Vol. 53, No. 2, pp. 16341–16346.

Lau, E.K. (2013), 'Understanding radiation safety of high-intensity light-emitting diodes', In *2013 IEEE Symposium on Product Compliance Engineering (ISPCE)*, pp. 1–3.

Lau, K.T., Baldwin, S., OToole, M., Shepherd, R., Yerazunis, W.J., Izuo, S., Ueyama, S. and Diamond, D. (2006), 'A low-cost optical sensing device based on paired emitterdetector light emitting diodes', *Analytica Chimica Acta*, Vol. 557, No. 1-2, pp. 111–116.

Laurent, S., Cockcroft, J., Van Bortel, L., Boutouyrie, P., Giannattasio, C., Hayoz, D., Pannier, B., Vlachopoulos, C., Wilkinson, I., Struijker-Boudier, H. and on behalf of the European Network for Non-invasive Investigation of Large Arteries (2006), 'Expert consensus document on arterial stiffness: methodological issues and clinical applications', *European Heart Journal*, Vol. 27, No. 21, pp. 2588–2605.

Lee, B., Kee, Y., Han, J. and Yi, W.J. (2011), 'Adaptive comb filtering for motion artifact reduction from PPG with a structure of adaptive lattice IIR notch filter', In *Engineering in Medicine and Biology Society, EMBC, 2011 Annual International Conference of the IEEE*, IEEE, pp. 7937–7940.

Lee, D.T. and Yamamoto, A. (1994), 'Wavelet analysis: theory and applications', *Hewlett Packard journal*, Vol. 45, pp. 44–44.

Lemyre, B., Sample, M. and Lacaze-Masmonteil, T. (2015), 'Minimizing blood loss and the need for transfusions in very premature infants', *Paediatric Child Health*, Vol. 20, No. 8, p. 6.

Lennox, W.G. (1935), 'Relationship of unconsciousness to cerebrel blood flow and to anoxemia', *Archives of Neurology And Psychiatry*, Vol. 34, No. 5, p. 1001.

Li, K. and Warren, S. (2012), 'A Wireless Reflectance Pulse Oximeter With Digital Baseline Control for Unfiltered Photoplethysmograms', *IEEE Transactions on Biomedical Circuits and Systems*, Vol. 6, No. 3, pp. 269–278.

Li, S., Jiang, S., Jiang, S., Wu, J., Xiong, W. and Diao, S. (2017), 'A Hybrid Wavelet-Based Method for the Peak Detection of Photoplethysmography Signals', *Computational and Mathematical Methods in Medicine*, Vol. 2017, pp. 1–8.

Li, Y., Li, S., Song, H., Shao, B., Yang, X. and Deng, N. (2019), 'Noninvasive blood pressure estimation with peak delay of different pulse waves', *International Journal of Distributed Sensor Networks*, Vol. 15, No. 3, p. 155014771983787.

Lin, T. (2017), 'Non-Invasive Glucose Monitoring: A Review of Challenges and Recent Advances', *Current Trends in Biomedical Engineering & Biosciences*, Vol. 6, No. 5.

Lind, N., Lindqvist Hansen, D., Sætre Rasmussen, S. and Nørgaard, K. (2021), 'Real-time continuous glucose monitoring versus self-monitoring of blood glucose in adults with insulin-treated type 2 diabetes: a protocol for a randomised controlled single-centre trial', *BMJ Open*, Vol. 11, No. 1, p. e040648.

Lindner, N., Kuwabara, A. and Holt, T. (2021), 'Non-invasive and minimally invasive glucose monitoring devices: a systematic review and meta-analysis on diagnostic accuracy of hypoglycaemia detection', *Systematic Reviews*, Vol. 10, No. 1, p. 145.

Lipnick, M.S., Feiner, J.R., Au, P., Bernstein, M. and Bickler, P.E. (2016), 'The Accuracy of 6 Inexpensive Pulse Oximeters Not Cleared by the Food and Drug Administration: The Possible Global Public Health Implications', *Anesthesia & Analgesia*, Vol. 123, No. 2, pp. 338–345.

Liu, J., Ren, Z.H., Qiang, H., Wu, J., Shen, M., Zhang, L. and Lyu, J. (2020), 'Trends in the incidence of diabetes mellitus: results from the Global Burden of Disease Study 2017 and implications for diabetes mellitus prevention', *BMC Public Health*, Vol. 20, No. 1, p. 1415.

Liu, R., Deng, B., Chen, W. and Xu, K. (2005), 'Next Step of Non-invasive Glucose Monitor by NIR Technique from the Well Controlled Measuring Condition and Results', *Optical and Quantum Electronics*, Vol. 37, No. 13-15, pp. 1305–1317.

Lowenthal, A., Evans, J.M., Punn, R., Nourse, S.E., Vu, C.N., Popat, R.A. and Selamet Tierney, E.S. (2014), 'Arterial Applanation Tonometry: Feasibility and Reproducibility in Children and Adolescents', *American Journal of Hypertension*, Vol. 27, No. 9, pp. 1218–1224.

Ma, Y., Choi, J., Hourlier-Fargette, A. and Huang, Y. (2018), 'Relation between blood pressure and pulse wave velocity for human arteries', *Proceedings of the National Academy of Sciences*, Vol. 115, No. 44, pp. 11144–11149.

Mahmud, A., Jatoi, N. and Feely, J. (2009), 'Assessment of arterial stiffness in hypertension: Comparison of oscillometric (arteriograph), piezo-electric (Compilor) , and tonometric (Sphygmocor) techniques', *Artery Research*, Vol. 3, No. 4, p. 162.

Mallat, S.G. (1989), 'A Theory for Multiresolution Signal Decomposition: The Wavelet Representation', *IEEE Transactions on Pattern Analysis and Machine Intelligence*, Vol. 11, No. 7, p. 20.

Mamkin, I., Ten, S., Bhandari, S. and Ramchandani, N. (2008), 'Real-Time Continuous Glucose Monitoring in the Clinical Setting: The Good, the Bad, and the Practical', *Journal of Diabetes Science and Technology*, Vol. 2, No. 5, pp. 882–889.

Mancia, G., Rosei, E.A., Azizi, M. and Desormais, I. (2018), '2018 ESC/ESH Guidelines for the management of arterial hypertension', *European Heart Journal*, Vol. 39, p. 98.

Mannheimer, P.D. (2007), 'The Light Tissue Interaction of Pulse Oximetry:', *Anesthesia & Analgesia*, Vol. 105, No. On Line Suppl., pp. S10–S17.

Mannheimer, P.D., Cascini, J.R., Fein, M.E. and Nierlich, S.L. (1997), 'Wavelength selection for low-saturation pulse oximetry', *IEEE Transactions on Biomedical Engineering*, Vol. 44, No. 3, pp. 148–158.

Marktech (2017a), 'MTSM5015-843-IR Datasheet', Nov.

Marktech (2017b), 'MTSM5016-843-IR Datasheet', Nov.

Marktech (2018), 'MTSM5014-843-IR Datasheet', Jun.

Marsters, B.L. (2020), 'The flash adhesive study: a randomized crossover trial using an additional adhesive patch to prolong freestyle libre sensor life among youth with type 1 diabetes mellitus', *Acta Diabetologica*, p. 8.

Martinez-Lemus, L.A. (2012), 'The Dynamic Structure of Arterioles: Anatomy of Resistance Arteries', *Basic & Clinical Pharmacology & Toxicology*, Vol. 110, No. 1, pp. 5–11.

Maruo, K. and Yamada, Y. (2015), 'Near-infrared noninvasive blood glucose prediction without using multivariate analyses: introduction of imaginary spectra due to scattering change in the skin', *Journal of Biomedical Optics*, Vol. 20, No. 4, p. 047003.

Maruo, K., Tsurugi, M., Tamura, M. and Ozaki, Y. (2003), '*In Vivo* Noninvasive Measurement of Blood Glucose by Near-Infrared Diffuse-Reflectance Spectroscopy', *Applied Spectroscopy*, Vol. 57, No. 10, pp. 1236–1244.

Maruo, K., Oota, T., Tsurugi, M., Nakagawa, T., Arimoto, H., Hayakawa, M., Tamura, M., Ozaki, Y. and Yamada, Y. (2006a), 'Noninvasive Near-Infrared Blood Glucose Monitoring Using a Calibration Model Built by a Numerical Simulation Method: Trial Application to Patients in an Intensive Care Unit', *Applied Spectroscopy*, Vol. 60, No. 12, p. 9.

Maruo, K., Oota, T., Tsurugi, M., Nakagawa, T., Arimoto, H., Tamura, M., Ozaki, Y. and Yamada, Y. (2006b), 'New Methodology to Obtain a Calibration Model for Noninvasive Near-Infrared Blood Glucose Monitoring', *Applied Spectroscopy*, Vol. 60, No. 4, pp. 441–449.

McAllister, D.A., Hughes, K.A., Lone, N., Mills, N.L., Sattar, N., McKnight, J. and Wild, S.H. (2014), 'Stress Hyperglycaemia in Hospitalised Patients and Their 3-Year Risk of Diabetes: A Scottish Retrospective Cohort Study', *PLoS Medicine*, Vol. 11, No. 8, p. e1001708.

McIntyre, H.D., Catalano, P., Zhang, C., Desoye, G., Mathiesen, E.R. and Damm, P. (2019), 'Gestational diabetes mellitus', *Nature Reviews Disease Primers*, Vol. 5, No. 1, p. 47.

McKinlay, C.J.D., Alsweiler, J.M., Anstice, N.S., Chase, J.G., Gamble, G.D., Harris, D.L. and Harding, J.E. (2017a), 'Association of Neonatal Glycemia With Neurodevelopmental Outcomes at 4.5 Years', *JAMA Pediatrics*, Vol. 171, No. 10, p. 972.

McKinlay, C.J., Alsweiler, J.M., Ansell, J.M., Anstice, N.S., Chase, J.G., Gamble, G.D., Yu, T.Y. and Harding, J.E. (2015), 'Neonatal Glycemia and Neurodevelopmental Outcomes at 2 Years', *New England Journal of Medicine*, Vol. 373, No. 16, pp. 1507–1518.

McKinlay, C.J., Chase, J.G., Dickson, J., Harris, D.L., Alsweiler, J.M. and Harding, J.E. (2017b), 'Continuous glucose monitoring in neonates: a review', *Maternal Health, Neonatology and Perinatology*, Vol. 3, No. 1, p. 18.

Mediray (2021), 'Freestyle Libre Flash Glucose Monitoring System', Sep.

Meigas, K., Kattai, R. and Lass, J. (2001), 'Continuous blood pressure monitoring using pulse wave delay', In *2001 Conference Proceedings of the 23rd Annual International Conference of the IEEE Engineering in Medicine and Biology Society*, Vol. 4, IEEE, Istanbul, Turkey, pp. 3171–3174.

Mendelson, Y. (1992), 'Pulse oximetry: theory and applications for noninvasive monitoring.', *Clinical Chemistry*, Vol. 38, No. 9, pp. 1601–1607.

Mendelson, Y. and Kent, J.C. (1989), 'Variations in optical absorption spectra of adult and fetal haemoglobins and its effect on pulse oximetry', *IEEE transactions on biomedical engineering*, Vol. 36, No. 8, pp. 844–848.

Mendelson, Y. and Ochs, B.D. (1988), 'Noninvasive pulse oximetry utilizing skin reflectance photoplethysmography', *IEEE Transactions on Biomedical Engineering*, Vol. 35, No. 10, pp. 798–805.

Mendis, S. (2015), *Global status report on noncommunicable diseases: 2014.*, World Health Organization, oCLC: 960026407.

Meneghini, M., Tazzoli, A., Mura, G., Meneghesso, G. and Zanoni, E. (2010), 'A Review on the Physical Mechanisms That Limit the Reliability of GaN-Based LEDs', *IEEE Transactions on Electron Devices*, Vol. 57, No. 1, pp. 108–118.

Millasseau, S.C., Patel, S.J., Redwood, S.R., Ritter, J.M. and Chowienczyk, P.J. (2003), 'Pressure Wave Reflection Assessed From the Peripheral Pulse: Is a Transfer Function Necessary?', *Hypertension*, Vol. 41, No. 5, pp. 1016–1020.

Millikan, A, G. (1942), 'The Oximeter, an Instrument for Measuring Continuously the Oxygen Saturation of Arterial Blood in Man', *Review of Scientific Instruments*, Vol. 13, No. 10, pp. 434–444.

Mims, F.M. (1992), 'Sun photometer with light-emitting diodes as spectrally selective detectors', *Applied Optics*, Vol. 31, No. 33, p. 6965.

Minder, A.E., Albrecht, D., Schäfer, J. and Zulewski, H. (2013), 'Frequency of blood glucose testing in well educated patients with diabetes mellitus type 1: How often is enough?', *Diabetes Research and Clinical Practice*, Vol. 101, No. 1, pp. 57–61.

Miyasaka, K., Shelley, K., Takahashi, S. and Kubota, H. (2021), 'Tribute to Dr. Takuo Aoyagi, inventor of pulse oximetry', *Journal of Anesthesia*, Vol. 35, No. 5, pp. 671–709.

Miyazaki, E., Itami, S. and Araki, T. (1998), 'Using a light-emitting diode as a high-speed, wavelength selective photodetector', *Review of Scientific Instruments*, Vol. 69, No. 11, pp. 3751–3754.

Morimont, P., Lambermont, B., Desaive, T., Janssen, N., Chase, G. and D'Orio, V. (2012), 'Arterial dP/dtmax accurately reflects left ventricular contractility during shock when adequate vascular filling is achieved', *BMC Cardiovascular Disorders*, Vol. 12, No. 1, p. 13.

Moser, O., Eckstein, M.L., Mueller, A. and Birnbaumer, P. (2019), 'Pre-Exercise Blood Glucose Levels Determine the Amount of Orally Administered Carbohydrates during Physical Exercise in Individuals with Type 1 DiabetesA Randomized Cross-Over Trial', *Nutrients*, Vol. 11, No. 6, p. 1287.

Murphy, L., Chase, J.G., Davidson, S.M., Smith, R. and Desaive, T. (2020a), 'Minimally Invasive Model Based Stressed Blood Volume as an Index of Fluid Responsiveness', *IFAC-PapersOnLine*, Vol. 53, No. 2, pp. 16257–16262.

Murphy, L., Davidson, S., Knopp, J.L., Chase, J.G., Zhou, T. and Desaive, T. (2019), 'State Analysis of Total Stressed Blood Volume and Arterial Elastance During Induced Sepsis', In *2019 41st Annual International Conference of the IEEE Engineering in Medicine and Biology Society (EMBC)*, IEEE, Berlin, Germany, pp. 2951–2954.

Murphy, L., Davidson, S., Chase, J.G., Knopp, J.L., Zhou, T. and Desaive, T. (2020b), 'Patient-Specific Monitoring and Trend Analysis of Model-Based Markers of Fluid Responsiveness in Sepsis: A Proof-of-Concept Animal Study', *Annals of Biomedical Engineering*, Vol. 48, No. 2, pp. 682–694.

N. A. B. Abd Salam, W. H. bin Mohd Saad, Z. B. Manap and F. Salehuddin (2016), 'The Evolution of Non-invasive Blood Glucose Monitoring System for Personal Application', *Journal of Telecommunication, Electronic and Computer Engineering*, Vol. 8, No. 1, pp. 59–65.

Naveen, G. and Nitish, G. (2000), 'Jugular Venous Pulse: An Appraisal', *Indian Acadamy of Clinical Medicine*, Vol. 1, No. 3.

Nemcsik, J., Egresits, J., El Hadj Othmane, T., Fekete, B.C., Fodor, E., Szabó, T., Járai, Z., Jekkel, C., Kiss, I. and Tislér, A. (2009), 'Validation of Arteriograph – A New Oscillometric Device to Measure Arterial Stiffness in Patients on Maintenance Hemodialysis', *Kidney and Blood Pressure Research*, Vol. 32, No. 3, pp. 223–229.

Nguyen, M., Han, J., Spanakis, E.K., Kovatchev, B.P. and Klonoff, D.C. (2020), 'A Review of Continuous Glucose Monitoring-Based Composite Metrics for Glycemic Control', *Diabetes Technology & Therapeutics*, Vol. 22, No. 8, pp. 613–622.

Nguyen, T.N. (2016), *An algorithm for extracting the PPG Baseline Drift in real-time*, PhD thesis, Edith Cowan University.

Nitzan, M., Noach, S., Tobal, E., Adar, Y., Miller, Y., Shalom, E. and Engelberg, S. (2014), 'Calibration-Free Pulse Oximetry Based on Two Wavelengths in the Infrared A Preliminary Study', *Sensors*, Vol. 14, No. 4, pp. 7420–7434.

Nunnally, M.E., Ferrer, R., Martin, G.S., Martin-Loeches, I. and Levy, M.M. (2021), 'The Surviving Sepsis Campaign: research priorities for the administration, epidemiology, scoring and identification of sepsis', *Intensive Care Medicine Experimental*, Vol. 9, No. 1, p. 34.

Nwosu, O. and Nwani, C. (2009), 'Stability of Serum/Plasma Glucose for the Diagnosis of Diabetes Mellitus', *Bio-Research*, Vol. 6, No. 2, pp. 380–383.

NXP Semiconductors (2020a), 'i.MX RT1060 Crossover Processors for Consumer Products', Jul.

NXP Semiconductors (2020b), 'PCA9745B - 16-channel SPI serial bus 57 mA/20 V constant current LED driver', .

Nybacka, L. (2016), 'FTIR spectroscopy of glucose', Examensarbete, Uppsala Universitet.

NZMS Diabetes (2021), 'Continuous Glucose Monitoring', Oct.

Oak, S.S. and Aroul, P. (2015), 'How to Design Peripheral Oxygen Saturation (SpO2) and Optical Heart Rate Monitoring (OHRM) Systems Using AFE4403', .

Obeid, H., Fortier, C., Garneau, C.A., Pare, M., Boutouyrie, P., Bruno, R.M., Khettab, H., Goupil, R. and Agharazii, M. (2021), 'Radial-digital pulse wave velocity: a noninvasive method for assessing stiffness of small conduit arteries', *American Journal of Physiology-Heart and Circulatory Physiology*, Vol. 320, No. 4, pp. H1361–H1369.

Olansky, L. and Kennedy, L. (2010), 'Finger-Stick Glucose Monitoring: Issues of accuracy and specificity', *Diabetes Care*, Vol. 33, No. 4, pp. 948–949.

Oltulu, P., Ince, B., Kokbudak, N., Findik, S. and Kilinc, F. (2018), 'Measurement of epidermis, dermis, and total skin thicknesses from six different body regions with a new ethical histometric technique', *Turkish Journal of Plastic Surgery*, Vol. 26, No. 2, p. 56.

O'Rourke, M.F., Staessen, J.A., Vlachopoulos, C., Duprez, D. and Plante, G.e.E. (2002), 'Clinical applications of arterial stiffness; definitions and reference values', *American Journal of Hypertension*, Vol. 15, No. 5, pp. 426–444.

Ortega, R., Hansen, C.J., Elterman, K. and Woo, A. (2011), 'Pulse oximetry', *N Engl J Med*, Vol. 364, pp. 33–6.

Otoole, M., Lau, K. and Diamond, D. (2005), 'Photometric detection in flow analysis systems using integrated PEDDs', *Talanta*, Vol. 66, No. 5, pp. 1340–1344.

ORourke, M.F. (2015), 'Carotid Artery Tonometry: Pros and Cons', *American Journal of Hypertension*, p. hpv194.

OToole, M. and Diamond, D. (2008), 'Absorbance Based Light Emitting Diode Optical Sensors and Sensing Devices', *Sensors*, Vol. 8, No. 4, pp. 2453–2479.

Paeme, S. (2013), *Mathmatical modelling of the mitral valve*, PhD, University of Liege, Liege, Belgium.

Pannier, B.M., Avolio, A.P., Hoeks, A., Mancia, G. and Takazawa, K. (2002), 'Methods and devices for measuring arterial compliance in humans', *American Journal of Hypertension*, Vol. 15, No. 8, pp. 743–753.

Parkes, J.L., Slatin, S.L., Pardo, S. and Ginsberg, B.H. (2000), 'A new consensus error grid to evaluate the clinical significance of inaccuracies in the measurement of blood glucose', *Diabetes Care*, Vol. 23, No. 8, pp. 1143–1148.

Pereira, T., Cabeliera, M., Matos, P., Borges, E., Almeida, V., Cardoso, J. and Correia, C. (2011), 'Optical methods for local pulse wave velocity assessment:', In *Proceedings of the International Conference on Bio-inspired Systems and Signal Processing*, SciTePress - Science and and Technology Publications, Rome, Italy, pp. 74–81.

Pereira, T., Correia, C. and Cardoso, J. (2015), 'Novel Methods for Pulse Wave Velocity Measurement', *Journal of Medical and Biological Engineering*, Vol. 35, No. 5, pp. 555–565.

Peter, L., Foltyn, J. and Cerny, M. (2015), 'Pulse wave velocity measurement; developing process of new measuring device', In *13th International Symposium on Applied Machine Intelligence and Informatics*, IEEE, pp. 59–62.

Phillips, J.P., Belhaj, A., Shafqat, K., Langford, R.M., Shelley, K.H. and Kyriacou, P.A. (2012), 'Modulation of finger photoplethysmographic traces during forced respiration: venous blood in motion?', In *Engineering in Medicine and Biology Society (EMBC), 2012 Annual International Conference of the IEEE*, IEEE, pp. 3644–3647.

Pintelon, R., Schoukens, J. and Renneboog, J. (1988), 'The geometric mean of power (amplitude) spectra has a much smaller bias than the classical arithmetic (RMS) averaging', *IEEE Transactions on Instrumentation and Measurement*, Vol. 37, No. 2, pp. 213–218.

Pironet, A., Desaive, T., Geoffrey Chase, J., Morimont, P. and Dauby, P.C. (2015), 'Model-based computation of total stressed blood volume from a preload reduction manoeuvre', *Mathematical Biosciences*, Vol. 265, pp. 28–39.

Plows, J., Stanley, J., Baker, P., Reynolds, C. and Vickers, M. (2018), 'The Pathophysiology of Gestational Diabetes Mellitus', *International Journal of Molecular Sciences*, Vol. 19, No. 11, p. 3342.

Poddar, R., Andrews, J.T., Shukla, P. and Sen, P. (2008), 'Non Invasive Glucose Monitoring Techniques: A review and current trends', Oct.

Polonsky, W., Fisher, L., Schikman, C., Hinnen, D., Parkin, C., Jelsovsky, Z., Amstutz, L., Schweitzer, M. and Wagner, R. (2010), 'The value of episodic, intensive blood glucose monitoring in non-insulin treated persons with type 2 diabetes: Design of the Structured Testing Program (STeP) Study, a cluster-randomised, clinical trial', *BMC Family Practice*, p. 10.

Polonsky, W.H., Jelsovsky, Z., Panzera, S., Parkin, C.G. and Wagner, R.S. (2009), 'Primary care physicians identify and act upon glycemic abnormalities found in structured, episodic blood glucose monitoring data from non-insulin-treated type 2 diabetes', *Diabetes Technology & Therapeutics*, Vol. 11, No. 5, pp. 283–291.

Rabiepour, M., Zhou, C., Rodgers, G.W. and Chase, J.G. (2022), 'Real-world application of hysteresis loop analysis for stiffness identification of an instrumented building across multiple seismic events', *Journal of Building Engineering*, Vol. 45, p. 103524.

Ralston, A.C., Webb, R.K. and Runciman, W.B. (1991), 'Potential errors in pulse oximetry III: Effects of interference, dyes, dyshaemoglobins and other pigments*', *Anaesthesia*, Vol. 46, No. 4, pp. 291–295.

Ramasahayam, S., Arora, L. and Chowdhury, S.R. (2017), 'FPGA Based Smart System for Non Invasive Blood Glucose Sensing Using Photoplethysmography and Online Correction of Motion Artifact', In S.C. Mukhopadhyay, O.A. Postolache, K.P. Jayasundera and A.K. Swain (editors), *Sensors for Everyday Life*, Vol. 22, pp. 1–21, Springer International Publishing, Cham.

Reuss, J. (2005), 'Multilayer Modeling of Reflectance Pulse Oximetry', *IEEE Transactions on Biomedical Engineering*, Vol. 52, No. 2, pp. 153–159.

Reynolds, K., De Kock, J., Tarassenko, L. and Moyle, J. (1991), 'Temperature Dependence of LED and its Theoretical Effect on Pulse Oximetry', *British Journal of Anaesthesia*, Vol. 67, No. 5, pp. 638–643.

Rhee, S., Yang, B.H. and Asada, H.H. (2001), 'Artifact-resistant power-efficient design of finger-ring plethysmographic sensors', *IEEE Transactions on Biomedical Engineering*, Vol. 48, No. 7, pp. 795–805.

Riddle, M.C. and Herman, W.H. (2018), 'The Cost of Diabetes CareAn Elephant in the Room', *Diabetes Care*, Vol. 41, No. 5, pp. 929–932.

Ritz, J.P., Roggan, A., Isbert, C., Müller, G., Buhr, H.J. and Germer, C.T. (2001), 'Optical properties of native and coagulated porcine liver tissue between 400

and 2400 nm: optical properties of porcine tissue', *Lasers in Surgery and Medicine*, Vol. 29, No. 3, pp. 205–212.

Rodbard, D. (2014), 'Characterizing Accuracy and Precision of Glucose Sensors and Meters', *Journal of Diabetes Science and Technology*, Vol. 8, No. 5, pp. 980–985.

Roden, M. and Shulman, G.I. (2019), 'The integrative biology of type 2 diabetes', *Nature*, Vol. 576, No. 7785, pp. 51–60.

Roze, S., Isitt, J.J., Smith-Palmer, J. and Lynch, P. (2021), 'Evaluation of the Long-Term Cost-Effectiveness of the Dexcom G6 Continuous Glucose Monitor versus Self-Monitoring of Blood Glucose in People with Type 1 Diabetes in Canada', *ClinicoEconomics and Outcomes Research*, Vol. Volume 13, pp. 717–725.

Sachdeva, S. (2009), 'Fitzpatrick skin typing: Applications in dermatology', *Indian Journal of Dermatology, Venereology and Leprology*, Vol. 75, No. 1, p. 93.

Salvi, P., Magnani, E., Valbusa, F., Agnoletti, D., Alecu, C., Joly, L. and Benetos, A. (2008), 'Comparative study of methodologies for pulse wave velocity estimation', *Journal of Human Hypertension*, Vol. 22, No. 10, pp. 669–677.

Schmid, S., Corbellini, G., Mangold, S. and Gross, T.R. (2013), 'LED-to-LED visible light communication networks', In *Proceedings of the fourteenth ACM international symposium on Mobile ad hoc networking and computing - MobiHoc '13*, ACM Press, Bangalore, India, p. 1.

Schneider, G.H., Helden, A.v., Lanksch, W.R. and Unterberg, A. (1995), 'Continuous monitoring of jugular bulb oxygen saturation in comatose patients ? Therapeutic implications', *Acta Neurochirurgica*, Vol. 134, No. 1-2, pp. 71–75.

Schoevers, J., Scheffer, C. and Dippenaar, R. (2009), 'Low-Oxygen-Saturation Quantification in Human Arterial and Venous Circulation', *IEEE Transactions on Biomedical Engineering*, Vol. 56, No. 3, pp. 846–854.

Schulmeister, K. (2013), 'The upcoming new editions of IEC 60825-1 and ANSI Z136.1 Examples on impact for classification and exposure limits', In *International Laser Safety Conference*, Laser Institute of America, Orlando, Florida, USA, pp. 330–337.

Scott Prahl (1998), 'Tabulated Molar Extinction Coefficient for Hemoglobin in Water', .

Segers, P., Kips, J., Trachet, B., Swillens, A., Vermeersch, S., Mahieu, D., Rietzschel, E., De Buyzere, M. and Van Bortel, L. (2009), 'Limitations and pitfalls of non-invasive measurement of arterial pressure wave reflections and pulse wave velocity', *Artery Research*, Vol. 3, No. 2, pp. 79–88.

Severinghaus, J. (2007), 'Takuo Aoyagi: Discovery of Pulse Oximetry : Anesthesia & Analgesia', *LWW*.

Shafqat, K., Langford, R.M. and Kyriacou, P.A. (2015), 'Estimation of instantaneous venous blood saturation using the photoplethysmograph waveform', *Physiological Measurement*, Vol. 36, No. 10, pp. 2203–2214.

Shah, A.R. and Rosenberg, D. (2009), 'Defining the Facial Extent of the Platysma Muscle: A Review of 71 Consecutive Face-lifts', *Archives of Facial Plastic Surgery*, Vol. 11, No. 6.

Shelley, K.H. (2007), 'Photoplethysmography: Beyond the Calculation of Arterial Oxygen Saturation and Heart Rate:', *Anesthesia & Analgesia*, Vol. 105, No. On Line Suppl., pp. S31–S36.

Shen, H., Yang, Y.H., Wu, C.C., Sune, S.T., Lee, Y.C., Lee, S.S., Zhang, W.C., Shih, Y.S., Huang, S.C., Huang, Y.C. and Chou, L.C. (2010), 'A novel 500 samples/sec 4 by 4 photoplethysmography (PPG) array based cosmetic chip design', In *2010 International Computer Symposium (ICS2010)*, IEEE, Tainan, Taiwan, pp. 942–947.

Sherebrin, M.H. and Sherebrin, R.Z. (1990), 'Frequency analysis of the peripheral pulse wave detected in the finger with a photoplethysmograph', *IEEE Transactions on biomedical engineering*, Vol. 37, No. 3, pp. 313–317.

Sherwani, S.I., Khan, H.A., Ekhzaimy, A., Masood, A. and Sakharkar, M.K. (2016), 'Significance of HbA1c Test in Diagnosis and Prognosis of Diabetic Patients', *Biomarker Insights*, Vol. 11, p. BMI.S38440.

Shin, D.Y. and Eom, I.Y. (2013), 'A Pair of Light Emitting Diodes for Absorbance Measurement', *Bulletin of the Korean Chemical Society*, Vol. 34, No. 10, pp. 3150–3152.

Shin, D.Y., Kim, J.Y. and Eom, I.Y. (2016), 'Spectral Responses of Light-Emitting Diodes as a Photodiode and Their Applications in Optical Measurements: LEDs as a Photodiode in Optical Measurements', *Bulletin of the Korean Chemical Society*, Vol. 37, No. 12, pp. 2041–2046.

Short, D.S. (1957), 'The Jugular Venous Pulse', *Postgraduate Medical Journal*.

Signal, M., Le Compte, A., Harris, D.L., Weston, P.J., Harding, J.E., Chase, J. and on behalf of the CHYLD Study Group (2012a), 'Using Stochastic modelling to identify unusual continuous glucose monitor measurements and behaviour, in newborn infants', *BioMedical Engineering OnLine*, Vol. 11, No. 1, p. 45.

Signal, M., Le Compte, A., Harris, D.L., Weston, P.J., Harding, J.E. and Chase on behalf of the CHYLD Study, J.G. (2012b), 'Impact of Retrospective Calibration Algorithms on Hypoglycemia Detection in Newborn Infants Using Continuous Glucose Monitoring', *Diabetes Technology & Therapeutics*, Vol. 14, No. 10, pp. 883–890.

Simone, G., Tordera, D., Delvitto, E., Peeters, B., Breemen, A.J.J.M., Meskers, S.C.J., Janssen, R.A.J. and Gelinck, G.H. (2020), 'HighAccuracy Photoplethysmography Array Using NearInfrared Organic Photodiodes with Ultralow Dark Current', *Advanced Optical Materials*, Vol. 8, No. 10, p. 1901989.

Singh, A.K. (2017), 'Comparative Evaluation of Accuracy of Pulse Oximeters and Factors Affecting Their Performance in a Tertiary Intensive Care Unit', *Journal of clinical and diagnostic research*.

Sjoding, M.W., Dickson, R.P., Iwashyna, T.J., Gay, S.E. and Valley, T.S. (2020), 'Racial Bias in Pulse Oximetry Measurement', *New England Journal of Medicine*, Vol. 383, No. 25, pp. 2477–2478.

Slade, A., Simpson, S. and Wood, A. (2016), 'New and emerging non-invasive glucose monitoring technologies', Technical, University of Birmingham, publisher: Horizon Scanning Research & Intelligence Centre.

Smith, J.L. (2017), *The Pursuit of Noninvasive Glucose*, The Pursuit of Noninvasive Glucose: Hunting the Deceitful Turkey, NIVG Consulting LLC, 5th ed.

Smith, R., Balmer, J., Pretty, C.G., Mehta-Wilson, T., Desaive, T., Shaw, G.M. and Chase, J.G. (2020), 'Incorporating pulse wave velocity into model-based pulse contour analysis method for estimation of cardiac stroke volume', *Computer Methods and Programs in Biomedicine*, Vol. 195, p. 105553.

Sorensen, G.L., Jensen, J.B., Udesen, J., Holfort, I.K. and Jensen, J.A. (2008), 'Pulse wave velocity in the carotid artery', In *2008 IEEE Ultrasonics Symposium*, IEEE, Beijing, China, pp. 1386–1389.

Spitzer, A.R., Juliano, P., Peeke, K. and Fox, W.W. (1984), 'Life-threatening infantile apnea - results of primary evaluation and long-term follow-up', *Pediatric Research*, Vol. 18, pp. 349A–349A.

Stojanovic, R. and Karadaglic, D. (2007a), 'A LEDLED-based photoplethysmography sensor', *Physiological Measurement*, Vol. 28, No. 6, pp. N19–N27.

Stojanovic, R. and Karadaglic, D. (2007b), 'An optical sensing approach based on light emitting diodes', *Journal of Physics: Conference Series*, Vol. 76, p. 012054.

Stojanovic, R. and Karadaglic, D. (2013), 'Design of an Oximeter Based on LED-LED Configuration and FPGA Technology', *Sensors*, Vol. 13, No. 1, pp. 574–586.

Stroffregen, P. (2021), 'PJRC Teensyduino', Jul.

SunLED (2017), 'XZM2MRTNI55W-8 Datasheet', Feb.

Tamada, J.A., Garg, S., Jovanovic, L., Pitzer, K.R., Fermi, S., Potts, R.O. and and the Cygnus Research Team (1999), 'Noninvasive Glucose Monitoring: Comprehensive Clinical Results', *JAMA*, Vol. 282, No. 19, p. 1839.

Tamura, T., Maeda, Y., Sekine, M. and Yoshida, M. (2014), 'Wearable Photoplethysmographic SensorsPast and Present', *Electronics*, Vol. 3, No. 2, pp. 282–302.

Tang, J.Y., Chen, N.Y., Chen, M.K., Wang, M.H. and Jang, L.S. (2016), 'Dual-wavelength optical fluidic glucose sensor using time series analysis of d(+)-glucose measurement', *Japanese Journal of Applied Physics*, Vol. 55, No. 10, p. 106601.

Tang, L., Chang, S.J., Chen, C.J. and Liu, J.T. (2020), 'Non-Invasive Blood Glucose Monitoring Technology: A Review', *Sensors*, Vol. 20, No. 23, p. 6925.

Thiele, R.H., Tucker-Schwartz, J.M., Lu, Y., Gillies, G.T. and Durieux, M.E. (2011), 'Transcutaneous Regional Venous Oximetry: A Feasibility Study', *Anesthesia & Analgesia*, Vol. 112, No. 6, pp. 1353–1357.

Thomas, F., Signal, M., Harris, D.L., Weston, P.J., Harding, J.E., Shaw, G.M., Chase, J.G. and on behalf of the CHYLD Study Group (2014), 'Continuous Glucose Monitoring in Newborn Infants: How Do Errors in Calibration Measurements Affect Detected Hypoglycemia?', *Journal of Diabetes Science and Technology*, Vol. 8, No. 3, pp. 543–550.

Thomas, F., Pretty, C.G., Desaive, T. and Chase, J.G. (2016), 'Blood Glucose Levels of Subelite Athletes During 6 Days of Free Living', *Journal of Diabetes Science and Technology*, Vol. 10, No. 6, pp. 1335–1343.

Thompson, P.R. and Larason, T.C. (2001), 'Method of Measuring Shunt Resistance in Photodiodes', In *2001 Measurement Science Conference*, Anaheim, CA, p. 6.

Tierney, M.J., Tamada, J.A., Potts, R.O., Eastman, R.C., Pitzer, K., Ackerman, N.R. and Fermi, S.J. (2000), 'The GlucoWatch ő biographer: a frequent, automatic and noninvasive glucose monitor', *Annals of Medicine*, Vol. 32, No. 9, pp. 632–641.

Tottman, A.C., Alsweiler, J.M., Bloomfield, F.H. and Wouldes, T.A. (2018), 'Long-Term Outcomes of Hyperglycemic Preterm Infants Randomized to Tight Glycemic Control', *The Journal of Pediatrics*, Vol. 193, pp. 68–75.e1.

Tremper, K. and Barker, S. (1989), 'Pulse Oximetry- Anesthesiology', *Anesthesiology*, Vol. 70, No. 1, pp. 98–108.

Tuncer, T., Dogan, S. and Subasi, A. (2020), 'Surface EMG signal classification using ternary pattern and discrete wavelet transform based feature extraction for hand movement recognition', *Biomedical Signal Processing and Control*, Vol. 58, p. 101872.

Umpierrez, G.E. and Klonoff, D.C. (2018), 'Diabetes Technology Update: Use of Insulin Pumps and Continuous Glucose Monitoring in the Hospital', *Diabetes Care*, Vol. 41, No. 8, pp. 1579–1589.

Umpierrez, G.E., Hellman, R., Korytkowski, M.T., Kosiborod, M., Maynard, G.A., Montori, V.M., Seley, J.J. and Van den Berghe, G. (2012), 'Management of Hyperglycemia in Hospitalized Patients in Non-Critical Care Setting: An Endocrine Society Clinical Practice Guideline', *The Journal of Clinical Endocrinology & Metabolism*, Vol. 97, No. 1, pp. 16–38.

Uwadaira, Y., Adachi, N., Ikehata, A. and Kawano, S. (2010), 'Factors Affecting the Accuracy of Non-Invasive Blood Glucose Measurement by Short-Wavelength near Infrared Spectroscopy in the Determination of the Glycaemic Index of Foods', *Journal of Near Infrared Spectroscopy*, Vol. 18, No. 5, pp. 291–300.

Uwadaira, Y., Ikehata, A., Momose, A. and Miura, M. (2016), 'Identification of informative bands in the short-wavelength NIR region for non-invasive blood glucose measurement', *Biomedical Optics Express*, Vol. 7, No. 7, p. 2729.

Vain, N.E. and Chiarelli, F. (2021), 'Neonatal Hypoglycaemia: A Never-Ending Story?', *Neonatology*, Vol. 118, No. 5, pp. 522–529.

van Veen, R., Sterenborg, H., Pifferi, A., Torricelli, A. and Cubeddu, R. (2004), 'Determination of VIS- NIR absorption coefficients of mammalian fat, with time- and spatially resolved diffuse reflectance and transmission spectroscopy', In *Biomedical Topical Meeting*, OSA, Miami Beach, Florida, p. SF4.

Vashist, S. (2013), 'Continuous Glucose Monitoring Systems: A Review', *Diagnostics*, Vol. 3, No. 4, pp. 385–412.

Vettoretti, M., Favero, S.D., Sparacino, G. and Facchinetti, A. (2019), 'Modeling the error of factory-calibrated continuous glucose monitoring sensors: application to Dexcom G6 sensor data', In *2019 41st Annual International Conference of the IEEE Engineering in Medicine and Biology Society (EMBC)*, IEEE, Berlin, Germany, pp. 750–753.

Vlachopoulos, C., Aznaouridis, K. and Stefanadis, C. (2010), 'Prediction of Cardiovascular Events and All-Cause Mortality With Arterial Stiffness', *Journal of the American College of Cardiology*, Vol. 55, No. 13, pp. 1318–1327.

Walton, Z.D., Kyriacou, P.A., Silverman, D.G. and Shelley, K.H. (2010), 'Measuring venous oxygenation using the photoplethysmograph waveform', *Journal of Clinical Monitoring and Computing*, Vol. 24, No. 4, pp. 295–303.

Webb, R.K., Ralston, A.C. and Runciman, W.B. (1991), 'Potential errors in pulse oximetry.: II. Effects of changes in saturation and signal quality', *Anaesthesia*, Vol. 46, No. 3, pp. 207–212.

Wentland, A.L., Grist, T.M. and Wieben, O. (2014), 'Review of MRI-based measurements of pulse wave velocity: a biomarker of arterial stiffness', *Cardiovascular Diagnosis and Therapy*, Vol. 4, No. 2, p. 14.

Westenberg, J.J., van Poelgeest, E.P., Steendijk, P., Grotenhuis, H.B., Jukema, J. and de Roos, A. (2012), 'Bramwell-Hill modeling for local aortic pulse wave velocity estimation: a validation study with velocity-encoded cardiovascular magnetic resonance and invasive pressure assessment', *Journal of Cardiovascular Magnetic Resonance*, Vol. 14, No. 1, p. 2.

Westhorpe, R.N. and Ball, C. (2008), 'The Pulse Oximeter', *Anaesthesia and Intensive Care*, Vol. 36, No. 6, p. 1.

Williams, R., Needles, A., Cherin, E., Zhou, Y.Q., Henkelman, R.M., Adamson, S.L. and Foster, F.S. (2007), 'Noninvasive Ultrasonic Measurement of Regional and Local Pulse-Wave Velocity in Mice', *Ultrasound in Medicine & Biology*, Vol. 33, No. 9, pp. 1368–1375.

Wilson, R.H., Nadeau, K.P., Jaworski, F.B., Tromberg, B.J. and Durkin, A.J. (2015), 'Review of short-wave infrared spectroscopy and imaging methods for biological tissue characterization', *Journal of Biomedical Optics*, Vol. 20, No. 3, p. 030901.

Winter, B.B. and Webster, J.G. (1983), 'Driven-right-leg circuit design', *IEEE Transactions on Biomedical Engineering*, Vol. BME-30, No. 1, pp. 62–66.

Wong, X.W., Chase, J.G., Le Compte, A.J., Hann, C.E., Lin, J. and Shaw, G.M. (2009), 'An adaptive clinical Type 1 diabetes control protocol to optimize conventional self-monitoring blood glucose and multiple daily-injection therapy', *International Journal of Adaptive Control and Signal Processing*, Vol. 23, No. 5, pp. 408–434, _eprint: https://onlinelibrary.wiley.com/doi/pdf/10.1002/acs.1069.

Würth Electronic (2021), 'WL-SIRW SMT Infrared Reverse mount Waterclear Dome', Mar.

Xu, M. (2002), *Local Measurement of the Pulse Wave Velocity using Doppler Ultrasound*, PhD thesis, MIT, Department of Electrical Engineering and Computer Science.

Yadav, J., Rani, A., Singh, V. and Murari, B.M. (2014), 'Near infrared LED based non-invasive blood glucose sensor', In *2014 International Conference on Signal Processing and Integrated Networks (SPIN)*, IEEE, Noida, Delhi-NCR, India, pp. 591–594.

Yadav, J., Rani, A., Singh, V. and Murari, B.M. (2015), 'Prospects and limitations of non-invasive blood glucose monitoring using near-infrared spectroscopy', *Biomedical Signal Processing and Control*, Vol. 18, pp. 214–227.

Yamakoshi, K. and Yamakoshi, Y. (2006), 'Pulse glucometry: a new approach for noninvasive blood glucose measurement using instantaneous differential near-infrared spectrophotometry', *Journal of Biomedical Optics*, Vol. 11, No. 5, p. 054028.

Yamakoshi, Y., Ogawa, M. and Tamura, T. (2009), 'Multivariate Regression and Classification Models for Estimation of Blood Glucose Levels Using a New Noninvasive Optical Measurement Technique Named Pulse-Glucometry', *The Open Optics Journal*, Vol. 3, No. 1, pp. 63–69.

Yamakoshi, Y., Matsumura, K., Yamakoshi, T., Lee, J., Rolfe, P., Kato, Y., Shimizu, K. and Yamakoshi, K.i. (2017), 'Side-scattered finger-photoplethysmography: experimental investigations toward practical noninvasive measurement of blood glucose', *Journal of Biomedical Optics*, Vol. 22, No. 6, p. 10.

Yoon, G., Amerov, A., Kye Jin Jeon, Ju Byung Kim and Yoen-Joo Kim (1998), 'Optical measurement of glucose levels in scattering media', In *Proceedings of the 20th Annual International Conference of the IEEE Engineering in Medicine and Biology Society. Vol.20 Biomedical Engineering Towards the Year 2000 and Beyond (Cat. No.98CH36286)*, Vol. 4, IEEE, Hong Kong, China, pp. 1897–1899.

Yung-Kang Chen, Hsien-Tsai Wu, Chih-Kai Chi, Wei-Chuan Tsai, Ju-Yi Chen and Ming-Chun Wang (2004), 'A new dual channel pulse wave velocity measurement system', In *Proceedings. Fourth IEEE Symposium on Bioinformatics and Bioengineering*, IEEE, Taichung, Taiwan, pp. 17–21.

Zaharieva, D.P., Turksoy, K., McGaugh, S.M., Pooni, R., Vienneau, T., Ly, T. and Riddell, M.C. (2019), 'Lag Time Remains with Newer Real-Time Continuous Glucose Monitoring Technology During Aerobic Exercise in Adults Living with Type 1 Diabetes', *Diabetes Technology & Therapeutics*, Vol. 21, No. 6, pp. 313–321.

Zhang, M., Wang, H., Qin, H., Zhao, W. and Liu, Y. (2018), 'Phase Difference Measurement Method Based on Progressive Phase Shift', *Electronics*, Vol. 7, No. 6, p. 86.

Zhong, W., Ji, Z. and Sun, C. (2021), 'A Review of Monitoring Methods for Cerebral Blood Oxygen Saturation', *Healthcare*, Vol. 9, No. 9, p. 1104.

Zhou, C., Chase, J.G. and Rodgers, G.W. (2017), 'Efficient hysteresis loop analysis-based damage identification of a reinforced concrete frame structure over multiple events', *Journal of Civil Structural Health Monitoring*, Vol. 7, No. 4, pp. 541–556.

Zhou, T., Dickson, J.L., Shaw, G.M. and Chase, J.G. (2018), 'Continuous Glucose Monitoring Measures Can Be Used for Glycemic Control in the ICU: An In-Silico Study', *Journal of Diabetes Science and Technology*, Vol. 12, No. 1, pp. 7–19.